Université de Toulouse

THÈSE

En vue de l'obtention du

DOCTORAT DE L'UNIVERSITÉ DE TOULOUSE

Délivré par :

Institut National Polytechnique de Toulouse (INP Toulouse)

Discipline ou spécialité :

Dynamique des fluides

Présentée et soutenue par :

M. BENJAMIN STRAUBHAAR

le lundi 30 novembre 2015

Titre :

PORE NETWORK MODELLING OF CONDENSATION IN GAS DIFFUSION LAYERS OF PROTON EXCHANGE MEMBRANE FUEL CELLS

Ecole doctorale :

Mécanique, Energétique, Génie civil, Procédés (MEGeP)

Unité de recherche :

Institut de Mécanique des Fluides de Toulouse (I.M.F.T.)

Directeur(s) de Thèse :

M. MARC PRAT

Rapporteurs :

M. FELIX BUCHI, INSTITUT PAUL SCHERRER

M. GAEL MARANZANA, UNIVERSITE DE LORRAINE

Membre(s) du jury :

M. YANN BULTEL, INP DE GRENOBLE, Président

M. CHRISTOPHE TURPIN, INP TOULOUSE, Membre

M. MARC PRAT, INP TOULOUSE, Membre

Contents

List of Figures

Acknowledgements - Remerciements

Je remercie tout d'abord chaleureusement les membres du jury d'avoir accepté d'analyser ce travail. The referees, Gaël Maranzana and Felix Büchi, thank you for your time and consideration, especially for the quality of your report. Merci aux examinateurs, Christophe Turpin et Yann Bultel - qui a aussi accepté de présider ce jury - pour leurs remarques et analyses pertinentes le jour de la soutenance. Une pensée va également en direction de Joël Pauchet qui malheureusement n'a pu se joindre à nous lors de l'exposé.

Ce travail n'aurait pas pu se faire sans la direction de Marc Prat. Merci Marc pour ton aide, ta patience, tes conseils. J'ai apprécié travailler avec toi et tu as été le directeur de thèse idéal pour moi.

This PhD was founded by European project IMPALA so my special thanks goes to all the partners, it was nice to meet you around Europe and work with you. I deeply thank the Paul Scherrer Institute for the quality of the images that you provided us. Plus généralement, je tiens à remercier l'Institut de Mécanique des Fluides de Toulouse et plus particulièrement la structure GEMP où se sont déroulés ces travaux.

Comment oublier Laetitia Mottet et Mauricio Duenas Velasco, tous deux arrivés au labo en ce 1er octobre 2012. Laetitia, j'ai passé près d'un an à partager ton bureau, appris à te connaître et à te voir chercher tes cuillères pingouins, et j'avoue que ça va me manquer. Mauricio, tu es toujours le premier à donner un coup de main en cas de soucis, ou à faire des blagues (parfois spéciales !) et je t'en remercie.

Un grand merci à Yohan Davit, également appelé « Malotendon », pour tous ces moments passés avec toi, vite qu'on se refasse un petit tennis.

En écrivant ces remerciements je pense à mon ami Lingguo Du, partager ton bureau m'a fait te découvrir en tant que superbe personne, et découvrir la culture chinoise.

Une pensée me vient pour les « vieux » de GEMP, je pense à Cyprien Soulaine, Sophie Roman, Philippe Lefort notamment, et plus récemment Jianwei Guo. Merci à vous pour l'accueil lors de mon arrivée et pour les moments partagés par la suite.
Tu as été notre partenaire chaque midi
Atouts, 8 pour une poignée
Rien d'aussi bon qu'une garde contre, et
O bout le petit
Tu emmèneras

Je parle ici du tarot et de ses experts, merci à vous pour ces midis endiablés : Myriam Peyrounette, Frédéric Pierre, Jacques Franc, Ruddy Soeparno, Sylvain Pasquier, Maha Touati, Ange Gourbil, Martin Pauthenet, Antoine Naillon et tous les doctorants / stagiaires que j'oublie.

Je remercie Cosinus, le service de calcul scientifique de l'IMFT, et plus particulièrement Annaig Pedrono qui m'a bien aidé au début de ma thèse : merci de ta disponibilité et de ta gentil-

lesse.

Merci au service informatique, notamment Yannick Exposito, que j'ai souvent appelé sans faire de ticket - honte à moi - dès que j'avais un problème.

Midi, synonyme de RU, et comme promis, un grand bravo au chef de St Agne qui nous a fait saliver et reprendre des forces.

Merci à mes copines Emmie et Jordy d'avoir été à Toulouse, nos moments Daurade, QL, et j'en passe.

Mon précédent parcours à Bordeaux m'a permis de vous rencontrer, Lolo, Guigui, Simon, Kéké & consorts, tout simplement merci.

Mes amis d'Agen sont fortement remerciés, pour les années impaires La Boude, La Mase, La Nougue, la Yoye pour ne citer qu'eux, ne changez pas ! Pour les années paires, la Basile Boligue est plébiscitée avec ses Tacalfred et ses valises à Nanard. Merci mes Amis.

Une petite dédicace pour mon grand Boulou, tu es le Fontaine de mon Bataille, ou le Fabulous Fab de mon Lolo Blanc, merci d'être là depuis plus de 6 ans mon pote. Et ce n'est que le début.

Je remercie ma famille toulousaine : Tatie Martine, Tonton JP, Pierrot, Kari, Luna, et le petit dernier Enzo: j'espère que tu es fier de ton parrain !

Mes petits frères, Adrian et Matthis, vous avez la vie devant vous et je serai là pour vous guider !

Ma sœur, Mathilde, sache que je serai toujours là pour toi et j'espère avoir assuré jusqu'à présent. Reste comme tu es.

Je remercie mes grands-parents mamie Lydia & papi Henri, mamie Michou & mon papi regretté André, ma tatie Brigitte. Merci pour m'avoir gâté et s'être occupé de moi comme vous l'avez fait.

Une grosse pensée va à toi Maité, j'apprécie ta culture et ton sens de l'humour, merci pour tout.

Enfin, mes parents Christine et Jean-Louis. Dans un contexte parfois difficile, merci pour tout ce que vous avez fait pour moi depuis 26 ans. Ce travail vous est dédié.

Benjamin

Chapter 1

Introduction

Usually hydrogen is produced from hydrocarbons (steam reforming) producing carbon dioxide and carbon monoxide. Hydrogen can now be obtained from cleaner or renewable processes. When hydrogen is produced from electricity coming from nuclear power, renewable sources (renewable electricity, solid biomass, biogas) or from steam reforming of natural gas associated to a CCUS[1] unit: it is called "low carbon" hydrogen. The carbon content of this hydrogen, or greenhouse gas emissions generated during the process, is reduced or even equal to zero. When hydrogen is only produced from renewable sources (renewable electricity, biomass, biogas), it is called "renewable" hydrogen. These definitions are taken from the latest strategic roadmap of ADEME[2] on hydrogen and fuel cells.

Utility of hydrogen, and especially "renewable" hydrogen, increases either as an energy carrier - in addition to natural gas - or as a fuel, as well as many types of applications related to fuel cell for stationary or portable applications. The potential of hydrogen as an alternative energy is huge. To fully exploit it, both academic and industrial research endeavours to improve performances and to reduce the cost of technologies that are used to produce it, store it and distribute it. In particular, this is the case of the vast program called Horizon Hydrogen Energy (http://www.horizonhydrogeneenergie.com/) aiming to contribute to the emergence of a sustainable and competitive hydrogen energy sector in France and in Europe. At the same time, large pilot sites are being implemented in France. In Corsica, the MyrtE program ([Darras et al., 2012], http://myrte.univ-corse.fr/) studies the storage of hydrogen obtained with photovoltaic electricity. In Dunkerque, the GrHyd project (http://www.gdfsuez.com/) aims to use "renewable" hydrogen in addition to natural gas [lar, November 2013].

One sector takes advantage of hydrogen use: Fuel Cells (FC) and especially Proton Exchange Membrane Fuel Cells (PEMFC). Its functioning is based on reverse electrolysis: instead of using electricity and water to produce hydrogen and oxygen, it combines both of them to produce electricity, water and heat.

1.1 Brief history

As a reminder, it is in 1839 that German (he was then naturalised Swiss) chemist Christian Schönbein (1799 - 1868) highlighted the "fuel cell effect": during chemics experiments he used to do in front of his students during this year - such as oxidation of phosphorus and electrolysis of water (invented in 1802 by Sir Henry David who formulated the possibility of producing electricity via hydrogen and oxygen) - he identified a distinctive odour similar to the one surrounding the electric discharges in air. Schönbein managed to associate this pronounced smell with a gas that he called "ozone", from a Greek word "ozein" meaning to "smell". Schönbein presented his research works in a letter addressed to the "Académie des Sciences de Paris" in 1840 [Schönbein, 1840]. Schönbein also discovered the heterogeneous catalysis of water with

[1] Carbon Capture, Use and Storage: a rising technology which, applied jointly with other mitigation solutions, could ultimately greatly reduce the amount of CO_2 emitted by heavy industries and power plants.

[2] French environment and energy management Agency.

platinum-coated foams, a technique at the root of actual ideas on fuel cells.

From 1839 to 1842, Sir William R. Grove (1811 - 1896), based upon Schönbein works, discovered the first fuel cell (aqueous KOH environment).

Strong development of other types of energy generators and high cost of the materials that were used for FCs had the effects of stopping the studies on FCs and it was only in 1932 that Francis T. Bacon (1904 - 1992), a British engineer, started again research on FCs and made a first prototype powering from 1kW in 1953 up to 5kW in 1959. Then, in the 1960's and 1970's, FCs were subject to numerous works especially in the spatial domain: supply in electrical power of Gemini spacecrafts (in the early 1960's, thanks to Thomas Grub and Leonard Niedrach works for General Electric who discovered the PEM technology). But technological complexity made Nasa to abandon this industry in favour of the Alkaline Fuel Cells (AFC) that were used for Apollo program and then space shuttles. However, General Electric kept its developments up on PEMFCs. In the early 1970's, DuPont de Nemours created the tetrafluoroethylene based fluoropolymer-copolymer (Nafion) - a proton conductor - that revived the PEM technology, especially thanks to Canadian company Ballard, in the 1990's and so far.

1.2 General operating of a PEM Fuel Cell

Like every electrochemical cell or battery, a fuel cell is made of two electrodes and one electrolyte [Barbir, 2012]. Even though fuel cells have similar performance and characteristics with a battery, the two systems are different in many ways. A battery is a device storing energy and the maximum of usable energy is determined by the amount of chemical reactant that is stored in the battery itself. Battery stops producing electricity when the reactant is ran out: the battery is then discharged. In a rechargeable battery, reactant are loaded again by charge, this implies to put energy in again from an external source. On the other hand in a fuel cell, contrary to what happens for batteries, electrodes are not consumed with time and all the products are not stocked inside the cell. Fuel and oxidant come from an external source and electricity can continue to circulate as long as they are supplied to the cell. For automotive applications this is a clear advantage: the duration of filling the tank with hydrogen only lasts few minutes (like a classical tank filling-up) whereas it takes several hours to charge batteries of an electrical vehicle.

Proton Exchange Membrane Fuel Cell (PEMFC) is one of the most common and studied fuel cell. It is made of a stack of elementary cells, as shown in Figures 1.1 and 1.2. The goal of the cell is to produce electricity via reverse electrolysis of water. See for instance [Larminie, 2003; Barbir, 2012] for more details on this technology.

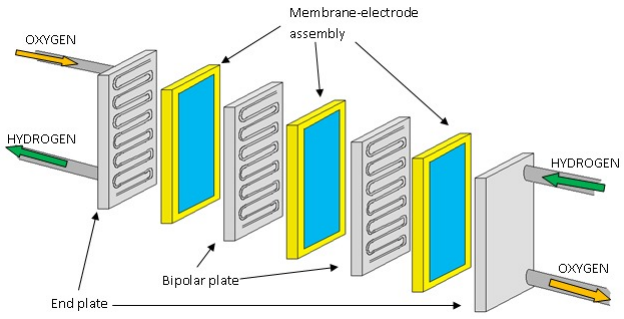

Figure 1.1: Fuel cell made of a stack of elementary cells.

Figure 1.3 sketches an elementary cell of PEMFC.

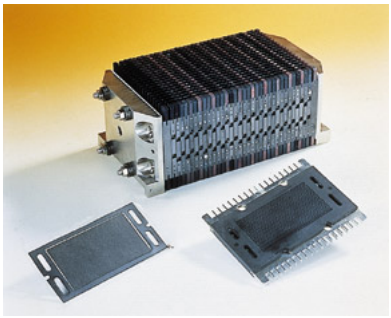

Figure 1.2: Picture of a PEMFC that is used at CEA.

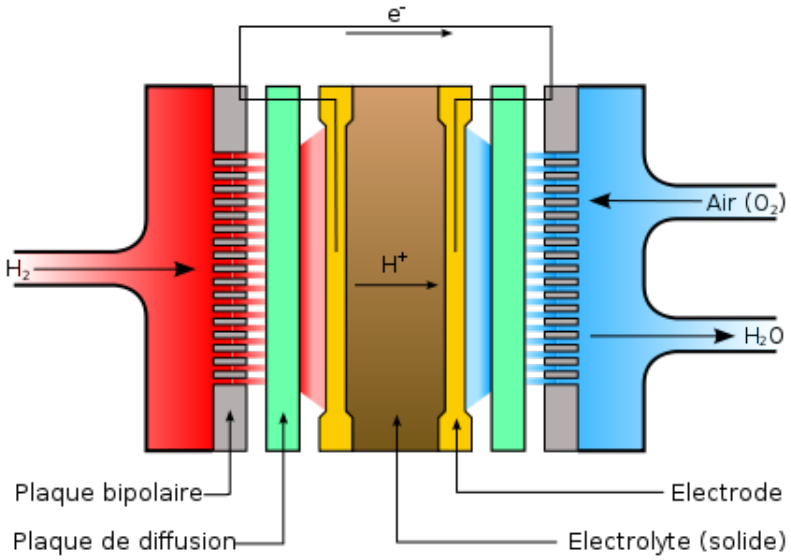

Figure 1.3: How works an elementary cell.

PEMFCs work at low temperature ($\sim 80°C$) allowing them to start quickly and make them particularly adapted to vehicles and portable applications.

Oxygen and hydrogen are carried by channels carved into the bipolar plates. Hydrogen is either used pure or obtained with on-board fuels like natural gas or methanol. Oxygen is usually the one naturally present in the air, compressed in liquid or gaseous form.

Gases invade the gas diffusion layers (at the cathode side for H_2 and at the anode side for O_2), via the adjacent channels of bipolar plates, ensuring also the removal of produced water.

The gas diffusion layers, the main topic of this thesis, have multiple functions that will be studied thereafter. They make it possible to:

- Diffuse gas towards the active layers more uniformly
- Transfer electrons from the electrodes to the bipolar plates
- Remove water from the cell

Indeed, GDLs' goal is to ensure a good water management: remove water (so as to avoid the flooding of the cell) while allowing a good humidification of the electrolyte conducting aqueous protons. GDL has to be porous and to be a good conductor. Carbon cloth or carbon paper are typically used to manufacture GDLs.

When dihydrogen comes to the anode, it is necessary to use a catalyst because chemical reactions are slow at this temperature. Among noble metals, the choice focused on platinum

which contributes to high cost of the cell. This metal coats the electrode and allows separation of dihydrogen in protons and electrons as expressed by the half redox reaction:

$$H_2 \rightarrow 2H^+ + 2e^- \tag{1.1}$$

Protons, produced during reaction 1.1 moves from the anode towards the cathode via the electrolyte (or membrane) which has to be humidified enough to make this transfer possible in aqueous phase. This membrane also prevents electrons to pass. Its thickness is about hundreds of microns. The displacement of positive charges through the membrane combined to the movement of electrons in the external electric circuit will create an electrical current: indeed, electrons that are produced at the anode with reaction 1.1 take the path illustrated Figure 1.3. They first go into the carbon fibres of the GDL, then they go in the bipolar plate, and finally they go through the external circuit to reach the cathode side.

A second reaction occurs next, according to the half redox reaction:

$$O_2 + 4H^+ + 4e^- \rightarrow 2H_2O \tag{1.2}$$

The amount of platinum coated on the electrodes is one of the major issue of PEMFCs. In order to reduce this amount and so as to reduce the costs, nano-structured electrodes have been studied [Álvarez et al., 2012; Carmo et al., 2005]. Researches are performed to combine platinum and other cheaper materials, which can cause stability problems [Collier et al., 2006] or to use other materials purely and solely replacing platinum by gold, palladium or non-noble metals [Wang, 2005].

Other issues concern the operating temperature of PEMFCs: in the presence of a negative temperature, we can naively imagine that the produced water freezes. In reality, this scenario is well understood for temperatures higher than -20°C, but below this threshold, it remains a challenge [Weber et al., 2014]. Studies have been done as well [Zhang et al., 2006] for temperatures higher than 100°C.

It appears that water management in the GDL is primordial because the maximum amount of oxygen that can be supplied is obtained when the GDL is totally dry and the maximum amount of protons is provided when the electrolyte is totally humidified. This is how to obtain the maximum efficiency.

Two extreme scenarii strongly affecting the performances of the cell have to be avoided:

- When the water production is not important enough, the membrane becomes dried and protons cannot pass through the GDL to react with oxygen: it is called cell drying.
- A contrario, when the produced water is not removed enough, the GDL is flooded and the gas access to the reaction sites is altered by this water: it is called cell flooding.

1.3 Concern

Thus, water management in fuel cells, and especially GDLs, is a major issue of PEM technology. To improve this technology, it is necessary to better understand phenomena involved in the process and that will be evoked thereafter such as water flows but also heat transfers controlling evaporation and condensation in GDLs. This study should indirectly contribute to the improvement of performances but also in a reduction of costs and an improvement of fuel cell lifespan.

The thickness of a GDL is about two hundreds of microns. This low thickness makes difficult to study experimentally internal phenomena and resulting flows. That is why we develop a numerical approach bringing into play key parameters such as porosity, wettability, permeability in order to describe at best the functioning of a GDL and of a PEMFC. In this thesis, the GDL will be modelled using a Pore Network Model (PNM) which will be described thereafter.

1.4 Goals and outline of the thesis

In this context, the goal of this thesis is to study water transfers in GDLs, to understand mechanisms and, with the use of numerical models, to predict the behaviour.

In the first part we propose a state of the art of water management in GDLs. The GDL is presented as well as the bipolar plate and the MPL, two-phase transfers in porous media are presented steering to pore network modeling. Finally a special focus on PNMs is done: all the relevant pore network models dealing with GDLs are referenced.

Then, in the second part, the pore network model we used for the thesis is presented. This model allows to compute two-phase flow with phase change and its organization and its features are developed.

The third part is a validation step of the numerical model for condensation. Calculations are made on a two-dimensional home-made micromodel. Condensation process is investigated using advection-diffusion equations for vapour transport.

The fourth part is another validation step made on comparisons with experiments taken from [LaManna et al., 2014]. A sensitivity study is performed to look at the impact of such parameters as the relative humidity in the channel, the current at the active layer / GDL interface, the in-plane and through-plane diffusion coefficients, the thermal conductivities of the GDL.

The fifth part consists in using our PNM for simulating the water management in a GDL of a working fuel cell. X-ray CT images made by PSI provide water patterns as well as saturation profiles which are compared with our simulations.

Finally, conclusion and prospects are evoked in the last part.

1.5 Funding

This work was developed within the framework of European Project IMPALA (IMprove PEMFC with Advanced water management and gas diffusion Layers for Automotive application) that was funded by the European Union's Seventh Framework Program (FP7/2007-2013) for the Fuel Cells and Hydrogen Joint Undertakink. Final goal of this project is to increase performance (with an ideal of 1 $\mathrm{W.cm^{-2}}$) and durability of PEMFCs for automotive applications improving design of gas diffusion layers (http://impala-project.eu/). This project gathers several European teams of different organisms - the Deutsches Zentrum für Luft- und Raumfahrt e.V. (Germany), the Paul Scherrer Institut (Switzerland), the European Commission - Directorate-General Joint Research Centre (JRC) - the Institute for Energy (The Netherlands), the Institut National Polytechnique de Toulouse (France), the Commissariat à l'Energie Atomique et aux Energies Alternatives (France), SGL Carbon GmbH (Germany) and Nedstack Fuel Cell Technology BV (The Netherlands) - and lasted three years (December 1st, 2012 - November 30th, 2015).

Figure 1.4: Logo of IMPALA project's partners

Chapter 2

State of the art

Contents

2.1 Presentation of the GDL

2.1.1 Introduction

In this chapter, gas diffusion layers are presented. A microscopic view is shown in Figure 2.1. GDLs are simple porous media (no electrochemical reactions) made from carbon fibres that can be of two types: carbon paper or carbon cloth as illustrated in Figure 2.1.

Carbon is a good conductor and enables electron transport. An ideal GDL has to be highly porous (better permeability, better diffusion), to be hydrophobic (we will see why later), to be a good electrical and thermal conductor, to not break under compression stress, not to oxidise, to not freeze. GDLs are treated with Polytetrafluoroethylene (PTFE), in order to make them hydrophobic. This property may be characterized by the contact angle concept, i.e. the angle formed between a surface and the interface of the two fluids of the study (here, water and air). The surface is said hydrophilic if the contact angle that is measured in the water is lower than $90°$. On the contrary, if the contact angle measured in the water is larger than $90°$ then the surface is told hydrophobic. In the presence of PTFE, the contact angle of water is about $110°$ whereas it is only $80°$ when carbon fibres are untreated.

As explained in the 2.3.1, hydrophobicity makes water to evacuate more efficiently. Unfortunately, the hydrophobic treatment of carbon fibres is generally non-uniform: they are not all covered of PTFE, and impurities, ageing, tend to reduce hydrophobicity, making some regions of the GDL hydrophilic. We talk of mixed wettability when there is coexistence, in the medium, of both hydrophilic and hydrophobic zones.

Other processes can also allow to evacuate water more efficiently of the GDL: [Markötter et al., 2012; Markötter et al., 2015] found that simply perforating GDL with a laser in the through-plane direction is an easy way to evacuate water from the GDL. With X-ray imaging (cf. 2.4.2), they also found that water goes preferentially along carbon fibres and can be blocked under the ribs before reaching the outlet.

2.1.2 Ahead of the GDL: the micro-porous layer (MPL)

The GDL that is presented above - that could be called GDL's mechanical support - is often completed with a microporous layer (or MPL). With a misuse of language, the term "GDL" means

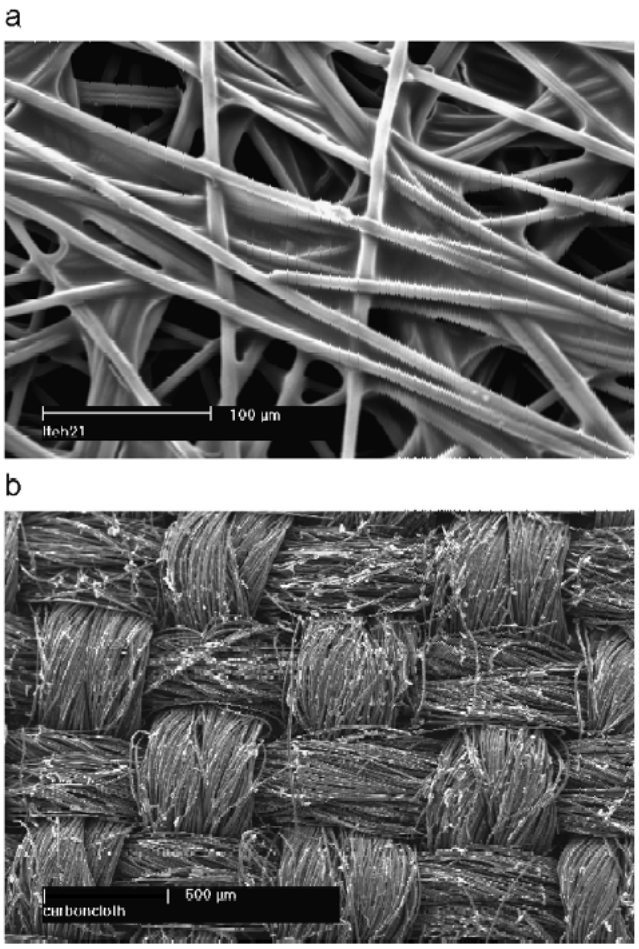

Figure 2.1: View of two types of gas diffusion layer obtained by Scanning Electron Microscopy: a) carbon paper and b) carbon cloth, from [Sinha and Wang, 2008].

"MPL + GDL's support". The MPL is made of carbon particles mixed with PTFE, so mostly hydrophobic. This ratio of hydrophobic pores is found to be optimal around 35% [Qi and Kaufman, 2002] in terms of water management. While the pore size of macroporous substrates is in the range of 1 to 100 µm, the pore size of the microporous layers is around hundreds of nanometers as it was said before. The thickness of the MPL, about 20µm, is much lower than the one of the GDL's support, as shown in Figure 2.2. The porosity of the MPL is about 50% whereas the porosity of the GDL is 70%.

The Pore Size Distribution (PSD) of the MPL varies from 0.1 µm (micropores) to few micrometers (macropores), according to [Chun et al., 2010], for instance. The MPL allows to increase the power of the PEMFC, especially at high current densities [Qi and Kaufman, 2002; Chen et al., 2004; Weber and Newman, 2005]. [Nam et al., 2009] also showed that in the presence of MPL, the size and the saturation level of water droplets at the GDL/channel interface were reduced. This enables to increase diffusion in the catalyst layer [Wang and Van Nguyen, 2010; Lu et al., 2010]. The MPL, acting like a valve, also reduces the number of water breakthrough points at the outlet of the GDL. This decreases the water saturation and so increases the oxygen diffusion through the GDL. The MPL also enables to reduce the ohmic loss and to avoid materials from the active layer to get into the large pores of the GDL's support. Moreover, another function is to reduce the water back diffusion from channels towards electrodes.

When the micro-porous layer operates under low relative humidity conditions, it is desirable to keep the membrane hydrated in order to keep the membrane resistance low enough, whereas under high relative humidity conditions, produced water has to be removed quickly from the reaction sites [Nishiyama and Murahashi, 2011], which is possible allowing water transport in hydrophilic micropores of the MPL and gas transport in the macropores.

[Wang and Van Nguyen, 2010] also showed that the higher the water pressure is (i.e. when the MPL is enough hydrophobic to contain water), the more this water goes upstream, namely towards the cathode. When coupled to electro-osmosis of water (upstream transport of water due to current), this phenomenon releases the access of active layer while hydrating the anode.

More recently, [Wang et al., 2015] conducted both experiments and numerical simulations on a double-layer GDL with different PTFE loadings. This double-layer GDL can be seen as the addition of a MPL to a GDL. They showed that the overall saturation level is decreased when the layer with higher PTFE loading is placed adjacent to the catalyst layer.

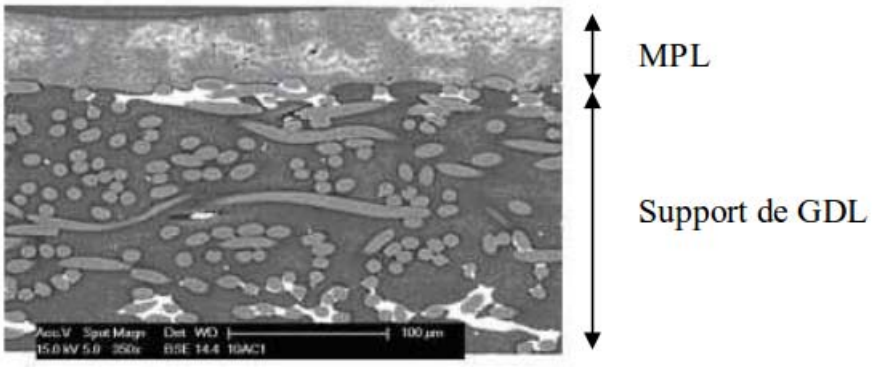

Figure 2.2: SEM view of a GDL's support and its MPL. Taken from [cha, 2010]

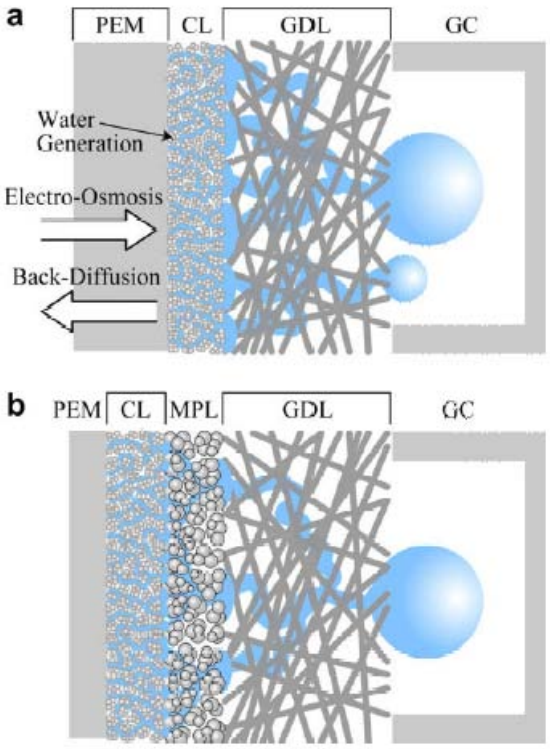

Figure 2.3: GDL with addition (b), or not (a), of a Micro Porous Layer. Taken from [Nam et al., 2009].

2.1.3 Downstream of the GDL: the bipolar plate

In most cases, bipolar plates are made of graphite - owing to its high strength to corrosion and to the fact that it is a good electrical conductor. However, because of its fragility and its lack of mechanical strength combined to its manufacturing cost for great quantity, graphite can

be considered as unsuitable for automotive industry, leading some researchers to be interested in materials such as stainless materials - coated or not [Cho et al., 2004; Tawfik et al., 2007]. Whether it is at the anode or at the cathode, bipolar plate's function is to take reactant gases from the channels to the electrodes, to evacuate produced water at the cathode, as well as electrically connect a cell to another (the stack is formed by a series of cell). Bipolar plate's role is also to support the fragile MEA (Catalist layer + Membrane). Finally, bipolar plates have to cool the system down, in the absence of a dedicated device [Li and Sabir, 2005]. Oxygen supply channels are carved on the bipolar plates: they can be straight, in serpentine, interdigitated, or fractals, as shown in Figure 2.4. We call "rib" or "land" the part of the bipolar plates that is in contact with the GDL. An elementary cell will be composed of a GDL, a supply channel and a rib in the cathode side for the most of the study as illustrated in Figure 2.5.

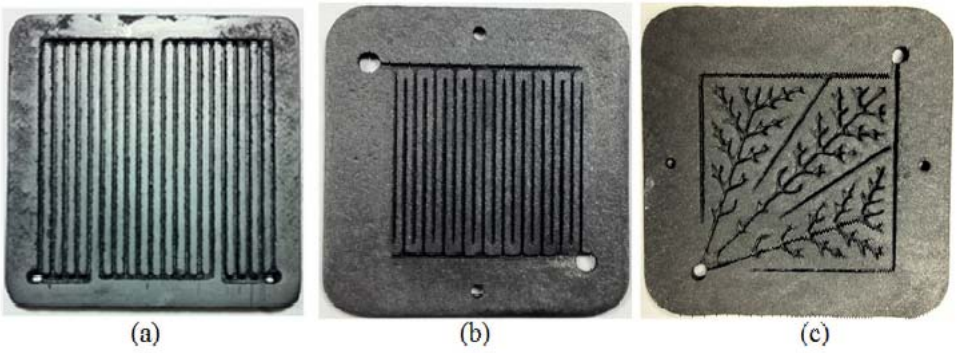

Figure 2.4: Several types of carved channels in a bipolar plate: a) serpentine, b) interdigitated, c) fractal.

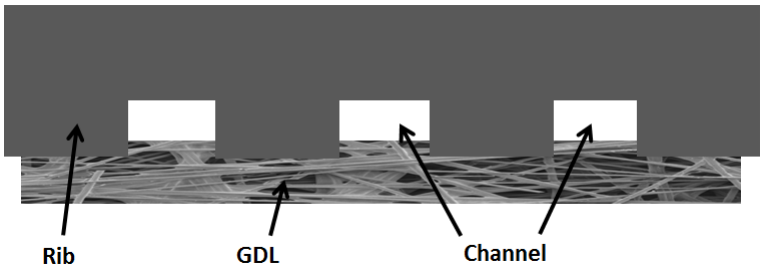

Figure 2.5: Example of an elementary cell used for numerical simulations.

Obviously flow field design can affect mechanisms of liquid-water transport. In interdigitated and serpentine flow-field designs, pressure gradients between adjacent channels induce convective transport through the GDL, which is called "cross flow". [Santamaria et al., 2015] showed with neutron radiography imaging that as cross-flow increased, permeability trended upward and saturation decreased.

2.2 Transfers in porous media

2.2.1 Two-phase flow model and presentation of pore networks

Two-phase flow studies in porous media are more often based on the generalized Darcy law and the concept of macroscopic capillary pressure (retention curve). Applied to the GDL water problem, this classical approach can be formulated as follows: considering the water production rate (presented in 2.3.2), an interesting analysis is done by [Pasaogullari and Wang, 2004] proving the unfounded nature of continuum models.

At steady state, if the air is fully saturated with water vapour, the liquid water mass flux is equal to the amount of water that is produced at the active layer. Supposing there is no water

transport from the active layer towards the membrane, we get:

$$\frac{1}{2F}M^{H_2O} = \frac{k_{rl}}{\nu}K[\nabla p_c + (\rho_l - \rho_g)g] \tag{2.1}$$

with F denotes the Faraday constant (= 96487 $\mathrm{C.mol^{-1}}$), M^{H_2O} the molar mass of water (in $\mathrm{kg.mol^{-1}}$), k_{rl} the relative permeability of water, ν the cinematic viscosity of water (in $\mathrm{m^2.s^{-1}}$), K the permeability of the medium (in $\mathrm{m^2.s^{-1}}$), p_c the capillary pressure, ρ_l and ρ_g the densities of water and air respectively (in $\mathrm{kg.m^{-3}}$) and g the gravity (in $\mathrm{m.s^{-2}}$).

Here it is supposed that the pressure in the gas phase remains constant and equal to the total pressure in the supply channel. Moreover, the GDL is a very thin medium and gravity effect may be neglected.

The capillary pressure between two phases is expressed as:

$$p_c = \sigma cos\theta_c \left(\frac{\epsilon}{K}\right)^{1/2} J(s) \tag{2.2}$$

with σ as the surface tension (in $\mathrm{N.m^{-1}}$), θ_c as the contact angle, ϵ as the porosity and $J(s)$ as the Leverett function.

So:

$$\frac{1}{2F}M^{H_2O} = -\frac{s^3}{\nu}K\sigma cos\theta_c \left(\frac{\epsilon}{K}\right)^{1/2} \nabla J(s) \tag{2.3}$$

with s the water saturation.

For an hydrophobic medium:

$$J(s) = 1.417s - 2.120s^2 + 1.263s^3 \tag{2.4}$$

Combining 2.1 et 2.2 we get:

$$\frac{1}{2F}M^{H_2O} = -\frac{\sigma cos\theta_c(\epsilon K)^{1/2}}{\nu} s^3(1.417 - 4.240s + 3.789s^2)\frac{\partial s}{\partial x} \tag{2.5}$$

To make the problem easier, one-dimensional transport is considered along the thickness of the GDL. It is reduced to a differential equation that can be solved analytically. For a hydrophobic medium, $\theta_c > 90°$:

$$s^3(1.417 - 4.240s + 3.789s^2)\frac{ds}{dx} = \frac{1}{2F}M^{H_2O}\frac{\nu}{\sigma cos\theta_c(\epsilon K)^{1/2}} \tag{2.6}$$

Integrating, we get:

$$s^4(0.35425 - 0.8480s + 0.6135s^2) = \frac{1}{2F}M^{H_2O}\frac{\nu}{\sigma cos\theta_c(\epsilon K)^{1/2}}x + C \tag{2.7}$$

The integration constant C depends on boundary conditions i.e. the liquid saturation at the interface GDL/canal. This calculation gives the "continuum model" curves as shown in Figure 2.6.

Validity of this model is questionable. The GDL is very thin and does not allow scale separation conditions and it is not possible to extract a REV (Representative Elementary Volume), e.g. [Rebai and Prat, 2009; Prat and Agaësse, 2015]. Typically, the thickness of the GDL is less than 300 μm, with average pore diameter of about 40 μm, corresponding to less than 10 pore sizes over the thickness. Actually, [Rebai and Prat, 2009] compared the saturation profiles obtained with both a continuum model (for a capillary number of $10^{-7}/10^{-8}$) and a PNM[1] (with IP[2] algorithm): the profiles obtained with the continuum model are quite different from the ones computed with the PNMs, see Figure 2.6.

[1] Pore Network Model
[2] Invasion Percolation

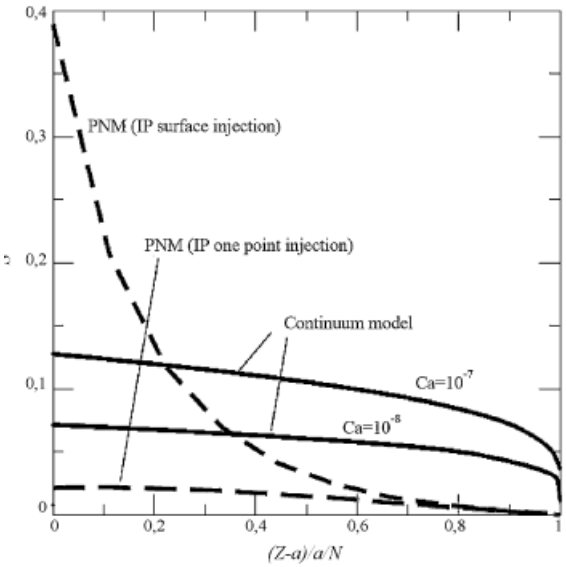

Figure 2.6: Comparison of saturation profiles using a Pore Network Model (for two injection conditions) and the classical continuum model (for two Capillary Numbers), from [Rebai and Prat, 2009].

Additionally, classical macroscopic parameters of the continuum model (capillary pressure, relative permeability) are difficult to measure but this is possible as shown in [Volfkovich et al., 2001; Gostick et al., 2006; Cheung et al., 2009; Fairweather et al., 2010].

All these reasons pushed us into developing a Pore Network Model representing the porous medium. This approach is classical for rocks, see [Fatt et al., 1956] for the first PNM and [Blunt, 2001; Blunt et al., 2002] for a review article on PNM developed for the study of two-phase flows in porous media. This approach seems to be less obvious to represent GDLs. Indeed, a GDL is a tangle of fibres, and it is difficult to differentiate pores from solid parts. These fibres give form to constrictions and we assimilate the skeleton of void to a pore network of interconnected pores and throats. The Pore Network Models are an alternative to continuum models. They are preferred to Direct Numerical Simulation (DNS) - computing saturation profiles, gas concentrations, fluid properties via a GDL pore scale resolution - because of their lower computational cost. Among DNS methods, we can list Volume Of Fluid (VOF) models [Hirt and Nichols, 1981], Mixture models [Wang and Cheng, 1996] and Lattice Boltzmann Methods (LBM) (e.g. [Rothman, 1988; McNamara and Zanetti, 1988; Shan and Kailath, 1988]).

The network is invaded by a fluid progressing pore by pore and throat by throat following physical laws related to capillary phenomenon.

The pore network is represented by a regular succession of pores and throats. See Figure 2.7 for an analogy between the fibre structure of the GDL and the equivalent cubic lattice representation.

Pores are located at the lattice junctions and are represented by cubes whose equivalent diameter is randomly chosen according to a uniform distribution in the range $[d_{pmin}, d_{pmax}]$. The pores are connected to throat whose equivalent diameter is also randomly chosen according to a uniform distribution in the range $[d_{tmin}, d_{tmax}]$. See Figure 2.8 to get an idea about the computational domain of a GDL. The values d_{pmin}, d_{pmax}, d_{tmin}, d_{tmax} as well as the sizes of the GDL are taken from the literature and from the data obtained in the framework of IMPALA European project. A zoom on a 3D computational domain showing the pore and throat diameters is illustrated in Figure 2.9.

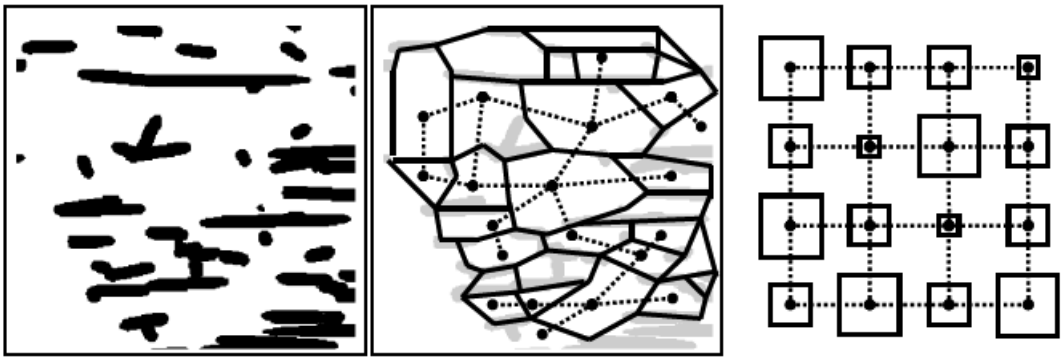

Figure 2.7: Left: In-plane view of a GDL. Middle: Conceptual sectioning of pore space into pore bodies and throats. Right: Cubic lattice of equivalent properties. Taken from [Gostick, 2008].

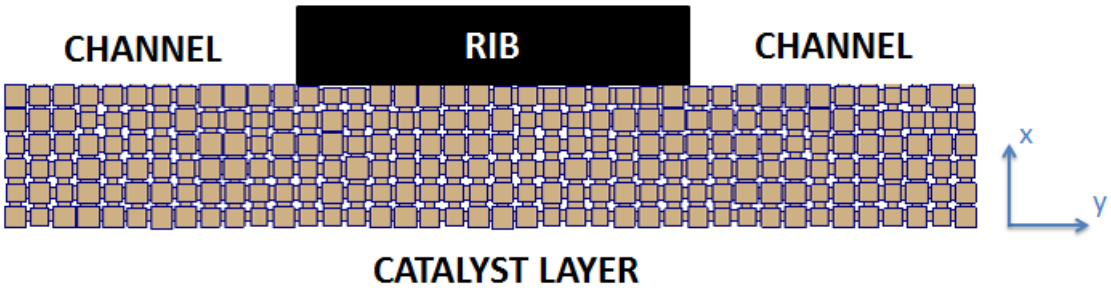

Figure 2.8: Sketch of a computational domain (2D illustrative example).

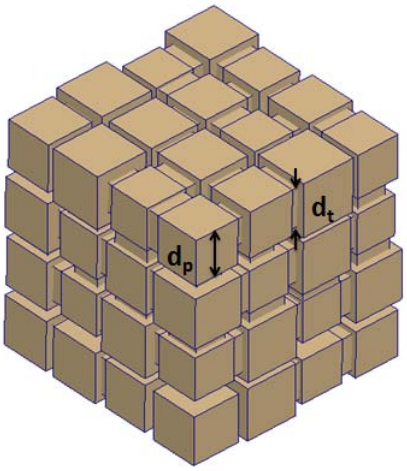

Figure 2.9: Zoom on a 3D computational domain. The pore and throat diameters are depicted.

2.2.2 Two-phase invasion in a porous medium

Two-phase flow in porous media depends on the competition between viscous forces and capillary forces. This competition affects directly the phase distribution. Water transport in the GDL is assimilated to a process called drainage, i.e. the displacement of a wetting fluid by a non-wetting one. Water is the non-wetting fluid in the presence of PTFE because the contact angle taken in the water is larger than $90°$, as illustrated in Figure 2.10.

[Lenormand et al., 1988] studied different types of flows of two non-miscible fluids in a drainage experiment and showed that invasion patterns depend on the Capillary Number Ca and on the ratio of viscosities M:

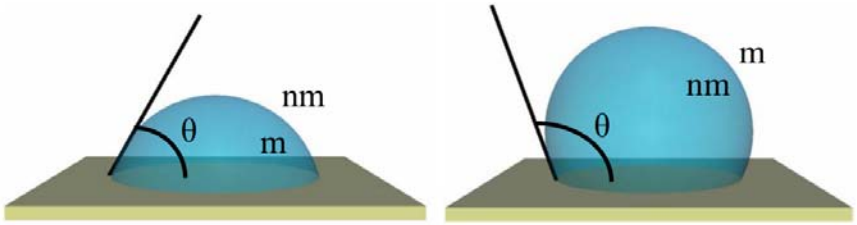

Figure 2.10: Representation of a wetting fluid (on the left) and a non-wetting one (on the right) [Ceballos, 2011].

$$Ca = \frac{\mu_l U}{\gamma} \tag{2.8}$$

and

$$M = \frac{\mu_l}{\mu_g} \tag{2.9}$$

with μ_l and μ_g are the dynamic viscosity of the non-wetting and the wetting fluid ($\mathrm{Pa.s}$) respectively, U its displacement velocity ($\mathrm{m.s^{-1}}$) and γ the surface tension between the two fluids ($\mathrm{N.m^{-1}}$).

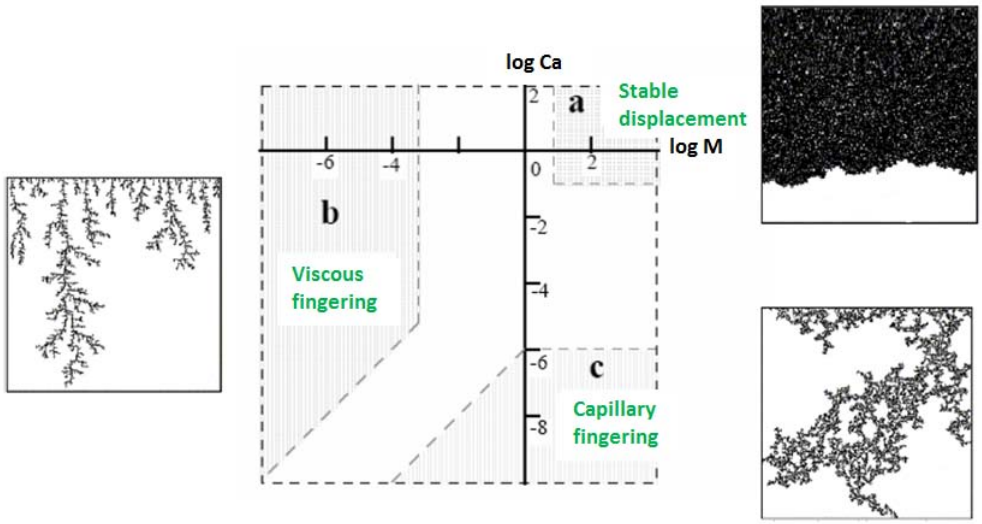

Figure 2.11: Illustration of the different regimes of displacement of a non-wetting fluid as a function of the capillary number and the ratio of the viscosities. The three invasion patterns are represented. Taken from [Ewing and Berkowitz, 2001].

[Lenormand et al., 1988] highlighted three asymptotic regimes as illustrated in Figure 2.11:

- The stable displacement (when the injected fluid is more viscous than the displaced fluid and the capillary number is high) corresponds to a flat front and most of the pores located behind the interface are filled: the viscous effects are dominant over the capillary effects.
- The viscous fingering regime (when the injected fluid is less viscous than the displaced fluid and the capillary number is high) is composed of straight liquid paths reaching quickly the outlet, without having large ramifications. Capillary effects are nigligible in this regime.
- The capillary fingering regime (when thecapillary number is small) is composed of liquid paths made of many tortuous ramifications. Capillary effects are dominant.

At 80°C, $M \simeq \frac{3,55.10^{-4}}{2.10^{-5}} \simeq 17,5$ and in the case of PEMFCs, Ca can be expressed as:

$$Ca = \frac{\mu_l i M_{H_2O}}{\gamma cos\theta_w 2F\rho_l} \tag{2.10}$$

where M_{H_2O} is the molar mass of water, ρ_l is the water density and θ_w is the contact angle measured in the wetting fluid. With $i = 1\text{A.cm}^{-2}$ and $\theta = 70°$, we get $Ca \simeq 10^{-7} - 10^{-8}$. That corresponds to the capillary fingering regime. At small Ca, the flow can be considered as being quasi-static. It is possible to simulate the capillary fingering regime using the Invasion Percolation algorithm developed by [Wilkinson and Willemsen, 1983]: the occupied pore the liquid is going to invade preferentially is the neighbouring throat of largest diameter, i.e. the one where the capillary pressure threshold is the smallest, see Figure 2.12. This is a direct consequence of the Young-Laplace equation:

$$p_c = \frac{4\gamma cos\theta}{d_i} \tag{2.11}$$

where p_c is the capillary pressure between the two phases, d_i is the diameter of the throat, θ is the contact angle and γ is the surface tension.

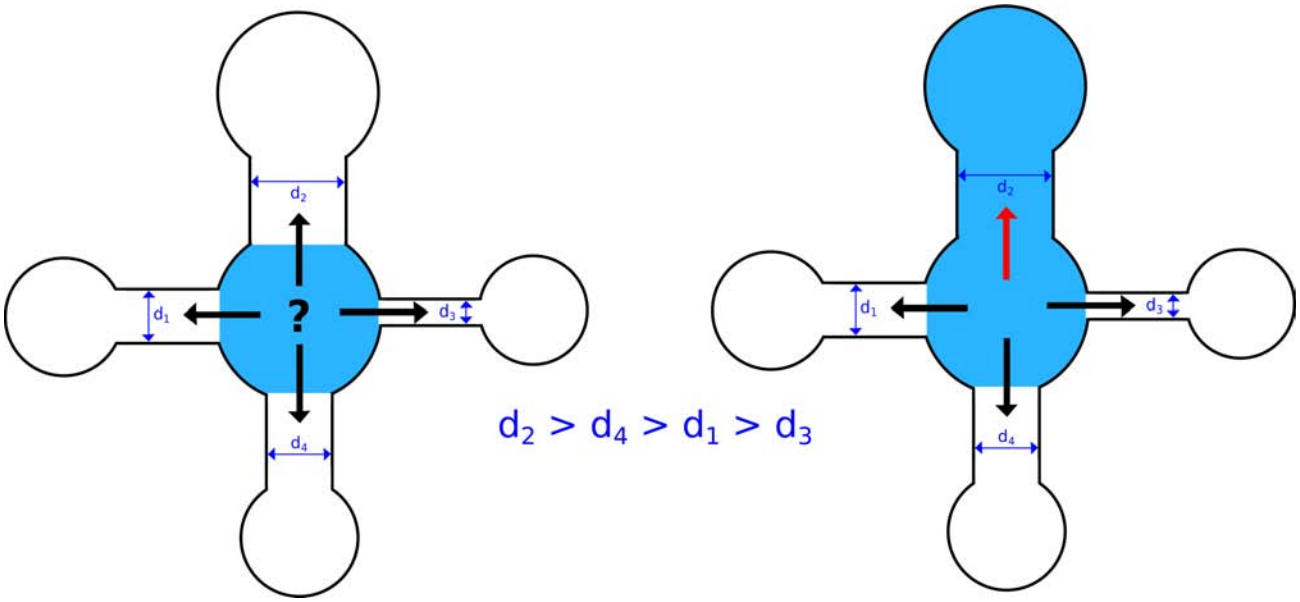

Figure 2.12: Illustration of the Invasion Percolation concept.

The conclusion is that the invasion regime expected in the GDLs is the capillary fingering regime, a regime that can be computed on a network thanks to the Invasion Percolation algorithm. Notice that this is only valid on a sufficiently hydrophobic medium.

2.2.3 Transport of species

Let N_A the number of moles of species A crossing a unit area in unit time. For simplicity only direction z is considered and this molar flux can be expressed as [Bird et al., 2002]:

$$\underbrace{N_{Az}}_{\text{combined flux}} = \underbrace{-cD_{A/B}\frac{\partial x_A}{\partial z}}_{\text{diffusion flux}} + \underbrace{x_A(N_{Az} + N_{Bz})}_{\text{convective flux}} \tag{2.12}$$

where the Fick's law has been used to express the diffusion flux.

This formulation assumes that there are only two components in the mixture. In our case, a binary mixture made of water vapour and air is considered. In reality, air is composed of many elements but mostly dinitrogen ($\sim 78\%$) and dioxygen ($\sim 21\%$). So a more accurate formulation of the diffusion equation - for future works - would be to take into account a ternary mixture

composed of water vapour, dinitrogen and dioxygen. Fick's law is no longer appropriate and a famous model for describing the multicomponent diffusion is the Maxwell-Stefan equation:

$$\nabla x_i = -\sum_{j=1(j\neq i)}^{N} \frac{1}{cD_{ij}} \left(x_j \dot{\mathbf{n}}_i'' - x_i \dot{\mathbf{n}}_j'' \right) \quad , \quad i = 1, 2, \cdots, N \ - 1 \qquad (28) \qquad (2.13)$$

where D_{ij} is the binary diffusivity from species i to species j, x_i and x_j are the molar fraction of species i and j respectively and $\dot{\mathbf{n}}_i''$ and $\dot{\mathbf{n}}_j''$ are the molar flux of species i and j respectively. Equation (2.13) was originally suggested by Maxwell [Maxwell, 1867] for a binary mixture based on kinetic theory and was extended to diffusion of gaseous mixtures of N species by Stefan [Stefan, 1871] .

For an N-component system, N(N–1)/2 diffusivities are required. The diffusion in a multicomponent system is different from diffusion in a binary system, because the movement of the i^{th} species is no longer proportional to the negative concentration gradient of the i^{th} species. It is possible that:

1. a species moves against its own concentration gradient, referred to as reverse diffusion
2. a species can diffuse even when its concentration gradient is zero, referred to as osmotic diffusion
3. a species does not diffuse although its concentration gradient is favourable to such diffusion, referred to as diffusion barrier

according to [Bird et al., 2002].

2.3 Application to gas diffusion layers of PEMFCs

2.3.1 Wettability

Wettability, i.e. the value of the contact angle at the water/air/solid triple line, plays a crucial role in the study of two phase flows in a GDL. Actually, wettability properties of GDLs are difficult to characterise. In reality, PTFE is not uniformly distributed throughout the GDL. A priori some regions of the GDL are not coated with PTFE (ageing, poor treatment) and the contact angle is about 80°: these are hydrophilic regions. In the zones that are treated with PTFE, the contact angle is about 110°: these are hydrophobic regions. [Chapuis et al., 2008] showed that contact angle has an influence on water saturation and on the invasion pattern of the porous medium, see Figure 2.13 for more details.

For the invasion patterns shown in Figure 2.13, the wettability is uniform but varies gradually on a range including the hydrophilic and hydrophobic regimes ($70° \rightarrow 110°$ for instance). The contact angle is therefore uniform for each calculation [Chapuis et al., 2008; Chraïbi et al., 2009]. Another kind of study of this type has been made with PNMs defining a fraction f of hydrophilic pores in a hydrophobic network: the value of the local contact angle is thus set either hydrophobic ($> 90°$) or hydrophilic ($< 90°$) [Gharbi and Blunt, 2012; Park and Popov, 2009; Pauchet et al., 2012; Sinha and Wang, 2008; Wu et al., 2012a; Weber et al., 2004].

[Kuttanikkad et al., 2011] showed that macroscopic properties of the GDL are independent of fraction f (%) of hydrophilic pores below a threshold corresponding to the percolation threshold of a hydrophobic network, i.e. the critical value f_c beyond which it exists at least a continuous path of hydrophilic pores connecting the inlet to the outlet of the network. This result qualitatively agrees with experimental studies showing that the capillary pressure curve is independent of the quantity of PTFE that is used if this value is larger than about 5 % [Fairweather et al., 2010; Wu et al., 2012a].

In this way, it is possible to link the quantity of PTFE with flow regimes established by Lenormand: the more there is PTFE, the more there are hydrophobic pores and the more the flow regime is likely to be the capillary fingering regime. A contrario, the less the GDL is treated with PTFE, the more there are hydrophilic pores and the more the flow regime is likely to lead

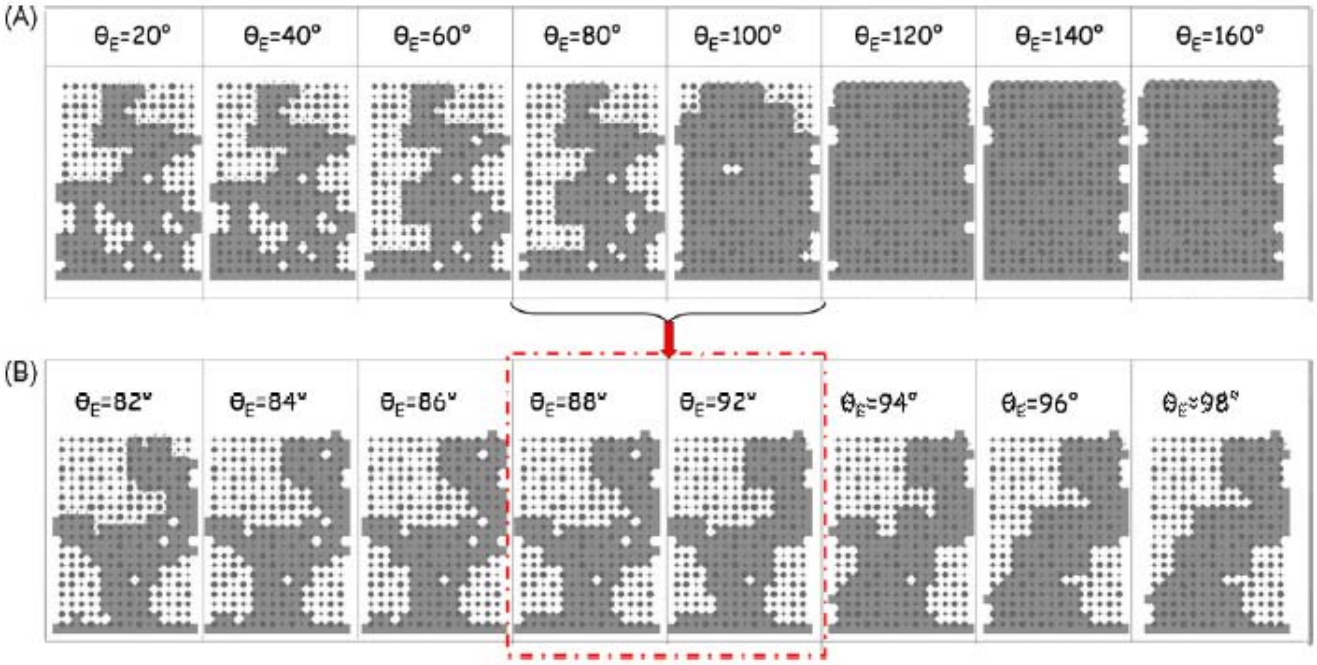

Figure 2.13: (A) Change in the invasion pattern at breakthrough in a model fibrous medium VS the contact angle in the defending fluid (air) Θ_E. The invading fluid is in grey. (B) Detailed progression for $\Theta_E \in [82°, 98°]$. Taken from [Chapuis et al., 2008].

to the formation of a flat front. Thus it is then obvious that the performance of the cell will be improved with addition of PTFE in order to avoid flooding [Shahraeeni and Hoorfar, 2014].

Studies have been made on loss of PTFE after numerous cycles [Borup et al., 2007; Ramasamy et al., 2008] and showed that the presence of MPL leads to decrease the hydrophobicity loss.

Unless otherwise mentioned, we will consider that PTFE is uniformly distributed throughout the GDL and thus that the contact angle remains constant all over the fibrous surface, on the order of 110° (if the surface is perfectly covered with Teflon). Under these conditions, the GDL is uniformly hydrophobic.

2.3.2 Liquid water formation on the cathode side

A crucial and somewhat unknown point is how the liquid water forms or appears in the GDL. Answering this question, even only partially, is perhaps the major objectives of this thesis. The water production rate can be easily estimated from the electro-chemical reaction as:

$$Q = \frac{iA}{2F} \tag{2.14}$$

where F is the Faraday constant (F = 96 485,34 $\mathrm{C.mol^{-1}}$), i the current density and A the in plane area over which the current is produced.

A significant fraction of the produced water at the cathode goes toward the cathode GDL. The main question is whether this water reaches the GDL in vapour form or in liquid form. Many previous studies were more or less explicitly based on the assumption that the water enters in liquid form into the GDL, leading to the consideration of a capillary driven process of liquid water transport within the GDL. On the other hand, several authors (references will be given in the next chapters) pointed out the probable importance of phase change phenomena within the cell. An alternative scenario is therefore that water enters the GDL in vapour phase and condenses. Naturally, mixed scenarios leading to the occurrence of liquid water both as a result of condensation and invasion in liquid phase from the catalyst layer or the MPL is not impossible (for example if condensation occurs in the MPL as well).

2.3.3 Recent examples of PNM

For the reasons that were mentioned before, pore networks have been frequently used in recent years for the study of water flow in PEMFC. In the first works, these models were isothermal, stationary and considering only the GDL. Then, with the improvement of calculation power of computers, the models became three-dimensional, non isothermal, dynamic, and able to represent the GDL and the channel, phase change, electron transport, anisotropy, compression, etc. More a model is complex, more the computer cost is important. These past few years, we can notice several noteworthy papers.

Oxygen diffusion is a key element of gas diffusion layers i.e. how to disseminate oxygen at best towards the active layer? [Gostick et al., 2007] studied the gas transport with two different setups: the first one when water fully invades the pore and so it prevents any connection with the neighbouring pores (pessimistic case) and another one when residual gas in the pores that have been invaded by water is conductive (optimistic case). The results of these simulations were compared with commonly used models of relative permeability and diffusivity. It was found that these models tended to agree with Case 2, which likely overestimates mass transfer in the gas phase.

In order to develop representative pore network models, it is necessary to consider the macroscopic parameters of the network. [Markicevic et al., 2007] created a two-dimensional square network and changed two parameters: the width of the network and the heterogeneity of throats, i.e. the variations of width between throats belonging to a same network. They showed that the more the network size increases, the more the relative permeability decreases, but the latter increases as the heterogeneity is important. Indeed, the throats with the largest radius are invaded more easily, leading to higher flows for the invading phase. Relative permeability is constant for low saturations and varies as a power law for higher saturations. This law does not depend on the size of the network.

[Sinha and Wang, 2007] were the first to investigate liquid water transport at the pore scale: they showed that the flow in GDLs happens at very low capillary number and than this leads to a capillary fingering regime in the presence of a uniformly hydrophobic medium. This is consistent with [Lenormand et al., 1988] work.

[Lee et al., 2009] showed numerically that the saturation curve along the GDL's profile was concave which means it is an Invasion Percolation process. More over, a "flux" boundary condition at the active layer/GDL was found to be better than a "pressure" boundary condition.

[Rebai and Prat, 2009] showed that classical continuum models lead to poor predictions of the water distribution in the GDL, because of a lack of length scale separation and because of the dominant capillary effects. In other words, the existence of a Representative Elementary Volume (REV) is not fulfilled. This article presents pro and con arguments for the use of pore network models.

[Ceballos and Prat, 2010], used an Invasion Percolation algorithm with multiple injections (water is injected via several injection points instead of the uniform pressure condition of classical IP simulations), to determine a droplet density at the GDL/channel interface as well as saturation profiles equivalent to what is observed in in-situ experiments.

[Mukherjee et al., 2011] made a review on modelling of PEMFC at the pore scale, studying the efficiency of Lattice-Boltzmann Methods (LBM), Pore Morphology (PM) - which is based on a real representation of the porous medium - and Pore Network Models. LBM simulations can be used to study the influence of the wettability on the two-phase flow but also the capillary pressure and relative permeability curves as a function of the water saturation. PM is a quick and interesting tool to simulate a quasi-static drainage experiment in order to estimate the Pc-s curve based on the analysis of the digitised structure. Pore networks are used to study two-phase transport, to compute Pc-s curves and are efficient for real operating conditions. More over, LBM and PNM allow to simulate low-capillary number flows.

[Wu et al., 2012b] studied the effect of cracks in the MPL using a three dimensional PNM. A higher pressure is necessary for water to reach the GDL in the presence of a MPL with no

defects, and both permeability and relative humidity decrease. The increase in the thickness of the MPL decreases the saturation in the GDL as well as the effective diffusivity of oxygen (for a certain capillary pressure). But the liquid permeability becomes higher with the increase of this thickness (except when S_w gets closer to 1). They showed that the liquid distribution in the GDL changes significantly in the presence of the MPL: a saturation jump is observed at the MPL/GDL interface. To sum up, the effective diffusivity of oxygen of the whole GDL/MPL - using a 25 microns thick GDL - is better at the breakthrough than the one of a GDL only.

In their following paper, [Wu et al., 2013] showed that in the presence of a MPL, the inlet saturation of the GDL is reduced (saturation jump). If the MPL has a crack (that is supposed to be under the rib), liquid preferentially moves along it. The addition of a MPL does not necessarily improve performances of the cell: if the difference between the effective diffusivity of oxygen between the GDL and the MPL is weak, then the presence of the MPL is beneficiary, if this difference if large, then it is not.

[Alink and Gerteisen, 2013], in order to get closer to the real structure of a GDL in two dimensions, developed a percolation model based on the fibrous structure rather than the pore structure, using the contact angle distribution of fibres, their size and direction, and the spatial porosities. So in this work, these are the stable water paths that are connected with unstable links and a percolation + condensation model is computed.

[Médici and Allen, 2013] showed with a two-dimensional model that at low temperature and high relative humidity in the channel, the liquid water could move through the GDL with a capillary fingering pattern and could breakthrough at the level of the channel, whereas at high temperature and low relative humidity, water partially evaporates and reaches the channel through vapour phase. However, in this case, water tends to pile up in the catalyst layer side: this is due to the high vapour concentration close to the active layer that reduces the evaporation rate at the air/water interface.

[Shahraeeni and Hoorfar, 2014] developed a three-dimensional PNM using fluorescence microscopy. They looked at the PTFE treatment effect and showed that the hydrophobic treatment limits the number of pores being invaded at the Active layer/GDL interface whereas without this PTFE treatment the liquid fills most of the pores that are available at the interface. Moreover, the hydrophobic treatment changes the flow regime from a stable displacement regime to a capillary fingering regime.

[Lee et al., 2014] studied the effect of ribs, in three dimensions: the water saturation was higher in the region located under the ribs than the one located under the channel. These results are attributed to the so-called "extra IP process", i.e. the liquid water has to cross more distance to reach the breakthrough when it is stuck under the rib. They also showed that the more the rib size increases, the more the water saturation under the rib increases but has less impact on the saturation level under the channel. In the same way, a thinner GDL decreases the saturation level under the channel but the level under the rib remains constant.

The following table summarises the features of these different Pore Network Models applied to GDLs.

Article	Size	Struct.	Type of physics	Network lattice	PSD and TSD	R.D.	Rib	Anis.	Wett.	Features	Cond.
[Nam and Kaviany, 2003]	Fibre stack 2D -> 3D 50×50×50	Fibrous	Continuous H_2O Conv. + O_2 Diff. + H_2O (g) Diff.	-	Relation between fibre and pore size	-	-	-	Constant 120°	First PNM for GDL	NO
[Gostick et al., 2007]	3D (10 or 11 pores along the thickness)	Cubic	H_2O Conv. + O_2 Diff.	T090: 25.2 µm 10BA : 40.5 µm	T090: 19 µm 10BA: 33 µm	Weibull	Yes	Yes	Constant 115°	Computation of effective properties + limiting current	NO
[Markicevic et al., 2007]	2D (N × N, N=1 to 100)	Cubic	H_2O Conv.	-	Pore: [350-450], [200-600], [100-700], [50-750], [20-780] µm and Throat: 400 µm then 40 µm	Uniform	No	Yes (H_2O)	Constant	Size and heterogeneity effect	NO
[Sinha and Wang, 2007]	3D: 30×30×11	Cubic	H_2O Conv.	25 µm	Pore: 10 µm and Throat: 6 µm	Normal	Yes	No	Constant 110°	-	NO
[Bazylak et al., 2008]	2D: 48×48 and 100×100	Cubic	IP	-	-	Several networks	Yes	Yes by def.	Constant	Creation of several PNMs and comparison XP/Numerical simulations	NO
[Chapuis et al., 2008]	2D: Circles puis 14×20	Superposition of circles	IP + Evap.	Metropolis algorithm + Voronoi diagram	[Rmin,Rmax] with Rmin = Rmax/3	Uniform	No	No	Variable	Visualizations of mixed wettability and comparison with PNM	NO
[Koido et al., 2008]	3D: 120×120×120	Topological skeleton	IP	-	Measured by porosimetry ∼ 35 µm	Normal	No	Yes by def.	Constant 162°	Pc-s measurement and comparison with XP	NO
[Sinha and Wang, 2008]	3D: 30×30×11	Cubic	H_2O Conv.	25 µm	Pore: 10 µm and Throat: 6 µm	Normal	No	No	Mixed	Effects of mixed wettability	NO
[Lee et al., 2009]	3D: 20×20×10	Cubic from fibrous	H_2O Conv. + O_2 Diff.	20 µm	Pore: 17.8 µm and Throat: 4.77 µm	Random	No	No	Constant 120°	Comparison of boundary conditions	NO
[Rebai and Prat, 2009]	3D: 40×40×N with N = [4,40]	Cubic	H_2O Conv.	50 µm	Pore: 40 µm and Throat: 27 µm	Uniform	Yes	No	Constant	Effects of compression	NO
[Ceballos and Prat, 2010]	3D: 40×40×N with N = [4,40]	Cubic	IP	50 µm	Pore: 40 µm and Throat: 27 µm	Uniform	Yes	No	Constant	Multiple injections	NO
[Hinebaugh and Bazylak, 2010]	2D	Spheric	H_2O Conv.	-	Pore: [9-12.5]µm and Throat: [4-8.5]µm	Uniform	Yes	No	Constant 110°	Condensation	NO
[Lee et al., 2010b]	3D: 20×20×10	Cubic	H_2O Conv.	25 µm	Pore: [17.5-22.5]µm and Throat: [5-17.5]µm	Uniform	No	No	Constant 120°	Constant flux 2 $A.cm^{-2}$ + Effects of GDL thickness + Effects of number of injection points	NO

[Lee et al., 2010a]	3D: 22×22×10	Cubic	IP then Hagen-Poiseuille for permeability calculation	25 µm	Pore: [17.5-22.5] µm and Throat: [5-17.5]µm	Uniform	No	No	Constant 120°	Comparison between classical/horizontal/vertical paths of GDLs	**NO**
[Luo et al., 2010]	3D	Spherical	IP then Hagen-Poiseuille for permeability calculation	Non constant	Pore "carbon paper": monomodal ∼ 20µm; Pore "carbon cloth": bimodal ∼ 20µm and 100µm; Throat: [8-10]µm	Taken from 3D images	No	Yes by def.	Constant 110°	Reconstruction of a PNM from a SEM image	**NO**
[Ceballos et al., 2011]	2D & 3D: variable size	Cubic	IP	2 mm	[200-900] µm	Uniform	No	No	Constant	Statistics on breakthrough	**NO**
[Kuttanikkad et al., 2011]	3D: 40×40×10	Cubic	-	-	Pore: 17.5 µm	-	-	-	Mixed (f hydrophilic)	-	**NO**
[Wu et al., 2012a]	3D: 80×80×12	Cubic	O_2 Diff.	25 µm	Pore: [8-12] µm and Throat: [2-7] µm	Uniform	No	No	Mixed (f hydrophilic)	Effects on the number of injection points (sequential)	**NO**
[Wu et al., 2012b]	3D: MPL: 200×200×[0-40] GDL: 20×20×[6-10]	Cubic	H_2O Conv.	25 µm	GDL: Pore: [8-12] µm and Throat: [2-7] µm and MPL: Pore: [8-12]µm and Throat: [2-7]µm	Uniform	Yes	No	Constant	GDL + MPL coupling	**NO**
[Alink and Gerteisen, 2013]	2D	Fibrous	O_2 Diff. (continuous) + Condensation	-	-	Yes	Yes	Yes by def.	Mixed	Based on the fibrous structure	**YES partially**
[Ceballos and Prat, 2013]	3D (variable size)	Cubic	IP + Diff.O_2	50 µm	-	Uniform	No	No	Mixed (f hydrophilic)	Sequential and kinetic algorithm + Trapping effects + Mixed wettability	**NO**
[Médici and Allen, 2013]	2D: 120×12	Cubic	H_2O Conv. + Calc. of T field + H_2O Diff.	25.2 µm	GDL: Pore: 19 µm	Weibull	Yes	No	Constant	Entire 2D model	**NO**
[Shahraeeni and Hoorfar, 2013]	3D: 15×15×10	Spherical	IP + H_2O Conv.	Length of throat is fixed: 11 µm	Pore: [10-20] µm and Throat: [5-10] µm	Uniform	No	No	Mixed (f hydrophilic)	Comparison XP/simulations (Fluorescence microscopy)	**NO**
[Wu et al., 2013]	3D: MPL: quasi-continuous and GDL: 40×40×12	Cubic	IP + O_2 Diff.	25 µm	Pore: [8-12] µm and Throat: [2-7] µm	Uniform	Yes	No	Constant	Position of cracks in the MPL	**NO**

[Lee et al., 2014]	3D: 20×80×10	Cubic	IP	25 µm	Pore: [17.5-22.5] µm and Throat: [5-17.5] µm	Uniform	Yes	No	Constant 120°	Influence of the rib + GDL thickness + Number of invaded pores at the inlet	**NO**
[Shahraeeni and Hoorfar, 2014]	3D: 15×15×N, N = 10,17,25,33	Spherical	IP + H_2O Conv.	Length of throat is fixed: 11 µm	Pore: [10-20] µm and Throat: [5-10] µm	Uniform	No	No	Mixed (n hydrophilic pores, based on %wt PTFE)	Comparison XP/simulations (Fluorescence microscopy) + Mixed wettability	**NO**
[Wu et al., 2014]	3D: 25×25×25	Cubic	IP (liquid) in drying + O_2 Diff.	25 µm	Pore: [5-7] µm (narrow) and [0-12] µm (large)	Uniform	Yes	No	Constant	Evaporation as a fonction of the PSD	**NO**
[Fazeli et al., 2015]	3D	Spherical	IP	-	Extracted from image	-	Yes	Yes by def.	Constant 110°	Influence of boundary conditions Reservoir VS Flux on a network extracted from X-ray pictures	**NO**
[Qin, 2015]	2D: 80×10	Cubic	H_2O(g) Conv.-Diff. + phase change	25 µm	Pore: [9-12.5] µm	Normal	Yes	No	Constant 180°	Dynamic PNM for air-water flow and phase change	**NO**
[Straubhaar et al., 2015]	2D: 40×6	Cubic	IP + Condensation	50 µm	Throat: [20-34] µm	Uniform	Yes	No	Constant	Thermal gradient, phase change (condensation)	**YES**

How to read the table:

- Article: Reference of the article. Articles are chronologically sorted.
- Size: Number of dimension and number of pores in each dimension.
- Struct.: Structure of the PNM.
- Type of physics: Type of physics that is used to solve oxygen and/or water transport.
- Network lattice: Length between the center of two adjacent pores.
- PSD and TSD: meaning of Pore Size Distribution and Throat Size Distribution, i.e. the average pore and throat size that are used in the PNM.
- R.D.: meaning of Random Distribution, i.e. the type of random distribution that is chosen for pores and throats.
- Rib: If the rib is taken or not into account.
- Anis.: If anisotropy is taken or not into account.
- Wett.: The value of the contact angle in water, i.e. considered as hydrophobic if larger than 90°.
- Features: Interests of the PNM.
- Cond.: If condensation is taken into account in the model.

Pore networks that were previously presented are all regular networks, i.e. they are made of pores and throats arranged on cartesian grids: for example in three dimensions, a pore has 6 neighbours in a simple cubic network. It is possible to create irregular networks, where the number of neighbours is not constant (the number of neighbours is called the coordination number). The goal of these works is to develop a pore network based on a random structure that would better illustrate the real structure of the GDL, which is also random. [Nam and Kaviany, 2003] investigated this way creating an algorithm that is able to generate a three-dimensional pseudo-random network specific to a fibrous medium. This model was reused by [Sinha and Wang, 2007], [Sinha and Wang, 2008] and then [Lee et al., 2009]. However this method is only a cubic network with reference points slighty shifted so it is not fully satisfactory. Another solution is to build a random network with Delaunay triangulation and Voronoi tessellations. [Bryant et al., 1993] invented this for a sphere bed, then [Thompson, 2002] reversed the technique using Voronoi tessellations to create the solid structure and Delaunay triangulation for the porous structure. Based on this technique, [Gostick, 2013] studied drainage and diffusion of the gaseous phase in a model GDL.

Another method consists in building a network from numerical images of the real GDL obtained by X-ray tomography or other techniques of imaging (cf. 2.4), see [Flückiger et al., 2011; Eller et al., 2011], Tristan Agaesse PhD thesis, for instance. It is then necessary to adjust such parameters as porosity, diameter and length of the fibres, direction, etc. This method allows to get a morphology that is much closer to reality but it is more difficult (identifying the throats and the pores is not necessarily easy) and computationally more costly to simulate the flows and capillary effects in these disordered networks.

Even if the development of morphological or non-structured networks - that are built from images of the micro structure - appears to be a very attractive solution, we still use in this work simple cubic networks. Cubic networks are easier to implement, less computationally costly and enough satisfactory when the objective is mostly phenomenological and aims to develop a better understanding of the processes at play.

2.4 Water visualisation in the GDL

Numerical models that were discussed before would be of limited interest if their results were not confirmed by reality. The observation of liquid water in the GDL - in in-situ or ex-situ experiments - is a very important step for the development of numerical models as well as their validation.

2.4.1 The different techniques

Several techniques of visualisation can be used such as Magnetic Resonance Imaging (MRI), neutron imaging, Scanning Electron Microscopy (SEM), X-ray radiography or even direct visualisation [Bazylak, 2009]. One of the most efficient method for water visualisation in GDLs is X-ray computed micro tomography. For example, neutron imaging has a small resolution (about 1 cm) and, although it is insensitive to the material of the GDL, it is interesting only for visualisation at the cell scale. MRI needs to not have materials sensitive to magnetic induction, the spatial resolution and contrast are limited and the procedure appears to be a big challenge for water visualisation in the GDL. X-ray micro tomography has a spatial resolution ten times larger (in the range of microns, [Hartnig et al., 2009]) than the other methods, which means it is an excellent candidate for the visualisation of liquid water in GDLs.

2.4.2 X-ray micro tomography

X-ray computed micro tomography (also referred as micro-CT), is a nondestructive technique allowing to reconstruct three-dimensial object [Flückiger et al., 2011; Hartnig et al., 2008; Manke et al., 2007; Zenyuk et al., 2015; Krüger et al., 2011]. Its principle is based on the multidirectionnel analysis of the interaction of a X-ray beam with matter (absorbtion of the phase), by recording with detectors the transmitted radiation after it goes through an object. Then it is necessary ro reconstruct numerically the radiographic slices of the sample that were taken for different angles regularly spaced by rotation. A CT slice image is composed of voxels and the gray levels in this slice image correspond to X-ray attenuation, which reflects the proportion of X-rays scattered or absorbed as they cross each voxel.

Given that the times of acquisition are compatible with quasi-static water invasion of the GDL, X-ray micro tomography allows to follow the dynamical evolution of the phenomenon.

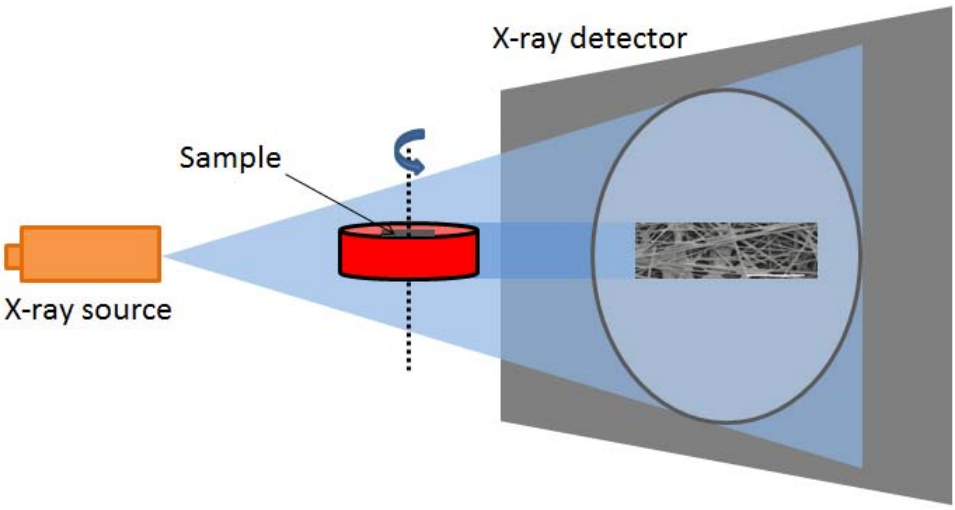

Figure 2.14: Schematic of X-ray micro tomography experiment.

2.5 Conclusion

There is absolutely no doubt that liquid water can be present in the GDL during the operation of PEMFC, at least for a sufficiently high current density and relative humidity in the channel. The exact mechanisms explaining the occurrence of liquid water within the GDL are somewhat an object of controversy. For instance, practically all the previous works using PNM were based on the assumption of capillary controlled invasion in liquid phase from the catalyst layer or the MPL. This is in contrast with other works (to be quoted later in the manuscripts) that consider vapour condensation as the main mechanisms of liquid water occurrence in the GDL. In the context, the main objective of the thesis is to contribute to elucidate this point, namely invasion in liquid phase or condensation. To this end, we have developed a pore network model (presented in the next chapter) enabling us to simulate the condensation process. Combined with state of the art X-ray tomography of the liquid water distribution in a dedicated fuel cell performed by IMPALA partner PSI, we hope to reach a conclusion on this crucial point from the comparison between the experimental distributions of the liquid water and the simulated ones.

Chapter 3

Condensation pore network model (CPNM)

Contents

3.1 Introduction

The article forming this chapter [Straubhaar et al., 2015] presents a discussion of various options for simulating the formation of liquid water with the GDL within the framework of pore network models. The simplest option assumes invasion of the GDL in liquid phase from the adjacent MPL or catalyst layer without any consideration of phase change phenomena. This is by far the most considered option in previous works. This option is most often considered using the standard invasion percolation algorithm since the two-phase flow regime expected in the GDL hydrophobic porous structure is the capillary fingering regime.

A somewhat more refined option is to take into account evaporation together with the liquid water invasion controlled by the capillary effects from the adjacent finer layer. This can be accepted for negligible temperature variations within the GDL. The two aforementioned options are however somewhat inconsistent in the presence of temperature variations because it is then necessary to take into account the condensation phenomenon.

The last option considered in the article is the liquid water formation by condensation of the water vapour arriving from the adjacent finer layer (MPL or catalyst layer). To this end, a condensation algorithm is described. This condensation algorithm is one of the main outcomes of the present thesis. This article also introduces the concept of condensation diagram (see Figure 2 of the article), useful to distinguish the regimes where water can be transferred only in vapour phase (without condensation) from the regimes where liquid water forms by condensation in the GDL.

The various regimes are illustrated in the article from 2D pore network simulations. The exploitation of the pore network code via 3D simulations is presented in the last two chapters of the thesis. Additional information on the structure of the numerical pore network code is presented in the thesis Appendix.

3.2 Article 1: Water transport in gas diffusion layer of a polymer electrolyte fuel cell in the presence of a temperature gradient. Phase change effect.

Water transport in gas diffusion layer of a polymer electrolyte fuel cell in the presence of a temperature gradient. Phase change effect

Benjamin Straubhaar [a,b], *Joel Pauchet* [c], *Marc Prat* [a,b,*]

[a] *INPT, UPS, IMFT (Institut de Mécanique des Fluides de Toulouse), Université de Toulouse, Allée Camille Soula, F-31400 Toulouse, France*

[b] *CNRS, IMFT, F-31400 Toulouse, France*

[c] *Fuel Cell Components Laboratory (LCPEM), LITEN, CEA, 17 rue des Martyrs, 38000 Grenoble, France*

ABSTRACT

The gas diffusion layer (GDL) is a crucial component as regards the water management in proton exchange membrane fuel cells. The present work aims at discussing the mechanisms of water transport in GDL on the cathode side using pore network simulations. Various transport scenarios are considered from pure diffusive transport in gaseous phase to transport in liquid phase with or without liquid–vapor phase change. A somewhat novel aspect lies in the consideration of condensation and evaporation processes in the presence of a temperature gradient across the GDL. The effect of thermal gradient was overlooked in previous works based on pore network simulations. The temperature gradient notably leads to the possibility of condensation because of the existence of colder zones within the GDL. An algorithm is described to simulate the condensation process on a pore network.

Introduction

The gas diffusion layer (GDL) in PEMFC has several functions, [1]. The GDL contributes to make more uniform the gas supply to the active layer. The GDL must also contribute to the water management by enabling the water in excess to leave the system on the cathode side without affecting too much the oxygen access to the active layer. A key question in this context is the nature of the water within the GDL, i.e. in gaseous phase or in liquid phase. Obviously, the transfer of the water in excess in vapor phase sounds the best option if the objective is to maintain all pores in the GDL accessible to oxygen. On the other hand, a GDL made hydrophobic generally leads to better performance. A possible effect of a hydrophobic agent makes sense only if water is present in liquid phase in the GDL. If the water transfer is in liquid phase, then as discussed in Ref. [2], it is indeed much better to make the GDL hydrophobic because this favors the formation of liquid capillary fingers occupying a small fraction of the pore space. The complementary fraction, free of water, is therefore available for the oxygen transport. Then it must be pointed out that a PEMFC typically operates at a temperature of about

* *Corresponding author*. INPT, UPS, IMFT (Institut de Mécanique des Fluides de Toulouse), Université de Toulouse, Allée Camille Soula, F-31400 Toulouse, France.

E-mail address: mprat@imft.fr (M. Prat).

80 °C, which corresponds to a relatively high vapor saturation pressure. Furthermore, as discussed for example in Ref. [3], a temperature difference is expected across the GDL with the highest temperature on the active layer side. Since the GDL is colder on the bipolar plate side, water condensation is likely and can be another mechanism leading to the occurrence of liquid water in the GDL [4,5]. Also, because of the temperature gradient or because the relative humidity in the bipolar plate channel can be lower than 100%, evaporation is also possible. In brief, several options are possible as regards the water transport across the GDL: 1) transport in vapor phase only, 2) transport in liquid phase only, 3) transport with liquid – vapor phase change.

In this context, the present work discusses different mechanisms of water transport in the gas diffusion layer (GDL) on the cathode side from a combination of simple estimate and two-dimensional pore network simulations in relation with the water management issue. The fuel cells motivating the study are classical PEMFC but the results could be of interest for the modeling of other categories of fuel cells, e.g. Ref. [6] for example.

Pore network simulations

The modeling of transport phenomena in porous media is generally performed within the framework of the continuum approach to porous media. This approach considers volume-average transport equations and relies on the concept of length scale separation, i.e. the averaging volume should be small compared to the size of the porous domain for the Darcy's scale equations to make sense. As discussed for instance in Ref. [7], a GDL is only a few pore sizes thick. This is an example of thin porous media [8] in which the length-scale separation criterion is not satisfied. Furthermore, as also discussed in Ref. [7], the scenario of slow liquid invasion in a hydrophobic porous medium leads to a regime called the capillary fingering regime, which is fractal and thus not compatible with the volume-averaged equations. The fact that the continuum approach is highly questionable is a strong argument in favor of an alternate approach. As in several previous works, e.g. Refs. [9–11], and references therein, we use a pore network approach. In the pore network approach, the pore space is represented by a network of pores interconnected by channels. The transport of interest is directly computed at the pore network scale outside the continuum framework. For simplicity, we consider a regular two-dimensional lattice as sketched in Fig. 1. The pores correspond to the nodes of the network. The interconnecting channels between two pores correspond to the constrictions or throats of the pore space. The pores are idealized as cubic bodies and the throats are ducts of square cross-section. The pore network is constructed by assigning pore body sizes from a Gaussian distribution in the range $[d_{tmin}, d_{tmax}]$ with d_{tmin} = 20 μm and d_{tmax} = 34 μm. The size of the porous domain isℓ x L where ℓ is the GDL thickness. As discussed in Ref. [7] representative values of L and ℓ are: L ~ 2 mm and ℓ ~ 300 μm. The lateral size L corresponds to a unit cell containing a rib and two half-channels of the bipolar plate. At the bipolar plate side, one part of the GDL is in contact with a solid phase, the rib, whereas the other part is in contact with the channel providing the oxygen. The lattice spacing (= the distance between two pores) is equal to 50 μm so that a 40 × 6 pore network in considered (40 is the number of pores in the lateral (in-plane) direction and 6 the number of pores across the GDL (thus in the through plane direction).

Water transfer in vapor phase

To discuss the nature of the water transfer within the GDL, we begin with some simple analytical computations. We assume that all the water produced in the active layer as a result of the electro–chemical reaction is directed toward the GDL on the cathode side. This is a conservative estimate since a fraction of the produced water should actually go toward the anode side. The production rate (in mol/s) is classically expressed as a function of the current density in the fuel cell as,

$$Q = \frac{iA}{2F} \tag{1}$$

where F is the Faraday's constant (F = 96485.34 C), i is the current density and A the cross-section surface area of the network (A = 40 × 50 μm × 50 μm with our 2D approach).

Suppose the water transfer takes place in vapor phase by diffusion and consider for simplicity the gas as a binary mixture of oxygen and water vapor. An important parameter is then the relative humidity, denoted by RH, in the channel. The gas at the fuel cell inlet is not dry but humidified. Considering automotive applications, we can take for example RH = 50% at the inlet. As a result of water production, the relative humidity is expected to increase along the channel and can even be expected to reach almost 100% RH at the outlet of the fuel cell. Accordingly, we vary in what follows RH from about 50% to 100%. An additional simplification is to suppose that the gas is fully vapor saturated in humidity at the inlet of the GDL (the GDL inlet is the interface between the active layer and the GDL). Under these circumstances, the diffusive transport of the vapor can be expressed as,

$$J = \frac{cA}{\ell} D_{app}[\ln(1 - RH\, x_{vsat}(T_c)) - \ln(1 - x_{vsat}(T_{al}))] \tag{2}$$

with $c = p/RT$ where p is the total pressure (p ~ 1.5 bar), R is the gas constant, ℓ is as before the thickness of the GDL (~6 × 50 μm); $x_{vsat}(T_{al})$ is the vapor mole fraction at the active layer – GDL where T_{al} is the temperature at this interface; $x_v = RH\, x_{vsat}(T_c)$ at the GDL/channel interface where x_v is the mole fraction of vapor and T_c is the channel temperature.

In Eq. (2), D_{app} is the apparent diffusion coefficient of the GDL. It differs from the molecular diffusion coefficient because of the presence of the porous microstructure. Using the same method as reported for instance in Ref. [12], this coefficient is computed from pore network simulations taking into account that the GDL is partially blocked by the rib as depicted in Fig. 1. Repeating the simulations for 10 different realizations of network and ensemble-averaging the results led to $D_{app}/(\varepsilon D) = 0.19$ where D is the molecular diffusion coefficient of vapor ($D = 3.1\ 10^{-5}$ m^2/s at 80 °C) and $\varepsilon \approx 0.65$ is the network porosity. This enables us to define the critical current density i_c beyond which it is not possible to transfer all the

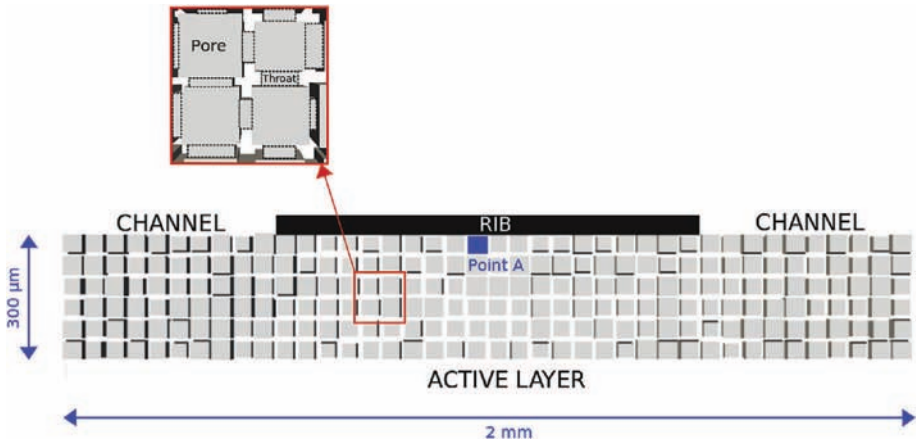

Fig. 1 – Sketch of GDL as a two-dimensional pore network.

produced water by diffusion in vapor phase through the GDL. This current is given by the equation $J = Q$. This yields,

$$i_c = \frac{2F\,c}{\ell} D_{app} \ln\left(\frac{1 - RH\, x_{vsat}(T_c)}{1 - x_{vsat}(T_{al})}\right) \quad (3)$$

The "critical" current i_c is plotted as a function of *RH* in Fig. 2 for the case $T_c = T_{al} = 80\ ^\circ C$.

As an example, the results plotted in Fig. 2 suggest that the produced water can be carried away in vapor phase as long as *RH* in the channel is lower than about 75% when $i = 1\ A/cm^2$. The conclusion of this section is therefore that at least two regions should be distinguished when analyzing the transport of water in the GDL in a fuel cell. In the region sufficiently away from the bipolar plate channel outlet for the relative humidity in the channel to be sufficiently low, the transfer could be in vapor phase only. Closer to the outlet, the transfer is not possible in vapor phase only and thus water should be present in liquid form, at least for sufficiently high current densities. Note, however, that the results shown in Fig. 2 were obtained assuming a uniform temperature across the GDL. As shown in Ref. [13] when a more accurate determination of critical current is presented, the existence of a temperature gradient changes the value of the critical current but not the main conclusion, i.e. the presence of liquid water when the relative humidity is sufficiently high in the channel.

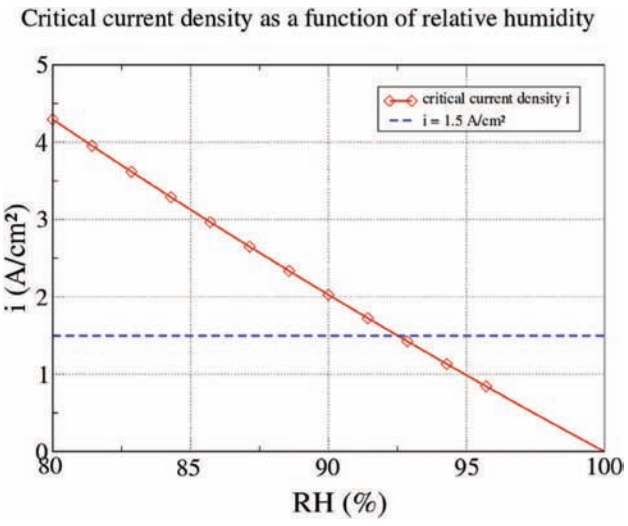

Fig. 2 – Critical current density i_c as a function of relative humidity RH in the channel.

Above the critical current, the produced water cannot be transferred only in vapor phase. This means that the GDL must be partially occupied by liquid water. Two main options are then possible depending on the boundary condition imposed at the active layer (AL) – GDL interface. The first option consists in assuming that water enters the GDL in liquid phase from the AL. By contrast, the second option is to consider that water enters the GDL in vapor phase from the AL. This second option can then lead to the formation of liquid water in the GDL only by condensation, i.e. when regions in the GDL are colder than the AL. The two options are discussed in what follows.

Transfer above the critical current density (negligible thermal gradient)

Transfer in liquid phase neglecting phase – change phenomena

Several authors have considered that water enters the GDL directly in liquid phase, e.g. Refs. [2,7,9–11,14,15], to cite only a few. Within the framework of pore network model, this scenario is simulated on a network using the classical invasion percolation (IP) algorithm [16]. Liquid water simulation with this algorithm consists of invading the network through a series of elementary invasion steps until the liquid reaches the channel. Each elementary step consists in invading the constriction (bond) of largest hydraulic diameter available along the liquid–gas interface as well as the gaseous pore adjacent to this constriction. This type of simulation typically leads to a capillary fingering invasion pattern as exemplified in Fig. 3. The 3D version of this pattern is qualitatively consistent with the experimental visualizations reported in Refs. [17], at least as regards the ramified structure of main liquid clusters.

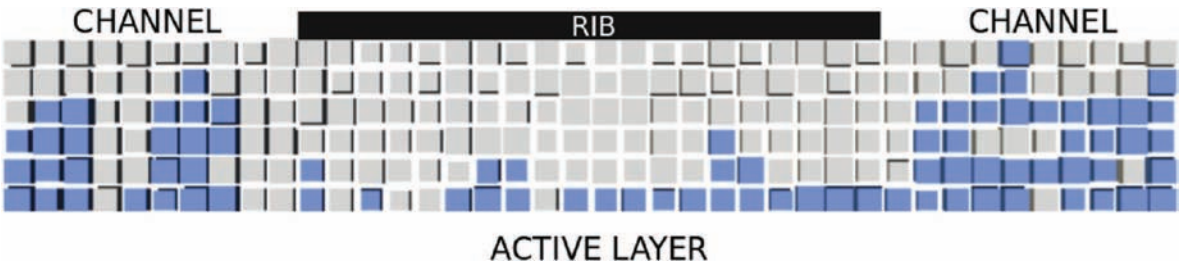

Fig. 3 – Two-dimensional typical slow invasion pattern in a hydrophobic layer from pore network simulation. Each square corresponds to a pore. Liquid phase in blue, gas phase in grey. (For interpretation of the references to color in this figure legend, the reader is referred to the web version of this article.)

As discussed in Refs. [9,18], one problem with this type of simulation lies in the boundary condition to be imposed at the inlet. It was argued in Ref. [18] that the consideration of independent multiple injection points at the GDL inlet was a better option that the traditional reservoir-like boundary condition. This, however, does not change the main feature of invasion pattern.

Transfer by evaporation with partial invasion of the GDL

In Section 5, we briefly consider the purely liquid invasion scenario ignoring the possible phase change phenomena. Since the vapor partial pressure at menisci along the boundary of the invading liquid cluster is the saturation vapor pressure then a transfer by vapor diffusion from these menisci toward the channel (supposed at a lower partial pressure in vapor) is possible.

This kind of situation can be easily simulated using a pore network model. The algorithm we developed for that purpose can be summarized as follows. Initially, the network is only occupied by the gas phase and the liquid/gas interface is supposed to coincide with the GDL/active layer interface. As for the other cases considered in this article, the medium is supposed to be fully hydrophobic so that the invasion percolation algorithm [16], can be used for modeling the liquid invasion on the network.

1) Let $i > i_c$. Determine the flow Q to be transferred from Eq. (1).
2) Determine the next throat to be invaded by the liquid using the classical invasion percolation algorithm [16]. Invade the corresponding throat and adjacent pore.
3) For the new position of the liquid–gas interface within the network, compute the molar flow J which is transferred by diffusion in vapor phase between the liquid/gas interface and the channel. Thus we impose $x_v = RH\ x_{vsat}(T)$ at the GDL/channel interface, a zero-flux condition at the GDL/rib interface and $x_v = x_{vsat}(T)$ on each meniscus which are in the system. This part of the algorithm is similar to the one presented in Ref. [12] for the calculation of the apparent diffusion coefficient D_{app}.
4) If $J < Q$ continue the invasion going back to 2). If $J \sim Q$, the steady-state solution with partial invasion is obtained.

An example of a result obtained with this algorithm is shown in Fig. 4.

We are not aware of in-situ visualizations, similar for example to the ones reported in Refs. [17], consistent with this scenario of partial liquid invasion with evaporation. It should be noted, however, that a special very small fuel cell was designed for making possible the visualizations reported in Ref. [17]. Thus, further investigations are needed to discuss the scenario illustrated in Fig. 4 from experiments.

Interestingly, a partial invasion of the GDL by the liquid water contributes to maintain a better access to oxygen compared to the situation, depicted in Fig. 3, where the evaporation phenomenon is not taken into account or is negligible (which can occur when the relative humidity in the channel is very high, close to 100% for example).

Transfer above the critical current density with consideration of thermal gradient

Until now, we have considered the temperature as uniform across the GDL. As mentioned before, authors, e.g. Ref. [3] for instance, have shown that a temperature difference ΔT of a few K occurs between the hotter active layer and the colder bipolar plate. Given the small thickness of the GDL (~300 μm) this represents a significant thermal gradient. This order of magnitude can be obtained from the following simple estimate. The electrochemical reaction is exothermic. The corresponding heat production per unit surface area (W m^{-2}) can be expressed as, e.g. Ref. [3],

$$\Phi = \left(\frac{h_{lv}}{2F} - U\right) i \tag{4}$$

where h_{lv} is the water latent heat of vaporization ($h_{lv} = 242{,}000$ J mol^{-1}), U the electrical tension.

It can be reasonably assumed that half of the produced heat goes toward the anode and half toward the cathode GDL. Using Fourier's law then leads to

$$0.5\,\Phi = 0.5\left(\frac{h_{lv}}{2F} - U\right) i = \lambda_{eff}\frac{T_{in} - T_{channel}}{H} \tag{5}$$

where λ_{eff} is the GDL effective thermal conductivity and H the thickness of the GDL. As representative value of the GDL thermal conductivity, we took $\lambda_{eff} = 1$ W m^{-1} K^{-1}. Application of Eq. (5) then leads to temperature differences across the GDL of a few K in qualitative accordance with the values reported in the literature. For a given temperature in the channel and

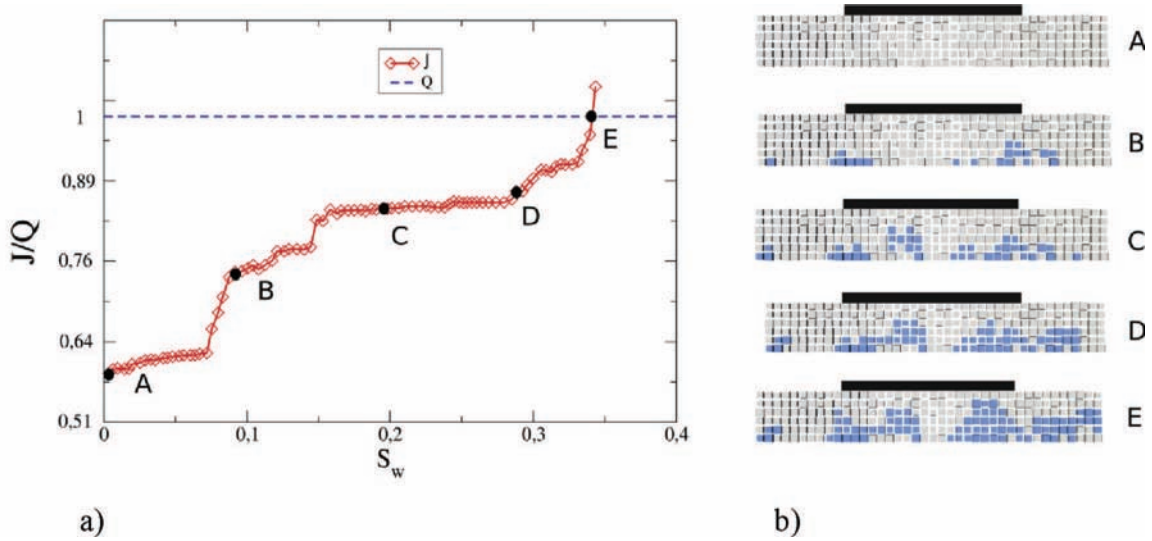

Fig. 4 – a) transferred water flux *J* for several invasion states of the GDL (T = 80 °C). S_w is the liquid saturation, b) invasion patterns corresponding to the points shown in Fig. 4a. The steady-state is reached (point E) when evaporation rate *J* is sufficient along the liquid–gas interface for transferring the produced water Q after partial invasion of network. Each little square corresponds to a pore. Liquid phase in blue, gas phase in grey. These results were obtained for *RH* = 96% (channel); *i* = 1.5 A/cm²; ΔT = 0 K (isothermal condition). (For interpretation of the references to color in this figure legend, the reader is referred to the web version of this article.)

given current density and electrical tension, Eq. (5) is used to determine T_{in} and then the temperature field in the GDL, which with the simplified approach considered in the present study is given by

$$T(x, y, z) = -\Delta T \frac{z}{H} + T_{in} \quad (6)$$

in which $\Delta T = T_{in} - T_{channel}$; x, and y are Cartesian coordinates in the in-plane direction and z in the through plane direction.

The first consequence of the temperature difference is that the transfer by vapor diffusion across the GDL is more efficient than for the uniform temperature situation with the same conditions in the channel because the equilibrium molar fraction x_{vsat} on the active layer/GDL interface increases with temperature. In other terms, the critical current plotted in Fig. 2 is underestimated when the temperature is not uniform and we consider that the vapor is saturated at the active layer – GDL interface, see Ref. [13] for more details.

The other important consequence of the temperature difference is the possible condensation of the vapor within the GDL because of the existence of the colder region on the channel side.

A first step in the study of the condensation process is to compute the vapor molar fraction field in presence of a thermal gradient in the domain shown in Fig. 1. Using again our pore network model, we impose the water production rate given by Eq. (1) at the active-layer/GDL interface, a given vapor molar fraction at the channel/GDL interface and zero flux condition at the rib/GDL interface. This computation is therefore similar to the one giving D_{app}. The result shows that the vapor molar fraction along the outlet of the GDL is located in the middle of the GDL – rib interface. This corresponds to point A in Fig. 1. The computation for realistic temperature differences shown that a condensation can indeed occur in the region of point A when the relative humidity is sufficiently high in the channel (the aforementioned computation leads to vapor molar fractions greater than the saturation vapor molar fraction at the corresponding temperature).

Interestingly, this is consistent with the experimental phase distributions reported in Ref. [17], which show the presence of a thin liquid layer all over the rib surface in contact with the GDL. Thus, under these conditions, a partial invasion in liquid phase of the GDL is expected from the growth of condensation clusters forming at the GDL/rib interface.

This situation can be simulated from pore network simulations using the following algorithm, which is presented in Ref. [13] in more details together with 3D simulations;

1) Determine and label the different water clusters present in the network. If two pores – totally or partially saturated in water – are adjacent, they belong to the same cluster. The first cluster at the very beginning is the pore in the network where the computed molar fraction is the highest above the saturation molar fraction.
2) Calculate the vapor molar fraction field x_v imposing the saturated molar fraction at the corresponding temperature along the boundary of each liquid cluster
3) Compute the molar flux F_k at the boundary of each cluster
4) Determine the throat of larger diameter along the boundary of each liquid cluster
5) Compute the invasion time t_k of each cluster *k*, i.e. the time required to fully invade the pore adjacent to the throat determined in #4 from F_k (step 3) and the volume remaining to invade in the considered pore.
6) Compute the time step $dt = \min(t_k)$.

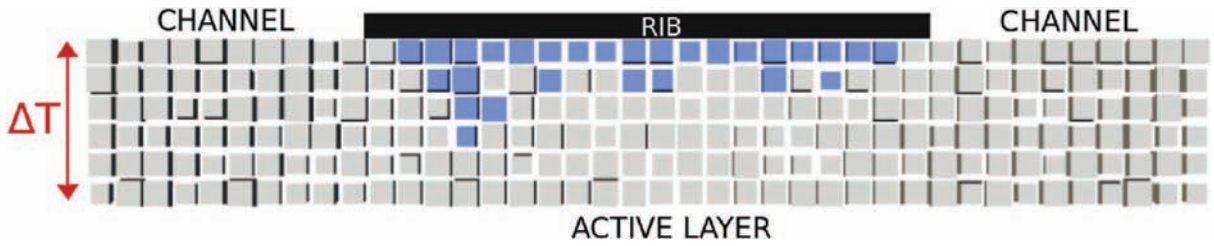

Fig. 5 – Partial liquid invasion of the GDL by condensation under the rib. Each little square corresponds to a pore. Liquid phase in blue, gas phase in grey. Pattern obtained for $RH = 97\%$ (channel); $i = 1.5$ A/cm^2; $\Delta T = 3.25$ K. (For interpretation of the references to color in this figure legend, the reader is referred to the web version of this article.)

7) Fully invade the pore corresponding to dt and update the volume of liquid in the invaded pore in the other clusters
8) Go back to step 1 until the water flux at the GDL outlet (GDL –channel interface) reaches a desired value, i.e. the water production rate given by Eq. (1).

Fig. 5 shows a typical phase distribution obtained with this algorithm for $T_{channel} = 80$ °C. As can be seen, this leads to an invasion pattern quite different from the ones depicted in Figs. 3 and 4. The liquid is moving forward, i.e. toward the bipolar plate, in the scenarios corresponding to Figs. 3 and 4 whereas it is rather moving on average toward the active layer in the condensation scenario.

Hence, the simulations illustrated in Fig. 5 do indicate a quite different liquid invasion scenario of GDL than considered in most previous pore network simulations.

As illlustrated in Figs. 6 and 7 the degree of liquid water invasion in the GDL due to condensation depends as expected on the curent density and the relative humidity in the channel. The greater the curent density for a given relative humidity RH in the channel, the greater the fraction of pores occupied by water in the GDL. Similarly, the greater the relative humidity RH for a given curent density, the greater the fraction of pores occupied by water in the GDL.

Discussion

Compared to most previous studies on water invasion of GDL by liquid water based on pore network simulations, the new feature introduced in the present article is the consideration of the liquid – vapor phase change process. In particular, the consideration of condensation leads to a quite different liquid invasion scenario of GDL than considered in most previous pore network simulations. It is therefore tempting to look at available experimental results in order to try to identify

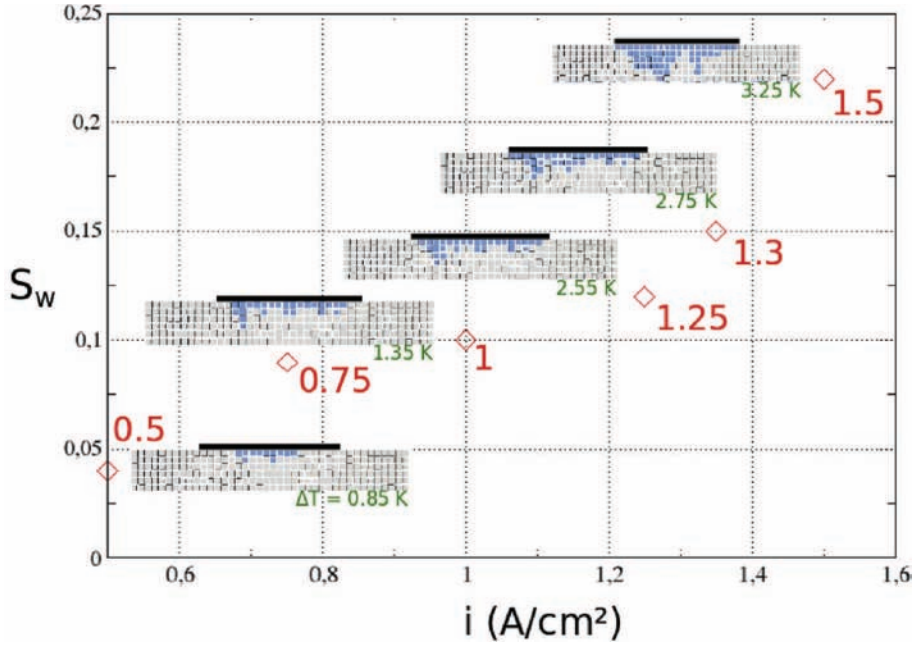

Fig. 6 – Variation of overall water saturation as a function of current density for $RH = 98\%$ together with corresponding condensation invasion patterns (shown for $i = 0.5$, 0.75, 1.25, 1.3 and 1.5 A/cm^2). Each little square corresponds to a pore. Liquid phase in blue, gas phase in grey. The temperature difference across the GDL corresponding to the imposed current density is indicated for each pattern shown. (For interpretation of the references to color in this figure legend, the reader is referred to the web version of this article.)

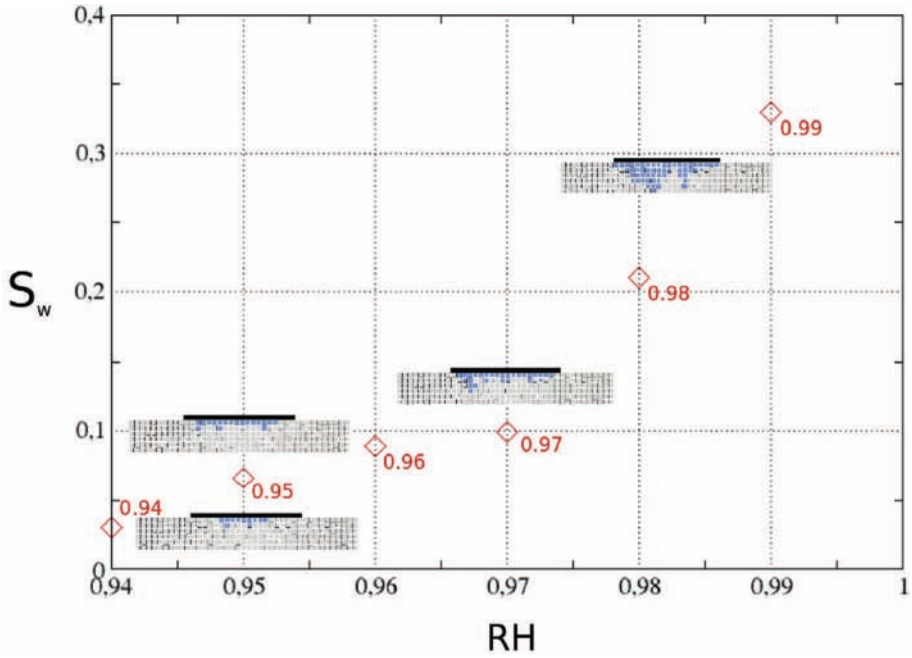

Fig. 7 – Variation of overall water saturation as a function of a channel relative humidity *RH* for $i = 1.5$ *A/cm²* together with corresponding condensation invasion patterns (for *RH* = 0.94, 0.95, 0.97 and 0.99 respectively). Each little square corresponds to a pore. Liquid phase in blue, gas phase in grey. $\Delta T = 3.25$ K. (For interpretation of the references to color in this figure legend, the reader is referred to the web version of this article.)

whether or not it is important to take into account condensation in the pore network simulations. A definitive conclusion is difficult to reach from the phase distributions obtained from X-ray tomography techniques [17]. The images of phase distribution reported in Ref. [17] present several features in favor of the condensation scenario. One can observe liquid clusters apparently disconnected from the AL/GDL interface and a massive presence of liquid under the ribs. However, one can also observe a droplet in the channel connected by a liquid cluster to the AL/GDL interface and is impossible to decide from the images whether the corresponding cluster is formed by condensation or by invasion in liquid phase from the AL. Also, we note that the visualizations reported in Ref. [17] were obtained for temperatures much lower (around 40 °C) than the temperature expected in an operating PEM (≈80 °C). A firm conclusion is also difficult to reach from the through plane saturation profiles reported in Ref. [19]. There are not in agreement with the pore network simulations considering only transport in liquid phase since the maximum in saturation can be in the middle of the GDL and not at the AL/GDL interface whereas the condensation simulations exemplified in Fig. 5 suggest a saturation maximum on the opposite side, that is to say on the channel – rib side. In brief none of the PN simulations performed so far led to a non-monotonous saturation profile with a maximum about in the middle of the GDL.

Actually, the condensation process is strongly dependent on the structure of the temperature field. Here, we are adopted a very simplified approach to compute this field, namely the analytical approach leading to Eq. (6). However, there are experimental evidences that the temperature is not uniform in the in-plane directions contrary to what we have assumed. The consideration of more representative temperature fields combined to 3D simulations is needed to go further in the comparison between experimental data and simulations. Naturally other aspects neglected in the present simulations such as the differential compression of the GDL under the rib and under the channel, the GDL anisotropy properties, the fact that the gas phase is a ternary mixture, etc, would need to be considered in a much more comprehensive approach.

The objective of the present paper was much more limited and was simply to discuss qualitatively various possible scenarios of water formation in GDL and for that we introduced the condensation algorithm. As mentioned before a much more extensive exploitation of this algorithm together with the consideration of more representative temperature fields will be presented in a forthcoming paper.

Conclusion

In addition to the classical purely capillarity controlled liquid invasion algorithm, two pore network models taking to account liquid – vapor phase change phenomena were described.

The results suggest that it could be important to distinguish different zones in the GDL along the channel of the bipolar plate on the cathode side in relation with the water management problem. Depending on the distance to the bipolar plate channel exit and for sufficiently high current densities, the different zones are as follows: a zone where the GDL is dry, a zone with partial liquid invasion and evaporation – condensation and finally a zone close to the exit of the channel with significant

liquid water invasion coming either directly in liquid phase from active layer or as a consequence of the evaporation – condensation process or both from the active layer in liquid phase and as a result of the condensation process.

The study also strongly suggests that liquid – vapor phase change phenomena are a crucial aspect in the analysis of water transfer in PEMFC. As a result of the phase change phenomena several mechanisms can contribute to the formation of liquid water in the GDL. Further studies are necessary to delineate more accurately the relative significance of each mechanism, namely capillary controlled liquid invasion, evaporation and condensation. This is important in relation with the design of GDL. This will be discussed in more details in a future work, notably from 3D pore network simulations.

Acknowledgments

The authors gratefully acknowledge the funding from the EU project IMPALA ("IMprove Pemfc with Advanced water management and gas diffusion Layers for Automotive application", project number: 303446) within the Fuel Cells and Hydrogen Joint Undertaking (FCHJU).

REFERENCES

[1] Barbir F. PEM fuel Cells: theory and practice. Elsevier Academic Press; 2005.
[2] Chapuis O, Prat M, Quintard M, Chane-Kane E, Guillot O, Mayer N. Two-phase flow and evaporation in model fibrous media. Application to the gas diffusion layer of PEM fuel cells. J Power Sources 2006;178:256–68.
[3] Thomas A, Maranzana G, Didierjean S, Dillet J, Lottin O. Thermal and water transfer in PEMFCs: investigating the role of the microporous layer. Int J Hydrogen Energy 2014;39(6):2649–58.
[4] Basu S, Wang CY, Chen KS. Phase change in a polymer electrolyte fuel cell. J Electroche Soc 2009;156(6):B748–56.
[5] Jiang FM, Wang CY. Numerical modeling of liquid water motion in a polymer electrolyte fuel cell. Int J Hydrogen Energy 2014;39:942–50.
[6] Celik C, Boyaci San FG, Sarac HI. Investigation of Ni foam effect for direct borohydride fuel cell. Fuel Cells 2012;12(6):1027–31.
[7] Rebai M, Prat M. Scale effect and two-phase flow in a thin hydrophobic porous layer. Application to water transport in gas diffusion layers of PEM fuel cells. J Power Sources 2009;192:534–43.
[8] Prat M, Agaësse T. Thin porous media, chapter 4. In: Vafai K, editor. Handbook of porous media-third edition. Taylor & Francis; 2015.
[9] Ceballos L, Prat M, Duru P. Slow invasion of a non-wetting fluid from multiple inlet sources in a thin porous layer. Phys Rev E 2011;84:056311.
[10] Ceballos L, Prat M. Slow invasion of a fluid from multiple inlet sources in a thin porous layer: influence of trapping and wettability. Phys Rev E 2013;87:043005.
[11] Gostick JT. Random pore network modeling of fibrous PEMFC gas diffusion media using Voronoi and Delaunay tessellations. J Electrochem Soc 2013;160(8):F731–43.
[12] Gostick JT, Ioannidis MA, Fowler MW, Pritzker MD. Pore network modelling of fibrous gas diffusion layers for polymer electrolyte membrane fuel cells. J Power Sources 2007;173:277–90.
[13] Straubhaar B, Pauchet J, Prat M. Pore network modelling of condensation in gas diffusion layers of proton exchange membrane fuel cells. [submitted 2015].
[14] Pasaogullari U, Wang CY. Liquid water transport in gas diffusion layer of polymer electrolyte fuel cell. J Electrochimic Soc 2004;151:A399–406.
[15] Nam JH, Kaviany M. Effective diffusivity and water-saturation distribution in single- and two layer PEMFC diffusion medium. Int J Heat Mass Transf 2003;46:4595–611.
[16] Wilkinson D, Willemsen JF. Invasion percolation: a new form of percolation theory. J Phys A Math Gen 1983;16:3365–76.
[17] Eller J, Rose T, Marone F, Stampanoni M, Wokaun A, Büchi FN. Progress in in situ x-ray tomographic microscopy of liquid water in gas diffusion layers of PEFC. J Electrochem Soc 2011;158(8):B963–70.
[18] Ceballos L, Prat M. Invasion percolation with multiple inlet injections and the water management problem in proton exchange membrane fuel cells. J Power Sources 2010;195:825–8.
[19] LaManna JM, Chakraborty S, Gagliardo JJ, Mench MM. Isolation of transport mechanisms in PEFCs using high resolution neutron imaging. Int J Hydrogen Energy 2014;39(7):3387–96.

3.3 Conclusion

We showed in this chapter that the electrochemical reaction makes necessary to take into account the temperature difference between the two sides of the GDL. This temperature variations could lead to condensation, a Pore Network Model taking into account this phenomenon is created. It is a novelty regarding to the standard models using Invasion Percolation algorithm. Thereafter, the CPNM is compared with micromodel experiments in order to try to validate it.

Chapter 4

Condensation in a microfluidic device

Contents

4.1 Introduction

This chapter is formed by two articles not yet submitted. Moreover, it is likely that they will eventually be merged and trimmed down to form a single article. The general objective is to validate the pore network condensation code from comparisons with condensation experiments in quasi-two-dimensional microfluidic devices (square networks of interconnected channels), referred to as micromodels.

The first article presents the experiments carried out by **Lingguo Du** as part of his PostDoc in 2013-2014. Noting that they have been performed for a hydrophobic micromodel, a hydrophilic one and a micromodel of mixed wettability half hydrophobic and half hydrophilic.

Numerical simulations with the commercial code COMSOL Multiphysics® are performed to understand certain features of the experiments, such as the occurrence of one or two condensation zones depending on the relative humidity imposed at the micromodel inlet or the asymmetry in the locations of condensation. A noticeable feature in these experiments is that the transport of the vapour within the micromodel is not only diffusive but results from convection and dispersion effects.

The second article presents the pore network model (similar to the one presented in 3 but taking into account in addition the convection-dispersion transport) and the comparison between the experiments and the pore network simulations (in terms of condensation patterns and condensation kinetics).

4.2 Article 2: Water invasion by condensation in a model porous medium

Water invasion by condensation in a model porous medium

Lingguo Du[1], Paul Duru[1], Benjamin Straubhaar[1], Sandrine Geoffroy[2], Marc Prat[1,3]

[1] University of Toulouse, INPT, UPS, IMFT, Institut de Mécanique des Fluides, Toulouse, France
[2] University of Toulouse, UPS, INSA, LMDC, Laboratoire Matériaux et Durabilité des Constructions, Toulouse, France
[3] CNRS, IMFT, F-31400 Toulouse, France

Abstract

Water vapour condensation driven by a temperature gradient in a porous medium is encountered in various applications. In this study, we analyzed the condensation process from visualization experiments performed using a quasi-two-dimensional model porous medium formed by a network of interconnected channels. The liquid invasion patterns as well as the condensation kinetics were compared between a hydrophobic system, a hydrophilic one and a system of mixed wettability containing a hydrophilic region and a hydrophobic one. Two condensation regimes were distinguished depending on whether a two-phase zone or a liquid saturated zone develops in the porous domain. The experiments were also characterized by the occurrence of a preferential condensation zone within the network in the two-phase zone regime. This was explained from the consideration of the velocity field induced in the network. In addition to a better understanding of the condensation process in a porous medium, these results provide pore network scale data for benchmarking numerical simulations.

Key words: condensation, temperature gradient, micromodel, porous medium

1. Introduction

The present study was developed in relation with the problem of liquid water formation in the so-called gas diffusion layer (GDL) of proton exchange membrane fuel cells (PEMFC), e.g. Barbir (2005). Whereas it has been clearly shown that liquid water form in the GDL during the operation of PEMFC, e.g. Eller et al. (2011), the exact mechanisms leading to the occurrence of water in the GDL are still to clarify, Straubhaar et al. (2015). Nevertheless it is well established that noticeable spatial temperature variations exist within the GDL. A simple analysis taking into account the existence of the temperature spatial variations then leads to the conclusion that condensation of the water vapour is a major mechanism of liquid water formation within the GDL Straubhaar et al. (2015).

However, the experimental study of the condensation process in a GDL is difficult because a GDL is thin, 3D and involved relatively small pores on the order of a few tens of microns making difficult the visualizations of the process.

Also, the experimental studies on vapour condensation in porous media are relatively scarce and often carried out using 3D samples of real materials, e.g. Larbi et al. (1995), making again very difficult the observations at the pore scale.

For this reason, we developed visualization experiments allowing the direct observation of the condensation process at the scale of a network of interconnected pores.

As in many previous studies, see for instance Laurindo and Prat (1997, 1998) as regards evaporation, an artificial quasi two-dimensional transparent model porous medium is used in the experiments. The main advantage of this type of microfluidic device, referred to as micromodel since the works of Lenormand on two-phase flow in porous media, e.g. Lenormand et al. (1988) and references therein, is well known. It allows the direct observation of the liquid and gas phase within the pore space. Although micromodels are a classical tool for studying two-phase flow in porous media, e.g. Berejnov et al. (2008), it seems that there is no previous study on condensation using micromodels.

An important and specific property of GDL is to be hydrophobic. However, because of the progressive degradation of the hydrophobic agent initially coating the porous matrix in a GDL, a GDL can become hydrophilic. Also, because the change in wettability is not uniform within the structure or because the initial hydrophobic treatment can be imperfect, a GDL is often considered as system of mixed wettability i.e. a system in which hydrophilic regions and hydrophobic regions coexist. As a result, an important aspect of the micromodels used for the present study is the control of the wettability. We consider three main variants: an uniformly hydrophobic micromodel (contact angle taken in the water on the order of 105°), an uniformly hydrophilic micromodel (contact angle on the order of 70°) and a micromodel of mixed wettability combining a hydrophobic strip with a hydrophilic one.

While motivated by the problem of water management in PEM fuel cells, the experimental study is naturally of broader interest since vapour condensation driven by thermal gradients in a porous medium can be encountered in other applications such as building physics, e.g. Hens (2007), soil physics, petroleum engineering (steam injection), e.g. Baibakov et al. (1989), or cooling systems, e.g. Faghri (1995), to name only a few.

In addition to a better understanding of the condensation process, the experimental data and visualizations will be useful to for comparisons with numerical simulations, as reported in the companion paper Straubhaar et al. (2015b).

The paper is organized as follows. The experimental set-up, the micromodel, the functionalization procedure (wettability) as well as other aspects of the experiments are presented in section 2. The experimental results are presented and discussed in section 3. A conclusion is presented in section 4.

2 Materials and methods

2.1 Micromodel design and fabrication

The micromodel of length L_y = 30 mm and width L_x = 20 mm used in the present study is designed as a 2-dimensional network of channels of rectangular cross-section, see Figure 1b. The network step (distance between two neighbour channel intersections in the network) is uniform and set to 1mm. The width of each channel is set randomly, following a Gaussian distribution with a mean and standard deviation values of 0.5 and 0.1 mm, respectively. The internal thickness of the micromodel, i.e. the height of channels, is 1 mm.

The micromodel is fed by a gas mixture of nitrogen and water vapour circulating in the inlet channel. This is a 20 mm long channel 3 mm in width and 1 mm deep in direct contact with the micromodel (the inlet channel is clearly visible along the right side of the micromodel in Figure 1). Two holes (corresponding to the outlet and inlet tubes visible in Fig.1b) are drilled next to the network in the inlet channel top plate and connected to the gas mixture inlet and outlet tubes as shown in Fig.1b.

The first stage of the fabrication process consists in obtaining a mold of such a microsystem. A first positive mold was obtained by a 3D printer (ProJet 3500 HD Max, 3DSYSTEMS) used in a high resolution mode. This mold was then surface treated by an overnight exposure to a FOTS ((Trichloro(1H, 1H, 2H, 2H-perfluorooctyl) silane) vapour saturated atmosphere. After rinsing with toluene and then alcohol, the mold was filled with a mixture of PDMS and curing agent (ratio of 1:10) and then baked during 1 hour at 70 °C. The resulting PDMS replica was removed from the mold and subsequently used as a negative mold for the remaining of the fabrication process.

The following steps involve the use of OSTE polymers, a new class of polymers that is increasingly used for microfabrication. Two commercial products were purchased from Mercene Labs (Sweden): OSTEmer Thiol80 and OSTEmer Allyl30. Both contain a mix of thiol and ally monomers, the first one have thiol monomers in excess (by 80%) and the second one a 30 % excess of allyl monomers. Once cured, these polymeric materials have a good optical clarity, swelling by common solvents is not occurring and their surface properties, in term of wettability, can be modified in a permanent and robust way. All these properties make them suitable for microfluidic device fabrication and a better choice than PDMS for instance.

OSTEmer Allyl30 was poured into the PDMS mold and then degased after being covered by a square piece of quartz (5×5 cm^2 and 2 mm thickness). A portable UV lamp with an illumination of 0:4mWcm^{-2} at wavelength 365 nm is used to insulate the OSTEmer Allyl30 during with 40 seconds. The transparent-to-UV quartz cover has two roles: first it allows to obtain a perfectly flat top surface for the polymer slab being cured and second, it protects the OSTEmer Allyl30 from atmospheric O_2, which is known to inhibit the curing reaction. The two inlet and outlet holes (2mm diameter) are drilled using syringe precision tips (EFD, Nordson, USA) after the cured Allyl 30 was removed from the PDMS mold.

OSTEmer Thiol80 is used to obtain the micromodel cover side. A simple parallelepipedic mold with a 1 mm depth is used. The polymer is first degased and then UV-insulated during 90 seconds.

The bounding is performed the following way. The Thiol80 cover is aligned and positioned on top of the Allyl30 slab. A manual, gentle compression between these two soft materials is performed, to ensure a complete contact. The definitive and permanent bonding is obtained after a 10 minutes UV insulation, which activates a chemical reaction between the surface thiol and allyl functional groups. Note that in the whole protocol, the tuning of the UV exposure (duration and power) plays a crucial role for the hardening/curing and bonding processes. For instance, overexposure may lead to polymers that are too stiff, with too few surfaces groups and so less efficient bonding.

In addition to uniformly hydrophobic or uniformly hydrophilic micromodels, we also made a micromodel of mixed wettability. In this micromodel, the upper half region of micromodel is hydrophobic whereas the lower half region is hydrophilic. To this end, the surface modification solutions are injected carefully only into a half of the micromodel. Then the micromodel is set with a little tilt under the UV light during 5 minutes. Afterwards, it is rinsed carefully with toluene and ethanol solutions.
Motivation for the consideration of a mixed wettability micromodel stems from the fact that the GDL are often considered as systems of mixed wettability owing to non-uniformities in the distribution of hydrophobic agent or aging problems, e.g. Kuttanikad et al. (2011) and references therein.

2.2 Wettability

The contact angle measured on a "native" flat Allyl30, respectively Thiol80, surface was measured with a Krüss DSA 100 drop shape analysis system to be θ = 68.2 ±3.4° and θ = 77.5 ±3.5° respectively. Therefore, a micromodel fabricated as described above is rather hydrophilic. Commercial surface modifier solutions from Mercene Labs containing fluorinated or hydroxylated methacrylate monomers can be used to render Allyl30 and Thiol80 surfaces hydrophobic or more hydrophilic, respectively. These groups can be grafted using a UV exposure to the excess allyl or thiol surface groups. In the present study, such surface chemistry was performed to obtain a hydrophobic micromodel, starting with an already sealed micromodel, obtained as just explained. To that end, the micromodel was filled with the hydrophobic surface modifier solution and then UV-insulated. Even with the small portable UV lamp used in the present study, enough UV light was able to pass through the 1 mm thick OSTEmer Thilo80top cover to initiate the reaction. Note that during insulation, the micromodel rested on a crumpled piece of aluminum paper.
Aluminum has a good UV reflectivity (88%) and the crumbled nature of the aluminum piece favors a diffuse back-reflection of the UV light transmitted through the micromodel, which improves the surface modification, notably on the micromodel vertical walls. Then, the micromodel is rinsed with toluene and ethanol. The hydrophobic-modified Allyl30 and Thiol80 surfaces have a contact angle of approximately θ = 105°.
Therefore, the surface properties of the inner walls of the hydrophobic micromodel are different, the contact angle being slightly larger on the top Thiol80 cover.
The fact that we were able to develop either hydrophobic micromodels or hydrophobic ones was verified from experiments where liquid water was very slowly injected in an initially dry hydrophilic micromodel or in a hydrophobic one as described in Appendix A. Injection of liquid water into a hydrophobic system corresponds to a drainage experiment (displacement of a wetting fluid, here the gas phase, by a non-wetting fluid, here the liquid water) whereas injection into a hydrophilic network corresponds to imbibition (immiscible displacement of a non-wetting fluid by a wetting one). It is well known that quasi-static drainage leads to capillary fingering patterns, e.g. Lenormand et al. (1988), whereas imbibition leads to much more compact patterns, e.g. Lenormand et al. (1984), Cieplak and Robbins (1990). As illustrated in Appendix A, this is qualitatively what is found with our micromodel. Water invasion in a hydrophobic micromodel leads to significantly more ramified water cluster structure than in the hydrophilic one, thereby confirming the effectiveness of the wettability control.

2.3 Experimental setup

2.3.1 Thermal control

As sketched in Figure 1, nitrogen is injected in the top right corner of the micromodel. The outlet is located in the bottom right corner. We wish to apply a thermal gradient along the micromodel transverse direction, i.e. from the left side to the right one (where nitrogen flows in and away from the micromodel). Water vapour is expected to be transported in the thermal gradient within the micromodel before eventually condensing.

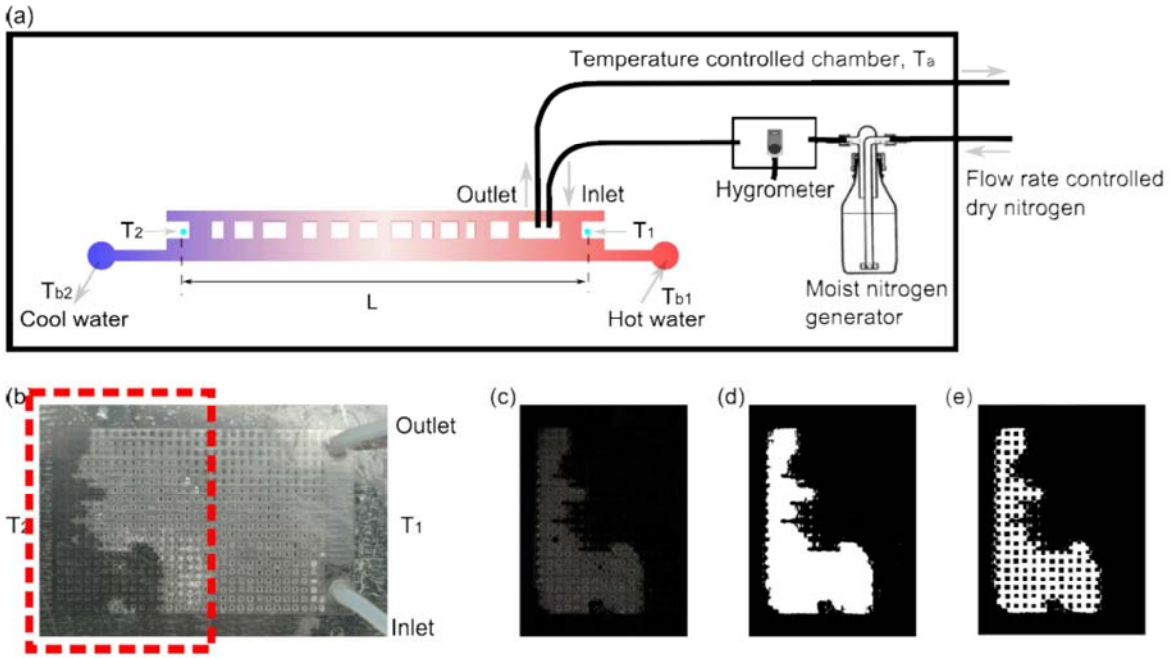

Figure 1 – a) Sketch of the experimental setup and photo of micromodel. b,c,d,e) Image processing (of the region of micromodel in the red frame in Fig.2b).

To generate such a thermal gradient, a 8 cm × 8 cm square bronze plate, with thickness e = 1 mm was welded between two bronze tubes (internal/external radii : R_i = 1.5 mm, R_e = 3mm), see Figure 1a. Hot (T_{b1} = 70°C) and cool (T_{b2} = 0.3°C) water flows in a counter-current configuration within these two tubes so that a stable temperature field with a linear thermal gradient is expected to be reached within the bronze plate. The micromodel is positioned on the bronze plate and optimal thermal contact is obtained using a thin layer of thermal paste between the micromodel and the bronze plate. The temperature within the micromodel is monitored at two positions, using two thermocouples that are integrated within the micromodel walls, at the same vertical location than the channels, see Figure 1a. The two temperatures measured, T_1 and T_2, are used to determine the thermal gradient in the system, $(T_1 - T_2)/L$, with L = 40 mm.

As sketched in Fig.1, the set-up is set in a chamber at controlled temperature. This chamber is cylindrical with a flexible pipe wound spirally around the chamber vertical wall in which a warm liquid circulates. The idea is to impose a temperature in the enclosure close to the average temperature of the bronze plate so as to limit the heat losses by free convection.

Hence, the thermal control actually involves the use of three cryostats: a Lauda E 200 was used for the hot water flow, a Fisher/Bioblock/Polysciences for the cold water flow and a Heto HMT 200 was used to control the temperature T_a in the enclosure.

Note that the tubes and the regions of bronze plate adjacent to the tubes were drowned in PDMS (a polymeric material of relatively low thermal conductivity $\lambda \approx 0.15$ W/m/K) so as to also limit the heat losses. The region of the bronze plate top surface free of PDMS and not in contact with the micromodel was covered by an insulating paste.
The heat transfer within this system was further analyzed from some numerical simulations based on a simple model as reported in Appendix B. The analysis indicated that the thermal gradient in the bronze plate should be as expected directed between the cold tube and the hot tub with very little temperature variations expected in the transverse direction.

2.3.2 Fluid management
Dry, compressed nitrogen is purchased from Alphagaz (Air Liquide). It first flows into a temperature-controlled chamber (at temperature T_a) which contains all the components of the experimental setup. Nitrogen humidification is performed in a gas washing bottle: nitrogen passes through a sintered glass disk and thus bubbles into water. The resulting nitrogen stream humidity can be tuned by varying T_a and/or the nitrogen flow rate. Typically, for a given fixed chamber temperature, the humidity rate increases roughly linearly with the gas flow rate before reaching a constant humidity when the flow rate is larger than a critical value. This critical flow rate value Q_c is a function of T_a, as shown in Figure 2 (for instance, Q_c = 0.07 *L* /min for T_a = 40 °C). Note that in the present experiments, the flow rate was typically set to values larger than the critical one, for each considered T_a temperature.

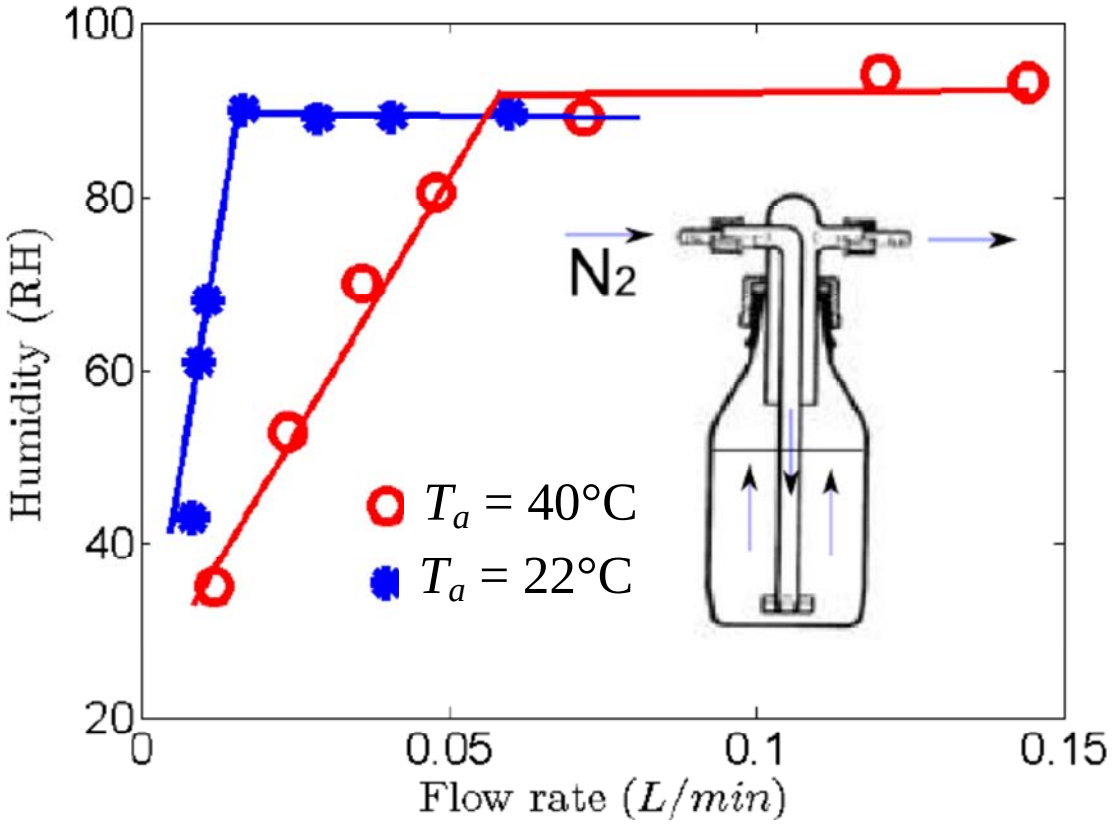

Figure 2 – Measured humidity in the gas mixture as functions of flow rate and temperature.

The nitrogen flow rate through the micromodel is controlled by a flow meter and recorded over the duration of an experiment by a mass flow sensor WTA L005 (flow range 0 to 5 *L* min^{-1}, with a 2% accuracy, purchased from First Sensor Technics). The humidity RH_0 and

temperature T_0 of the moist nitrogen entering the micromodel are measured 20 cm before the micromodel inlet by a hygrometer (Kit EK-H4, Sensirion).

2.3.3 Experimental protocol

Before the introduction of moist nitrogen in the micromodel, the system is left at rest at least one hour, to reach stable thermal operating conditions and dry nitrogen is first flowed into the microsystem for a while, to saturate it with nitrogen. After switching the gas injection to moist nitrogen, pictures of the micromodel are taken every 10 minutes with a computer-controlled Nikon D70 camera. Note that the micromodel back side was painted with a black spray paint to enhance the contrast between the dry and wet regions seen on the recorded images. As already mentioned, temperatures T_1 and T_2, nitrogen humidity and flow rate are recorded over the full duration of an experiment, that can last typically a few weeks.

2.3.4 Image processing. Micromodel porosity

A typical image of the experimental setup after condensation began to occur is shown in Figure 1b. The micromodel region invaded by liquid water appears as a darker zone on such an image. Image processing is performed as follows for each recorded image. First, an image background consisting in an image of the initially dry microsystem is subtracted to the considered image. The resulting image (shown in Figure 1c) is then binarized (Figure 1d). To accurately measure the amount of condensed water, a numerically generated binary mask of the micromodel is used and superimposed to the binarized experimental image, see Figure 1e). The amount of condensed water in the micromodel can thus be obtained on each image and its evolution plotted versus time, thus allowing to measure a condensation rate.

Actually, we measure from the image processing the surface area A_ℓ occupied by water in the micromodel. Then we determine the liquid saturation S as $S = \frac{A_\ell}{A_f}$ where A_f ($A_f = 4.8210^{-4} m^2$) is the surface area left free between the pillars in the micromodel ($A = A_f + A_p$ where A is the surface of micromodel seen from top (A = 6.31 10^{-4} m^2) and A_p is the (projected) surface of the pillars (A_p =1.48 10^{-4} m^2)). The micromodel porosity is thus $\varepsilon = \frac{A_f}{A_f + A_p} = 0.764$ assuming that the thickness e of channels is elsewhere equal to 1 mm.

3 Results

3.1 Parameters

In summary, the main parameters which can be varied in our set-up are: the contact angle (the system can be hydrophobic (θ = 105°) or hydrophilic (θ = 70°), the temperatures T_h and T_c of the hot and cold sides of the system, the relative humidity in the micromodel inlet channel. Table 1 summarizes the values of parameters considered in the various experiments. As can be seen, two main parameters were actually varied, namely the contact angle and the relative humidity in the micromodel inlet since the variations of cold side and hot side temperature T_c and T_h are relatively weak between the various experiments.

Experiment #	Nucleation mode (Colder edge = CE, colder edge + inside = CE+I)	Contact angle (°) θ	T_a (°C) Enclosure Temperature	Rh_{in}(%) Measured relative humidity in gas mixture at T_a	T_c (°C) Colder edge Temperature	T_h (°C) Hot side (inlet channel) Temperature	Rh_{ch}(%) Relative humidity in inlet channel	Q (L/min) Gas mixture injection flow rate	Condensation rate (10-7 s-1) dS/dt (first phase of liquid growth)
1 (20140117)	CE	105	32.5	88	27.3	46.7	41.2	2.2	4
2 (20131206)	CE	105	35.1	94.2	27.2	47.3	49.5	0.45	4.3
3 (20131220)	CE+I	105	45.4	98	27.2	47.3	89.0	0.7	15
4 (20140107)	CE+I	105	45.1	98	26.5	48	84.5	2.78	15.3
5 (20140110)	CE+I	105	42.7	98	26.7	47.4	75.1	2.55	11.4
6 (20140303)	CE	70	35.4	89	26.7	46.7	48.3	2.4	3.2
7 (20140313)	CE+I	70	40.5	95	26.7	47.9	64.7	1.8	16.9
8 (20140326)	CE+I	Mixed wettability	44.2	82.7	27.8	46.1	75	1.6	27

Table 1. Main characteristics of the seven experiments considered in the paper. The meaning of nucleation mode is explained in §3.2. The condensation rate $\frac{dS}{dt}$ in Table 1 is computed by image analysis from the variation of liquid saturation S (see 2.3.4) as a function of time.

Two main steps can be distinguished, namely liquid water nucleation and growth of the liquid clusters as discussed hereafter.

3.2 Nucleation

Condensation occurs as a result of the transport of water vapour within the pore space in the micromodel when the water vapour reaches sufficiently cold regions. Two steps are actually observed:

– prewetting. This is detected from a change in the contrast in the images of the micromodel. There is no visible liquid formation, i.e. droplets or channel fillings, during this phase. It takes generally several minutes (5 to 60 minutes) after the beginning of the gas mixture circulation in the inlet channel to observe the contrast change. A characteristic time of diffusion transport in the micromodel is given by $t_{dif} = \frac{L_y^{\,2}}{D^*}$, where L_y is the micromodel length (L_y = 30 mm) and D^* = O(D) is the effective diffusion of the micromodel; D is the molecular diffusion coefficient of water vapour in nitrogen ($D \approx 2.5\ 10^{-5}$ m^2/s). This gives $t_{dif} \approx 40$ s. Thus prewetting consistently appears after the water vapour diffuses into the micromodel. In fact, as discussed later, there is a significant convective transport of the vapour within the micromodel. Thus, the vapour invades the micromodel faster than considering a pure diffusive transport.

– liquid formation. This is detected from the observations of droplets at various locations within the micromodel. As illustrated in Fig. 3, which shows the liquid–gas distribution within the micromodel well after the appearance of first droplets, two main situations are observed: i) liquid only form along the colder edge of micromodel (this corresponds to Fig.

3a), ii) liquid form over a much larger region with two preferential liquid cluster growth regions: the cold edge of micromodel and a more central region with a clear preferential condensation in the lower region of micromodel.

.

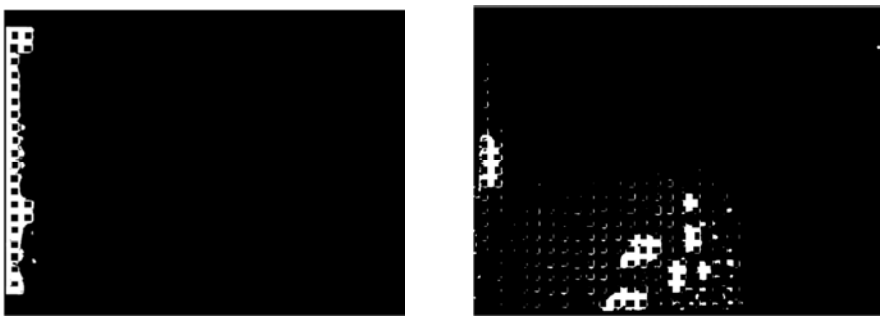

a) b)

Figure 3. Illustration of the two modes of nucleation: a) liquid phase growth from the colder edge only (mode “CE”), b) multisite growth with two main distinct regions: the micromodel colder edge and a more central region referred to as the “dew point region” (mode “CE+I”, where “I” stands for “inside” and CE for “colder edge”).

In the first case, i.e. when liquid forms only along the micromodel colder edge, many droplets grow simultaneously and coalesce when entering in contact. The pore space located between the micromodel colder edge and the first row of pillar is first invaded by liquid water. Then a first throat oriented along the thermal gradient is invaded. It takes usually hours (from 300 to 600 minutes) to reach this stage.

Droplets forming away from the cold side (mode “CE+I”), first grow separately. Then, they coalesce when touching each other to form liquid clusters. Differently from the CE mode, numerous visible droplets appear immediately. As illustrated in Fig. 3b, they form in the lower half strip of the micromodel (this point is further discussed below). The observation reveals that they first appear in the horizontal channels about 30 minutes after the beginning of experiment. The number of droplets increases significantly during 60 minutes. Then liquid clusters appear after about 150 minutes inside the micromodel. Liquid clusters form about at the same time along the colder edge of micromodel.

The mode of “nucleation”, i.e. either at the colder edge (mode “CE” in Table 1) or both at the colder edge and away from the colder edge (mode “CE+I” in Table 1), is reported in Table 1 for each experiment. As can be seen, the two modes are observed in both the hydrophilic micromodel and the hydrophobic one. As depicted in Fig.4, the discriminatory factor between the two modes is the relative humidity in the micromodel inlet channel. Mode “CE+I” is observed for relative humidity (*RH*) greater than about 60% whereas mode “CE” is observed for *RH* close to 50 % and below.

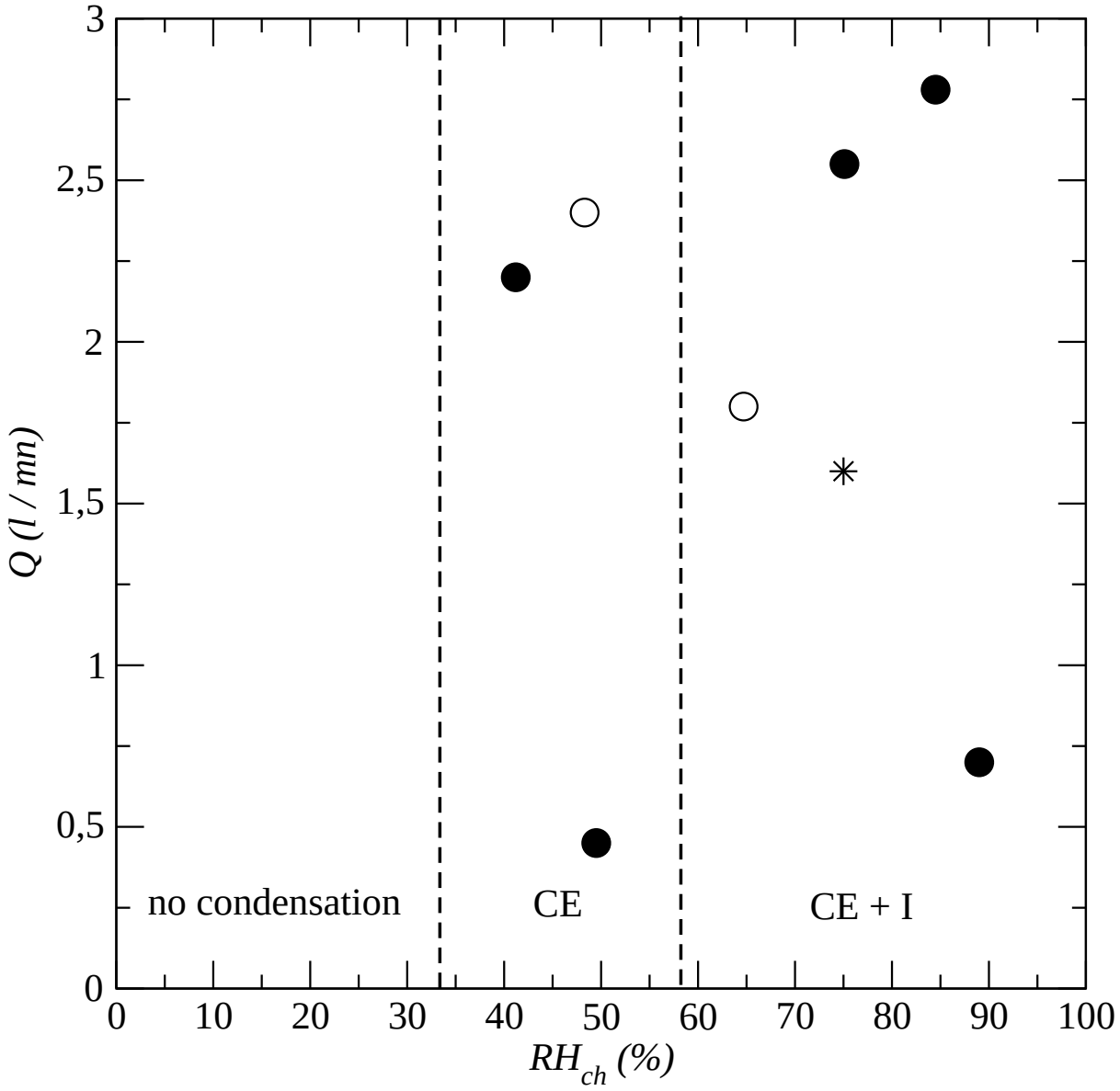

micromodel colder edge only: CE+I = condensation starts both from colder edger and the inside of micromodel.

To explain both the existence of the two modes “CE” and “CE+I” and the dissymmetry clearly visible in Fig.3b, we studied the transport of the vapour within the micromodel.
The idea here is to look at the vapour molar fraction field $X_v(x,y)$ within the micromodel right before the liquid clusters begin to form. To this end, we developed some numerical simulations using the commercial simulation software COMSOL Multiphysics®. The governing equations and associated boundary and initial conditions are described in Appendix C. As discussed in this Appendix, a key aspect of the experimental set-up is that the permeability contrast between the inlet channel and the channel network is not high. As a result, a (filtration) velocity field **U** is generated within the gas phase. This is illustrated in Fig. 5. From this velocity field, one can compute the local Peclet number $Pe = \frac{\|\mathbf{U}\| a}{D_{eff}}$, where a

is the lattice spacing (distance between two intersections in the network and D_{eff} is the effective diffusion coefficient of the network (see Appendix C). A representative distribution of the local Peclet number in the network is shown in Figure 5b. As can be seen, the value of the local Peclet number is greater than one over a significant region of the network. This indicates that the transport of the vapour within the network at the pore scale is due to the combination of convective and diffusive effects. Within the continuum framework used to perform the simulations, this means that both convection and dispersion effects, e.g. Fried and Combarnous (1971), must be taken into account.

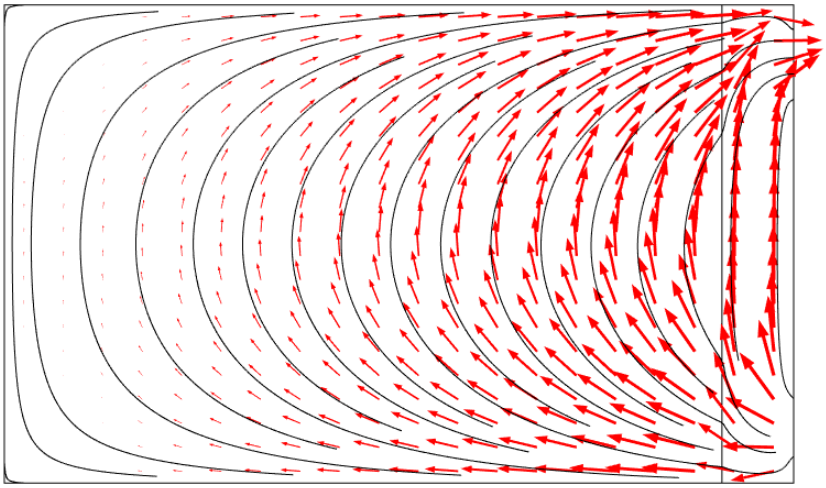

a)

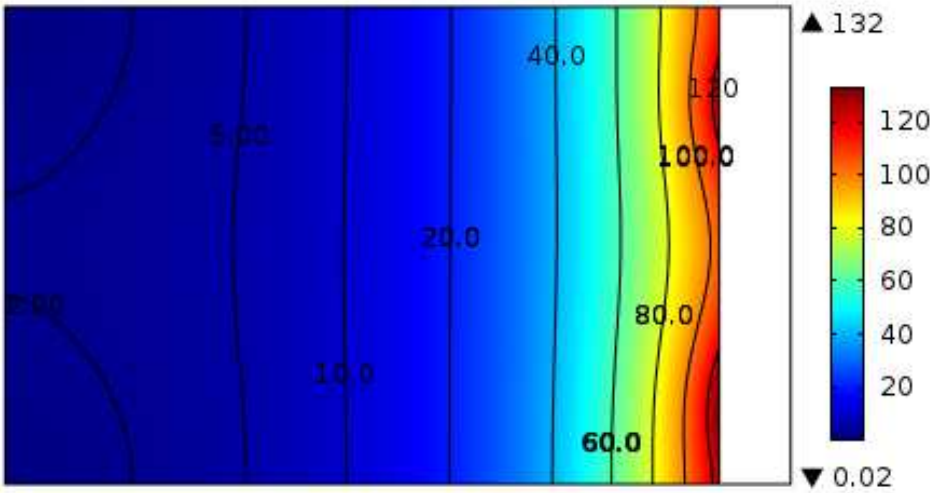

b)

Figure 5. a) Example of stream lines and velocity field induced in the micromodel (Q = 2.78 *l*/*mn*), b) corresponding local Peclet number distribution in the network.

Thus as discussed in Appendix D, the governing equation for the vapour in the micromodel reads,

$$\varepsilon \frac{\partial c X_v}{\partial t} + \nabla.(c X_v \mathbf{U}) = \nabla.\left(c \mathbf{D}^* . \nabla X_v\right) \qquad (1)$$

where ε is the micromodel porosity, c is the molar density of the gas mixture and $\mathbf{D}^*$ the dispersion tensor (specified in Appendix C). From the numerical solution of Eq.(1), we can compute the local relative humidity field $RH_l(x,y) = \frac{X_v(x,y)P_{ref}}{P_{vs}(T(y))}$, where P_{ref} is the gas mixture total pressure ($P_{ref} \approx 101325$ Pa) and P_{vs} is the vapour saturation pressure at the considered point.

Based on the simulations of the temperature field presented in Appendix B, the temperature field within the micromodel can be considered as independent of x and is given by $T(y) = T_c + (T_h - T_c)(1 - y/L_y)$ where T_c is the temperature on the cold edge of the micromodel and T_h the temperature in the inlet channel (hot edge of micromodel). Figure 6 shows two examples of the computed steady-state distribution of RH_l in the micromodel corresponding to Exp # 1 (20140117) and #4 (20140107) respectively.

The idea is that the region where $RH_l > 1$ should correspond to the incipient condensation region. Consistently with the experiments, the incipient condensation region ($RH_l > 1$) is confined to the colder edge of micromodel for a sufficiently low relative humidity in the inlet channel (as illustrated in Fig. 6b), whereas the condensation region extends over a significant region of the micromodel for a sufficiently large RH_{ch} (as illustrated in Fig. 6a). This is also clealy illustrated from the black and white insets in Figure 6 showing in white the region where $RH > 1$. Also a clear dissymmetry between the top and bottom sides of micromodel can be observed in Fig. 6 with greater RH_l on the side of the micromodel the closest to the inlet gas injection hole, i.e. the micromodel lower edge, consistently again with the experiments. The dissymmetry is thus due to the velocity field induced in the micromodel. As illustrated in Fig. 5a, the velocities are approximately oriented toward the micromodel upper edge, which breaks the symmetry between the upper and lower sides of micromodel.

According to the model presented in Appendix C, the occurrence of regime CE or of regime CE+I depends on two parameters: the relative humidity in the injected gas, denoted by RH_{ch} and the gas mixture injection flow rate Q (assuming all other parameters fixed as it is about the case in the experiments). This is of course for a sufficiently high RH_{ch}. We thus note first that no condensation is expected when the relative humidity in the gas mixture entering the system is sufficiently low. The corresponding threshold relative humidity is simply given by $RH_{chth} = \frac{P_{vs}(T_c)}{P_{vs}(T_h)}$. With 47°C and 27°C as representative values for T_c and T_h, this gives $RH_{chth} \approx 33$ %.

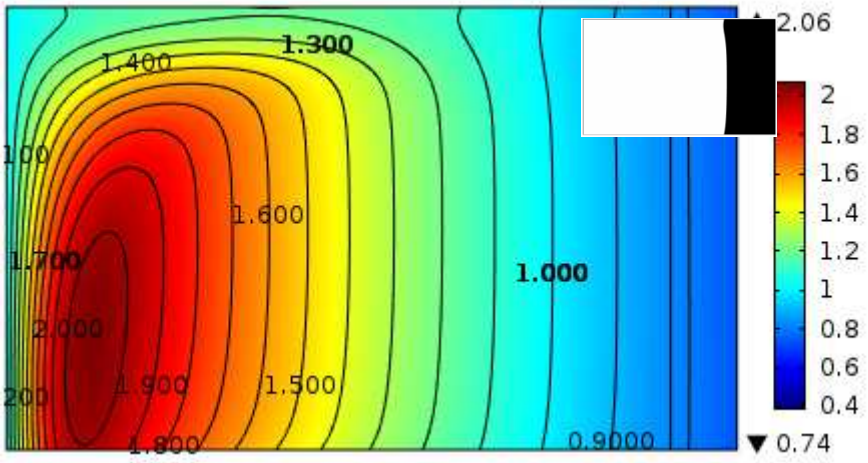

b)

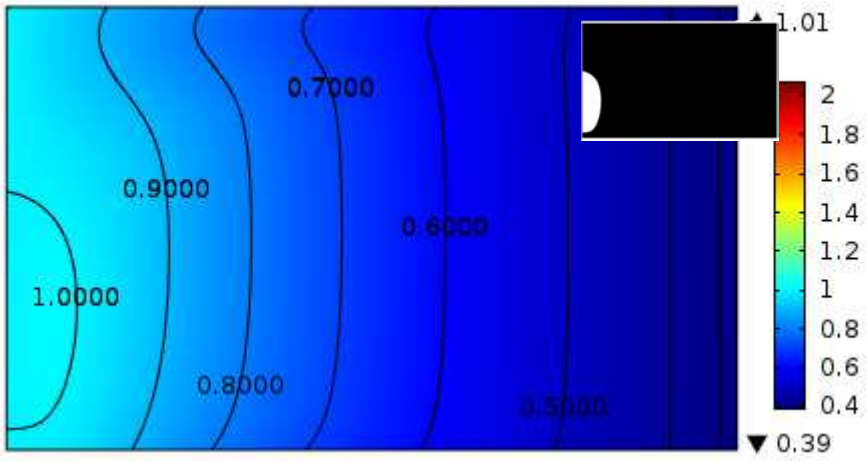

c)

Figure 6. Computed steady state distribution of RH_l within the micromodel corresponding to Exp #4 (20140107) (RH_{ch} = 84.5 %, Q = 2.78 *l/mn*, (a) and #1 (20140117) (RH_{ch} = 41.2 % , Q = 2.2 *l/mn*, (b)). The inset in black and white shows a binarized version of each figure with in black the region where RH_l < 1 and in white the region where RH_l >1. Note that the same color map is used for both figures.

To distinguish between regime CE and regime CE+I in the simulations when $RH_{ch} > RH_{chth}$, consider the black and white binarized images of RH_l distributions as exemplified in Fig.6 (insets). Then we introduce RH_{th} as a threshold value for the binarization. For the images shown as insets in Figure 6, RH_{th} = 1. If we adopt this value we found that the colder edge was in contact with both the black and white regions in the simulations corresponding to the experiments leading to regime CE (an example is Fig.6c). By contrast, the colder edge is exclusively in contact with a white region (i.e. $RH_l > RH_{th}$) in the simulations corresponding to the experiments leading to regime CE+I (an example is Fig.6b). This provides a criterion to distinguish between regime CE and regime CE+I. One can also increase the binarization threshold. For instance if one takes RH_{th} = 1.2, the micromodel is entirely black in the simulations corresponding to the CE experiments while a white zone ($RH_l > RH_{th}$) is present in the simulations corresponding to the CE+I experiments. Also, one can look at max(RH_l) and see that regime CE corresponds to max(RH_l) <1.2 and regime CE+I to to max(RH_l) >1.2.

Using one these criteria, one can use the simulations to add additional points in the phase diagram shown in Fig.4.

In summary the simulation results are qualitatively consistent with the experimental results summarized in Fig. 4. They show that below a certain relative humidity in the inlet channel nucleation is expected only along the micromodel colder edge whereas for a greater relative humidity nucleation can take place along the colder edge as well as inside the micromodel consistently with the experimental observations.

3.3 Patterns

After nucleation, the micromodel is progressively invaded by liquid water as a result of the condensation process. The liquid pattern depends on the regime (CE or CE+I) and the wettability of the system.

3.3.1 Regime CE

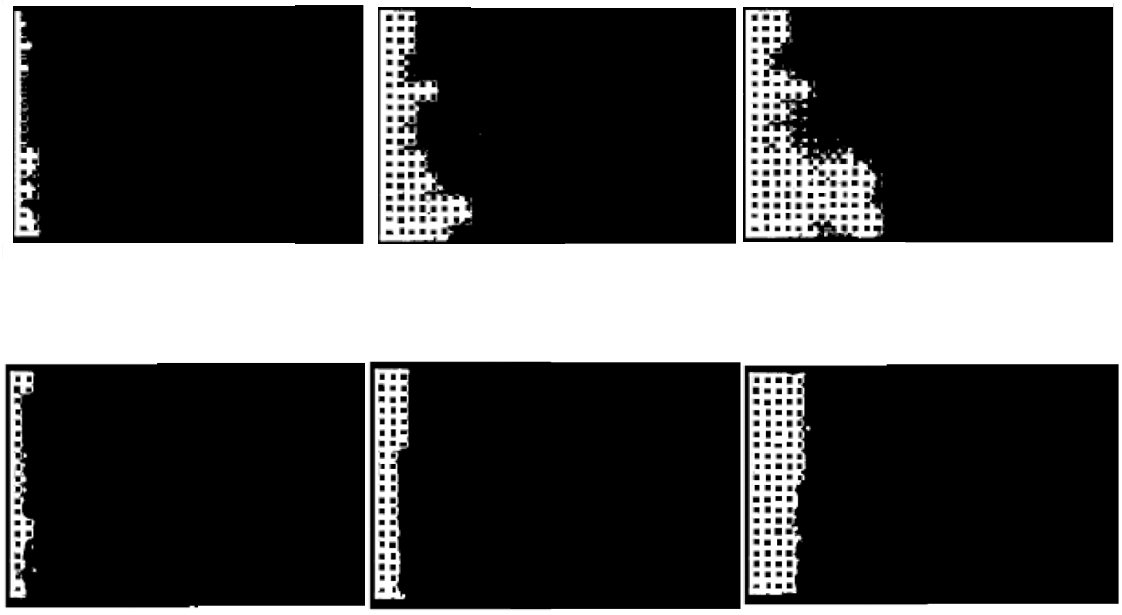

a)

b)

Figure 7 (4.6). Liquid water distributions in the micromodel in Regime CE (water in white, solid phase and gas phase in black): a) hydrophobic case, b) hydrophilic case. The experimental patterns correspond to Exp #2 at times 0.72, 3.07 and 5.40 days with the hydrophobic micromodel (a) and to Exp. #6 at times 0.38, 1.45 and 4.36 days with the hydrophilic micromodel (b).

The liquid invasion patterns obtained by condensation when liquid formation occurs from the micromodel colder edge (situation “CE”) are shown in Fig.7. The observed patterns are consistent with the patterns observed in slow drainage or imbibition (see Appendix A): the pattern is compact in the hydrophilic micromodel as a result of the predominance of the phenomenon of coalescence between adjacent growing menisci in pores, see Lenormand et al. (1984), Cieplak and Robbins (1990) for more details on the local invasion mechanisms, whereas the pattern is more much ramified when condensation occurs in the hydrophobic

systems. This is due to the predominance of the so-called burst events as local invasion mechanism, see again Cieplak and Robbins (1990) for more details. Note also that there is no occurrence of new condensation spots in the region ahead of the liquid-gas interface as this interface moves forward into the micromodel.

3.3.2 Regime CE+I

Figure 8 shows the condensation patterns obtained when liquid forms both along the colder edge and within the micromodel (regime CE+I). One can distinguish two main regions of liquid cluster growth, at least in a first phase of the invasion: the colder edge region and an inside region close to the dew point line (located at distance δ from the hotter edge as discussed in section 3.4). There is clear dissymmetry as regards the inside region with liquid region developing in the lower half region of micromodel and not in the upper half region. It is important to note that the lower region is on the side of the gas mixture inlet (see Fig.1). As discussed in section 3.2, the dissymmetry is due to the flow induced in the micromodel. Of course the flow structure changes with the growth of liquid clusters but the flow is still present in the network, at least in the dry region adjacent to the inlet channel, thus maintaining the dissymmetry also during the growth of the liquid clusters.

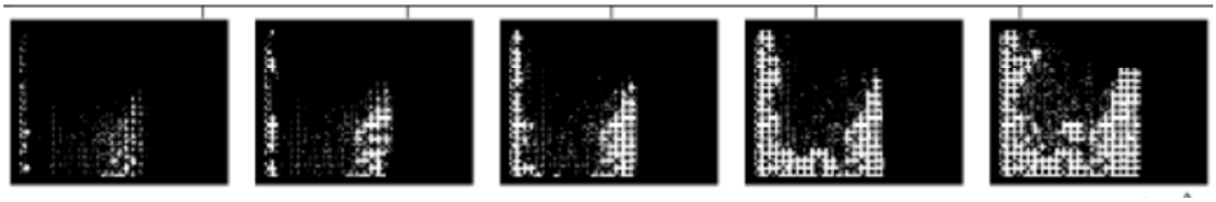

Hydrophobic (20140110 EXP 5), Evolution of liquid–gas distribution in micromodel. Patterns are shown at 0.17 0.90 1.99 3.08 and 6.50 days.

a)

Hydrophilic (20140313 EXP 6), Condensation process of a hydrophilic situation Time, 0.38 1.454.36 days. the area percent : 0.030, 0.067, 0.136.

b)

Figure 8 – Liquid water distributions in the micromodel in regime CE+I (water in white, solid phase and gas phase in black): a) hydrophobic case, b) hydrophilic case. The experimental patterns correspond to Exp #5 with the hydrophobic micromodel (a) and to Exp. #6 with the hydrophilic micromodel (b). The red circle indicates the formation of new cluster.

The two main aforementioned regions eventually merge and form a single liquid cluster (with trapping of a few gas pores) in the hydrophobic micromodel. As expected the liquid clusters are compact and faceted in the hydrophilic micromodel. Several clusters are visible in Fig. 8b (hydrophilic). Thus, roughly, more clusters are present in the micromodel in the hydrophilic case, at least for sufficiently large overall saturations. Also, as can be seen in Fig. 8b, new

clusters can form in the hydrophilic micromodel while the clusters previously formed continue to grow.

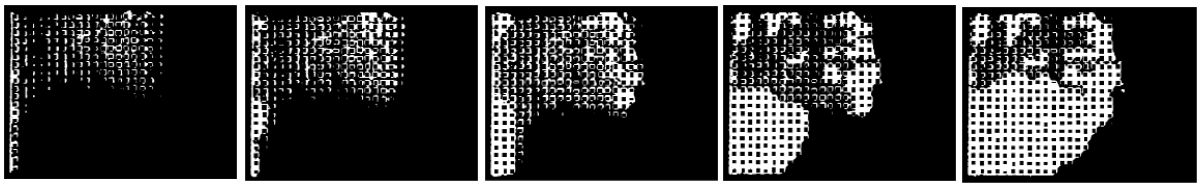

Figure 9 – Liquid water distributions in the micromodel of mixed wettability in Regime B + I (water in white, solid phase and gas phase in black): a) hydrophobic case, b) hydrophilic case. Note that the inlet and outlet of the inlet channel were inversed compared to the experiments shown in Figs. 7 and 8. Thus, the inlet was on the inlet channel top and the outlet was on the bottom (the opposite of what is shown in Fig. 1b).

Finally, Fig.9 shows the pattern obtained in a micromodel of mixed wettability for conditions leading to regime CE+I. The top half region of the micromodel is hydrophobic whereas the bottom half region is hydrophilic. A first interesting point is that the gas mixture inlet and gas mixture outlet were inversed compared to the other experiments. Thus, their respective positions are the opposite of what is shown in Fig.1b. Consistently with the analysis of pattern dissymmetry discussed previously, the region of preferential condensation is here the upper half region, i.e. the region on the side of the gas mixture inlet. This confirms the major role of convective effects in the occurrence of the pattern dissymmetry.
Also, this suggests that the possible temperature non-uniformities in the transverse direction, if any, are not the main reason of the occurrence of the preferential condensation region. Indeed, it could be surmised that the isotherms in the micromodel are not parallel to the cold and hot edges of micromodel either due to too low circulation flow rates in the bronze tubes (see Appendix B) or to a misalignment of the micromodel. This could cause temperature differences between the upper half and lower half regions of micromodel. Note that the direction of flow in the end bronze tubes was kept the same in all experiments. Combined with the temperature field computations reported in Appendix B, the conclusion is that the temperature transversal variations, if any, cannot explain the preferential condensation region seen in the experiments whereas the change in the position of the gas mixture inlet and outlet fully support the explanation via the impact of the convective transport of the vapour.
A striking difference compared to Figure 8 lies in the marked invasion of the hydrophilic region, i.e here the micromodel half region close to the gas outlet (lower region in Fig. 9). The corresponding region (upper region in Fig. 8 because of the outlet-inlet inversion) is little invaded comparatively. The fact that the lower half region is invaded could be expected since water should preferentially invade hydrophilic regions. Further analysis of this observation is however left for the companion paper Straubhaar et al. (2015b).
Thus, a mixed of CE and CE+I regimes is actually observed with the micromodel of mixed wettability. Liquid invasion only takes place from the colder edge in the hydrophilic half layer (CE regime) whereas liquid cluster growth is observed from both the colder edge and inside the micromodel in the hydrophobic region (CE+I regime).
The invasion is compact in this region in Fig.9 which was expected since this region is hydrophilic. Also, the images in Fig. 9 suggest that the growth of liquid clusters in the hydrophobic region becomes quite weak after a first phase while the cluster in the hydrophilic

region continues to grow significantly. This is clearly illustrated in Fig. 10, which shows the variation of the liquid saturations in the different zones of the micromodel.

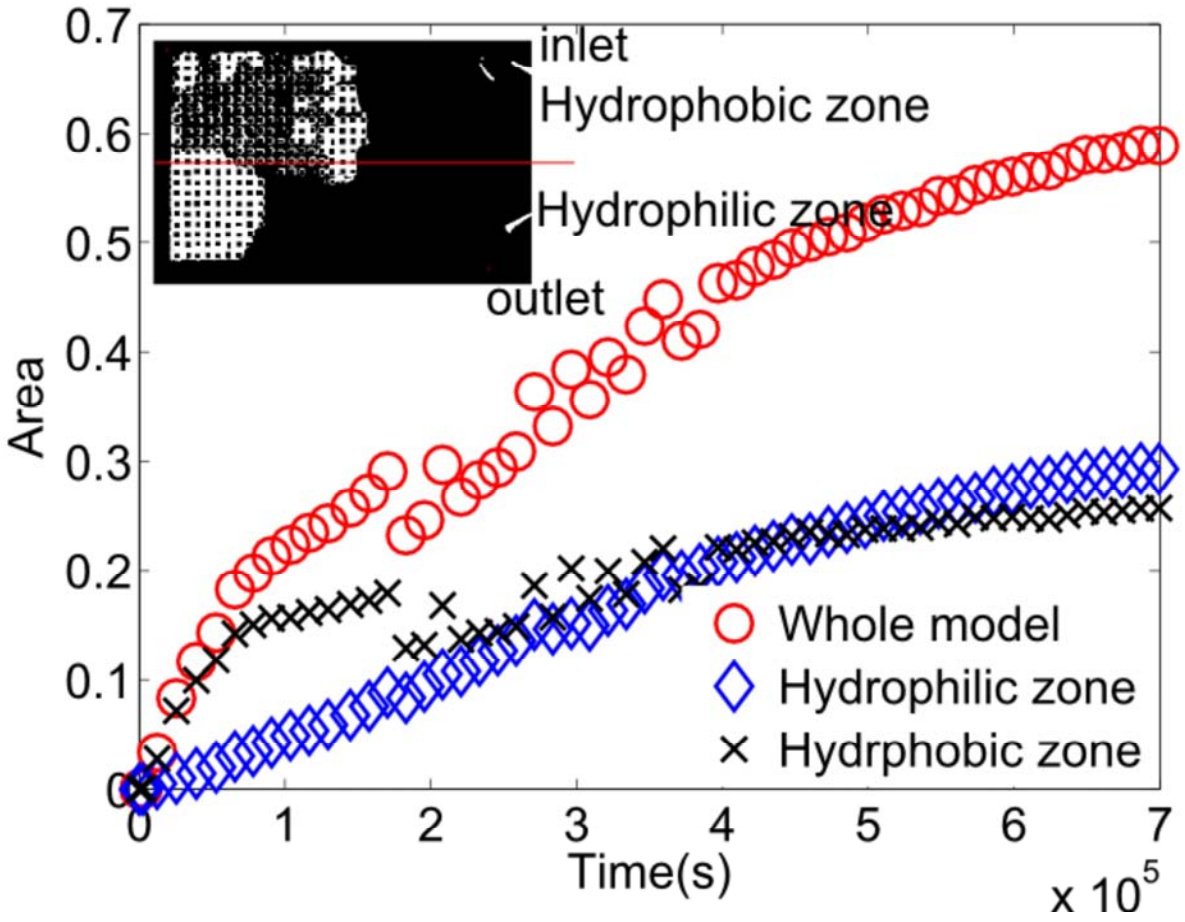

Fig. 10. Liquid saturation variations in the micromodel of mixed wettability.

As confirmed in Fig.10, the condensation dynamics is quite different in each region. The liquid region growth rate is relatively low but steady in the hydrophilic region. It tends to decrease for the longer times shown in Fig. 10. This evolution is in fact pretty much the same as the one observed for the CE mode in system of uniform wettability (see section 3.6). The situation is quite different in the hydrophobic strip, with a condensation kinetics similar to the one observed for the CE+I mode in system of uniform wettability (see section 3.6): a first phase of rapid growth is followed after about one day by a second phase of much slower kinetics. As a result, the overall kinetics is mainly affected by the liquid growth in the hydrophobic region in a first phase and then by the progressive invasion of the hydrophilic strip in a second phase as illustrated in Fig. 9.

3.4 Maximum extent of two phase zone in micromodel

At a meniscus forming in the region partially invaded by the liquid phase, the water vapour pressure is given by $P_{vs}(T(y))$. Since a certain water vapour pressure $P_v(0) = P_{vs}(0)RH_{ch}$ is

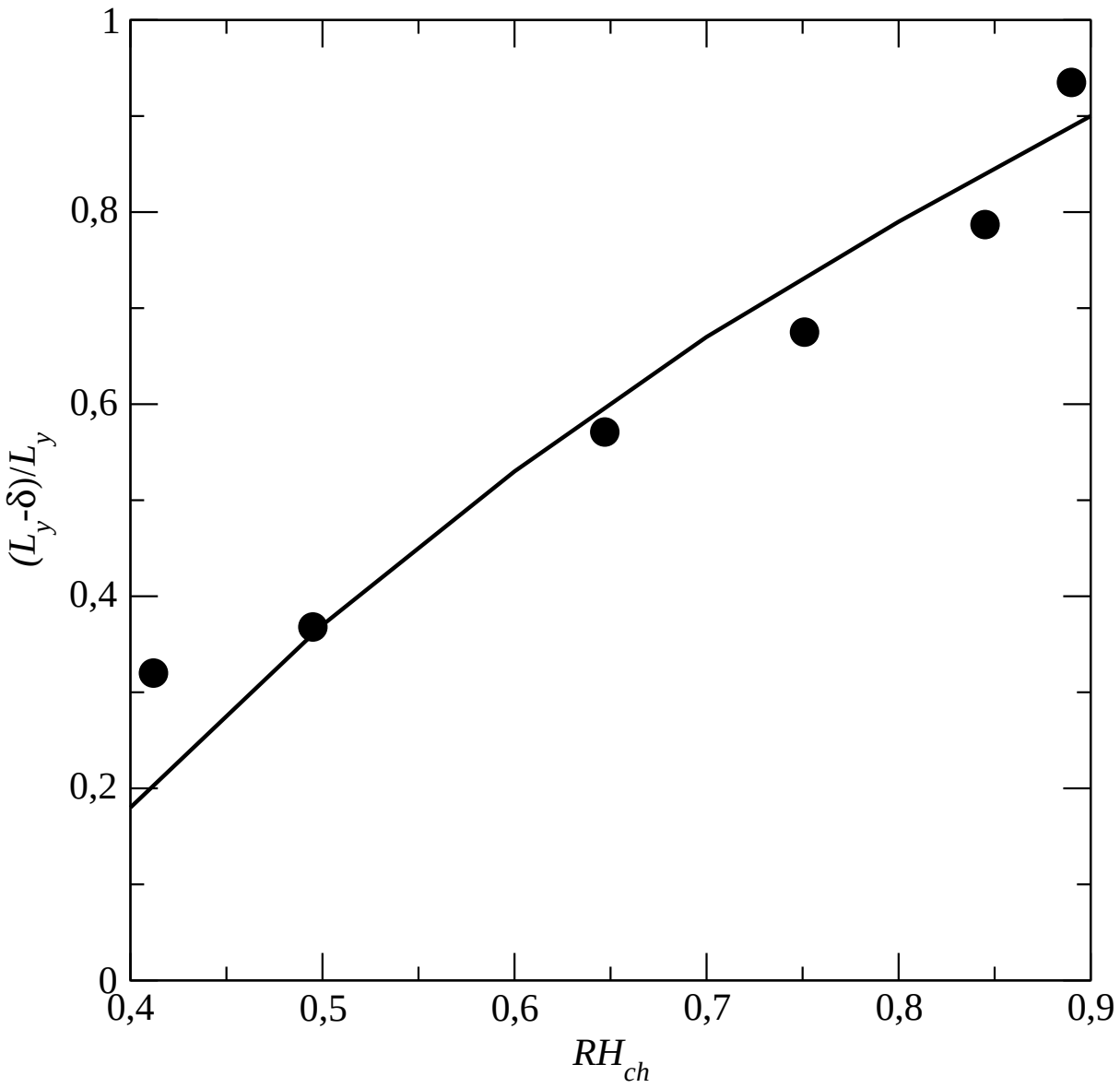
1
0,8
0,6
0,4
0,2
0
0,4
0,5
0,6
0,7
0,8
0,9
$(L_y-\delta)/L_y$
RH_{ch}

Taking T_c=27°c and T_h = 47.5 °C., as representative temperatures of our experiments and solving Eq. (2) gives the variation of $L_y - \delta$ with RH_{ch} depicted in Fig. 11. We have also plotted in Fig. 11 the maximum size of two-phase zone observed in the various experiments. The size δ in the experiments corresponds to the size of the dry black region on the right of the micromodel in Fig. 7-9. This size (distance between the most advanced liquid point and the inlet channel / micromodel interface) was measured on the last available image for each experiment. As can be seen, there is a fair agreement between the computed extents of two-phase zone and the measured ones.
Actually, the distance δ corresponds to the location of the dew point within the micromodel. It should be also noted that liquid water can enter the region between the dew point and the inlet channel in case of liquid fingering (evaporation at a finger tip can be compensated by condensation in the region located beyond δ). By contrast, no liquid is expected to be present in the region $y < \delta$ if the condensation process leads to the formation of a (almost) flat front.

3.5 Condensation kinetics

The variation of the overall liquid saturation as a function of time is depicted in Fig.12 for all the experiments (except the experiment with the micromodel of mixed wettability already discussed).

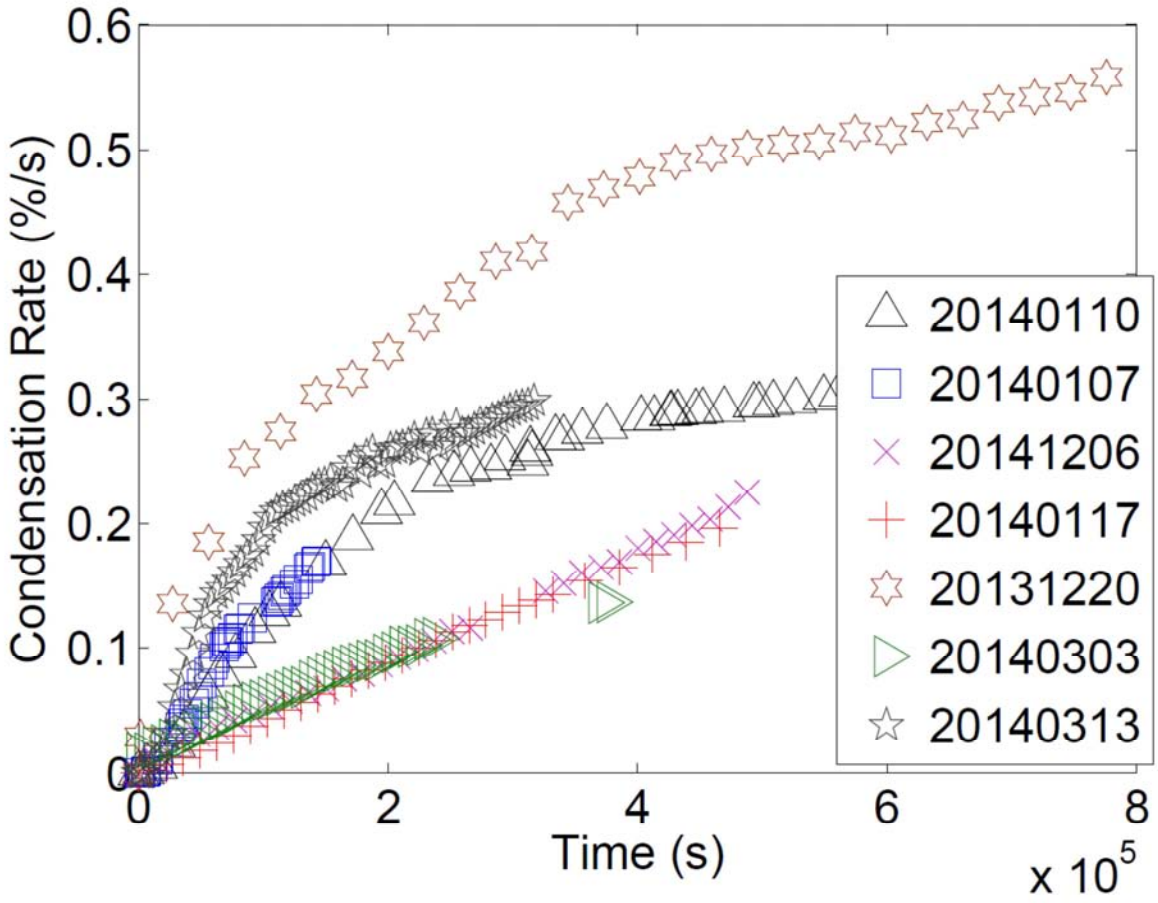

Figure 12. Variation of overall saturation as a function of time for the various experiments.

As discussed in §3.4, a steady state is expected if the experiment lasts sufficiently long. This corresponds to the plateau visible for some experiments. However, the condensation rate tends to become very small as the steady-state is approached and this makes the experiment

quite long. As a result, the experiment was sometimes stopped too early to really observe the steady state. Also, it is difficult to maintain perfect steady boundary conditions since it is difficult to avoid temperature variations in the enclosure and in the end bronze tubes.

Two groups of curves can be clearly distinguished in Fig.12.
The first group is characterized by lower condensation rate and a quasi-linear evolution of the overall saturation during most of the experiment. This group gathers all the experiments corresponding to the CE regime and thus corresponds to comparatively lower relative humidity in the inlet channel (see Table 1). Thus as expected, the greater the relative humidity in the inlet channel, the faster the invasion, at least in a first phase of the process.
The quasi-linear variation was a bit unexpected since the size of the dry zone through which the vapour is transported to the condensation front diminishes as the condensation front moves into the micromodel. Since the vapour flux should be roughly inversely proportional to the distance between the front and the inlet channel, an acceleration of the front could be expected. However, another important driving parameter is the vapour molar fraction difference between the inlet channel and the front: $\Delta X_{vf} \approx \frac{RH_{ch}\, p_{vs}(T_h) - p_{vs}(T_f)}{P_{ref}}$ where P_{vs} is the vapour saturation pressure and T_f the temperature at the front. Since the temperature at the front increases as the front moves into the micromodel, ΔX_{vf} decreases as the front moves toward the hotter edge of micromodel. Thus, it seems that the two effects, namely the decreasing of ΔX_{vf} and the increasing of vapour transport conductance due to the decreasing in the dry zone size, compensates each other to lead to an almost constant condensation rate over a long period of the micromodel invasion. Also, the fact that the curves corresponding to Exp. #20140117 (hydrophobic micromodel) and to Exp. #20140303 (hydrophilic micromodel) are almost superimposed was unexpected from the consideration of the patterns (note that Q and RH_{ch} are comparable in these two experiments). It was in fact expected that the fingering of the front in the hydrophobic micromodel would accelerate the invasion compared to the almost flat front observed in the hydrophilic micromodel. In fact this is not so obvious for the same reasons as we have just discussed regarding the linear variation of the saturation since the most advanced points of a rough front is at a higher temperature than the mean position of the front while a less advanced point is at a colder temperature (and thus at a vapour pressure less close to the one existing in the inlet channel than a more advanced point of the front). The computation of the slope $\frac{dS}{dt}$ leads to $4\ 10^{-7} s^{-1}$ and to $3.2\ 10^{-7} s^{-1}$ for Exp. #20140117 and to Exp. #20140303 respectively, suggesting that the fingering observed in the hydrophobic micromodel does lead to a faster invasion.
The second group of curves in Fig.12 corresponds to condensation in CE+I. Two main phases can be distinguished with this regime. The first phase is a phase of greater saturation variation, i.e. of greater overall condensation rate. Then the condensation rate progressively diminishes to reach a phase where the condensation rate is significantly lower than in the first phase and the saturation varies again quasi-linearly. The condensation rate in the first phase clearly increases in the hydrophobic micromodel with the relative humidity in the inlet channel as expected. Contrary to regime CE, the condensation rate is clearly greater in the hydrophilic system in this regime compared to the hydrophobic one as shown by the comparison between Exp. #20140313 (hydrophilic, RH_{ch} = 65%) and Exp. #20140110 (hydrophobic, RH_{ch} = 75%) or Exp. #20140107 (hydrophobic, RH_{ch} = 84.5 %). This is however not obvious to explain from the observation of the patterns in Fig.8.

6. Conclusions

Visualization experiments of condensation driven by a temperature gradient in a quasi- two-dimensional model porous medium were presented and analyzed. Comparisons were performed between hydrophobic and hydrophilic systems as well as with a micromodel of mixed wettability.

The experiments allowed us to distinguish two main condensation regimes: a regime where the condensation zone is initially confined along the colder wall of the system and a regime where the incipient condensation can take place over a significant region of the porous medium, i.e. both along the colder wall and within the porous domain. In our system, the first regime was observed for a sufficiently low relative humidity and the second for greater relative humidity but it should be clear that other parameters, such as the temperature gradient for example, can also be varied to move from one regime to the other. The temperature gradient was pretty much the same in all our experiments and this was therefore not explicitly shown.

The first regime is characterized by a liquid zone growing from the colder wall into a dry medium whereas the second regime leads to the formation of a two-phase zone.

The wettability has an impact of the structure of the growing liquid cluster(s). As expected, compact faceted liquid clusters were observed in the hydrophilic medium whereas capillary fingering was observed in the hydrophobic system.

For similar conditions except the wettability, the experiment indicated slower saturation variations in the hydrophilic medium in the first regime whereas the opposite was observed in the second regime. However further experiments are desirable to confirm these trends.

Our system was characterized by the existence of a significant convective flow within a large fraction of the porous domain. This flow induced a symmetry breaking (compared to a purely diffusive solution) resulting in the preferential condensation of the vapour in the half region of the system the closest to the humid gas inlet. It would be desirable to perform the experiments under purely diffusive conditions in the porous domain so to consider conditions probably more representative of what happens in many applications, including in the gas diffusion layers of PEMFC.

In addition to a better understanding of the condensation process in porous media, the experimental data and visualizations presented in the present could be used to benchmark numerical models.

Acknowledgements:

The authors gratefully acknowledge the funding from the EU project IMPALA (“IMprove PEMFC with Advanced water management and gas diffusion Layers for Automotive application”, project number: 303446) within the Fuel Cells and Hydrogen Joint Undertaking (FCHJU).

References

F. Barbir, PEM Fuel Cells: theory and practice, Elsevier Academic Press, 2005.

N.K. Baibakov,A.R. Garushev,W.J. Cieslewic Thermal Methods of Petroleum Production, Elsevier , New-York (1989)

V.Berejnov , N. Djilali, D. Sinton, Lab-on-chip methodologies for the study of transport in porous media: energy applications, Lab Chip, 8**,** 689-693 (2008)

Cieplak, M., M.O. Robbins, Influence of contact angle on quasistatic invasion of porous media, Phys. Rev. B 41, 508–521, 1990

J.Eller, T. Rose, F.Marone, M. Stampanoni, A. Wokaun and F. N. Büchi, Progress in In Situ X-Ray Tomographic Microscopy of Liquid Water in Gas Diffusion Layers of PEFC Journal of The Electrochemical Society, 158 (8) B963-B970 (2011)

A. Faghri, Heat pipe science and technology, Taylor and Francis (1995).

J.J. Fried and M.Combarnous, Dispersion in Porous Media. Advances in Hydroscience, Vol.7, pp.169-282, Academic Press (1971)

Hens, H., Building Physics-Heat, Air and Moisture. Ernst & Sohn, Wiley (2007)

S. P. Kuttanikkad, M. Prat, J. Pauchet, Pore-network simulations of two-phase flow in a thin porous layer of mixed wettability: Application to water transport in gas diffusion layers of proton exchange membrane fuel cells, *J. of Power Sources* 196, pp. 1145–1155 (2011)

S.Larbi, G.Bacon, S.A.Bories, Diffusion d'air humide avec condensation de vapeur d'eau en milieu poreux Int.,J Heat Mass Transfer. Vol. 38, No. 13, pp. 2411-2426, 1995

J.B.Laurindo et M.Prat. Numerical and experimental network study of evaporation in capillary porous media. Phase distributions. *Chem.Eng.Sci.*, Vol.51,No.23, pp.5171-5185 (1996)

J.B.Laurindo et M.Prat. Numerical and experimental network study of evaporation in capillary porous media. Drying rates. *Chem.Eng.Sci*., Vol.53,No.12, pp.2257-2269 (1998)

Lenormand, R., Zarcone, C.: Role of roughness and edges during imbibition in square capillaries. SPE 13264, presented at the 59th Annual Technical Conference and Exhibition of the Society of Petroleum Engineers, Houston, Tex. , September 16-19 (1984).

Lenormand R., E. Touboul, C. Zarcone, Numerical models and experiments on immiscible displacements in porous media, Journal of Fluid Mechanics, Volume 189, April 1988, pp 165-187 (1988)

B.Straubhaar, J. Pauchet, M. Prat, Water transport in gas diffusion layer of a polymer electrolyte fuel cell in the presence of a temperature gradient. Phase change effect. *International Journal of Hydrogen Energy,* 40 (35) 11668–11675 (2015a)

B.Straubhaar, L. Du, P.Duru[1], M.Prat Pore network modelling of liquid water invasion by condensation in a model porous medium, to be submitted (2015b)

APPENDIX A Liquid water injection experiment

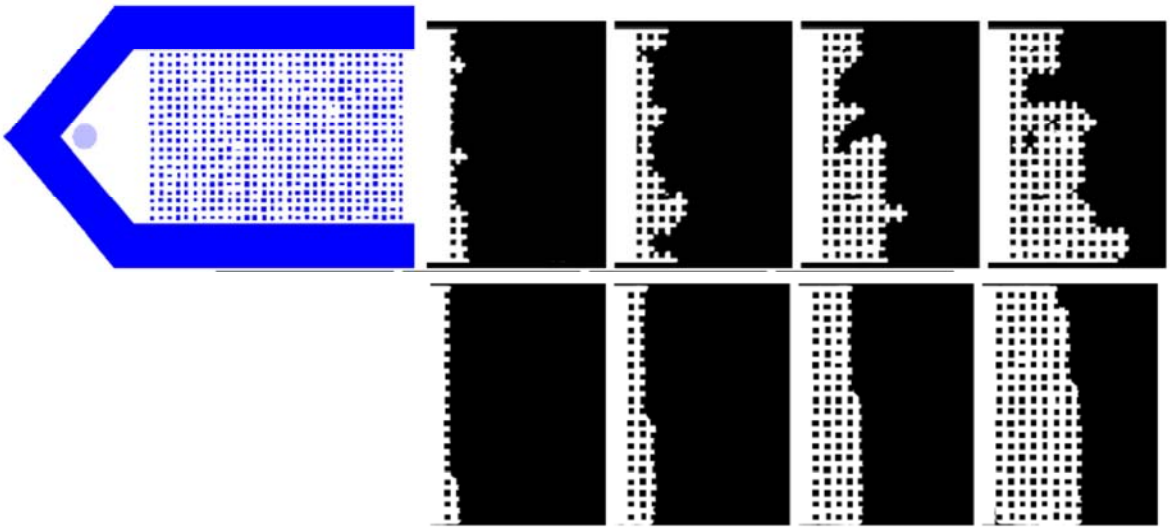

Figure A1. Summary of liquid invasion experiments. Top view of micromodel (image on top left). Patterns with hydrophobic micromodel (top row of black and white images) and with hydrophilic experiments (bottom row of black and white images). The liquid water is in white and the gas phase in black.

Figure A1 shows the main results of the liquid water injection experiment. The experiment is performed at the room temperature. The micromodel is initially dry (occupied by air). Liquid water is slowly injected (Q = 10 $\mu L/h$) through the circular hole visible in the top view of micromodel in Fig. A1. Then liquid water flows in the inlet chamber (of triangular shape in Fig. A1) forming a moving flat interface until it reaches the network. As expected, the invasion in the hydrophobic network leads to a rough front characteristic of capillary fingering whereas a faceted and compact front can be observed in the hydrophilic network. This clearly shows that the desired wettability is well imposed in the two cases.

APPENDIX B ***Simulation of temperature field in the bronze plate***

The appendix describes numerical simulations of the temperature in the bronze plate. A major objective is to determine the structure of temperature field in the plate and thus in the micromodel.

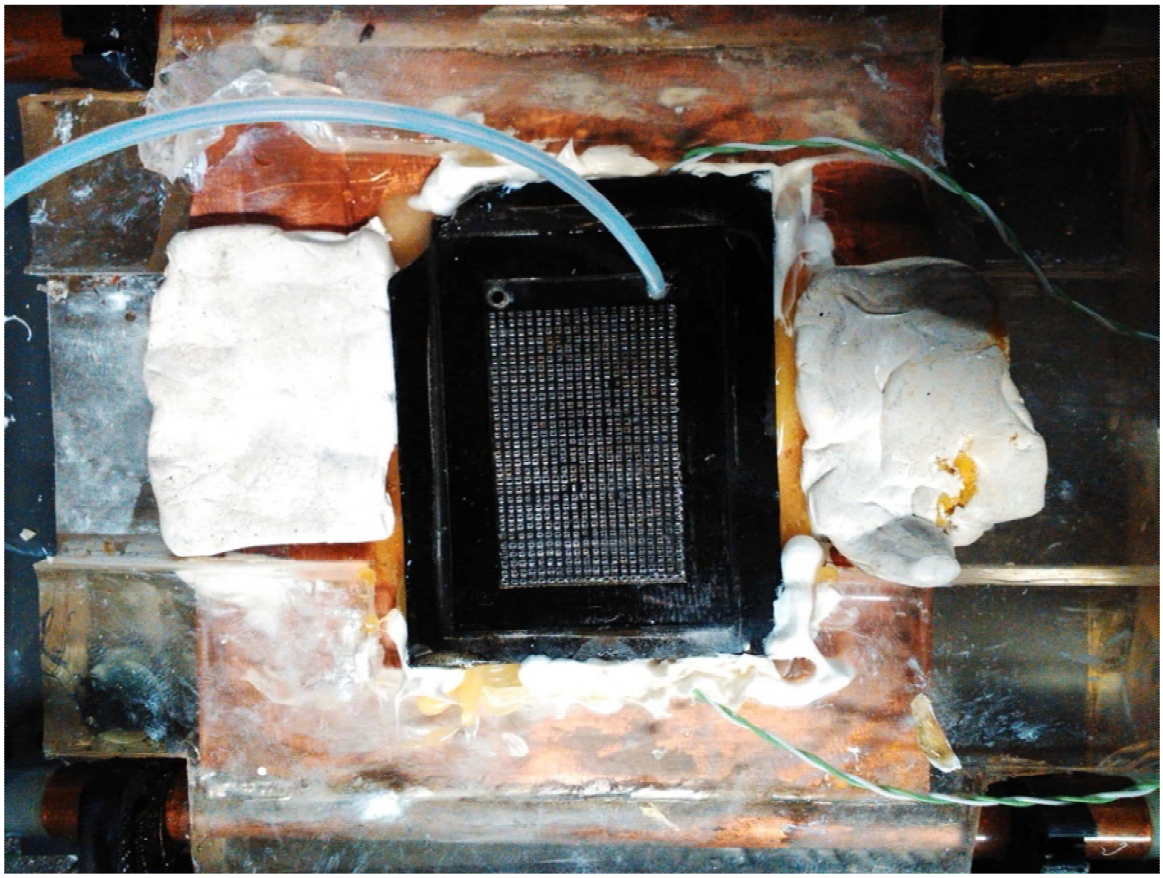

The above image gives a top view of micromodel together with the bronze plate, the adjacent bronze tubes. Note the 90° anti-clockwise rotation compared to the images and Figures shown in the main text. The PDMS used as insulation material is also visible together with the insulation paste (in white).

From the above photograph, the domain of interest for the thermal field computation is sketched in Fig. B1.

The domain in yellow corresponds to the 8 cm x 8 cm square bronze plate of thickness e_{br}= 1mm.

The red domain corresponds to the hot bronze tube of internal radius R_i = 1.5 mm and external radius R_e= 3mm welded to the bronze plate (the cold tube dimensions are identical).

The green rectangle corresponds to the polymeric micromodel (further details in Fig.B2). Its thickness is 1 mm. It is assumed that its thermal conductivity is similar to the one of PDMS.

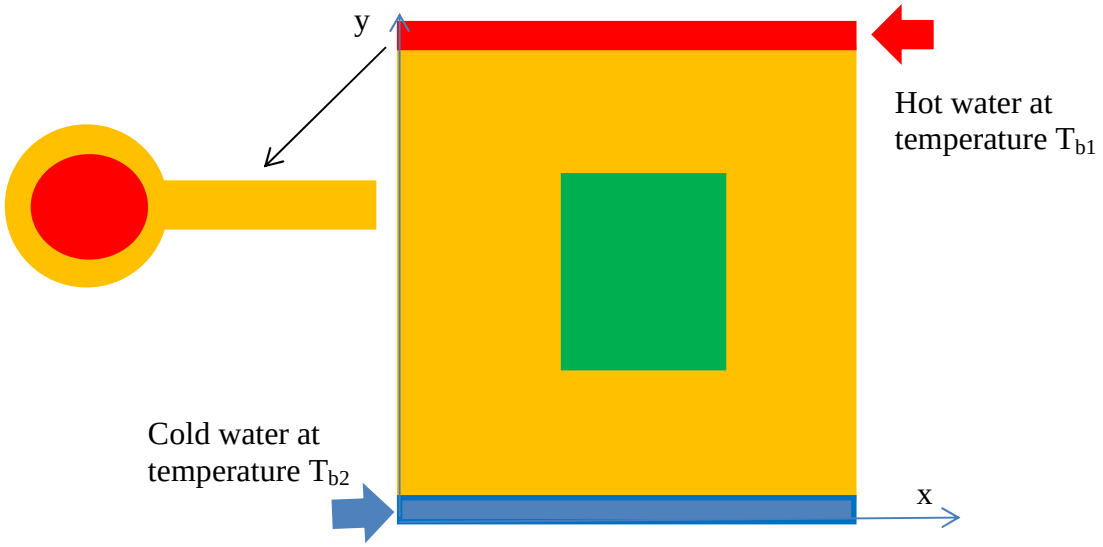

Fig. B1 The bronze plate (in yellow), the cold tube (in blue), the hot tube (in red) and the micromodel (in green).

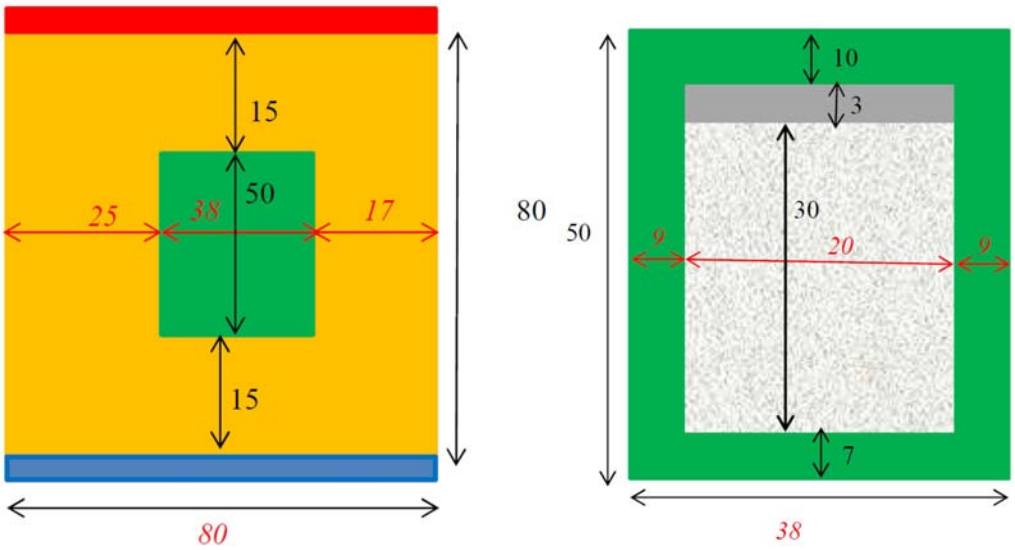

a) b)

Fig. B2. a) Dimensions (in mm) with an example of micromodel positioning. As illustrated here the micromodel is not necessarily centered in an experiment. It can also happen that the

micromodel lateral edges are not perfectly parallel to the bronze plate lateral edges; b) details for the micromodel.

The heat conduction equation to solve in the bronze plate reads

$$\nabla.(\lambda \nabla T) = 0. \tag{B1}$$

Using differential operators depending only on x and y, Eq.(B1) is expressed as

$$\nabla.(\lambda \nabla T) + \frac{\partial}{\partial z}\left(\lambda \frac{\partial T}{\partial z}\right) = 0. \tag{B2}$$

Integrating over the plate thickness e yields

$$\int_0^e \left(\nabla.(\lambda \nabla T) + \frac{\partial}{\partial z}\left(\lambda \frac{\partial T}{\partial z}\right)\right) dz = 0. \tag{B3}$$

leading to

$$\nabla.(\lambda \nabla T) = -\frac{\lambda}{e}\frac{\partial T}{\partial z}_{z=e} = \frac{h}{e}(T - T_{amb}) \tag{B4}$$

where h is a free convection coefficient and T_{amb} is the ambient temperature in the enclosure. The equation to be solved is therefore

$$\nabla.(\lambda \nabla T) = \frac{h}{e}(T - T_{amb}) \tag{B5}$$

together with the following boundary conditions. A free convection heat transfer is assumed along the two lateral edges of the plate (vertical edges in Fig.B1).

$$\lambda \frac{\partial T}{\partial x} = h_b\,(T - T_{amb}) \text{ (left edge) and } \lambda \frac{\partial T}{\partial x} = -h_b\,(T - T_{amb}) \text{ (right edge)} \tag{B6}$$

The heat transfer between the tubes is described assuming that the heat flux φ through the tube wall is approximately constant.
Following an approach similar to the one described in Incropera et al. (2007) p. 498, the temperature variation along the cooling tube is given by

$$T = T_{m0c} + \lambda \frac{\partial T}{\partial y}\frac{P_{pl}}{q_c c_p}x + \frac{(T_{amb} - T)}{R_i}\frac{P_{hl}}{q_c c_p}x\left[\frac{Ln(R_e/R_i)}{\lambda_b} + \frac{Ln(R_{out}/R_i)}{\lambda_{PDMS}}\right] \tag{B7}$$

where q_c (kg/s) is the water flow rate in the tube; c_p the liquid water heat capacity and T_{m0c} is the temperature at the tube entrance; $P_{pl} = 2\pi R_i/6$; $P_{hl} = 10\pi R_i/6$. The last term on the tight hand side of Eq.(B7) represents the heat losses through the PDMS wrapping the tube while the second term represents the heat exchange between the tube and the plate, $R_{out} = R_e + e_{PDMS}$ (thickness of PDMS).

Similarly we have for the hot tube

$$T = T_{m0w} - \lambda \frac{\partial T}{\partial y} \frac{P_{pl}}{q_w c_p}(L-x) + \frac{(T_{amb}-T)}{R_i} \frac{P_{hl}}{q_w c_p}(L-x)\left[\frac{Ln(R_e/R_i)}{\lambda_b} + \frac{Ln(R_{out}/R_i)}{\lambda_{PDMS}} \right] \quad \text{(B8)}$$

Eqs. (B7) and (B8) provide the boundary conditions on the horizontal edges of the plate.

The data used for the computation are summarized in Table C1. The correlation used for determining the heat transfer by free convection is for a plate surface at uniform temperature. This is obviously not case in our situation. However, the computations indicate that the heat losses by free convection do not affect the temperature field in the plate.

Table B1. Values of parameters used for the computation of temperature field in bronze plate.

λ_{bronze} *(W/m/K)*	400	
λ_{PDMS} *(W/m/K)*	0.15	
λ_{air} *(W/m/K)*	0.027	
c_p *(eau) (J/ kg.K)*	4200	
q_c *(kg/s)*	Max : 17 l/min (=0.28 kg/s)	Corresponds to Re = 10^5
q_w *(kg/s)*	Idem q_f	
h_b	$= h$	
h	$h = Nu\lambda_{air}/l$	Free convection heat transfer coefficient.
l	Surface /(surface perimeter) = 20 mm (eq.(9.29) in Incropera et al.(2007)	Length scale for computing the free convection heat transfer coefficient
L	80 mm	Side length of bronze plate
Nu	Nu = 0.54 $Ra^{1/4}$ si $10^4 \leq$ Ra $\leq 10^7$	Nusselt number
Ra	$Ra = \frac{g\beta(T_{sur}-T_{amb})l^3}{\nu\alpha}$ g = 9.81 m.s^{-2} ; ν=16.2 10^{-6} m^2/s; α =22.9 10^{-6} m^2/s; β = 2/(T_{surf} + T_{amb}) (with T en K)	Rayleigh number
$T_{amb} = T_{b3}$ *(°C)*	45	
$T_{m0f} = T_{b2}$ *(°C)*	0.3	
$T_{m0c} = T_{b1}$ *(°C)*	70	
T_{sur}	$0.5(T_{b2}+T_{b1}) \approx 35°C$	
R_e *(mm)*	3.	Tube external diameter
R_i *(mm)*	1.5	Tube internal diameter
e_{bronze} *(mm)*	1	
e_{PDMS} *(mm)*	1	PDMS, Micromodel, insulating material (see photo)

A major unknown is the flow rate in the cooling and the warming tubes. The maximum flow rate that can be produced by the cryostats is about 17 l /mn as indicated in the Table.

Unfortunately, the flow rate effectively circulating in each tube during an experiment was not measured. Owing to the various pressure drops in each circuit, the flow rate is expected to be lower than the maximum flow rate. Fig.B3 shows the isotherms within the plates computed for four values of the flow rate (taken identical in both tubes): q_{ref} = 17 l/mn; q_{ref} /10, q_{ref} /100 and q_{ref} /1000 respectively.

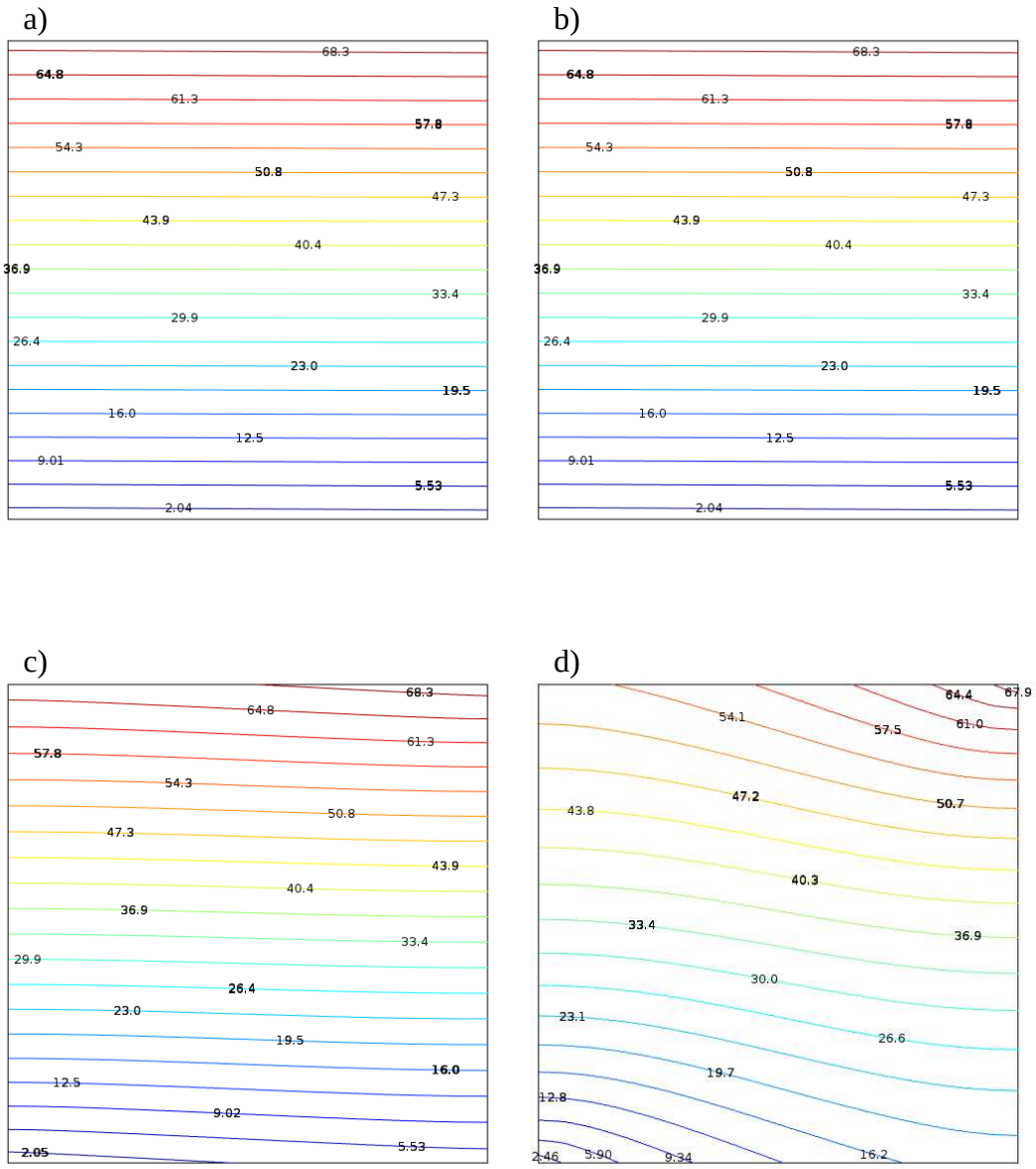

Fig. B3 – Simulated temperature field within the bronze plate. q_{ref} = q_c = q_f = 17 l/min. a) q_{ref} b) q_{ref}/10 c) q_{ref}/100 c) q_{ref}/1000.

As can be seen, these results suggest that the distortion of isotherms becomes effective for very low circulating flow rates in the tube. The expected flow rates are in the range [1 l/mn – 17 l/m]. The conclusion is therefore that the isotherms should be parallel to the end tubes in the experiments (as illustrated in Fig. B3a and B3b).

Reference (Appendix)

F.P. Incropera, D. P. DeWitt, T. L. Bergman, A. S. Lavine, Fundamentals of Heat and Mass Transfer 6th Edition, Wiley (2007)

Appendix C Simulation of vapour convective – dispersive transport within the micromodel.

Computational domain

The computational domain, denoted by Ω, is sketched in Fig. C1. Note the 90° anti-clockwise rotation compared to the images and Figures shown in the main text.

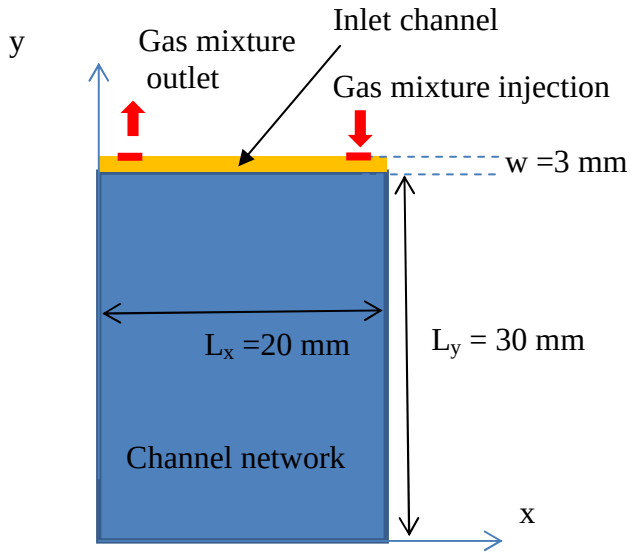

Fig.C1. Computational domain Ω.

Governing equations

The flow is first computed using Darcy's law. This is an approximation since the Reynolds number (based on the inlet channel thickness *e)* in the inlet channel is high (it can be as high as about 600). Thus inertial effects are certainly non negligible at least in the first rows of pores in the micromodel (as illustrated in Fig. 5a the velocity in the micromodel rapidly decreases with the distance from the inlet channel. Combining the continuity equation and Darcy's law leads to the consideration of the following equation,

$$\nabla.(K\nabla P) = 0. \qquad \text{(C1)}$$

where K is the local permeability (it differs between the inlet channel and the channel network) and P is the pressure. Eq. (C1) is solved subject to the following boundary conditions,

$$\nabla P.\mathbf{n} = 0 \quad \text{at } \partial\Omega - \partial\Omega_{in} - \partial\Omega_{out} \qquad \text{(C2)}$$

where $\mathbf{n}$ is unit vector normal to the boundary. $\partial\Omega$, $\partial\Omega_{in}$, $\partial\Omega_{out}$ denote the boundary of the computational domain, the section of the boundary where the gas mixture is injected and the section of the boundary where the gas mixture leaves the system respectively; $\partial\Omega_{in}$ and $\partial\Omega_{out}$

correspond to the two segments in red in Fig. C1 (the width of the segments is 3.14 mm so as to impose the same injection and exit areas as the holes of the experimental set-up. The segments are also positioned so as to respect the position of the holes as much as possible.

$$U_y = -\frac{K}{\mu}\frac{\partial P}{\partial y} = -\frac{Q}{ew} \text{ at } \partial\Omega_{in} \quad \text{(C3)}$$

where μ is the gas mixture viscosity and Q is the gas mixture injection flow rate.

$$P = P_{ref} \quad \text{at } \partial\Omega_{out} \quad \text{(C4)}$$

where P_{ref} is a reference pressure (P_{ref} = 101325 Pa).
The velocity field is then computed from Darcy's law,

$$\mathbf{U} = -\frac{K}{\mu}\nabla P \quad \text{(C5)}$$

Once the flow is computed, the steady state version of Eq. (1), namely

$$\nabla.(cX_v\mathbf{U}) = \nabla.\left(c\mathbf{D}^*.\nabla X_v\right) \quad \text{(C6)}$$

is solved with the following boundary conditions,

$$\nabla X_v.\mathbf{n} = 0.\ \partial\Omega - \partial\Omega_{in} - \partial\Omega_{out} - \partial\Omega_{bottom} \quad \text{(C7)}$$

where $\partial\Omega_{bottom}$ denotes the cold edge of channel network located at y = 0.

$$X_v = \frac{P_{vs}(T_c)}{P_{ref}} \text{ at } \partial\Omega_{bottom} \quad \text{(C8)}$$

where $P_{vs}(T_c)$ is the vapour saturation pressure at the temperature of the channel network cold edge.

$$X_v = RH_{ch}\frac{P_{vs}(T_h)}{P_{ref}} \text{ at } \partial\Omega_{in} \quad \text{(C9)}$$

where $P_{vs}(T_h)$ is the vapour saturation pressure at the temperature of the inlet channel and RH_{ch} is the relative humidity at the entrance of the inlet channel.

$$\frac{\partial X_v}{\partial y} = 0 \text{ at } \partial\Omega_{out} \quad \text{(C10)}$$

Parameters

The inlet channel permeability is computed a using the formula proposed in Idelchik (1986),

$$K = \frac{k(e,w)}{ew} = \frac{e^2 w^2}{8(e+w)^2 \alpha} \qquad \text{(C11)}$$

where $\alpha = -0.707267\chi^3 + 1.96214\chi^2 - 1.86763\chi + 1.50244$ and $\chi = \min(e/w, w/e)$. Application of Eq. (C11) yields $K_{inletchannel} = 6.56\ 10^{-8}$ m^2.

Similarly, the channel permeability was computed as

$$K = \frac{2k(e_c, w_c)}{ae_c} = \frac{e_c{}^2 w_c{}^3}{4a(e_c + w_c)^2 \alpha} \qquad \text{(C12)}$$

leading to $K_{network} = 1.43\ 10^{-8}$ m^2. The values selected for e_c, w_c, etc, are specified in Table C1. As can be seen, the permeability contrast is not high between the inlet channel and the channel network.

The dispersion tensor (in Eq.(C6)) is classically expressed as

$$\mathbf{D}^* = \begin{bmatrix} D_{eff} + \left(\alpha_T \|\mathbf{U}\| + (\alpha_L - \alpha_T)U_x^2 / \|\mathbf{U}\|\right) & (\alpha_L - \alpha_T)U_x U_y / \|\mathbf{U}\| \\ (\alpha_L - \alpha_T)U_x U_y / \|\mathbf{U}\| & D_{eff} + \alpha_T \|\mathbf{U}\| + (\alpha_L - \alpha_T)U_y^2 / \|\mathbf{U}\| \end{bmatrix} \qquad \text{(C13)}$$

While the dispersivities α_L and α_T can be reasonably estimated in the inlet channel using the classical Taylor dispersion expression in a slit, i.e. $\alpha_L = \alpha_T = \frac{ePe}{210}$, the situation is less obvious for the network. For instance, the array of obstacles in the channel network region is confined between two plates and thus different from the array studied in Amaral Souto and Moyne (1997). We have tested a Taylor dispersion formulation (as reported in Table C1) and a porous medium formulation (dispersivities for a granular material as reported in Fried and Combarnous (1971)). We found that the results were sensitive to the adopted formulation but not to an extent that this modify the main results discussed and presented in the present paper. Although this point would certainly deserve to be studied in more depth, e.g. Goldsztein (2007), we proceeded with the Taylor dispersion formulation summarized in Table C1 on the ground that the disorder was relatively weak in the network and its structure was relatively close to long channels.

References (Appendix)

H. P. Amaral Souto and C. Moyne, Dispersion in two-dimensional periodic porous media. Part II. Dispersion tensor. Phys. Fluids 9, 2253 (1997)

J.J. Fried and M.Combarnous, Dispersion in Porous Media. Advances in Hydroscience, Vol.7, pp.169-282, Academic Press (1971)

G.H. Goldsztein, Solute transport in porous media: Dispersion tensor of periodic networks, Appl. Phys. Lett. 91, 054102 (2007)

I.E. Idelchik, Handbook of Hydraulic Resistance, Hemispshere, New-York, USA (1986)

4.3 Article 2 bis: Pore network modeling of liquid water invasion by condensation in a model porous medium

Pore network modelling of liquid water invasion by condensation in a model porous medium

Benjamin Straubhaar[1], Lingguo Du[1], Paul Duru[1], Marc Prat[1,2]

[1] *INPT, UPS, IMFT (Institut de Mécanique des Fluides de Toulouse), Université de Toulouse, Allée Camille Soula, F-31400 Toulouse, France and*
[2] *CNRS, IMFT, F-31400 Toulouse, France*

Abstract
A pore network model is proposed to simulate the formation of liquid water by condensation in the presence of a temperature gradient. Simulations are compared with visualization experiments performed in quasi-two-dimensional model porous media for different wettability conditions, namely hydrophobic, hydrophilic and mixed wettability. The comparison leads to a quite good agreement showing that the proposed pore network model can be used with confidence for the simulation of condensation.

Key words: Pore network modeling, condensation, evaporation, temperature gradient

1. Introduction

Water vapour condensation driven by a temperature gradient in a porous medium is encountered in important applications such as building physics, e.g. Hens (2007), soil physics, petroleum engineering (steam injection), e.g. Baibakov et al. (1989), or cooling systems, e.g. Faghri (1995), to name only a few. It is now also widely admitted that condensation is a key factor in the formation of liquid water in the gas diffusion layers (GDL) of proton exchange membrane fuel cells (PEMFC), e.g. Straubhaar et al. (2015) and references therein. Surprisingly, however, it can be noted that the studies on condensation in porous media are relatively scarce, at least compared to the numerous studies on evaporation in porous media, a process which can be considered as the process reverse to condensation. One can mention the studies devoted to the condensation on a plate embedded in a porous medium, e.g. Kaviany (1986) or the ones where condensation results from the convective injection of vapour into a porous matrix, e.g. Yortsos (1982). Additional references can be also found in Kaviany's book (1991). All these studies, including the one of Larbi et al. (1995) on condensation in sand samples, were developed using the classical concepts of the continuum approach to porous media. They have actually little to do with the present study which focuses on the condensation process at the pore network scale. Performing studies are the pore network scale is now classical with the development of pore network models (PNM), e.g. Blunt (2001). However, in contrast with evaporation, e.g. Prat (2002), (2011), it seems that the PNM used in the present work which is a variant of the one proposed in Straubhaar et al. (2015) is among the very first ones allowing the study of condensation in a temperature gradient.
In addition to providing a better understanding the physics at the pore scale, a motivation for the development of a mesoscale approach such as a pore network model lies in the fact that some systems cannot be modelled properly using the classical Darcy's scale model. As discussed in Rebai and Prat (2009), this is the case for the aforementioned GDLs because of

the lack of length scale separation across the GDL thickness. Indeed, a GDL is a thin system with typically less than 10 pores over its thickness see Prat and Agaësse (2015) for a more general discussion of thin systems. This feature, i.e. the lack of length scale separation, is common to many thin porous media and can even be considered as a definition of a thin porous medium.
The main objective of the present study is to present a PNM allowing one to simulate the condensation process and to assess the performance of the PNM from comparisons with the experiments presented in Du et al. (2015). Beyond this validation objective, we are of course also interested in a better understanding of the condensation process in a porous medium from the simulations.
The study of Du et al. (2015) presents an analysis of the condensation process from visualization experiments performed using a quasi-two-dimensional model porous medium formed by a network of interconnected channels. The liquid invasion patterns as well as the condensation kinetics were compared between a hydrophobic system, a hydrophilic one and a system of mixed wettability containing a hydrophilic region and a hydrophobic one. It was shown that two condensation regimes could be distinguished depending on whether a two-phase zone or a liquid saturated zone develops in the porous domain. The experiments were also characterized by the occurrence of a preferential condensation zone within the network in the two-phase zone regime. This was explained from the consideration of the velocity field induced in the network. The challenge is to reproduce well all these observations with the PNM, which in addition provides information difficult to obtain experimentally.
The paper is organized as follows. The condensation pore network model is described in section 2. Comparisons between the PNM simulations and the experiments are presented in section 3. A conclusion is presented in section 4.

2 Pore network model

2.1 Pore network structure

Figure 1 shows a top view of micromodels used in Du et al. (2015). One can distinguish two main regions: the inlet channel and the network of interconnected channels. The network is a two-dimensional square network of interconnected channels of rectangular cross-section. The network step (distance between two neighbor channel intersections in the network) is uniform and set to 1 mm. The width of each channel is distributed randomly, following a Gaussian distribution with a mean and standard deviation values of 0.5 and 0.1 mm, respectively. The internal thickness e of the micromodel, i.e. the height of channels, is 1 mm.
The micromodel is fed by a gas mixture of nitrogen and water vapour circulating in the inlet channel. This is a 20 mm long channel 3 mm in width and 1 mm deep in direct contact with the micromodel (the inlet channel is clearly visible along the right side of the micromodel in Figure 1a). Two holes are drilled next to the network in the inlet channel top plate to allow the gas mixture injection (through the inlet hole) and the gas exit (through the outlet hole). The other boundaries are walls. Thus outlet hole is the only possible gas exit.
The pore network (PN) structure is similar as the micromodel structure. The pore space is represented by a two-dimensional square network of pores (a “pore” corresponds to a channel intersection) interconnected by narrower channels, also referred to as bonds or throats. The pores correspond to the nodes of the network and the channels between the pores represent the narrower passage between two adjacent pores. The bonds are ducts of rectangular cross section $e\ d_t$, where e is the channel depth (e = 1mm throughout the pore space) and d_t is the distance between the two pillars bordering the duct. The size d_t varies according to the same random distribution as in the micromodel. The pores are bodies of height e specified so that

the overall porosity ε in the pore network is about the same as in the micromodel (ε = 0.76). The in-plane size d_p of a pore body is defined as $d_p = \sqrt{\frac{4V_p}{\pi e}}$, where V_p is the volume of the pore body. The lattice spacing a – which is the distance between the centers of two adjacent pores – is equal to 1 mm as in the micromodel. As in the micromodel a row of pores in the transverse direction contains 21 pores and row of pores in the longitudinal direction contains 31 pores. Thus the PN simulations are performed over a 21×31 pore network. The inlet channel is also taken into account in the computational domains. Additional computational nodes are placed in the channel leading to a computational domain containing 21×34 nodes.

a)

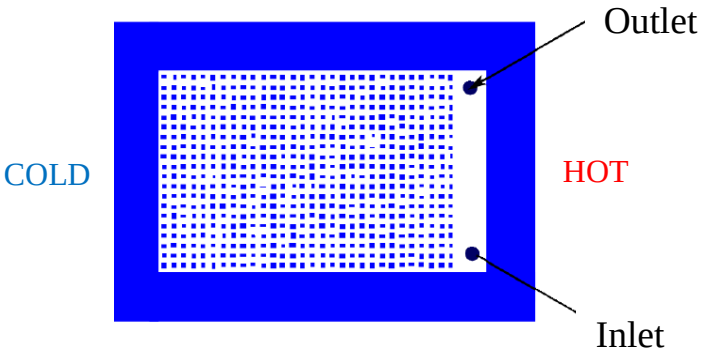

b)

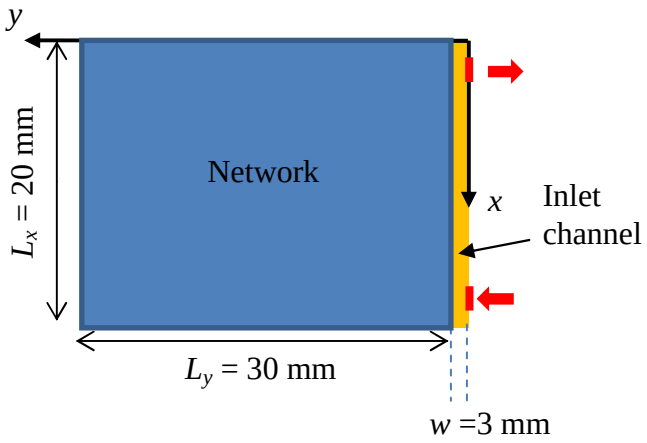

Figure 1 – a) Sketch of micromodel used in Du et al. (2015); the solid obstacles are in blue, the pore space in white, b) PNM computational domain.

As shown in Figure 1b, the gas mixture inlet and outlet respectively are positioned on the right edge of the computational domain. They are of width δ and start 1.5 mm from lateral edge. The network thickness is e = 1 mm. The inlet and outlet widths are specified so as to have the same cross section area as the inlet and outlet cross section area in the experiment (circular holes of 2 mm in diameter leading to δ = *3.14* mm).

In summary, the PNM network is specified so as to have same porosity, the same throat width statistical distribution the same permeability (see Appendix A), the same effective diffusion coefficient (see Appendix A) as the micromodel. However, we do not impose in the PNM the same local geometry as in the micromodel. This means that there is not a one to one exact correspondence between the channel width in the moicromodel and the simulation. The correspondence should be understood as statistical only.

The temperature varies in the y direction, i.e. in the direction perpendicular to the inlet channel as $T(y) = T_c + (T_h-T_c)(1-y/L_y)$ where T_c is the temperature on the cold edge of the

micromodel and T_h the temperature in the inlet channel (hot edge of micromodel). Temperatures T_c and T_h slightly vary from one experiment to the other, i.e. Du et al. (2015) but can be taken as $T_h \approx 47.5$ °C and $T_c \approx 27$ °C. The temperature field is an input data for the simulations.

2.2 Water vapour transport.

A key ingredient is the modelling of the vapour transport in the system. As discussed in Du et al. (2015), the vapour is transported by both convection and diffusion in the network. So the velocity field in the network must be computed.

The equations are discretized over the lattice grid. The discretization steps are denoted by *dx* and *dy* with *dx = dy. Thus dx=dy =a,* where *a* is the lattice spacing (distance between two intersections of the network)

Flow computation
Using the classical concept of pore network modelling the flow rate between two points of the grid is expressed as,

$$q_{ij} = g_{hij} \Delta P_{ij} \tag{1}$$

where $\Delta P_{ij} = P_i - P_j$ is the pressure difference between the two nodes; g_{hij} is the hydraulic conductance between the two nodes. The hydraulic conductance is expressed as a function of the permeability *K* in each region (inlet channel (in yellow in Fig. 1b and micromodel (in blue in Fig. 1b).

$$g_{hij} = \frac{K}{\mu} e \tag{2}$$

where μ is the gas mixture dynamic viscosity (μ = 1.8 10^{-5} Pl).
The various parameters are specified in Table 1.

The boundary conditions are zero flux on all boundaries except at the inlet and outlet of width δ (see Figure 1b). Zero flux is imposed through a throat containing liquid water.

The next step is to express the mass conservation at each gas node of the network

$$\sum_{j=1,4} q_{ij} = 0. \tag{3}$$

At the outlet the pressure is imposed,

$$P = P_{ref} \text{ at } y = 0,\ 1.5 \text{ mm} \le x \le 1.5 \text{ mm} + \delta \tag{4}$$

At the inlet the flow rate is imposed (assuming that *n* nodes form the inlet)

$$Q / n. = g_{hij} \Delta P_{ij} \qquad \text{at } y = 0,\ L_x\text{-}1.5\text{mm} - \delta \le x \le L_x\text{-}1.5 \text{ mm} \tag{5}$$

where *Q* is the volumetric flow rate entering into the system.

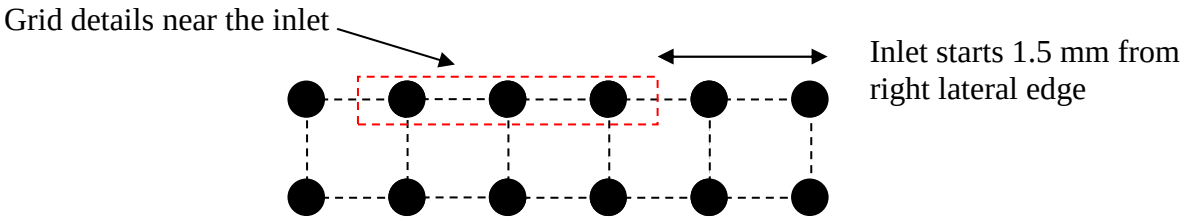

Figure 2. Details of computational grid in the inlet channel near the inlet. Inlet corresponds to the dashed red frame. Example for an inlet forms by three nodes.

There is no flow through bonds occupied by the liquid (Fig.3).

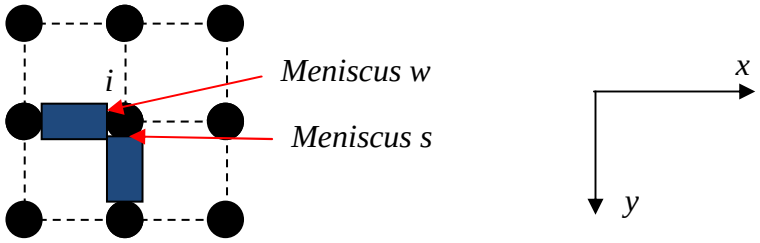

Figure 3. Example of a node adjacent to two liquid throats.

Once the pressure is computed, the filtration velocity in each "gas" throat is computed as

$$u_{ij} = \frac{q_{ij}}{edx} = \frac{g_{hij}}{edx}\Delta P_{ij} = \frac{K}{\mu dx}\Delta P_{ij} \tag{6}$$

Vapour molar fraction computation

The next step is to determine the molar fraction field $X_v(x,y)$ within the network. The corresponding Darcy' scale equation reads,

$$\varepsilon\frac{\partial cX_v}{\partial t} + \nabla.(cX_v\mathbf{U}) = \nabla.\left(c\mathbf{D}^*.\nabla X_v\right) \tag{7}$$

where $\mathbf{D}^*$ is the dispersion tensor, ε the local porosity, $\mathbf{U}$ is the velocity vector (Darcy velocity), $c = P_{ref}/RT_{ref}$ (see Table 1 for the numerical values of parameters)

A reasonable assumption is to consider the vapour transport as quasi-steady (the condensation process is slow compared to characteristic time of vapour transport)

$$\nabla.(cX_v\mathbf{U}) = \nabla.\left(c\mathbf{D}^*.\nabla X_v\right) \tag{8}$$

Consider a passage between two nodes of grid in the *x* direction (the formulation is similar in the *y* direction), the total flux of vapour between the two nodes is

$$\phi_v = \left(cX_v u_x - cD_v^* \frac{\partial X_v}{\partial x} \right) ed_y \tag{9}$$

where u_x is the average velocity between the two nodes (Eq.(6)):

$$u_x = \left(-\frac{K}{\mu} \frac{\partial P}{\partial x} \right) \tag{10}$$

D_v^* is given by (Taylor dispersion)

$$D_v^* = \frac{D}{\tau} + \frac{\tau (e u_x)^2}{48 D} \tag{11}$$

in the micromodel and

$$D_v^* = \frac{D}{\tau} + \frac{\tau (e u_x)^2}{210 D} \tag{12}$$

in the inlet channel, where D is the vapour molecular diffusion coefficient ($D = 2.7\ 10^{-5}\ m^2/s$) and τ is a "tortuosity" factor: $\tau = 1$ in inlet channel; $\tau = 1.42$ in pore network.

Table 1. List of parameters for the PNM simulations

	Inlet channel	Micromodel	Micromodel–inlet channel boundary
a (m)	10^{-3}	10^{-3}	10^{-3}
d_t	= *a*	= *(1-β)a* (mean value)	= *a*
dx=dy	*a*	*a*	*a*
D (m^2/s)	2.7 10^{-5}	2.7 10^{-5}	2.7 10^{-5}
e (m)	10^{-3}	10^{-3}	10^{-3}
K (m^2)	6.56 10^{-8} m^2	1.44 10^{-8} m^2	6.56 10^{-8} m^2
ℓ (m)	= *dx*	= *dx*	= *dx*
S_{ij} (m^2)	*dxe*	*dxe*	*dxe*
S_{tij} (m^2)	*edx*	*adx*	*adx*
μ	1.8 10^{-5} Pl	1.8 10^{-5} Pl	1.8 10^{-5} Pl
P_{ref}	101325 Pa	101325 Pa	101325 Pa
T_{ref}	311 K	311 K	311 K
R	8,314462 J·mol^{-1}·K^{-1}	8,314462 J·mol^{-1}·K^{-1}	8,314462 J·mol^{-1}·K^{-1}
β	-	0.48	-
τ	1	1.55	1

A finite-difference upstream scheme is used to solve the pore network version of the convection–dispersion problem,

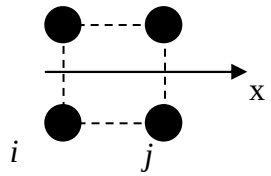

Figure 4. Details of computational nodes

Hence the discretized form of the flux between nodes *i* and *j* is expressed as

$$\phi_{vij} = \left(cX_i u_x - cD_v^* \frac{X_{vj} - X_{vi}}{dx} \right) edy \text{ for } u_x > 0 \tag{13}$$

$$\phi_{vij} = \left(cX_j u_x - cD_v^* \frac{X_{vj} - X_{vi}}{dx} \right) edy \text{ for } u_x < 0 \tag{14}$$

The next step is to express the mass conservation at each gas node of network assuming perfect mixing at each node

$$\sum_{j=1,4} \phi_{vij} = 0. \tag{15}$$

The boundary conditions are as follows. Zero flux conditions are imposed along the domain edges except on the colder edge (located at $y = L_y$) and at the domain inlet and outlet. Vapour is supposed to have condensed along the colder edge. Thus

$$X_v(x_i, L_y) = P_{vs}(T(x_i, L_y)) / P_{ref} \qquad \text{at } y = L_y \tag{16}$$

where P_{vs} is the vapour saturation pressure at the node temperature $T(x_i, L_y)$. This boundary condition as long as a pore adjacent to the considered point along the edge is not filled with liquid as a result of condensation.

The vapour molar fraction is known at the inlet

$$X_v(x_i, L_y) = RH_{ch} P_{vs}(T(x_i, y_i)) / P_{ref} \quad \text{at } y = 0,\ L_x\text{-}1.5\text{mm} - \delta \le x \le L_x\text{-}1.5 \text{ mm} \tag{17}$$

Grid details near the outlet

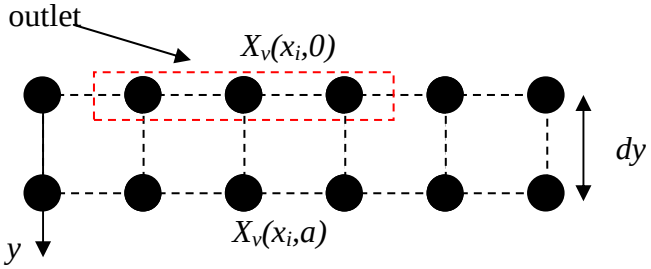

Figure 5. Details of computational grid in the inlet channel near the outlet. Outlet corresponds to the dashed red frame.

A free outlet boundary condition is imposed at the outlet (see Fig.5),

$$X_v(x_i,0) = X_v(x_i, dy) \quad \text{at } y = 0,\ 1.5\text{mm} \le x \le \delta + 1.5\ \text{mm} \tag{18}$$

The vapour molar fraction is the equilibrium vapour molar fraction at each gas node (pore) adjacent to a meniscus (an example is given in Fig.4)

$$X_v(x_i, y_i) = P_{vs}(T(x_i, y_i)) / P_{ref} \tag{19}$$

where P_{vs} is the vapour saturation pressure at the node temperature $T(x_i, y_i)$.

The numerical solution to Eq.(15) gives the vapour mass fraction at each grid node. The condensation flux on a meniscus is then determined from the field $X_v(x,y)$.

As an example, consider the situation shown in Fig.3. The total condensation /evaporation rate in pore *i* is (with subscript *n* for the node on the north end *e* for the node on the east)

$$\phi_{toti} = \phi_{in} + \phi_{ie} \tag{20}$$

with

$$\phi_{in} = \left(cX_{vn}u_y - cD_v^* \frac{X_{vi} - X_{vn}}{dy} \right) edx \ \text{ for } u_y > 0 \tag{21}$$

$$\phi_{in} = \left(cX_{vi}u_y - cD_v^* \frac{X_{vi} - X_{vn}}{dy} \right) edx \ \text{ for } u_y < 0 \tag{22}$$

$$\phi_{ie} = \left(cX_{ve}u_x - cD_v^* \frac{X_{vi} - X_{ve}}{dx} \right) edy \ \text{ for } u_x > 0 \tag{23}$$

$$\phi_{ie} = \left(cX_{vi}u_x - cD_v^* \frac{X_{vi} - X_{ve}}{dx} \right) edy \ \text{ for } u_x < 0 \tag{24}$$

The permeability K and the tortuosity coefficient τ in the network and in the inlet channel are determined as explained in the Appendix.

2.3 Simplified numerical solution

Actually, numerical tests have shown that the computation could be simplified considering only the network (region in blue in Fig.1b). In this case we simply impose along the edge corresponding to the network-inlet channel interface the pressure distribution given by

$$P(x) = \mathrm{P}_{ref} - \frac{\mu Q}{ewK_{channel}} \left(1 - \frac{x}{L_x} \right) \tag{25}$$

and the vapour molar fraction corresponding to RH_{ch}.
This solution was used to obtain the results shown in what follows.

2.4 Nucleation

Two main steps must be distinguished to simulate the vapour condensation process in the network: the nucleation step and the growth step. The nucleation step consists in selecting pores where the condensation is likely to start. A procedure to this end was proposed in

Straubhaar et al. (2015). The procedure begins by determining the vapour partial pressure field in the network assuming no condensation. To this end, we solve the transport problem governing the vapour transport within the network, i.e. the PN form of Eq.(7), i.e. Eq.(14). The numerical solution of Eq.(14) with the associated boundary conditions gives X_v at each node of network, and therefore the vapour partial pressure at each node of network: $P_v(x_i, y_j) = X_v(x_i, y_j)P_{ref}$. We then compute the local relative humidity at each node of network as $RH(x_i, y_j) = P_v(x_i, y_j) / P_{vsat}(T(x_i, y_j))$.

No condensation occurs when $RH(x_i, y_j) < 1$ in each node of network. This could happen for example when RH_{ch} is too low in the inlet channel. Condensation is assumed to occur when $RH(x_i, y_j) \geq \eta$ at least at one node in the network. It often happens that the condensation criterion is met not in a single node but at several nodes in the network. We proceed step by step considering first only one first condensation node, the one corresponding to $\max(RH(x_i, y_j), RH(x_i, y_j) \geq 1)$. At this node, we impose $RH(x_i, y_j) = 1$, or more exactly the mole fraction X_v corresponding to $RH(x_i, y_j) = 1$. We solve again the problem expressed by Eq. (14) taking into account the new boundary condition $RH(x_i, y_j) = 1$ at the first condensation node. This gives a new field $RH(x_i, y_j) = 1$ and we check whether new nodes are such that $RH(x_i, y_j) \geq \eta$. If yes we repeat this procedure until all the condensation nodes have been identified.

Nucleation parameter η

Physically, condensation is not expected to occur with a significant supersaturation, meaning that we should take η = 1. However, this leads to detect too many condensation sites compared to the experiments notable because the numerical computation of the vapour molar fractions is performed over a relatively coarse grid. As a result, a site can have a local relative humidity slightly greater than one only because of this. For this reason, we took η > 1. After some tests, we found that η = 1.05 led to satisfactory results.

2.5 Liquid cluster growth (hydrophobic network)

The next step is the liquid phase growth step resulting from the condensation process. This step can be summarized as follows.

Each node (pore) specified as liquid in the nucleation step is assumed fully saturated by liquid. If two of such liquid nodes are first neighbours, they belong to the same cluster. Thus, a first step consists in identifying all the liquid clusters formed at the end of nucleation step, where a cluster is defined as a group of connected liquid pores. Starting from this initial distribution of liquid clusters, the growth step is performed using the following algorithm:

1. Determine and label the different water clusters. If two pores – totally or partially saturated in liquid water – are adjacent, they belong to the same cluster.
2. Compute the vapour molar fraction field X_v by solving the PNM discretised form of Eq.(8). In each liquid pore (of coordinates x_i,y_i,) in contact with a gas node, the local saturation pressure is imposed. Hence $X_v = P_{vs} / P_{ref}$, where $P_{vs} = P_{vs}(T(x_i, y_i))$ and P_{ref} is the total pressure of the gas mixture.
3. If the vapour partial pressure computed in step 2 is greater than the local vapour saturation pressure in some gaseous pores, then identify the pore among those pores

corresponding to $\max(RH(x_i, y_j), RH(x_i, y_j) \geq \eta)$ and impose $X_v = P_{vs}(T(x_i, y_i))/P$ in the corresponding pore.

4. Go back to #2 and repeat steps #2 and #3 until there is no gaseous pore anymore such that $RH(x_i, y_j) \geq \eta$.

5. Compute the molar condensation rate Fk at the boundary of each liquid cluster.

6. Apply the invasion percolation rule at each cluster, i.e. determine the bond of larger diameter along the boundary of each liquid cluster.

7. Compute the invasion time t_k of each cluster *k*, i.e. the time required to fully invade the pore adjacent to the bond determined in #6: $t_k = c_\ell V_{adk} / F_k$, where V_{adk} is the volume remaining to invade in the considered pore, c_ℓ is the mole concentration of liquid water.

8. Compute the time step $dt = min(t_k)$

9. Fully invade the pore corresponding to *dt* and update the volume of liquid in the invaded pore in the other clusters.

10. Go back to #1 and repeat the different steps 1-9 until a steady-state solution is reached, i.e. the overall phase-change rate becomes nil.

2.6 Liquid cluster growth (hydrophilic network)

The algorithm is similar to the one for the hydrophobic network. The only but important difference lies in the local invasion rule that is applied in step #6 of the PN algorithm. This is discussed in several previous papers, e.g. Kuttanikkad et al. (2011), Ceballos and Prat (2013) and references therein. An invasion potential is assigned to each element (pore or bond) in the network. The invasion potential of a bond is defined as $\phi = -2a\cos\theta / d_t$, where θ is the contact angle ($\theta < 90°$ in a hydrophilic element and $\theta > 90°$ in a hydrophobic element). Similarly, the invasion potential of a hydrophobic pore can be defined as $\phi = -2a\cos\theta / d_p$. The invasion potential of a hydrophilic pore depends on the number of adjacent bonds already invaded by liquid water. A simple expression adapted from Mani and Mohanty (1999) reads

$$\phi = -2a\cos\theta[1 + 0.25(m-1)]/d_p \tag{26}$$

where *m* is the number of adjacent bonds already occupied by liquid water. Thus we simply modify step #6 as

6. Apply the local invasion rule at each cluster, i.e. determine the element (bond or pore) of smallest potential along the boundary of each liquid cluster.

3. Results

3.1 Reference experiments

The PNM simulations are compared with experiments presented in Du et al. (2015). The main characteristics of the considered experiments are summarized in Table 2. The meaning of "nucleation mode" CE or CE+I is explained in § 3.2. The number of the experiment refers to the number used in Du et al. (2015).

Table 2. Main characteristics of the experiments considered for comparison with the PNM simulations

Experiment #	Nucleation mode Experiment (Colder edge =CE , colder edge + inside = CE+I)	Nucleation mode PNM	Contact angle (°) θ	T_c (°C) colder edge temperature	T_h (°C) hot side (inlet channel) temperature	RH_{ch} (%) Relative humidity in inlet channel	Q (l/mn) Gas mixture injection flow rate
1 (20140117)	CE	CE	105	27.3	46.7	41.2	2.2
5 (20140110)	CE+I	CE+I	105	26.7	47.4	75.1	2.55
6 (20140303)	CE	CE	70	26.7	46.7	48.3	2.4
7 (20140313)	CE+I	CE+I	70	26.7	47.9	64.7	1.8
8 (20140326)	CE+I	CE+I	Mixed wettability	27.8	46.1	75	1.6

3.2 The two regimes

Two regimes were distinguished in Du et al. (2015). For sufficiently low relative humidity in the inlet channel, the incipient formation of liquid water takes place only along the colder edge of micromodel (left edge in Fig.1). This regime was referred to as 'regime CE', where CE stands for colder edge. For sufficiently large RH_{ch}, condensation starts not only from the colder side but also inside the micromodel. This regime was referred to as 'regime CE+I' (Colder edge + Inside). It was shown that the CE regime was observed for RH_{ch} lower than 50% whereas the CE+I regime was observed for greater relative humidity in the inlet channel. As can be seen from Fig.5, these two regimes are well predicted by the PNM simulations

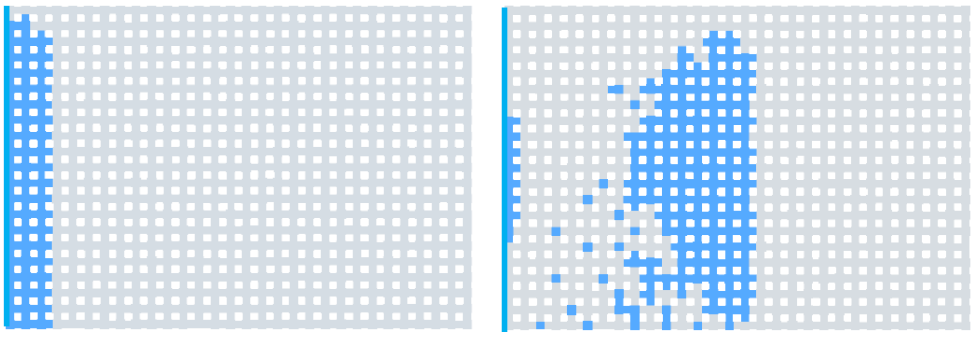

a) b)

Figure 5. Example of PN simulations of phase distributions within the PN. a) Exp#6 (CE regime), b) Exp # 7 (CE+I regime). Liquid in blue, gas phase in light grey.

As can be seen from Fig.5, the distributions of liquid water is not symmetric in the CE+I regime with more occupied sites in the lower region of the pore network. This was also

observed in the experiments and is explained by the loss of symmetry (between the upper half and lower half regions of the network) due to the velocity field induced in the pore network. When the gas injection inlet is as shown in Fig.1, i.e. on the bottom, the flow is on average directed from the lower edge to the upper edge. This induces greater water vapour molar fractions in the lower half region, i.e. in the half region the closest to the gas injection inlet. See Du et al. (2015) for more details.

3.3 Patterns

3.3.1 CE Regime

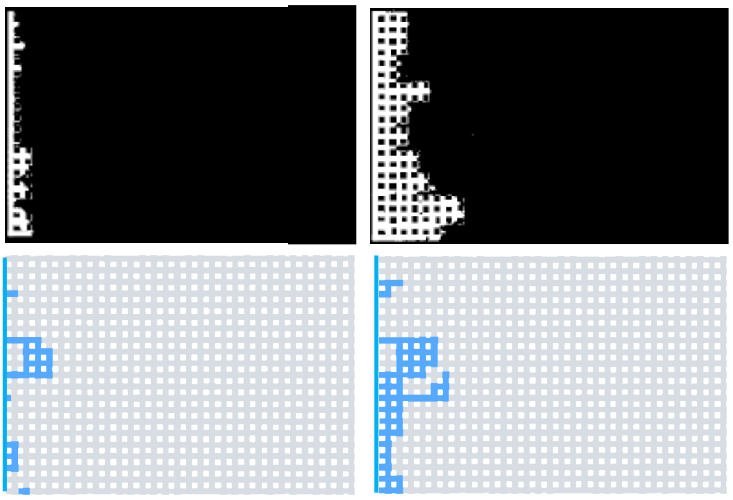

a)

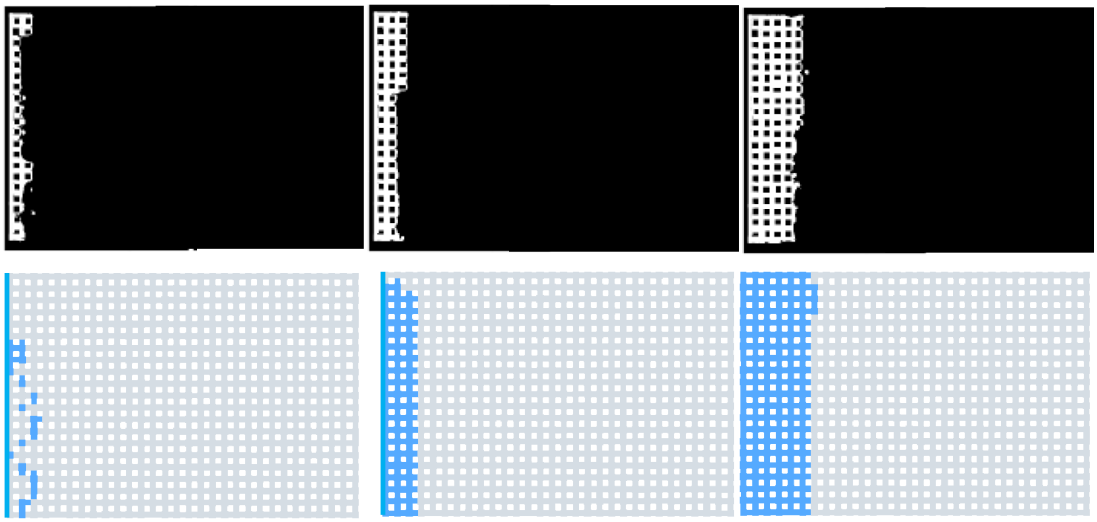

b)

Figure 6. CE Regime. Liquid water distributions in the micromodel (water in white, solid phase and gas phase in black) compared with patterns obtained in PNM simulations (liquid in blue, solid in white, gas phase in grey) for similar saturations: a) hydrophobic case (Exp#1), b) hydrophilic case (Exp#6).

The simulated condensation liquid invasion patterns obtained when liquid formation occurs from the micromodel bottom (regime “CE”) are compared with the experimental patterns in

Fig. 6. The pattern is compact in the hydrophilic micromodel as a result of the predominance of the phenomenon of coalescence between adjacent growing menisci in pores, see Lenormand et al. (1984), Cieplak and Robbins (1990) for more details on the local invasion mechanisms, whereas the pattern is more much ramified when condensation occurs in the hydrophobic systems. This is due to the predominance of the so-called burst events as local invasion mechanisms, see again Cieplak and Robbins (1990) for more details. As can be seen the PNM simulations lead to patterns in agreement with the experimental patterns for both type of micromodel, i.e. hydrophilic or hydrophobic.

3.3.2 CE+I Regime

Figure 7 shows the condensation patterns obtained when liquid forms both along the colder edge and within the hydrophobic micromodel (regime CE+I). One can distinguish two main regions of liquid cluster growth, at least in a first phase of the invasion: the colder edge region and an inside region close to the dew point line (located at distance δ from the hotter edge as discussed in section 3.4). There is clear dissymmetry as regards the inside region with liquid region developing in the lower half region of micromodel and not in the upper half region. It is important to note that the lower region is on the side of the gas mixture inlet (see Fig.1). As discussed in section 3.2, the assymmetry is due to the flow induced in the micromodel. Of course the flow structure changes with the growth of liquid clusters but the flow is still present in the network, at least in the dry region adjacent to the inlet channel, thus maintaining the dissymmetry also during the growth of the liquid clusters.

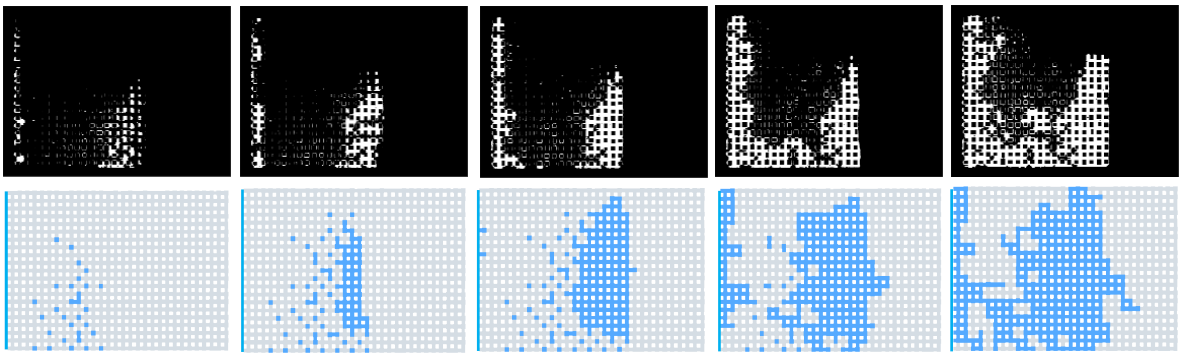

Figure 7 – Liquid water distributions in the hydrophobic micromodel in regime CE+I for Exp #5 (water in white, solid phase and gas phase in black) compared with patterns obtained in PNM simulations (liquid in blue, solid in white, gas phase in grey) for similar saturations.

As can be seen from Fig.7, all these features are well reproduced by the PNM simulation. One can however note that the growth of liquid cluster along the colder edge occurs earlier in the experiment than in the simulation. Note also that the two main aforementioned regions eventually merge and form a single liquid cluster (with trapping of a few gas pores) in both the experiment and the simulation.

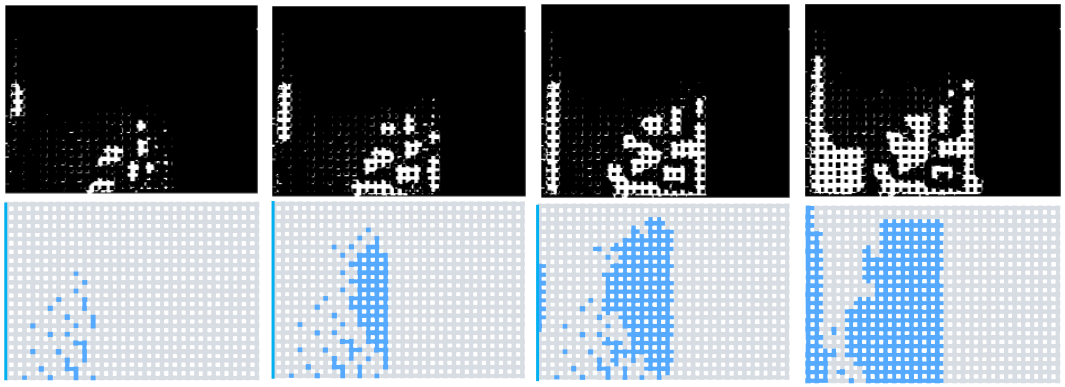

Figure 8 – Liquid water distributions in the hydrophilic micromodel in regime CE+I for Exp. #7 (water in white, solid phase and gas phase in black) compared with patterns obtained in PNM simulations (liquid in blue, solid in white, gas phase in grey) for similar saturations.

Figure 8 shows the comparison between Exp.#7 (hydrophilic micromodel, regime CE+I) and the PNM simulations. As expected the liquid clusters are more compact and faceted compared the experiment with the hydrophobic micromodel shown in Fig. 7. Here also the growth of liquid cluster along the colder edge occurs earlier in the experiment compared to the PNM simulations. Also several clusters are clearly visible in the inside of the micromodel in Fig. 8 whereas the PNM simulation rather leads to a single bigger cluster. Contrary to the hydrophobic case (see Fig.7), the cluster growing from the colder edge and the ones growing in the inside do not eventually merge. This is well reproduced by the PNM simulation.

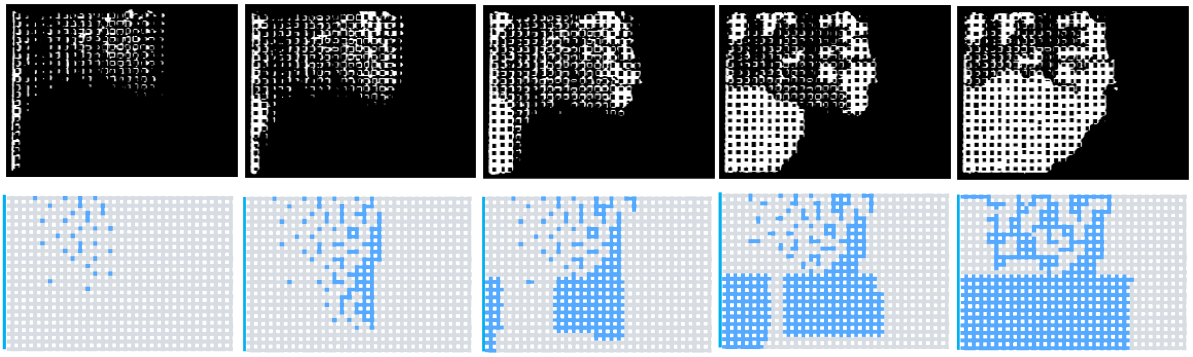

Figure 9 – Liquid water distributions in the micromodel of mixed wettability in regime CE+I (Exp. # 8, water in white, solid phase and gas phase in black) compared with patterns obtained in PNM simulations (liquid in blue, solid in white, gas phase in grey) for similar saturations. Note that the inlet and outlet of the inlet channel were inversed compared to the experiments shown in previous figures. Thus, the inlet was on the inlet channel top and the outlet was on the bottom (the opposite of what is shown in Fig. 1). The hydrophobic strip forms the upper half region of micromodel and the hydrophilic one the lower half region.

Finally, Fig.9 shows the pattern obtained in a micromodel of mixed wettability for conditions leading to regime CE+I. The top half region of the micromodel is hydrophobic whereas the bottom half region is hydrophilic. A first interesting point is that the gas mixture inlet and gas mixture outlet were inversed compared to the other experiments. Thus, their respective positions are the opposite of what is shown in Fig.1. Consistently with the analysis of pattern

dissymmetry discussed previously, the region of preferential condensation is here the upper half region, i.e. the region on the side of the gas mixture inlet. This confirms the major role of convective effects in the occurrence of the pattern dissymmetry. This is well reproduced by the PNM simulation.
A striking difference compared to Figure 8 lies in the marked invasion of the hydrophilic region, i.e here the micromodel half region close to the gas outlet (lower region in Fig. 9). The corresponding region (upper region in Fig. 8 because of the outlet-inlet inversion) is little invaded comparatively. The fact that the lower half region is invaded could be expected since water should preferentially invade hydrophilic regions. This is again well reproduced by the PNM simulation.
The invasion is compact in the bottom half region in Fig.9 which was expected since this region is hydrophilic. Also, the images in Fig. 9 suggest that the growth of liquid clusters in the hydrophobic region becomes quite weak after a first phase while the cluster in the hydrophilic region continues to grow significantly. All these features are well reproduced by the PNM simulation.

3.4 Condensation kinetics

The agreement between the experimental patterns and the computed ones is considered as good to very good since the PNM used in this paper is seemingly the first one proposed in the literature aiming at simulating the condensation process. However, the comparison between the experimental condensation kinetics (variation of overall saturation as a function of time) and the simulated ones is poor with the PNM kinetics substantially faster than the experimental ones. This is explained by a wrong estimate of vapour flux at the periphery of nucleation pores during the nucleation sequences. Work is in progress to improve this point and hopefully satisfactory kinetics results will be presented for the defense.

4. Conclusions

PNM simulations of vapour condensation were compared to experimental data obtained from visualization experiments in micromodels for three wettability conditions: hydrophobic, hydrophilic, mixed wettability micromodels.
The comparison led to quite good results in terms of condensation patterns. Many features of the experimental patterns were quite well reproduced provided that the PNM nucleation parameter is set a bit greater than one (1.05), which corresponds to considering a slight vapour supersaturation effect.
The main conclusion is that the condensation PNM can be considered as validated for predicting liquid distribution in porous media resulting from condensation.
However, the PNM simulations led to condensation kinetics faster than in the experiments. The PNM code must therefore be improved to obtain a better agreement with the experiments in this respect. Work in this direction is in progress.

Acknowledgements:
The authors gratefully acknowledge the funding from the EU project IMPALA (“ IMprove Pemfc with Advanced water management and gas diffusion Layers for Automotive application”, project number: 303446) within the Fuel Cells and Hydrogen Joint Undertaking (FCHJU).

References

N.K. Baibakov,A.R. Garushev,W.J. Cieslewic Thermal Methods of Petroleum Production, Elsevier , New-York (1989)

M.J Blunt, Flow in porous media — pore-network models and multiphase flow, *Current Opinion in Colloid & Interface Science,* Volume 6, Issue 3, Pages 197–207 (2001)

L.Du, P.Duru, B. Straubhaar, S. Geoffroy, M.Prat,Water invasion by condensation in a model porous medium, to be submitted (2015)

L. Ceballos, M. Prat, Slow invasion of a fluid from multiple inlet sources in a thin porous layer: influence of trapping and wettability, *Phys. Rev. E* **87**, 043005 (2013)

M.Cieplak, M.O. Robbins, Influence of contact angle on quasistatic invasion of porous media, *Phys. Rev. B* 41, 508–521, 1990

A. Faghri, Heat pipe science and technology, Taylor and Francis (1995).

H.Hens, Building Physics - Heat, Air and Moisture. Ernst & Sohn, Wiley (2007)

M.Kaviany, Boundary-layer treatment of film condensation in the presence of a solid matrix, *Int. J. Heat and Mass Transfer* 29, 951-054 (1986).

M.Kaviany, Principles of heat transfer in porous media, Springer-Verlag (1991).

S. P. Kuttanikkad, M. Prat, J. Pauchet, Pore-network simulations of two-phase flow in a thin porous layer of mixed wettability: Application to water transport in gas diffusion layers of proton exchange membrane fuel cells, *J. of Power Sources* 196, pp. 1145–1155 (2011)

S.Larbi, G.Bacon, S.A.Bories, Diffusion d'air humide avec condensation de vapeur d'eau en milieu poreux *Int.,J Heat Mass Transfer*. Vol. 38, No. 13, pp. 2411-2426, 1995

Lenormand, R., Zarcone, C.: Role of roughness and edges during imbibition in square capillaries. SPE 13264, presented at the 59th Annual Technical Conference and Exhibition of the Society of Petroleum Engineers, Houston, Tex. , September 16-19 (1984).

V. Mani and K.K Mohanty, Effect of pore-space spatial correlations on two-phase flow in porous media, *Journal of Petroleum Science and Engineering* 23, 173-188 (1999).

M.Prat, Recent advances in pore-scale models for drying of porous media, *Chem. Eng. J.*, Volume 86, Issues 1-2, Pages 153-164 (2002).

M.Prat, Pore network models of drying, contact angle and films flows, *Chem. Eng. Technol., 34*, No. 7, 1029–1038 (2011)

M.Prat, T. Agaësse, Thin porous media, Chapter 4, pp. 89-112 , in Handbook of Porous Media 3rd Edition, Edited by K.Vafai, Taylor (2015).

M.Rebai, M.Prat, Scale effect and two-phase flow in a thin hydrophobic porous layer. Application to water transport in gas diffusion layers of PEM fuel cells, *J. of Power Sources,* 192, pp.534-543 (2009)

B.Straubhaar, J. Pauchet, M. Prat, Water transport in gas diffusion layer of a polymer electrolyte fuel cell in the presence of a temperature gradient. Phase change effect. *International Journal of Hydrogen Energy,* 40 (35) 11668–11675 (2015)

Y.C. Yortsos, Effect of heat losses on the stability of thermal displacement fronts in porous media, *AIChE J.*, 28, 480-486 (1982)

APPENDIX A Effective diffusion coefficient and permeability of the network

Estimate of effective diffusion coefficient in the network

The network unit cell is approximately as sketched in Fig. A1

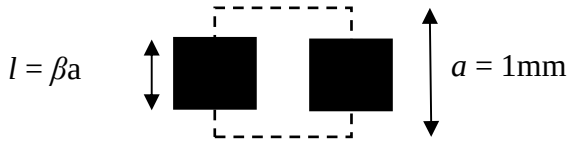

Fig. A1. Network unit cell (solid phase in black)

The porosity of the network is known ε = 0.7638. An average β can thus be deduced from $\varepsilon \approx \frac{a^2(1-\beta^2)}{a^2}$ leading to $\beta \approx \sqrt{1-\varepsilon} \approx 0.48$

The effective diffusion coefficient is then computed as the combination of three resistances in series leading to

$$\frac{D_{eff}}{D} = \frac{1-\beta}{(1-\beta)^2+\beta} = 0.7 \tag{A-1}$$

We want the PNM computation to give the effective diffusion coefficient when dispersion effects are negligible. This implies

$$J = cD_{eff}\, ae \frac{\Delta X_v}{a} = c\frac{D}{\tau} ae \frac{\Delta X_v}{a} \tag{A-2}$$

leading to

$$\tau = \frac{D}{D_{eff}} \approx 1.42 \tag{A-3}$$

Estimate of permeability

Inlet channel:

$$Q = \frac{k(e,w)}{\mu}\frac{\Delta P}{\ell} = \frac{K}{\mu} we \frac{\Delta P}{\ell} \tag{A-4}$$

where

$$k(e,w) = \frac{e^3 w^3}{8(e+w)^2 \alpha} \tag{A-5}$$

with $\alpha = -0.707267\chi^3 + 1.96214\chi^2 - 1.86763\chi + 1.50244$ and $\chi = \min(e/w, w/e)$

leading to $K_{canal} = \frac{k(e,w)}{ew} = 6.56\ 10^{-8}\ \mathrm{m}^2$.

Pore network:

The method is similar (combination of three hydraulic resistances in series). The permeability is determined from the unit cell depicted in Fig. A1.

$$Q = \frac{K}{\mu} ae \frac{\Delta P}{a} = \frac{K_1}{\mu} ae \frac{2\Delta P_1}{(1-\beta)a} = \frac{K_2}{\mu} ed_t \frac{\Delta P_2}{\beta a} = \frac{K_1}{\mu} ae \frac{2\Delta P_3}{(1-\beta)a} \tag{A-6}$$

with $\Delta P = \Delta P_1 + \Delta P_2 + \Delta P_3$
This leads to

$$K = \frac{1-\beta}{(1-\beta)^2 K_1^{-1} + \beta K_2^{-1}} \tag{A-7}$$

With $K_1 = \frac{e^2}{12}$ and $K_2(e,d_t) = \frac{e^2 {d_t}^2}{8(e+d_t)^2 \alpha}$ and $\alpha = -0.707267\chi^3 + 1.96214\chi^2 - 1.86763\chi + 1.50244$
and $\chi = \min(e/d_t, d_t/e)$

This yields K = $1.44\ 10^{-8}\ \mathrm{m}^2$.

4.4 Conclusion

The first article (the experimental study) shows that varying several parameters such as relative humidity at the inlet, temperature difference, wettability could lead to condensation zones. Also, the vapour transport of the vapour within the micromodel is not only diffusive but also results from convection and dispersion effects.

The second article compares the CPNM with the experimental study. Good agreement is found in terms of condensation patterns.

This chapter provides a validation for the CPNM and thereafter the CPNM is used in the particular case of water transport in gas diffusion layers of PEM fuel cells.

Chapter 5

Condensation scenario from 3D pore network simulations

Contents

5.1 Introduction

This chapter is formed by an article not yet submitted. The objective is to study in details the condensation scenario in a GDL unit cell (= one rib + 2 channels) from 3D pore network simulations. The effect of the relative humidity in the channel and current density is investigated.

A sensitivity analysis is performed to notably assess the influence of GDL thermal conductivity, thermal conductivity anisotropy factor, throat size distributions and GDL effective diffusion coefficient.

5.2 Article 3: Pore network modeling of condensation in gas diffusion layers of Proton Exchange Membrane Fuel cells.

PORE NETWORK MODELING OF CONDENSATION IN GAS DIFFUSION LAYERS OF PROTON EXCHANGE MEMBRANE FUEL CELLS.

Benjamin Straubhaar[1], Joel Pauchet[2], Marc Prat[1*]

[1] *INPT, UPS, IMFT (Institut de Mécanique des Fluides de Toulouse), Université de Toulouse, Allée Camille Soula, F-31400 Toulouse, France and CNRS, IMFT, F-31400 Toulouse, France*

[2] *CEA, LITEN, LCPEM, Laboratory of Fuel Cell Components, Electrolysers and Modeling, 17 rue des Martyrs, 38054 Grenoble, France*

Abstract

A pore network model (PNM) proposed in a previous work is exploited to simulate the liquid water formation by vapour condensation in the gas diffusion layer (GDL) considering the spatial temperature variations within the GDL. The computed distributions are markedly different from the ones computed in previous works assuming capillarity controlled invasion in liquid phase from the active layer and found to be in quite good agreement with several experimental observations. A sensitivity analysis is performed from a series of PNM simulations. It shows that the liquid distribution within the GDL is highly sensitive to parameters such as the through-plane thermal conductivity and diffusion coefficient or the isotropic or non-isotropic nature of the pore size distributions.

Key words: Pore network modeling, condensation, evaporation, temperature gradient, gas diffusion layer

1. Introduction

In spite of many studies, the exact mechanisms of water transfers in the various layers forming a proton exchange membrane fuel cell (PEMFC) are not fully understood. Although the physics involved is much simpler than in the active layer or the membrane, this also holds for the gas diffusion layers (GDL). In what follows, we concentrate on the GDL on the cathode side, which is a priori more critical than the anode side as regards the water management problem.

As discussed in Straubhaar et al. (2015), different mechanisms can be invoked as regards the transfer across the GDL of the water generated by the electrochemical reaction in the active layer: transfers in vapour phase, transfers in liquid phase with negligible liquid-vapour phase change phenomena, transfers with evaporation – condensation mechanisms. Although detailed in-situ visualizations of liquid phase distributions in a GDL are possible using mini PEMFC dedicated for X-ray tomography, e.g Eller et al. (2011), it is difficult to infer from the visualizations the exact mechanisms at play. Under these circumstances, it is useful to resort on modelling and numerical simulations.

As for other problems involving multiphase flows in porous media, many techniques have been used in relation with PEM fuel cells. The most classical one is based on the continuum approach to porous media and involved the generalized Darcy's law and the concepts of capillary pressure curves and relative permeabilities. Although widely used, notably in CFD

[*] Corresponding author : mprat@imft.fr

commercial codes, the relevance of this classical approach was questioned, e.g. Rebai and Prat (2009), because this type is modelling is not adapted to simulate the capillary forces dominated regime prevailing in GDL. There is also a lack of length scale separation since the thickness of a GDL is typically less than 10 pore sizes. Alternative approaches are therefore necessary. These notably include the direct simulations, such the LBM ones, e.g. Hao and Peng (2010), the Monte Carlo simulations Seidenberger et al. (2013) and the simulations based on pore network models (PNM). The objective here is not to discuss the advantages and drawbacks of each method. We simply note that the computational time of PNM over domain of comparable sizes, i.e. containing the same number of pores, are typically orders of magnitude smaller than for the two other methods. This greatly facilitates the parametric studies.

The present study is therefore based on a PNM approach. Because of their simplicity, PNMs have become a somewhat popular tool to study transfers in GDL, e.g. Sinha et Wang (2007), Gostick et al. (2007), Markicevic et al. (2007), Luo et al. (2010), Gostick (2013), Bazylak et al. (2008), Hinebaugh et al. (2010), Lee et al. (2009, 2010, 2014), Kuttanikkad et al. (2011), Ceballos and Prat (2010, 2013), Ceballos et al. (2011), Wu et al. (2012, 2013), Fazeli et al. (2015), Qin (2015). However, it can be noted that the majority of these studies do not consider phase change phenomena and assumed that all the water coming from the adjacent active layer enters the GDL in liquid phase and flows through the GDL in liquid phase. This assumption of liquid water invasion is also made in the work of Medici and Allen (2013), but with the consideration of an additional phenomenon, the possible evaporation of the liquid within the GDL, see also Straubhaar et al. (2015). In brief, to the best of our knowledge, no previous study based on PNM or related approaches has considered the vapour condensation process if one excepts the qualitative studies of Hinebaugh and Bazylak (2010) and Alink and Gerteisen (2013) limited to 2D simulations and without explicit consideration of the temperature variations across the GDL, a key aspect for the simulation of condensation, and our recent paper Straubhaar et al. (2015), where a condensation algorithm was presented and briefly illustrated through a few simulations in a 2D pore network only. This situation is somewhat surprising since condensation is considered as an essential process by several authors, e.g. Nam and Kaviany (2003), Basu et al. (2009), Caulk and Baker (2010,2011), Alink and Gerteisen (2013), Thomas et al. (2012, 2013, 2014).

The objective of the present article is therefore to present and to analyze PNM simulations of liquid water formation by condensation in a GDL. It should be pointed out that the consideration of condensation process is intimately related to the consideration of a non-uniform temperature field across the GDL. This is in contrast with most of PNM based previous studies of GDL, where the temperature was in fact more or less implicitly assumed as uniform and constant over the GDL. Actually, there are clear indications that the average temperature is greater at the GDL –active layer interface than at the GDL – bipolar plate interface and greater at the channel –GDL interface than right below the ribs of bipolar plate, e.g. Basu et al. (2009), Thomas et al. (2012, 2014). The existence of a colder region below the ribs clearly suggests a possibility of condensation.

Amon other things we will check whether the PNM simulations are consistent with the experimental behaviors presented in LaManna et al. (2014) and the in situ visualizations from Boillat et al. (2008) with the objective of elucidating the mechanisms leading to the occurrence of liquid water in GDL.

The paper is organized as follows. The computational domain and boundary conditions for the mass and heat transfer problems are described in section 2. The pore network is presented in section 3 together with some numerical simulation results. The condensation algorithm on the pore network is presented in section 4. The condensation diagram is presented in section 5.

Liquid distribution is discussed section 6 from a series of PNM simulations. A conclusion is presented in section 7.

2. GDL unit cell and boundary conditions

2.1 Polarization curve. GDL unit cell.

A PEMFC is sketched in Fig.1. We are interested in the GDL on the cathode side (see the caption of Fig.1 for additional details).

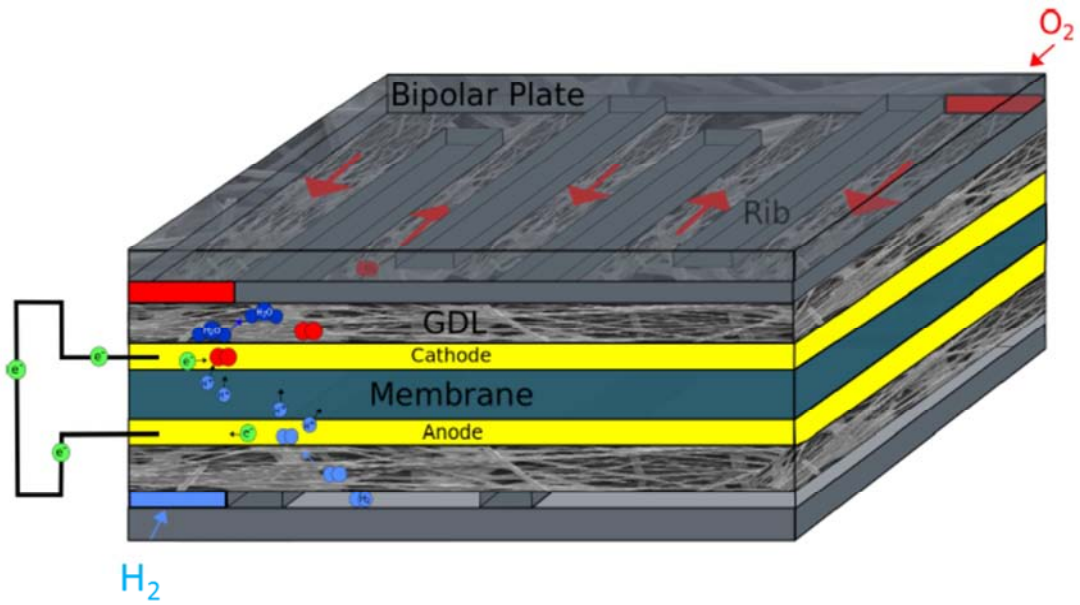

Figure 1. Sketch of a PEMFC. The GDL at the cathode side is a fibrous material sandwiched between the active layer and the bipolar plate (assumed to be in graphite in this paper). A serpentine channel is etched in the bipolar plate for supplying oxygen to the system. The gas flow in the channel (actually a mixture of water vapour and air) is indicated by arrows.

A PEMFC is globally characterized by its polarization curve. For the present study we adopted the polarization curve depicted in Fig. 2. It corresponds to the polarization curve presented in LaManna et al. (2014). The GDL specifications are from IMPALA European project (see acknowledgement section) unless otherwise mentioned.

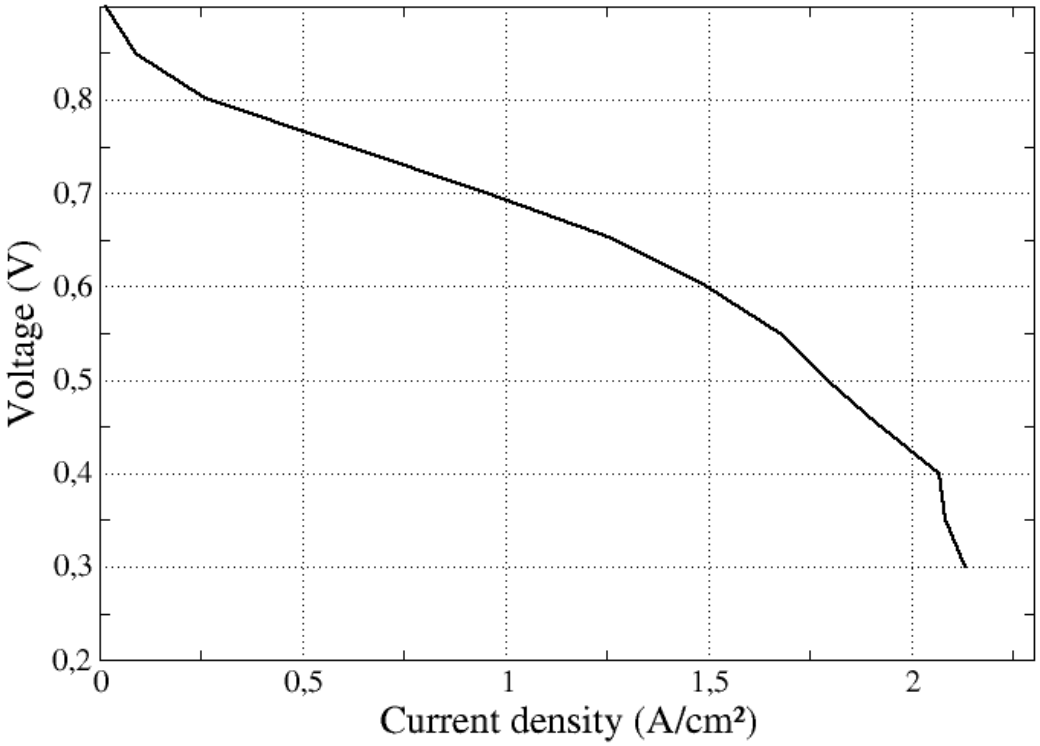

Figure 2. The polarization curve used throughout this paper (adapted from LaManna et al. (2014))

As in many previous studies, only a sub-region on the cathode side is considered. This sub-region is illustrated in Fig.3 and referred to as a GDL unit cell. As sketched in Fig.3, the lateral size L of the unit cell is equal to the cumulated widths L_r + L_c of one rib and one channel. We took representative values, namely L = 1 mm with L_r = 0.96 mm L_c = 0.96 mm. The lateral size L_y of the considered GDL sub-region in the y direction is L_y = 2.96 mm. The GDL is thin. We took for its thickness δ_c = 120 μm. This corresponds to the GDL in situ that is a compressed GDL (as indicated by the subscript "c". The uncompressed GDL thickness is δ_{unc} = 190 μm (using the subscript "unc" for properties of the uncompressed region). Different GDL properties will be specified in the region below the rib and in the regions below the channels so as to take into account the differential compression of the GDL. For example, the porosity of the uncompressed GDL (region below the channels) is ε_{uc} =74%. The porosity of the compressed GDL (region below the rib) is estimated from the relationship $\varepsilon_c = 1 - \frac{\delta_{uc}}{\delta_c}(1-\varepsilon_{uc})$. This gives ε_c = 59%.

The channel height is H_{ch} = 0.48 mm. As can be seen, the rib is at the center of the GDL outlet. The GDL unit cell inlet corresponds to the GDL-active layer interface (or the micro porous layer (MPL) – GDL interface when a MPL is present).

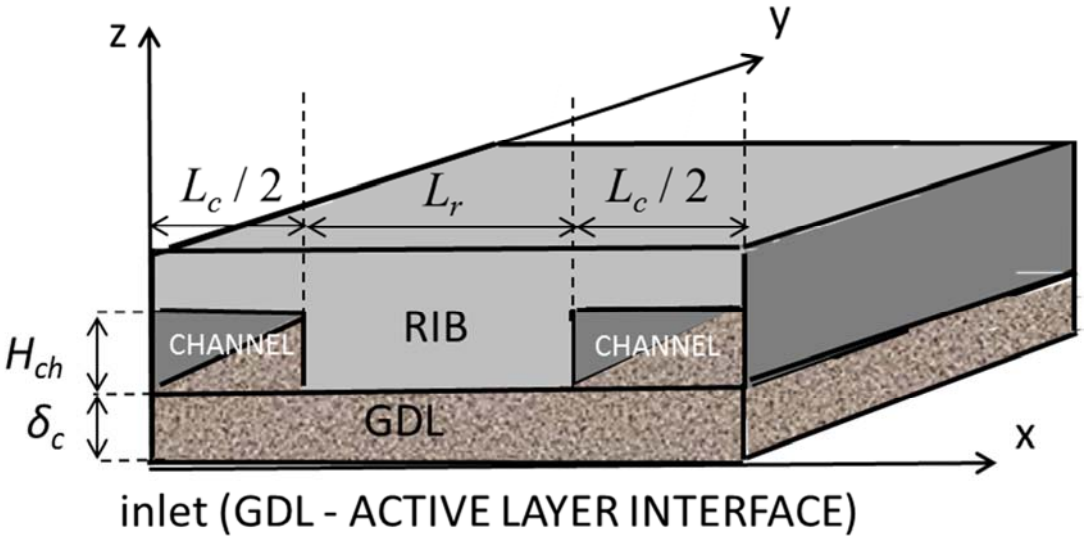

Figure 3. GDL unit cell with rib and two half channels.

2.2 Boundary conditions for the water transport

The relative humidity and gas total pressure at the outlet of unit cell ($z = \delta_c$) are input parameters. They are denoted by RH_{ch} and P_{ref} *respectively*. We took P_{ref} = 1.5 bar. RH_{ch} will be varied. At the GDL inlet ($z = 0$), a water injection flux (mol. $m^{-2}. s^{-1}$) is imposed. It is classically expressed as a function of local current density i as

$$Q = \beta \frac{i}{2F} \tag{1}$$

where F is the Faraday's constant ($F = 96485.34\ C$). Note that it is assumed that water is injected in vapour form and not in liquid form. This is a noticeable difference compared with previous works on GDLs using PNM. Actually not all the water produced at the cathode goes to the GDL. A fraction is transported in direction of the membrane. The coefficient β is the fraction directed toward the cathode GDL. Throughout this paper, we made the simplifying assumption that this fraction was independent of i and we took β =0.8.
The boundary conditions for the water transport are summarized in Figure 4 together with the heat transfer problem.

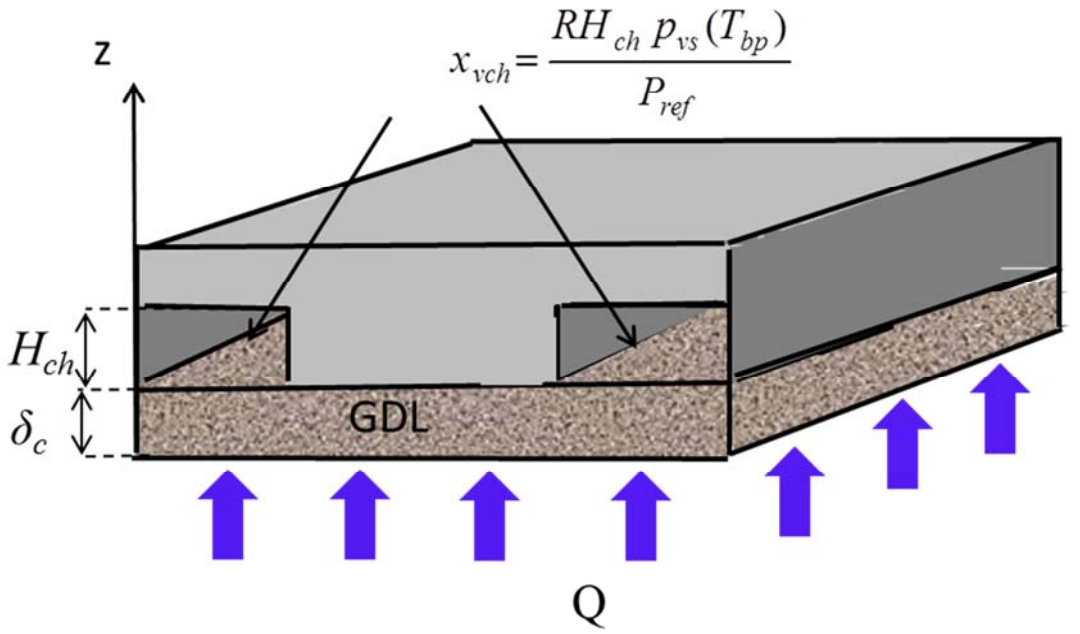

a)

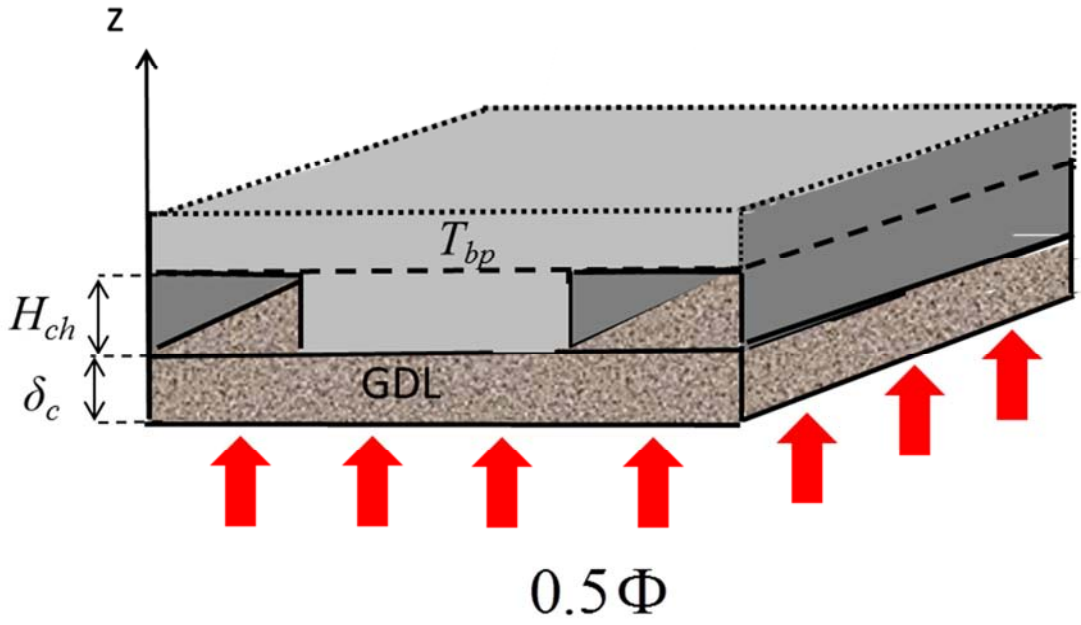

b)

Figure 4. Schematic drawing of the studied problem. a) water transfer problem: a fraction of the water produced in the active layer is directed toward the cathode GDL; given relative humidity and total gas pressure are imposed in the channels, b) heat transfer problem: a heat flux is applied at the GDL inlet whereas the temperature T_{bp} is imposed all over the surface in the x-y plane at the position $z = \delta_c + H_{ch}$.

2.3 Heat transfer

The temperature field *T(x,y,z)* within the GDL is a crucial ingredient for the computation of water invasion by condensation. This field is determined numerically by solving the steady state heat conduction problem,

$$\nabla.(\boldsymbol{\lambda}.\nabla T) = 0 \qquad (2)$$

in the domain depicted in Fig. 4b using a classical finite volume technique. Note that this problem is actually solved in two-dimensions over a cross-section of the domain shown in Fig.4b. Then the temperatures so computed are distributed over the pores of the pore network model (see § 3). This is for when the impact of liquid water on thermal conductivity is neglected. When this effect is taken into the temperature field must be computed in 3D and after each invasion of a pore by the liquid water.

No flux boundary conditions are imposed on the lateral sides of the domain whereas a uniform temperature $T = T_{bp}$ is imposed along the top boundary in Fig. 4b. Numerical simulations indicated that it was not necessary to take into account explicitly the part of the bipolar plate above the rib in Fig.4b. Owing to the high thermal conductivity of the bipolar plate, it is sufficient to impose the temperature T_{bp} directly at the x-y plane located at the position $z = \delta_c + H_{ch}$ in Fig. 4b.

The electrochemical reaction is exothermic. The corresponding heat production per unit surface area (W.m^{-2}) can be expressed as, e.g. Thomas et al. (2014),

$$\Phi = \left(\frac{h_{lv}}{2F} - U \right) i \qquad (3)$$

where h_{lv} is the enthalpy of reaction (h_{lv} = 242000 J.mol^{-1}), U the electrical tension. It can be reasonably assumed that half of the produced heat goes toward the anode and half toward the cathode GDL. Therefore, the boundary condition imposed at the GDL inlet for the heat transfer problem is

$$0.5\,\Phi = 0.5\left(\frac{h_{lv}}{2F} - U \right) i = -\lambda_{\perp}^{*} \frac{\partial T}{\partial z} \qquad \text{at } z = 0. \qquad (4)$$

where z is a Cartesian coordinate in the through-plane direction (z = 0 at the GDL inlet); $\lambda_{\perp}^{*}$ is the GDL effective thermal conductivity in the through-plane direction. The GDL is a highly anisotropic material owing to the preferential orientation of the fibers in the in-plane direction with a much higher thermal conductivity in the plane direction. Also, owing to the differential compression of the GDL between the rib and channel, the thermal conductivity is higher under the rib region than under the channel. As representative values of a dry GDL, e.g. Zamel and Li (2013), we took $\lambda_{\perp uc}^{*}$ = 0.25 Wm^{-1}K^{-1} (through-plane direction) and $\lambda_{/\!/\,uc}^{*}$ =4 Wm^{-1}K^{-1} (in-plane direction) in the regions of the GDL under the channel and $\lambda_{\perp c}^{*}$ = 0.25 Wm^{-1}K^{-1} (through-plane) and $\lambda_{/\!/\,c}^{*}$ =6.64 Wm^{-1}K^{-1} in the GDL under the rib. The thermal conductivity in the channel is λ_{ch} = 0.027 W. m^{-1}.K^{-1} (air) whereas the thermal conductivity of the bipolar plate is λ_{bp} = 150 W. m^{-1}.K^{-1}.

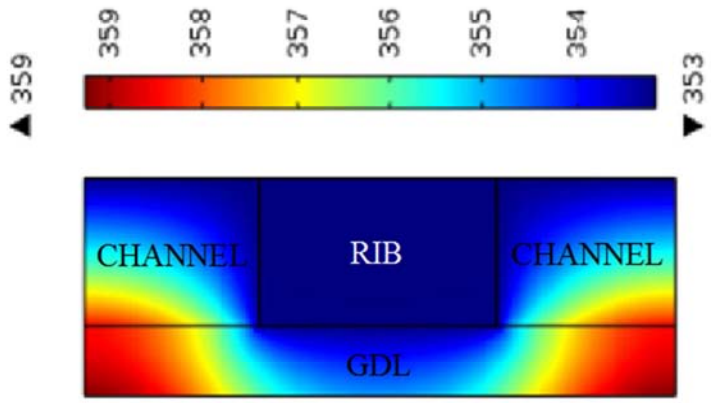

Figure 5. Example of Temperature field (K) computed for i = 1 A/cm² (which corresponds to 0.5Φ = 2900 W/m²) and an isotropic thermal conductivity for T_{bp} =80°C.

An example of temperature field so obtained is shown in Fig. 5. This field was actually obtained with the commercial code Comsol Multiphysics® used to validate our finite volume computation. As can be seen, the temperature field is characterized not only by through-plane variations but also by significant in – plane variations. Globally, the region in the GDL underneath the rib is colder than the region under the channel. The hottest region in the GDL is at the GDL – AL interface below the channel whereas the colder spot is in the middle of the rib along the GDL – rib interface. This is, however, for an isotropic thermal conductivity. When the anistropy of the thermal conductivity is taken into account the in-plane temperature variations are much less than depicted in Fig.5

The order of magnitude of temperature variations depicted in Fig.5 are consistent with the values reported in the literature, e.g. Basu et al. (2009), Thomas et al. (2014). Naturally, the lower the thermal conductivity of the GDL, the greater the temperature variations across the GDL, all other things being equal.

For a given current density i and the values of parameters specified in this section, the temperature field within the GDL is computed. This field is considered as input data for the pore network simulation of condensation described in section 4. Thus it should be clear that the temperature field is computed in a preprocessing step prior to the PNM simulation of condensation. Actually, it can be surmised that the temperature field changes during the invasion of GDL by liquid water. This point is further discussed in section 6.

3. Pore network structure.

Most of previous works on GDL using PNM were based on structured pore networks, typically cubic networks such as the one depicted in Fig.7. An exception is the work presented in Gostick (2013) where unstructured pore networks were generated using a tessellation technique. It is also possible to construct an unstructured network from X-ray tomography images of GDL as shown in Agaesse et al. (2015). The simple cubic network sketched in Fig. 7 was, however, used for the present work for simplicity. Nevertheless, it should be clear that the condensation algorithm described in section 4 can be implemented on unstructured networks as well. The GDL pore space is thus represented by a three-dimensional cubic network of pores interconnected with channels, also referred to as throats. The pores are cubic bodies corresponding to the nodes of the network whereas the throats are very short ducts of square cross-section representing the narrower passage between two adjacent pores. The

analysis of images of SGL 24BA reported in Lamibrac et al. (2015) indicates that the lattice spacing is different in the in-plane direction with approximately $a_{//} = 80\mu m$ from the lattice spacing in the through-plane direction with approximately $a_{\perp} = 40\mu m$. We considered a cubic network with a = 80 µm in both the in-plane and through plane directions but we took into account the fact that the real lattice spacing is actually twice as small in the through-plane direction by modifying the transport properties adequately (for example the through-plane thermal conductivity was multiplied by a factor 2 so as to have the through-plane network thermal conductance $\lambda_{\perp}/\delta$ identical to the GDL one). Based on the size of the domain occupied by the GDL in the experiment, this leads to represent the GDL by a 25×38×4 pore network (the figures indicate the number of pores along the directions of a Cartesian grid). Hence, the GDL unit cell has 4 pores in the through-plane direction.

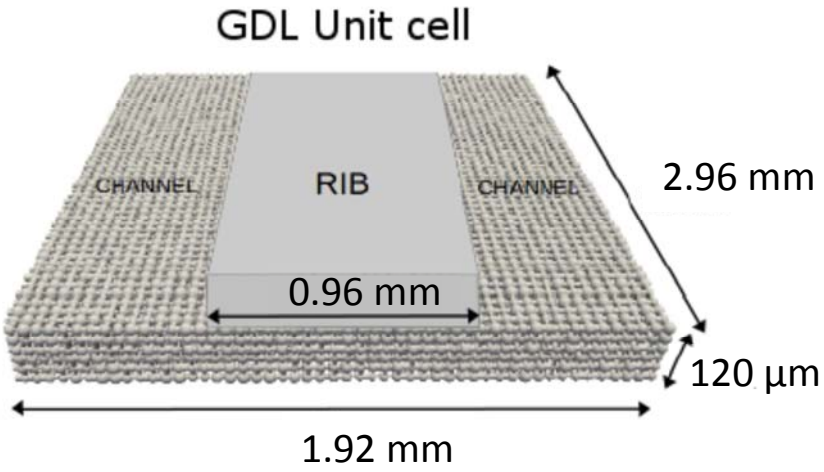

Figure 6. Sketch of cubic network used to represent the GDL. The lattice spacing $a_{//}$ (distance between two neighbor pore) is 80 µm in the plane directions. The GDL is represented by a 25 x 38 x 4 cubic network.

The throat size and pore sizes are specified as follows.
Because of the GDL anisotropic fibrous structure throats are narrower by about a factor 2 in the in-plane directions compared to the through-plane direction, Lamibrac et al. (2015). To reflect this anisotropy, the through-plane throat sizes were randomly distributed according to a uniform distribution of mean $\bar{d}_{t\perp c}$ = 43 µm , in the range $[d_{t\perp \min,c} - d_{t\perp \max,c}]$ with $d_{t\perp \min,c}$ = 32 µm and $d_{t\perp \max,c}$ = 54 µm whereas the in-plane throat sizes were randomly distributed according to a uniform distribution of mean $\bar{d}_{t//c}$ = 21.5 µm in the range $[d_{t// \min,c} - d_{t// \max,c}]$ with $d_{t// \min,c}$ = 16 µm and $d_{t// \max,c}$ = 27 µm .It was further assumed that these data corresponds to the compressed GDL (regions under the ribs). The GDL was supposed not compressed below the channel assuming that this could be taken into account by assuming that the throat size in the through-plane direction was not significantly modified whereas the throat sizes in the in-plane directions are larger on average in the uncompressed regions by a factor $\sqrt{\delta_{uc}/\delta_c}$ = 1.14.
The throats are considered as volumeless. Thus all the pore volume is in the nodes. The throat sizes are first distributed as indicated above depending on the location of the throat (compressed or uncompressed regions) and orientation of the throat (through-plane or in-plane).

The volume of a pore is first simply computed from adjacent throat sizes as $V_p = (\max(d_t))^3$ where $\max(d_t)$ is the size of the largest throat to which the pore is connected. Then the pore volume are corrected, i.e. multiplied by a correction factor, so as to obtain a desired porosity in the considered region (ε_{uc} = 74% in the uncompressed regions, ε_c = 66% in the compressed regions, not considering the porosity of the binder).
The correction is as follows.

The total pore volume $V_{pcomp} = \sum_{i=1}^{n_{pc}} V_{pi}$ in the compressed region (where there are n_{pc} pores). The real pore volume is $V_{pcomp,\exp} = \varepsilon_c V_{comp}$ where V_{comp} is the volume of the region defined as the compressed GDL (there are three such regions according to Fig.1c). V_{comp} = *rib surface area*$\times\delta_c$. This allows introducing a correction factor defined as $\eta = \frac{V_{pcomp,\exp}}{V_{pcomp}}$,which is applied to each pore of the considered compressed region, $V_{pinew} = \eta V_{pi}$.
In such the way, the porosity in the network is the same as in the experiment.
A similar procedure is applied to the uncompressed regions starting again from the same pore size distribution (where $\varepsilon = \varepsilon_{uc}$ =74%).

4. Pore network model of condensation (and evaporation)

Two main steps must be distinguished to simulate the vapour condensation process in the network: the nucleation step and the growth step.

4.1 Nucleation step

The objective of the nucleation step is to determine points in the network where the condensation is likely to start. The procedure begins by determining the vapour partial pressure field in the network assuming no condensation. To this end, we solve the diffusion problem governing the vapour transport within the network. Since the gas mixture on the cathode side is made of air, oxygen and water vapour, we should consider the gas as a ternary mixture. Furthermore, water vapour cannot be considered as dilute and thus we should rely on the complete model implying coupling between the transports of the three species, e.g. Quintard et al. (2006). Although going into this direction is certainly desirable, a simplified approach was adopted so as to simplify the numerical simulation. Although certainly less accurate we believe that the simpler approach adopted here does not affect the main conclusions of the paper. Hence, the transport of water vapour in the GDL is simply modeled using Fick's law. Expressed in terms of computation on a pore network, the vapour diffusion flux between two nodes (pores) *i* and *j* of network is therefore expressed as

$$N_A = g_{ij}(x_{v,j} - x_{v,i}) \tag{5}$$

where x_v is the mole fraction of water vapour and g_{ij} is the diffusive conductivity of the throat connecting the two pores. Traditionally, e.g. Gostick et al. (2007), g_{ij} is expressed as a function of the throat cross section area (i.e. $d_{t,ij}^2$ for a throat of square cross-section), which means that g_{ij} varies (randomly) from one throat to the other. Here we proceed differently following the concepts of the so-called mixed pore network presented in Mottet et al. (2015). The local conductance does not vary randomly anymore and is expressed as indicated in

Table 1. In Table 1, c is the mole concentration of the gas phase: $c \approx \frac{P_{ref}}{RT_{bp}}$ where R is the ideal gas constant. Note that the total pressure is supposed uniform and constant over the computational domain and equal to P_{ref}.

Coefficients $D^*_{\perp c}$, $D^*_{//c}$, $D^*_{\perp unc}$, $D^*_{//unc}$ in Table 1 are the GDL effective diffusion coefficients in the through-plane direction (subscript "$\perp$") and in the in-plane direction (subscript "// ") for the GDL compressed region (subscript "c") and the uncompressed region (subscript "unc"). Hence, an advantage of the mixed pore network formulation is to directly express the local conductance as a function of the medium effective transport properties. We took $D^*_{\perp c}/D = 0.25$, where D is the binary diffusion coefficient ($D \approx 3.\ 10^{-5}$ at 80°C). In spite of narrower passages in the in-plane directions, the effective diffusion coefficient in this direction is greater than the effective diffusion coefficient in the through-plane direction by at least about a factor 2, e.g. Zamel et al. (2013), Garcia-Salaberri et al. (2015) because of a greater tortuosity effect. Thus, $D^*_{//c}/D = 0.5$. Assuming no significant change in the tortuosity in the through-plane direction between the compressed region and the uncompressed one, we took $D^*_{\perp unc} = D^*_{\perp c}/D = 0.25$. It was assumed that the in –plane coefficient is slightly greater in the uncompressed region with $D^*_{//unc} = 0.7\ D$.
With the local conductivity defined as specified in Table 1, the pore network effective diffusion coefficients are of course $D^*_{\perp c}$, $D^*_{//c}$, $D^*_{\perp unc}$, $D^*_{//unc}$. The advantage of the mixed pore network approach is to use directly the values of the effective coefficients to specify the local conductivities.

Table 1 Expression of throat diffusive conductivity in the various regions of GDL; $a_{//} = 80\mu m$; $a_{\perp} = 40\mu m$

Region	direction	
Compressed	Through-plane	$g_{\perp c} = c\frac{a_{//}^2}{a_{\perp}} D^*_{\perp c}$
Compressed	In-plane	$g_{//c} = ca_{\perp} D^*_{//c}$
Uncompressed	Through-plane	$g_{\perp unc} = ca_{//}^2 \frac{D^*_{\perp uc}}{a_{\perp}} \frac{\delta_c}{\delta_{uc}}$
Uncompressed	In-plane	$g_{//unc} = ca_{\perp} \frac{\delta_{uc}}{\delta_c} D^*_{//uc}$

The species conservation equation at each network node is expressed as:

$$\sum_{j=1}^{n} g_{ij}(x_{v,j} - x_{v,i}) = 0. \tag{6}$$

where n is the number of neighbors to considered pore i; $n = 6$ for the cubic network depicted in Fig. 6.

Boundary conditions must be specified in order to solve numerically the system given by Eq.(6). As illustrated in Fig.4 and also in Fig.7, the relative humidity *RH* is imposed in the channel taking as reference saturation vapour partial pressure p_{vs} the pressure at T_{bp}, i.e. at the temperature of the coldest region in the channel. The vapour partial pressure imposes along the GDL - channel interface is therefore $p_v = RH_{ch}\, p_{vs}(T_{bp})$. Thus $x_{vch} = RH_{ch}\, p_{vs}(T_{bp}) / P_{ref}$ at this interface. A zero flux condition is imposed at the rib – GDL interface while spatially periodic boundary conditions are imposed on the lateral sides of the computational domain. At the GDL inlet (active layer or MPL – GDL interface), the vapour flux is imposed using Eq.(1).

The numerical solution of Eq.(7) with the associated boundary conditions gives x_v at each node of network, and therefore the vapour partial pressure at each node of network: $p_{vi,j,k} = x_{vi,j,k} P_{ref}$. We then compute the local relative humidity at each node of network as $RH_{i,j,k} = p_{vi,j,k} / p_{vs}(T(i,j,k))$.

No condensation occurs when $RH_{i,j,k} < 1$ in each node of network, which means that all the water coming from the active layer can be transported in vapour phase across the GDL. Condensation is assumed to occur when $RH_{i,j,k} > \eta$ at least at one node in the network. For most of the simulations presented later in the paper, we took $\eta = 1$. Thus no supersaturation was assumed. It is of course not a problem to consider a possible supersaturation effect taking $\eta > 1$. Whatever the chosen criterion, it often happens that the condensation criterion is met not in a single node but at several nodes in the network. Under these circumstances, several options are certainly possible. We decided to proceed step by step considering first only one first condensation node, the one corresponding to $\max(RH_{i,j,k}, RH_{i,j,k} > \eta)$. At this node, we impose $RH_{i,j,k} = 1$, or more exactly the mole fraction x_v corresponding to $RH_{i,j,k} = 1$. We solve again the problem expressed by Eq. (7) taking into account the new boundary condition $RH_{i,j,k} = 1$ at the first condensation node. This gives a new field $RH_{i,j,k}$ and we check whether new nodes are such that $RH_{i,j,k} > \eta$. If yes we can then repeat this procedure until all the condensation nodes have been identified.

This gives the initial distribution of liquid nodes for the growth step. This step is schematically illustrated in Fig.7

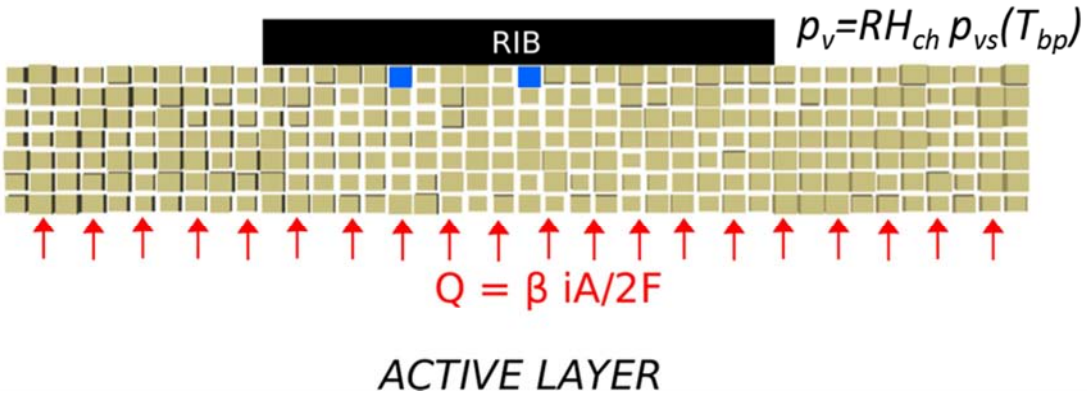

Figure 7. Sketch of nucleation step. Sketch of two nucleation pores (in blue) under the rib.

4.2 Liquid cluster growth algorithm for a hydrophobic network

For simplicity, each liquid node identified at the end of nucleation step is assumed fully saturated by liquid. Another option would be to first compute the condensation – evaporation rate and to determine the filling time of each initial liquid pores. Testing this option is left for a future work. If two of such liquid nodes are first neighbours, they belong to the same cluster. Thus, a first step consists in identifying all the liquid clusters formed at the end of nucleation step, where a cluster is defined as a group of connected liquid pores. Starting from this initial distribution of liquid clusters, the growth step is performed using the following algorithm:

1. Determine and label the different water clusters. If two pores – totally or partially saturated in liquid water – are adjacent, they belong to the same cluster.
2. Compute the vapour molar fraction field x_v from the solution of the system represented by Eq.(7). In each liquid pore (of coordinates x_i,y_i,z_i) in contact with a gas node, the local saturation pressure is imposed. Hence $x_v = p_{vs} / P_{ref}$, where $p_{vs} = p_{vs}(T(x_i, y_i, z_i))$. The boundary conditions on the sides of computational domain are the same as the ones presented in § 4.1.
3. If the vapour partial pressure computed in step 2 is greater than the local vapour saturation pressure in some gaseous pores, then identify the pore among those pores corresponding to $\max(RH_{i,j,k}, RH_{i,j,k} > \eta)$ and impose $x_v = p_{vs}(T(x_i, y_i, z_i)) / P_{ref}$ in the corresponding pore.
4. Go back to #2 and repeat steps #2 and #3 until there is no gaseous pore anymore such that $RH_{i,j,k} > \eta$.
5. Compute the molar condensation rate Fk at the boundary of each liquid cluster.
6. Apply the invasion percolation rule at each cluster, i.e. determine the throat of larger diameter along the boundary of each liquid cluster.
7. Compute the invasion time t_k of each cluster *k*, i.e. the time required to fully invade the pore adjacent to the throat determined in #6: $t_k = c_\ell V_{adk} / F_k$, where V_{adk} is the volume remaining to invade in the considered pore, c_ℓ is the mole concentration of liquid water.
8. Compute the time step $dt = min(t_k)$
9. Fully invade the pore corresponding to *dt* and update the volume of liquid in the invaded pore in the other clusters.
10. Go back to #1 and repeat the different steps 1-9 until a steady-state solution is reached, i.e. the overall phase-change rate becomes nil.

It should be clear that both evaporation and condensation occur during the growth of a liquid cluster as well as when the steady-state is reached. The steady – state is actually reached when the evaporation rate exactly balances the condensation rate at the boundary of each liquid cluster within the numerical accuracy of our model. This is sketched in Fig.8

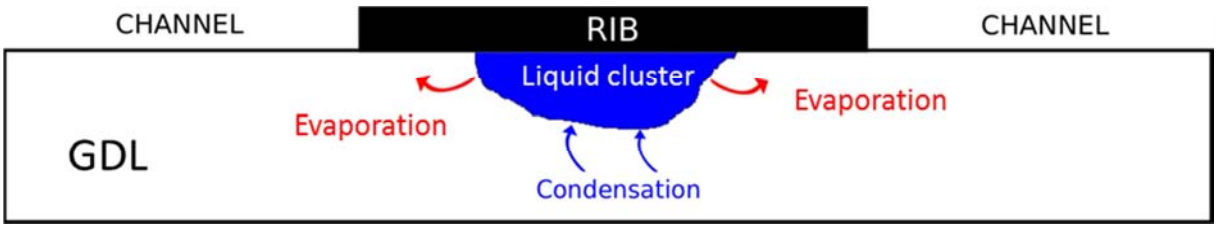

Figure 8. Illustration that the computed liquid water distribution corresponds to a steady state where the evaporation rate at the boundary of a liquid clusters exactly compensates the condensation rate.

5. Condensation diagram

5.1 Localization and occurrence of first condensation spots

According to the algorithm presented in § 4, condensation occurs when $RH_{i,j,k} > \eta$ somewhere in the network. To get insight into the most likely place of condensation, one can look at the distribution of *RH* within the network computed assuming no liquid in the network: $RH(x,y,z) = x_v(x,y,z)P_{ref} / p_{vs}(T(x,y,z))$. For the boundary conditions considered in the present article, an example of local relative humidity distribution is depicted in Fig. 10.

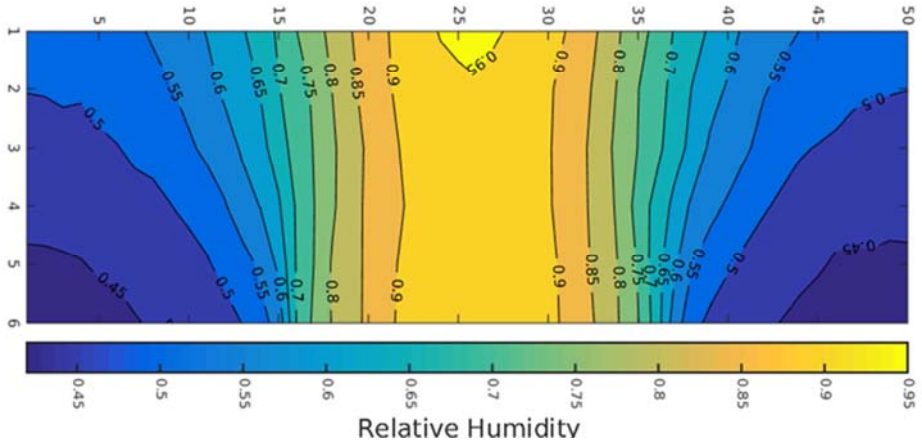

Figure 10. Exemple of local relative humidity distribution in a cross section of the network in the absence of condensation. This field was computed for i = 1 A/cm^2 and RH_{ch}= 50%. The spatial dimensions are in pore network unit (a pore network unit is equal to the pore network lattice spacing *a* (distance between two neighbour pores)). Note that the through-plane scale is dilated for clarity. The GDL appears much thicker than it is actually

As can be seen from Fig.10, the most likely place on incipient condensation is in the region of GDL located below the rib. A noticeable feature is that the local relative humidity is quite high not only right below the rib but all over the thickness of the GDL below the rib consistently with the temperature field depicted in Fig.4 showing that all the region below the rib is colder.

5.2 Condensation phase diagram

Another interesting aspect lies in the range of parameters leading to possible condensation. In our model, there are four parameters: the current density *i*, the tension *U*, the GDL effective thermal conductivity and the relative humidity in the channel RH_{ch}. Here we only explore the impact of the relative humidity in the channel RH_{ch} and the current density *i*. The polarization curve is the one depicted in Fig.2.
Solving the vapour diffusion problem in the GDL using the pore network model varying RH_{ch} and *i* leads to the phase diagram depicted in Fig.11. To construct the diagram we impose a current density and progressively increase RH_{ch} starting from a relatively low value,

computing the vapour partial pressure field in the network for each considered pair (RH_{ch} , i). The procedure is stopped when the PN computation of vapour partial pressure field in the network indicates the presence of a first condensation spot ($RH_{local} \geq 1$ in one pore within the GDL). This corresponds to the determination of one point on the curve shown in Fig.11. The procedure is then repeated varying i so as to obtain the complete curve.

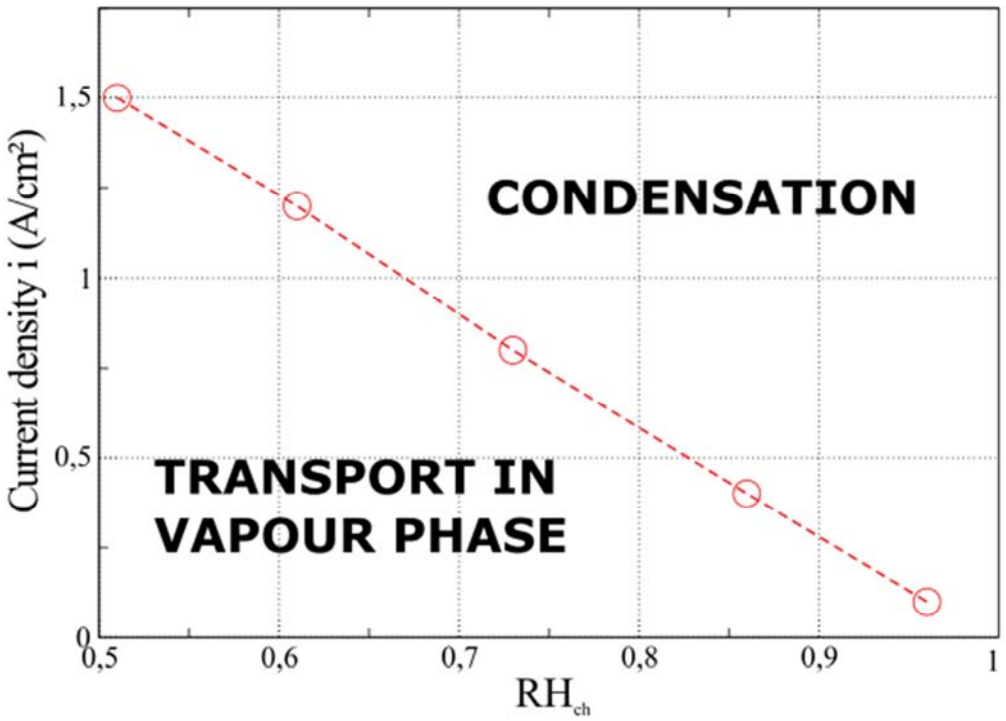

Figure 11. Condensation phase diagram obtained for the polarization curve depicted in Fig. 2. The water produced in the active layer can be entirely transferred in vapour phase through the GDL for the operating points located below the curve. Liquid water formation occurs in the GDL for the operating points located above the curve.

This diagram specified the operating condition for which condensation must occur, i.e. it is not possible to transfer all the water produced in the active layer by diffusion in vapour phase across a dry GDL network when i and RH_{ch} corresponds to a point located in the condensation region of the diagram.

6. Liquid water distribution

6.1 Performed simulations

Simulations of liquid water formation and growth of formed liquid clusters were performed for the conditions and parameter values summarized in Tables 1-4.

Impact of RH	$\lambda^*_{\perp unc}$	$\lambda^*_{\perp c}$	$\lambda^*_{//unc}$	$\lambda^*_{//c}$	$\lambda^*_{\perp c}(S)$	$D^*_{\perp unc}/D$	$D^*_{\perp c}/D$	$D^*_{//unc}/D$	$D^*_{//c}/D$	i	RH_{ch}	T_{bp}
S7	0.25	0.25	4	6.64	NO	0.25	0.25	0.7	0.5	1.5	90	80
S7bis	0.25	0.25	4	6.64	NO	0.25	0.25	0.7	0.5	1.5	60	80
S7ter	0.25	0.25	4	6.64	NO	0.25	0.25	0.7	0.5	1.5	70	80
S7qua	0.25	0.25	4	6.64	NO	0.25	0.25	0.7	0.5	1.5	80	80

Table 1. Impact of channel relative humidity. Thermal conductivities are in $Wm^{-1}K^{-1}$, *i* in A/cm^2, RH_{ch} in %, T_{bp} in °C.

Impact of current density	$\lambda^*_{\perp unc}$	$\lambda^*_{\perp c}$	$\lambda^*_{//unc}$	$\lambda^*_{//c}$	$\lambda^*_{\perp c}$ (S)	$D^*_{\perp unc}/D$	$D^*_{\perp c}/D$	$D^*_{//unc}/D$	$D^*_{//c}/D$	i	RH_{ch}	T_{bp}
S8	0.25	0.25	4	6.64	NO	0.25	0.25	0.7	0.5	0.1	90	80
S9	0.25	0.25	4	6.64	NO	0.25	0.25	0.7	0.5	0.4	90	80
S10	0.25	0.25	4	6.64	NO	0.25	0.25	0.7	0.5	0.8	90	80
S11	0.25	0.25	4	6.64	NO	0.25	0.25	0.7	0.5	1.2	90	80
S12 = S3bis	0.25	0.25	4	6.64	NO	0.25	0.25	0.7	0.5	1.5	90	80

Table 2. Impact of current density. Thermal conductivities are in $Wm^{-1}K^{-1}$, *i* in A/cm^2, RH_{ch} in %, T_{bp} in °C.

Impact of TSD	$\lambda^*_{\perp unc}$	$\lambda^*_{\perp c}$	$\lambda^*_{//unc}$	$\lambda^*_{//c}$	$\lambda^*_{\perp c}$ (S)	$D^*_{\perp unc}/D$	$D^*_{\perp c}/D$	$D^*_{//unc}/D$	$D^*_{//c}/D$	i	RH_{ch}	T_{bp}	Comment
S18	0.25	0.25	4	6.64	NO	0.25	0.25	0.7	0.5	0.8	90	80	Isotropic TSD
S18bis	0.25	0.25	4	6.64	NO	0.25	0.25	0.7	0.5	1.5	90	80	Isotropic TSD
Impact of thermal conductivity Anisotropy Factor	$\lambda^*_{\perp unc}$	$\lambda^*_{\perp c}$	$\lambda^*_{//unc}$	$\lambda^*_{//c}$	$\lambda^*_{\perp c}$ (S)	$D^*_{\perp unc}/D$	$D^*_{\perp c}/D$	$D^*_{//unc}/D$	$D^*_{//c}/D$	i	RH_{ch}	T_{bp}	Comment
S19	0.25	0.25	0.25	0.25	NO	0.25	0.25	0.7	0.5	1.5	90	80	λ isotropic
S20	0.25	0.25	40	66.4	NO	0.25	0.25	0.7	0.5	1.5	90	80	Greater anisotropy factor
Impact of through plane thermal conductivity	$\lambda^*_{\perp unc}$	$\lambda^*_{\perp c}$	$\lambda^*_{//unc}$	$\lambda^*_{//c}$	$\lambda^*_{\perp c}$ (S)	$D^*_{\perp unc}/D$	$D^*_{\perp c}/D$	$D^*_{//unc}/D$	$D^*_{//c}/D$	i	RH_{ch}	T_{bp}	Comment
S29	0.5	0.5	4	6.64	NO	0.25	0.25	0.7	0.5	0.8	90	80	
S30	1	1	4	6.64	NO	0.25	0.25	0.7	0.5	1.5	90	80	
Impact of diffusion coefficient	$\lambda^*_{\perp unc}$	$\lambda^*_{\perp c}$	$\lambda^*_{//unc}$	$\lambda^*_{//c}$	$\lambda^*_{\perp c}$ (S)	$D^*_{\perp unc}/D$	$D^*_{\perp c}/D$	$D^*_{//unc}/D$	$D^*_{//c}/D$	i	RH_{ch}	T_{bp}	Comment
S23	0.25	0.25	4	6.64	NO	0.25	0.25	0.7	0.5	1.5	90	80	idem S3bis
S24	0.25	0.25	4	6.64	NO	0.1	0.1	0.7	0.5	1.5	90	80	Greater anisotropy contrast

Table 3. Impact of TSD, thermal conductivity anisotropy factor, diffusion coefficients. Thermal conductivities are in $Wm^{-1}K^{-1}$, *i* in A/cm^2, RH_{ch} in %, T_{bp} in °C.

Impact of nucleation parameter	$\lambda^*_{\perp unc}$	$\lambda^*_{\perp c}$	$\lambda^*_{//unc}$	$\lambda^*_{//c}$	$\lambda^*_{\perp c}$ (S)	$D^*_{\perp unc}/D$	$D^*_{\perp c}/D$	$D^*_{//unc}/D$	$D^*_{//c}/D$	i	RH_{ch}	T_{bp}	η
S2bis	0.25	0.25	4	6.64	NO	0.25	0.25	0.7	0.5	1.5	90	60	1
S3bis	0.25	0.25	4	6.64	NO	0.25	0.25	0.7	0.5	1.5	90	80	1
S25	0.25	0.25	4	6.64	NO	0.25	0.25	0.7	0.5	1.5	90	60	1.05
S26	0.25	0.25	4	6.64	NO	0.25	0.25	0.7	0.5	1.5	90	80	1.05
S27	0.25	0.25	4	6.64	NO	0.25	0.25	0.7	0.5	1.5	90	60	1.1
S28	0.25	0.25	4	6.64	NO	0.25	0.25	0.7	0.5	1.5	90	80	1.1

Table 4. Impact of nucleation parameter (vapour supersaturation). Thermal conductivities are in $Wm^{-1}K^{-1}$, *i* in A/cm^2, RH_{ch} in %, T_{bp} in °C.

As can be seen from Tables 1-4, the impact of channel relative humidity, current density were investigated as well as the impact of parameters such as the GDL thermal conductivity anisotropy factor, in-plane vs through-plane throat size distribution, diffusion coefficients and nucleation parameter η (vapour supersaturation impact), etc. The impact of liquid saturation on thermal conductivity and current density spatial variation at the GDL –catalyst layer interface are discussed in Straubhaar et al. (2015b).

The impact of these various factors are analyzed through the consideration of:

- the through plane saturation profiles
- the in-plane saturation profiles
- the liquid distribution in in-plane slice #2 (see Fig.12)
- the liquid distribution in a through-plane cross-section (see Fig.12)
- 3D numerical visualizations of liquid water distribution.

Using the Cartesian coordinate system indicated in Fig.3, the through-plane saturation at discrete coordinate *z* is the fraction of the pore volume in the corresponding in-plane row of pores occupied by liquid over all the GDL computational domain depicted in Fig.3.
Similarly, the in-plane saturation at discrete coordinate *x* is the fraction of the pore volume in the corresponding y-z plane row of pores occupied by liquid over all the GDL computational domain depicted in Fig.3. It corresponds to the average saturation over the GDL thickness in *y-z* plane at position *x*.
The in-plane slice #2 corresponds to the second row of pores in the x-y plane (the first row corresponds to the GDL- Catalyst layer (or MPL) interface and the last row to the GDL – rib (or channel) interface.

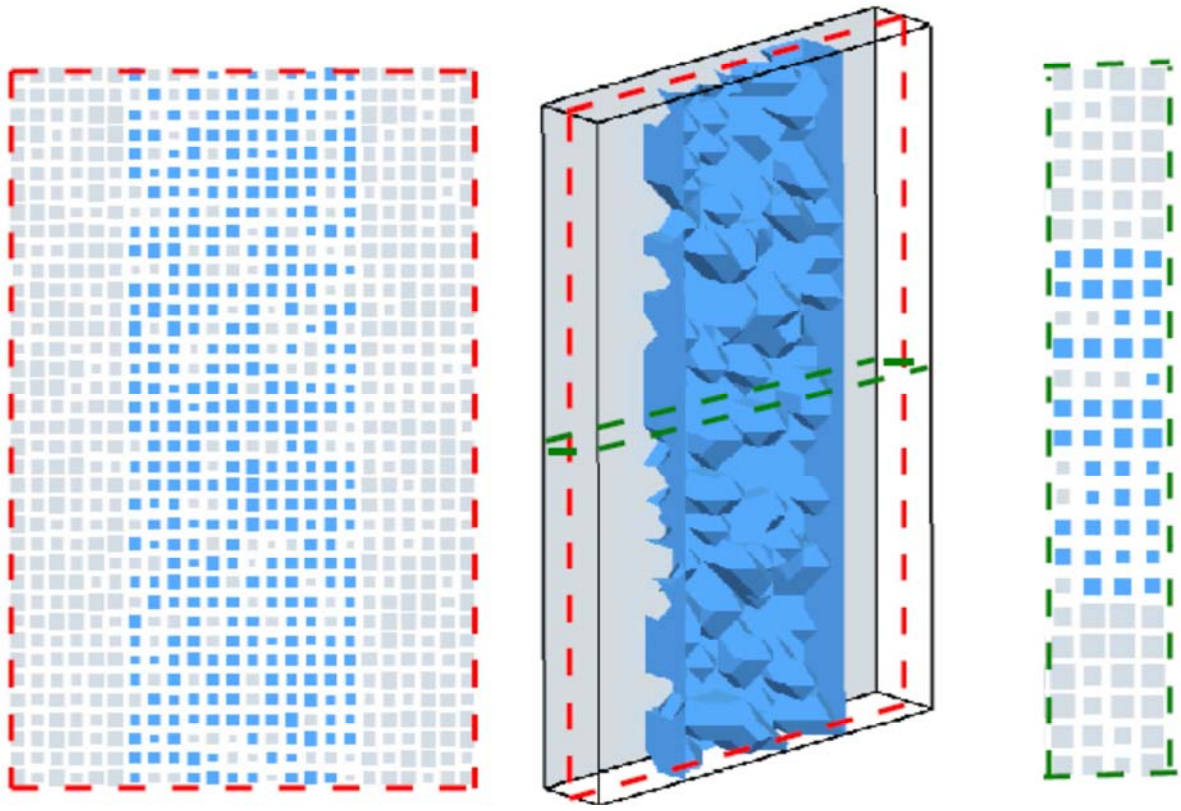

Figure 12. Examples of in-plane liquid distribution in slice #2 (red dashed frame), 3D visualization and through-plane distribution in the x-z plane delimited by the green dashed frame. Liquid water in blue, gas phase in grey. The rib –channel interface is on the right side of right figure. These images corresponds to simulation S3bis.

6.2 *Impact of channel relative humidity.*

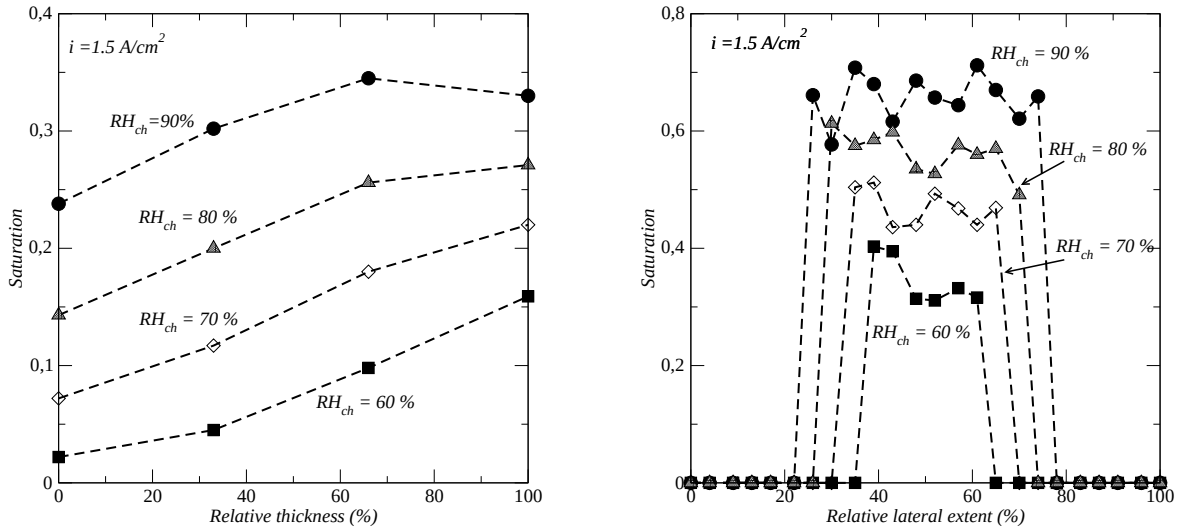

Figure 13. Impact of relative humidity: a) through-plane saturation profile, b) in-plane saturation profile.

6.3 Impact of current density

The impact of current density is illustrated in Fig.14 and Fig.15. The change in the through-plane saturation profile is also qualitatively similar to the results reported in LaManna et al. (2014) (see Fig. 9 in this reference), where however a lower temperature was considered (60°C instead of 80°C in the PNM). One observes a change from a monotonous profile to a concave one as the current density is increased.

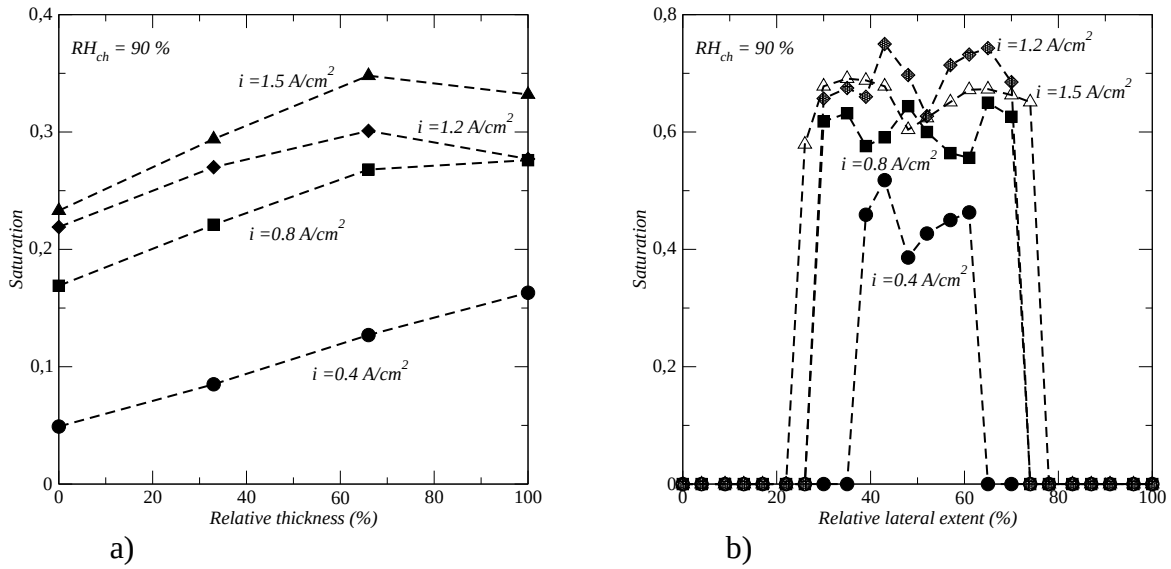

Figure 14. Impact of current density: a) through-plane saturation profile, b) in-plane saturation profile.

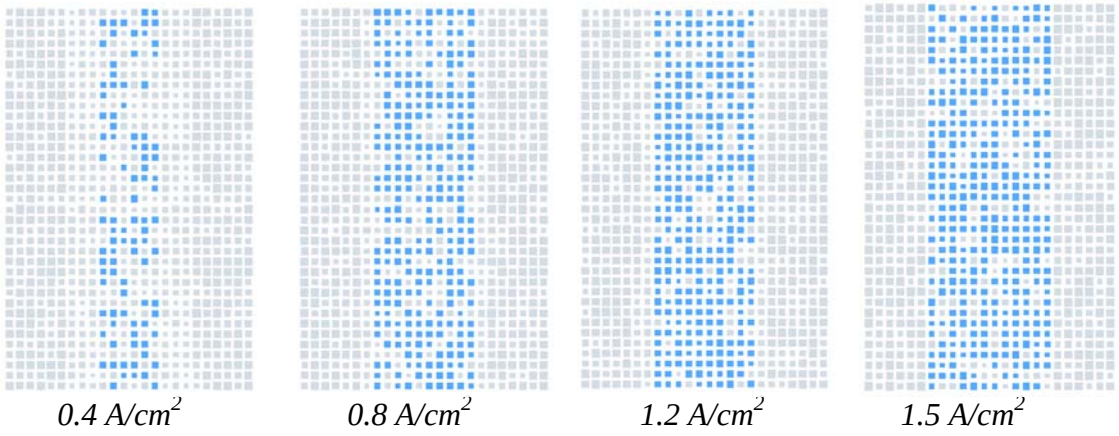

Figure 15. Impact of current density on liquid water (in blue) distribution in in-plane slice #2 RH_{ch} =90%.

As can be seen from Fig.14b and Fig.15, liquid water is mostly concentrated in the GDL region below the rib and tends to progressively invaded a bit the under channel region close to the rib.

6.4 Impact of TSD

We compare in Fig.16 the results obtained using the reference TSD (throat size distribution) distribution (throat sizes smaller in the in-plane direction than in the through-plane direction) with the ones for an isotropic TSD (same TSD in in-plane and through-plane directions) all other parameters being kept unchanged between the simulations with the isotropic TSD and the ones with the reference anisotropic TSD.

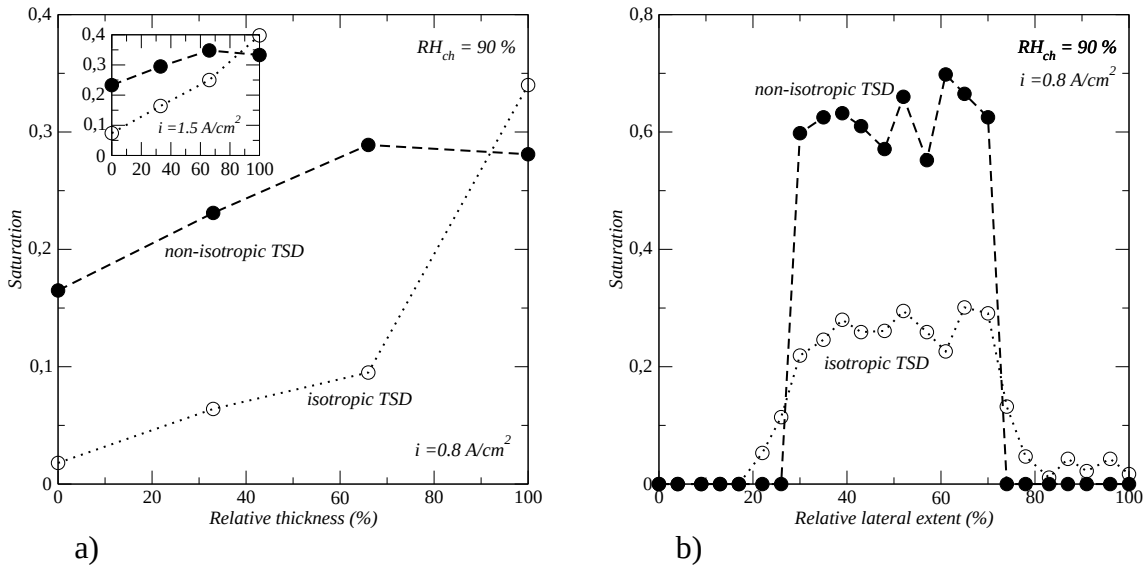

Figure 16. Impact of TSD: a) through-plane saturation profile, b) in-plane saturation profile for i = 0.8 A/cm^2.

As can be seen from Fig.16, this has a strong impact on the liquid saturation profiles. The through-plane saturation is almost inverted. The saturation increases monotonously from the GDL inlet to the rib – channel interface with a maximum saturation under the rib. This is in contrast with the anisotropic PSD characterized with a maximum through-plane saturation at a relative distance from the GDL inlet of about 60% of the GDL thickness.

The liquid clusters are forced to growth in the through-plane direction before growing into the in-plane directions with the anisotropic TSD leading to preferential cluster growth in the through-plane direction. By contrast, the growth is much more isotropic with the isotropic TSD. As can be seen from the in-plane saturation profiles (Fig.16b), this results in some invasion of the under channel GDL region with the isotropic TSD whereas the liquid water is essentially confined in the GDL region under the RIB with the anisotropic TSD.
This is further illustrated in Fig.17.

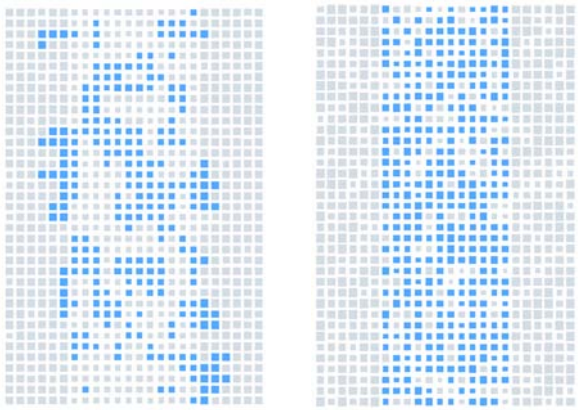

a) Isotropic TSD *b) anisotropic TSD*

Figure 17. Comparison between liquid water (in blue) distribution in in-plane slice #2 between the isotropic TSD (S18 bis) and the anisotropic TSD (S3bis); i =1.5 A/cm^2, RH_{ch} =90%.

6.5 Impact of through-plane thermal conductivity and thermal conductivity anisotropy factor

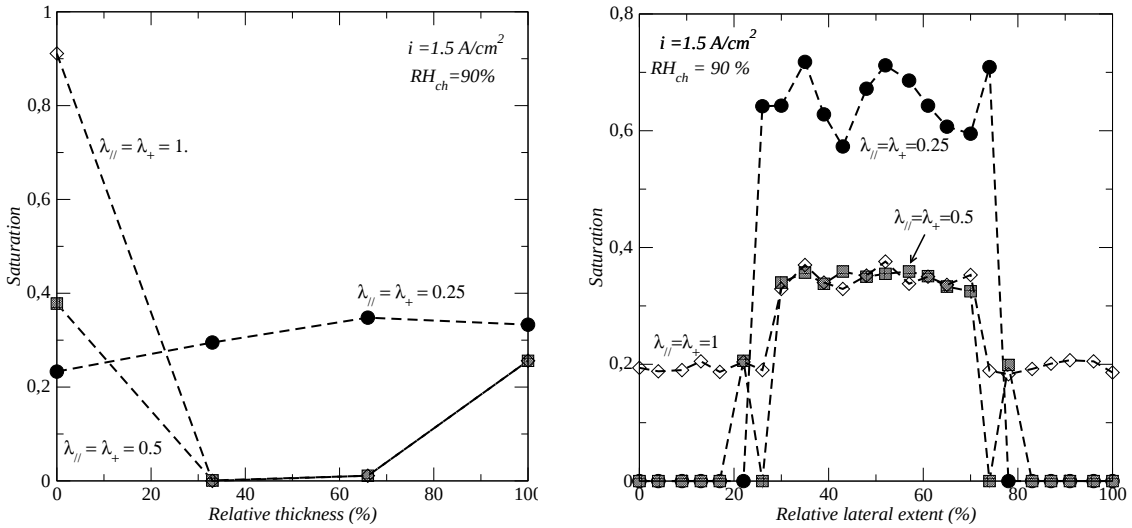

Figure 18. Impact of through-plane thermal conductivity: a) through-plane saturation profile, b) in-plane saturation profile. i =1.5 A/cm^2, RH_{ch} = 90%.

To explore the impact of anisotropy factor, we kept $\lambda^*_{\perp uc} = 0.25$ Wm^{-1}K^{-1} and varied the GDL thermal conductivity anisotropy factor $\lambda^*_{//uc} / \lambda^*_{\perp uc}$. As shown in Fig.19b and Fig.20, the impact of this factor is not very important as regards the in-plane liquid water distribution. The impact is quite weak when the anisotropy factor is increased from an already significant value (from 16 to 160 in our example) meaning that the temperature field is not significantly modified. The impact is somewhat greater when the anisotropy factor varies in the range [1-16] as exemplified in Fig. 20. As shown in Fig.19a, the impact of this factor on the through-plane saturation profile is however noticeable and subtle since the trend is not monotonous with this factor.

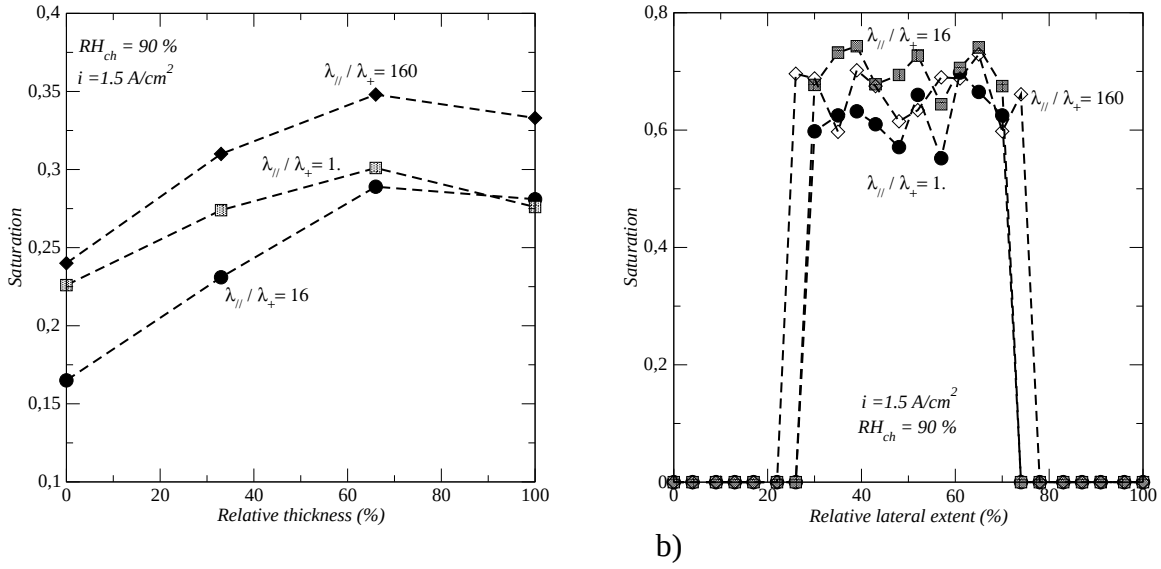

Figure 19. Impact of thermal conductivity anisotropy factor: a) through-plane saturation profile, b) in-plane saturation profile. i =1.5 A/cm^2, RH_{ch} = 90%.

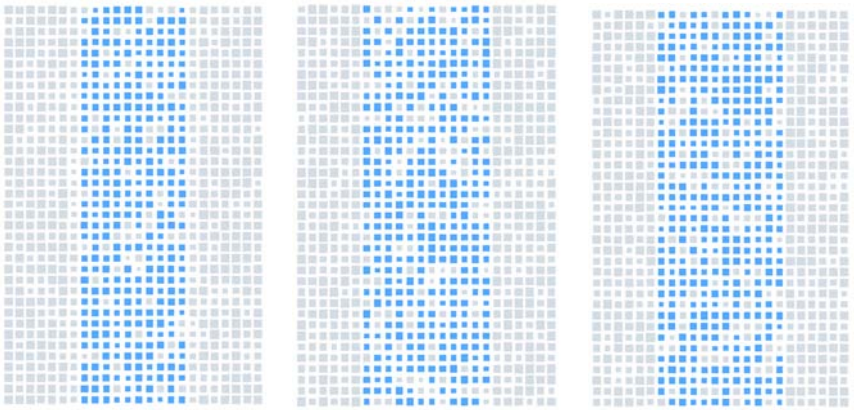

a) $\lambda^*_{//uc} / \lambda^*_{\perp uc} = 1$ *b)* $\lambda^*_{//uc} / \lambda^*_{\perp uc} = 16$ *c)* $\lambda^*_{//uc} / \lambda^*_{\perp uc} = 160$

Figure 20. Comparison between liquid water (in blue) distribution in in-plane slice #2 for three different GDL thermal conductivity anisotropy factor a) $\lambda^*_{//uc} / \lambda^*_{\perp uc} = 16$ (S3bis), b) $\lambda^*_{//uc} / \lambda^*_{\perp uc} = 1$ (S19), c) $\lambda^*_{//uc} / \lambda^*_{\perp uc} = 160$ (S20), i =1.5 A/cm^2, RH_{ch} = 90%.

6.6 Impact of through-plane diffusion coefficients

As depicted in Fig.21, the impact of through-plane diffusion coefficient is significant. The situation is somewhat similar to the one obtained when the through-plane thermal conductivity was varied (see § 6.5). For the lowest value of the diffusion coefficient, almost no liquid forms in the middle slices of the GDL (see Fig.21a) and the water spreads all over the GDL inlet surface as indicated by Fig.21b)

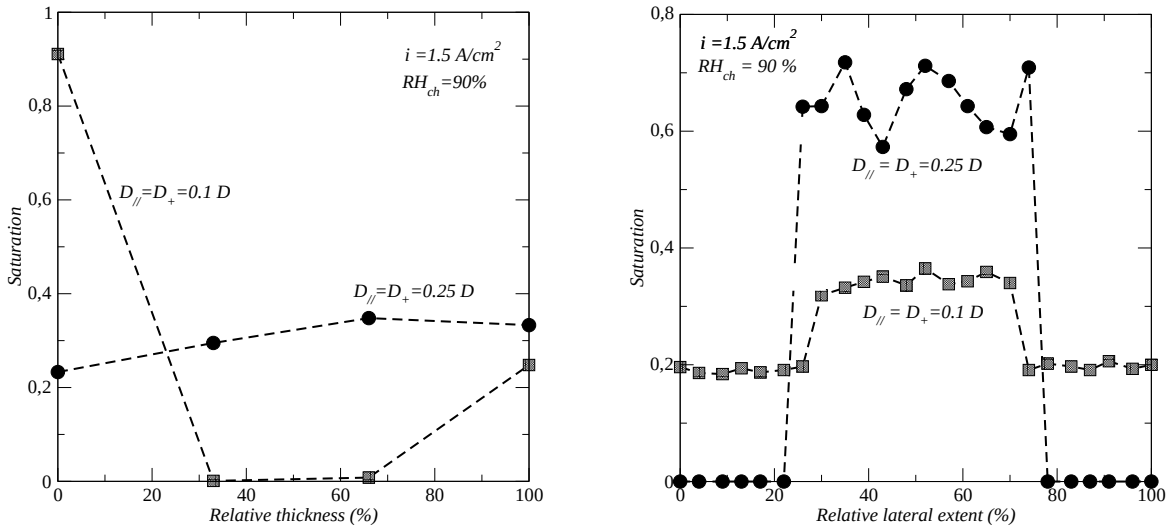

Figure 21. Impact of through-plane diffusion coefficient: a) through-plane saturation profiles, b) in-plane saturation profiles. i =1.5 A/cm^2, RH_{ch} = 90%.

6.7 Impact of nucleation parameter

The nucleation parameter η has an interesting impact. First, it affects the shape of both the through-plane and in-plane saturation profiles. This is illustrated in Fig. 22. Note in particular in Fig.22a that the through-plane saturation right below the rib becomes lower that the saturation at the GDL inlet (i.e. at the GDL - catalyst layer interface) when the nucleation parameter is increased whereas the opposite is observed for η =1.
As depicted in Fig.22b, the liquid water remains mostly confined in the region of the GDL below the rib but tends to invade a bit the region under the channel as this parameter is increased.

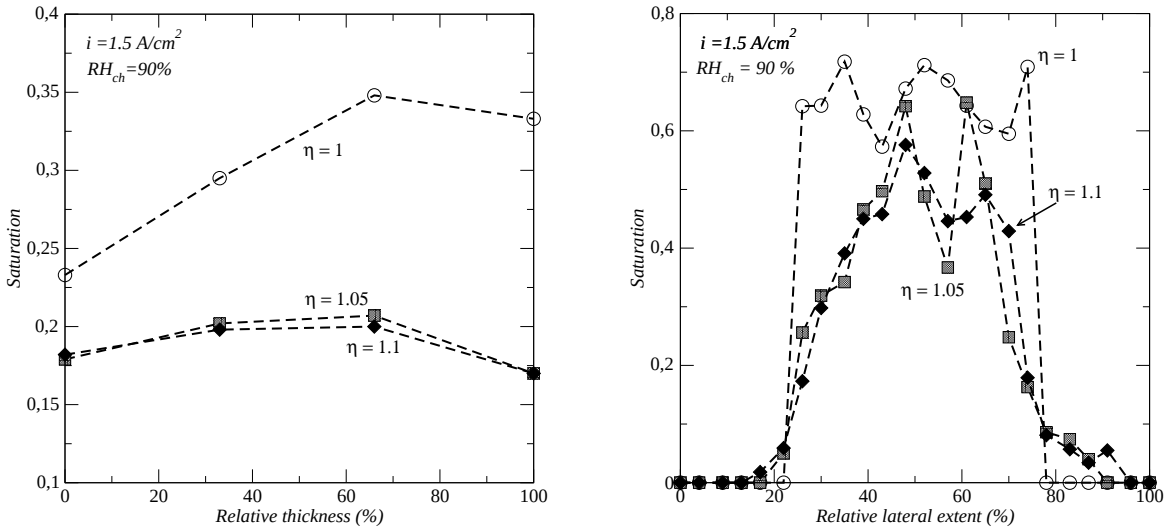

Figure 22. Impact of nucleation parameter: a) through-plane saturation profile, b) in-plane saturation profile. i =1.5 A/cm^2, RH_{ch} = 90%.

This is further illustrated in Fig.23, which interestingly shows that the liquid water occupancy within the region below the rib tends to become sparser as η is increased. This is well illustrated by the through-plane cross-section corresponding to η =1.1 with the liquid confined below the edges of the rib and no liquid below the central region of the rib.

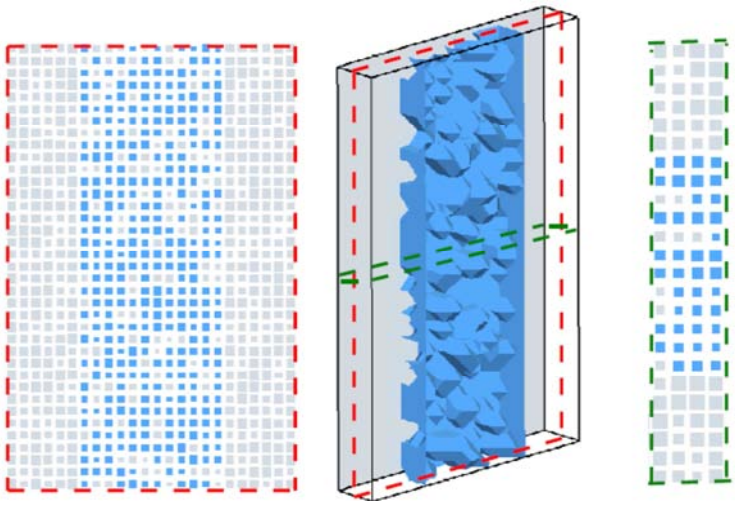

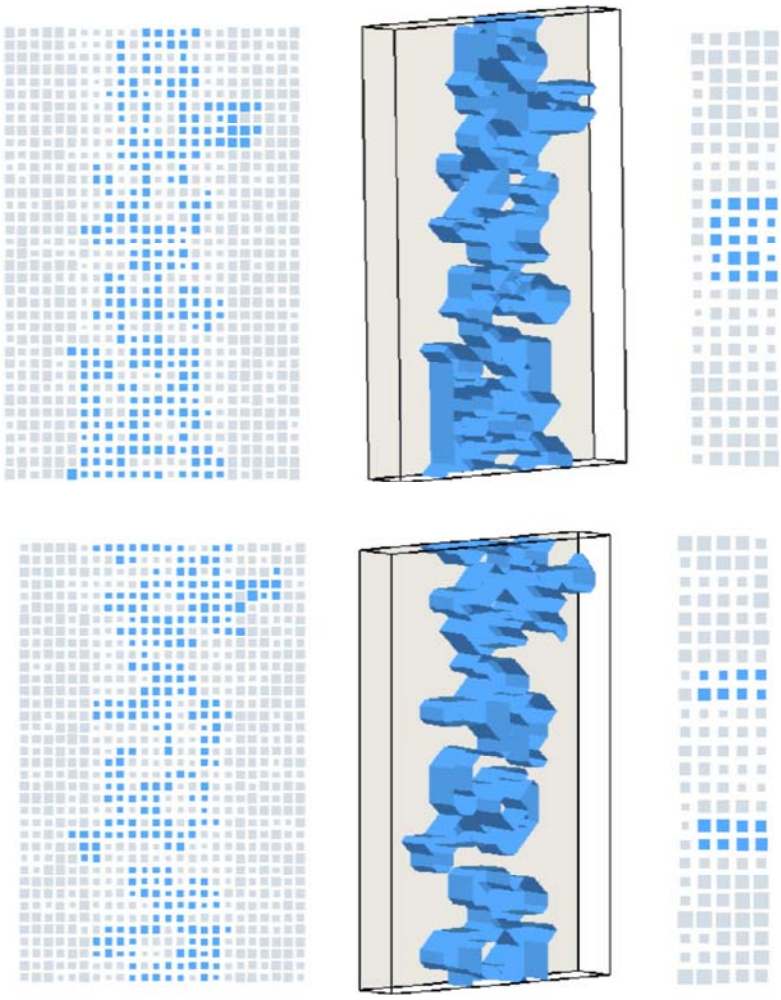

Figure 23. Impact of nucleation parameter: from top to bottom η= 1, η=1.05, η=1. *i* =1.5 A/cm^2, RH_{ch} = 90%.

7. Conclusion

In this paper, condensation in a GDL unit cell was simulated using a condensation pore network model (PNM). The liquid – gas distribution in the GDL resulting from the condensation process was found to be markedly different from the distribution typically reported in most of previous studies on two-phase flow in GDL using PNM and assuming that the occurrence of water in the GDL results from the capillary controlled invasion in liquid phase from the adjacent MP or catalyst layer..

The trends obtained with the condensation PNM are in quite good agreement with the experimental observations reported for example in La Manna et al. (2014) as regards the impact of current density and relative humidity. Also the simulations are in quite good agreement with the observation reported in Boillat et al. (2008) indicating a “strong separation of the water content under the ribs and under the channels”. In our simulations as well “water tends to gather preferentially under the rib”.

However, these results are quite sensitive to the through-plane thermal conductivity, through-plane diffusion coefficient and anisotropy of pore size distributions. All these parameters must therefore be characterized carefully.

As regards the PNM algorithm itself, it was found that the nucleation parameter was a sensitive parameter, less however that the aforementioned GDL properties. This parameter

was introduced to take into account a possible supersaturation effect of the vapour and also to limit the impact of possible numerical inaccuracies in the computation of the local relative humidity. Further investigations are needed to specify this parameter so as not consider it as a possible adjustment parameter.

Acknowledgements:

The authors gratefully acknowledge the funding from the EU project IMPALA (" IMprove Pemfc with Advanced water management and gas diffusion Layers for Automotive application", project number: 303446) within the Fuel Cells and Hydrogen Joint Undertaking (FCHJU).

References

T.Agaesse, A.Lamibrac, F.Büchi, J.Pauchet, M.Prat, Comparison between pore network simulations and X-Ray tomography images of ex-situ water distributions in a gas diffusion layer of proton exchange membrane fuel cell. Submitted (2015)

R.Alink, D.Gerteisen, Modeling the liquid water transport in the gas diffusion layer for polymer electrolyte membrane fuel cells using a water path network, *Energy*, 6, 4508-4530 (2013)

S.Basu, C.Y.Wang, K.S.Chen. Phase Change in a Polymer Electrolyte Fuel Cell, *J Electroche Soc.*; 156 (6): B748-B756 (2009).

A Bazylak, V Berejnov, B Markicevic, D Sinton, N Djilali, Numerical and microfluidic pore networks: Towards designs for directed water transport in GDLs, *Electrochimica Acta* 53 (26), 7630-7637, 2008.

P. Boillat, D. Kramer, B. C. Seyfang, G. Frei, E. Lehmann, G. G. Scherer, A. Wokaun, Y. Ichikawa, Y. Tasaki, and K. Shinohara, *Electrochem. Commun.*, 10, 546(2008).

D.A.Caulk, D.R. Baker, Heat and water transport in hydrophobic diffusion media of PEM fuel cells, *Journal of The Electrochemical Society*, 157 (8) B1237-B1244 (2010)

D.A.Caulk, D.R. Baker, Modeling two-phase water transport in hydrophobic diffusion media for PEM fuel cells, *Journal of The Electrochemical Society*, 158 (4) B384-B393 (2011)

L.Ceballos, M.Prat, Invasion percolation with multiple inlet injections and the water management problem in Proton Exchange Membrane Fuel Cells, *J. of Power Sources* 195, pp. 825–828(2010)

L. Ceballos, M. Prat, and P. Duru, Slow invasion of a nonwetting fluid from multiple inlet sources in a thin porous layer. *Phys. Rev. E* **84**, 056311 (2011)

L. Ceballos, M. Prat, Slow invasion of a fluid from multiple inlet sources in a thin porous layer: influence of trapping and wettability, *Phys. Rev. E* **87**, 043005 (2013)

J.Eller, T. Rose, F.Marone, M. Stampanoni, A. Wokaun and F. N. Büchi, Progress in In Situ

X-Ray Tomographic Microscopy of Liquid Water in Gas Diffusion Layers of PEFC, *Journal of The Electrochemical Society*, 158 (8) B963-B970 (2011)

M Fazeli, J Hinebaugh, A Bazylak, Investigating Inlet Condition Effects on PEMFC GDL Liquid Water Transport through Pore Network Modeling, *Journal of The Electrochemical Society*, 162 (7) F661-F668 (2015)

P.A. Garcia-Salaberri, G.Hwang, M.Vera, A.Z.Weber and J.T. Gostick, Effective diffusivity in partially-saturated carbon-fiber gas diffusion layers: Effect of through-plane saturation distribution. *Int. J. of Heat and Mass Tr.*, 80, 319-333 (2015)

J.T. Gostick, M. A. Ioannidis, M.W. Fowler, M.D. Pritzker, Pore Network modelling of fibrous gas diffusion layers for polymer electrolyte membrane fuel cells, *J. Power Sources*, 173 277-290, (2007).

Gostick. J.T. 2013. Random pore network modeling of fibrous PEMFC gas diffusion media using Voronoi and Delaunay tessellations. *Journal of The Electrochemical Society* 160 (8): F731-F743 (2013)

L.Hao, P.Cheng, Lattice Boltzmann simulations of water transport in gas diffusion layer of a polymer electrolyte membrane fuel cell, *Journal of Power Sources* 195 (12), pp. 3870–3881 (2010).

Hinebaugh, J., Bazylak, A. "Condensation in PEM fuel cell gas diffusion layers: A pore network modelling approach." *Journal of the Electrochemical Society*, 157(10), B1382-1390 (2010).

Hinebaugh, J. and Fishman, Z. and Bazylak, A. Unstructured Pore Network Modeling with Heterogeneous PEMFC GDL Porosity Distributions, *Journal of the Electrochemical Society*, Vol. 157, pp. B1651-B1657 (2010)

J. M. LaManna, S.Chakraborty, J. J. Gagliardo, M. M. Mench, Isolation of transport mechanisms in PEFCs using high resolution neutron imaging *Int. J. of Hydrogen Energy* 39, 3 3 8 7 - 3 3 9 6 (2014)

A. Lamibrac, J. Roth, M. Toulec, F. Marone, M.Stampanoni, F.N. Büchi, Characterization of Liquid Water Saturation in Gas Diffusion Layers by X-ray Tomographic Microscopy, Submitted to the *Journal of the Electrochemical Society* (2015)

K. J. Lee, J. H. Nam, and C. J. Kim, Pore-network analysis of two-phase water transport in gas diffusion layers of polymer electrolyte membrane fuel cells, *Electrochim. Acta* **54**, 1166-1176 (2009).

KJ Lee, JH Kang, JH Nam, CJ Kim, Steady liquid water saturation distribution in hydrophobic gas-diffusion layers with engineered pore paths: An invasion-percolation pore-network analysis, *Journal of Power Sources* 195 (11), 3508-3512 (2010).

KJ Lee, JH Kang, JH Nam, Liquid water distribution in hydrophobic gas-diffusion layers with interconnect rib geometry: An invasion-percolation pore-network analysis, *International Journal of Hydrogen Energy* 39, 6646-6656 (2014).

Luo, Gang, et al., Modeling liquid water transport in gas diffusion layers by topologically equivalent pore network. 19, *Electrochimica Acta* , Vol. 55, pp. 5332-5341 (2010)

Markicevic, B., Bazylak, A. and Djilali, N. Determination of transport parameters for multiphase flow in porous gas diffusion electrodes using a capillary network model. 2, *Journal of Power Sources*, Vol. 171, pp. 706-717. (2007)

Medici, E., F., Allen, J. S., 2013, "Evaporation, Two Phase Flow, and Thermal Transport in Porous Media with Application to Low-temperature Fuel Cells," *International Journal of Heat and Mass Transfer*, Vol. 65, pp.779-788 (2013)

L.Mottet, T.Coquard, M.Prat, Three dimensional liquid and vapour distribution in the wick of capillary evaporators, *Int. J. of Heat and Mass Tr*., vol. 83, 636-651 (2015)

J.H. Nam, M. Kaviany, Effective diffusivity and water-saturation distribution in single- and two layer PEMFC diffusion medium, *Int. J. of Heat and Mass Transfer*, 46 4595-4611, (2003).

S. P. Kuttanikkad, M. Prat, J. Pauchet, Pore-network simulations of two-phase flow in a thin porous layer of mixed wettability: Application to water transport in gas diffusion layers of proton exchange membrane fuel cells, *J. of Power Sources* 196, pp. 1145–1155 (2011)

C. Qin, Water Transport in the Gas Diffusion Layer of a Polymer Electrolyte Fuel Cell: Dynamic Pore-Network Modeling Journal of the Electrochemical Society, 162 (9) F1036-F1046 (2015)

M. Quintard, L. Bletzacker, D. Chenu, S. Whitaker, Nonlinear, Multicomponent, Mass Transport in Porous Media, *Chem. Eng. Sci.* 61 (8) 2643–2669 (2006)

A. Radhakrishnan, Thermal Conductivity Measurement of Gas Diffusion Layer Used in PEMFC, Master of sciences Thesis, Department of Mechanical Engineering, Kate Gleason College of Engineering Rochester Institute of Technology, Rochester, NY, USA, November 5, (2009)

M. Rebai, M. Prat, Scale effect and two-phase flow in a thin hydrophobic porous layer. Application to water transport in gas diffusion layers of PEM fuel cells, *J. of Power Sources*, 192 534-543, (2009).

K. Seidenberger, F. Wilhelm, J. Haußmann, H. Markötter, I. Manke, J. Scholta, Grand canonical Monte Carlo study on water agglomerations within a polymer electrolyte membrane fuel cell gas diffusion layer, *Journal of Power Sources*, Volume 239, 1, pp. 628–641 (2013).

Sinha PK, Wang CY. Pore-network modeling of liquid water transport in gas diffusion layer of polymer electrolyte fuel cell. *Electrochimica Acta* ;52:7936-45 (2007).

B.Straubhaar, M. Prat**,** Water transport in gas diffusion layers of PEM fuels cells in presence of a temperature gradient. Phase change effect. *Int. J. of Hydrogen Energy*, 40 (35) 11668–11675 (2015a)

B. Straubhaar, A.Lamibrac, F.Buechi, J.Pauchet, M.Prat, Condensation as major mechanism of liquid water formation in the gas diffusion layer of a proton exchange membrane fuel cell, to be submitted (2015b)

A. Thomas, G.Maranzana, S. Didierjean, J. Dillet,O. Lottin, Thermal Effect on Water Transport in Proton ExchangeMembrane Fuel Cell, *Fuel Cells* 12 (2), 212–224 (2012)

A. Thomas, G. Maranzana, S. Didierjean, J. Dillet, O. Lottin Measurements of electrode temperatures, heat and water fluxes in PEMFCs: conclusions about transfer mechanisms, *Journal of The Electrochemical Society*, 160 (2) F191-F204 (2013)

A. Thomas, G. Maranzana, S. Didierjean, J. Dillet, O. Lottin, Thermal and water transfer in PEMFCs: Investigating the role of the microporous layer, *International Journal of Hydrogen Energy*, 39(6):2649–2658 (2014).

M.M. Tomadakis, S.V. Sotirchos, Ordinary and transition regime diffusion in random fiber structures, *AIChE J.* 39, 397–412, (1993)

D. Wilkinson, J.F. Willemsen, Invasion percolation: a new form of percolation theory, *J.Phys.AMath.Gen.*, 16 3365-3376, (1983)

R.Wu, Impacts of the mixed wettability on liquid water and reactant gas transport through the gas diffusion layer of proton exchange membrane fuel cells . 9-10, *International Journal of Heat and Mass Transfer*, Vol. 55, pp. 2581-2589.(2012)

Wu R., Xun Zhu, Qiang Liao, Rong Chen, Guo-Min Cui, Liquid and oxygen transport in defective bilayer gas diffusion material of proton exchange membrane fuel cell, *International Journal of Hydrogen Energy*, 38 (10), pp 4067–4078 (2013).

N.Zamel, X. Li, Effective transport properties for polymer electrolyte membrane fuel cells – With a focus on the gas diffusion layer, *Progress in Energy and Combustion Science* 39, 111-146 (2013).

5.3 Conclusion

In this chapter we carried out a sensitivity analysis to assess the influence of key parameters such as thermal conductivity, thermal conductivity anisotropy factor, throat size distributions, GDL effective diffusion coefficient and the so-called nucleation coefficient. Based on this knowledge, the next chapter compares our CPNM to experimental results obtained with X-ray tomography.

Chapter 6

Comparison with X-ray tomography data from PSI

Contents

6.1 Introduction

This chapter is formed by an article not yet submitted and not yet reviewed by the other authors. The objective is to compare condensation pore network simulations with experimental data obtained from X-ray tomography in an operating PEMFC. The experimental data are through plane saturation profiles and (2D) liquid water distribution in the mean plane of the GDL. The pore network is specified so as to take into account the GDL properties as well as possible from data available in the literature of from IMPALA project.

6.2 Article 4: Condensation as major mechanism of liquid water formation in the gas diffusion layer of a proton exchange membrane fuel cell

Condensation as major mechanism of liquid water formation in the gas diffusion layer of a proton exchange membrane fuel cell

B. Straubhaar[3], A.Lamibrac[1], F.Büchi[1], J.Pauchet[2], M.Prat[3*]

[1] Electrochemistry Laboratory, Paul Scherrer Institut, 5232 Villigen PSI, Switzerland
[2]CEA, LITEN, LCPEM, Laboratory of Fuel Cell Components, Electrolysers and Modeling, 17 rue des Martyrs, 38054 Grenoble, France
[3]Université de Toulouse; INPT, UPS; IMFT, Avenue Camille Soula, F-31400 Toulouse, France
CNRS; IMFT, F-31400 Toulouse, France

Water management is a key issue for the operation of proton exchange membrane fuel cell. However, the exact mechanisms of liquid water formation in the various components of the fuel cell are still an open question. Here we discuss the case of the gas diffusion layer on the cathode size and show that water vapour condensation is a major phenomenon from a combination of pore network simulations and images of the liquid water phase on the pore scale of the materials obtained using X ray tomographic microscopy.

Proton exchange membrane fuel cells (PEMFC) are a subject of intense studies and developments, notably as a candidate to replace internal combustion engines for automotive applications. A key issue in this system is the water management[1]. In brief, the polymer electrolyte that separates the anode and the cathode must be sufficiently hydrated while avoiding excess liquid water in the adjacent catalyst and porous transport layers so as not to impede reactant transport. Although this technology has motivated a great deal of studies, the exact mechanisms of water formation and transport in the PEMFC are still somewhat elusive. This is a primary bottleneck for developing rationale and systematic approaches aiming at optimizing the fuel cell performances or better controlling ageing issues. Studies too often resort to trial and error test series leading to results that can possibly go in the good direction but short of a sufficient understanding of the processes at play to really explain the cause of the observed beneficial modifications, if any.

Here, we concentrate on the gas diffusion layer on the cathode side. The gas diffusion layer (GDL) is a porous transport layer which is a key element of fuel-cell electrode. This is a highly porous layer composed of carbon fibers coated by a hydrophobic agent (Fig.1). The GDL must notably provide efficient pathways for gaseous reactants and liquid water through its pore space. Since the presence of liquid water can block the gaseous reactant transport, it is crucial to well understand how liquid water can form in the GDL.

The short review of literature presented in ref. (2) indicates that two main scenarios have been considered so far. As considered in many previous works[3-16], scenario #1 assumes a capillarity controlled invasion in liquid phase from adjacent catalyst layer where water is produced as a result of the electrochemical reactions. Scenario #2 analyzes the liquid water formation in the GDL as the result of the condensation of the water vapour produced in the catalyst layer. Although the mention of the condensation process is not unusual in the PEMFC literature[17-22], it can be noted that scenario #2 has been by far much less studied than scenario #1. The emergence of the condensation scenario is intimately linked to the characterization of the temperature field within the GDL. Whereas the temperature variations within the GDL are essentially ignored in many previous works considering scenario #1, this is a crucial aspect for the condensation scenario[2,21,22].

The fact that the temperature varies in both the in-plane and the through plane directions within the GDL in an operating fuel cell is now well established[21-24] and thus must be taken into account.

In this context, the main objective of the present work is to determine which scenario is the most relevant.

The study is based on comparison between data obtained from X ray tomographic microscopy and from pore network simulations considering the two aforementioned scenarios: capillarity controlled invasion in liquid phase from the adjacent finer layer,

*author for correspondance: mprat@imft.fr

invasion by condensation of water vapour coming from adjacent finer layer.

In most previous studies considering scenario #1, only liquid transport is considered and phase change phenomena are ignored. A simple procedure is to use the standard invasion percolation (IP) algorithm[4,25]. Although the boundary condition to be used in conjunction with the IP algorithm has been a subject of discussion[6,26], we use the IP algorithm with the standard boundary condition in the present work since it has been by far the most used algorithm in the literature in relation with scenario #1.

The Condensation Pore Network Model, referred to as CPNM, used in the present work was introduced in ref.(2). It is briefly presented in the appendix as well as the properties of the network. Here we just mention that it takes into account the strong anisotropy of the GDL thermal conductivity, the anisotropy of the effective diffusion tensor, the fact that the sizes of the constrictions (a constriction is a passage between two pores) are smaller in the in-plane directions than in the through plane direction, the fact that the properties can be different in the compressed region of the GDL compared to the uncompressed region. Also, the spatial variation of the current density at the GDL inlet has been taken into account. The impact of liquid water on the thermal conductivity has been considered in one simulation.

On the experimental side, a special mini PEMFC was developed to make possible the X-ray microscopy. This system is described in ref. 27 (pending PSI ref.). The details are therefore not repeated here. The geometrical details useful for the present work are shown in Fig.1. The GDL material in this system is shown in Fig.1a and is a commercial GDL referred to as SGL 24BA. It can be noted that this GDL has no MPL (microporous layer).

X-ray tomographic microscopy imaging was performed at the Tomcat beamline14 of the Swiss Light Source (SLS) with a beam energy of 13.5 keV, exposure times of 15 ms per projection and 2001 projections per tomographic scan. With the PCO edge camera and the 2-4x zoom microscope used, a pixel edge length of 2.2 μm. The entire sample did fit into the field of view and dark (no beam) and flat (no sample) images were taken for each scan to correct for lateral fluctuation of the beam intensity.

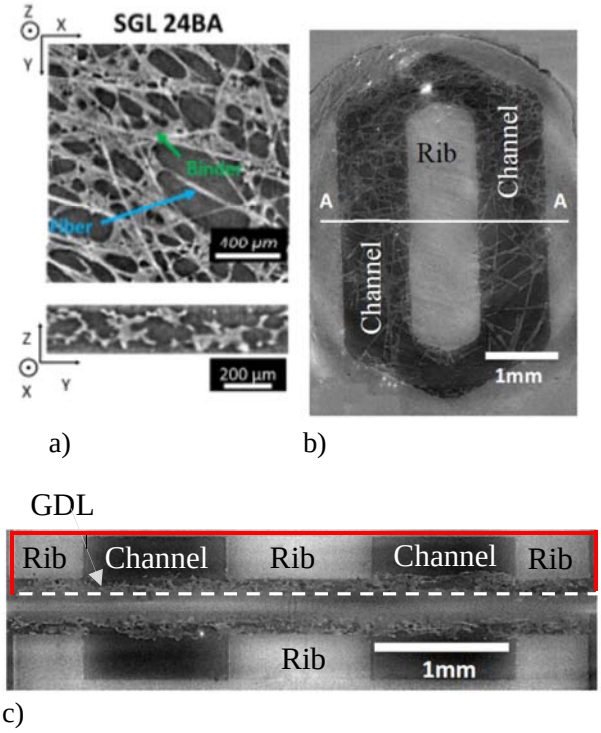

FIG.1. a) Through-plane (top) and in-plane (bottom) slices of SGL 24BA; b) Top: horizontal slice through cell at the level of the interface of channel and GDL; c) Bottom: vertical slice at the position of A – A in the horizontal slice. The frame formed by the white dashed line and the red lines corresponds to the boundary of computational domain considered in the numerical simulations.

From the XTM scan grey scale 3D images of the samples are reconstructed using the gridrec reconstruction algorithm[28]. For quantitative analysis the images need to be segmented into the different phases (solid, liquid and void). Due to the similar X-ray linear attenuation coefficients of carbon and water, accurate segmentation cannot be made by simple thresholding. The workflow used here is similar to previously described protocols[29,30] following the general route of subtraction of binary images (not grey scale images).

Fig.1a shows horizontal and vertical grey scale slices of the dry material whereas Fig.2 horizontal slice in the middle of the cathode GDL in the format of the ternary structures (solid, liquid water and void) at automotive and limiting current conditions (see Table 1).

Table 1. Automotive and limiting current conditions. RH_{ch} is the relative humidity in the channel, T_{ext} the temperature (on external boundary of channel). ; U is the electrical tension and i the current density.

	T_{ext} (°C)	RH_{ch} (%)	U	i (A/cm^2)
Automotive conditions	80	90	0.5 V	0.9
Limiting current cond.	80	90	≤ 50 mV	1.5

The following experimental results become apparent from Fig. 2:

• there is no saturation in the channel region.

• both conditions (automotive and limiting current) lead to similar liquid distribution and saturations.

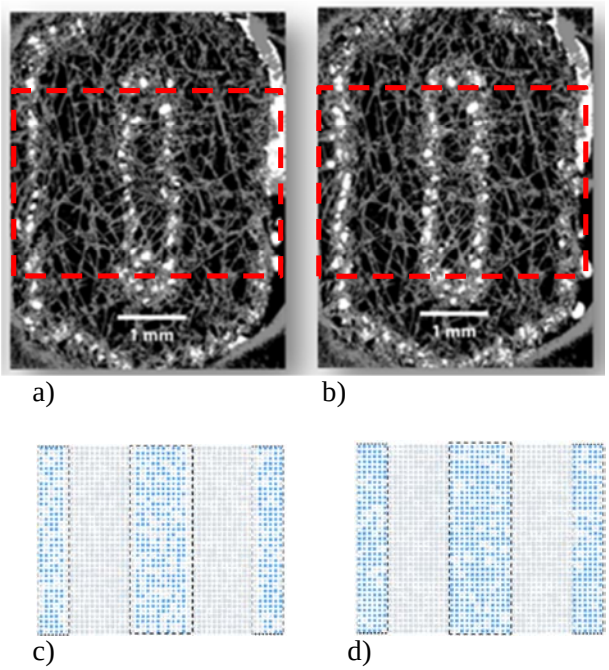

FIG.2. Horizontal slice through cathode GDL 24 BA: a) experimental liquid water distribution (in white) for the automotive condition, b) experimental liquid water distribution for the limiting current condition, c)liquid (in blue) distribution in slice #2 from CPNM simulation for automotive condition, d) liquid (in blue) distribution in slice #2 from CPNM simulation for limiting current condition. The dashed red frame in Fig.2a and Fig.2b corresponds to the CPNM computational domains shown in Figs 2c and 2d. The dashed black frames (Fig.2c and 2d) correspond to the ribs.

As can be seen from Fig. 2c and 2d and also from Fig.3, these two features are well reproduced by the CPNM simulations.

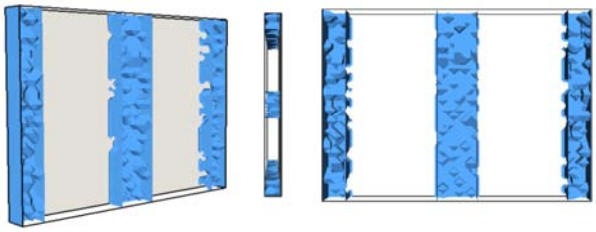

FIG.3. Representative 3D distribution of liquid water (in blue) as predicted by the CPNM simulations. The liquid water is confined in the region of the GDL located below the ribs. The distibution for the two conditions are quite similar. The in plane width of the liquid regions is actually slightly greater for the limiting current condition compared to the automotive conditions but this would be hardly discernable in this type of 3D image. This can be seen, however from Fig.2 (looking carefully at the lateral extent of central liquid region within the dashed black frame).

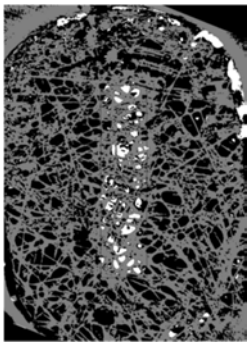

FIG. 4. Horizontal slice through cathode GDL 24 BC: liquid water distribution (in white) for the automotive condition.

A difference, however, is that liquid water appears mostly at the edge of the rib in the experiment whereas the liquid is present all over the regions below the ribs in the simulations. This difference remains to be explained but could be due to the simple cubic structure of our pore network. It is surmised that a more advanced pore network model directly built on 3D images of the real microstructure, as exemplified in ref. (31) for example for ex-situ liquid invasion simulations,

would capture this effect. Interestingly, similar experiments performed with SGL 24BC, i.e. with a MPL, leads to a distribution much closer to the PNM distribution as illustrated in Fig.4. As can be see, the liquid water is present in this case all over the region under the central rib as in the simulations and not only along the rib edge. It is surmised that the conditions imposed at the GDL inlet in the CPNM simulations are somewhat more representative of the conditions at a MPL /GDL interface than at a catalyst layer / GDL interface.

The saturation of the water is quantified in Fig. 5. The saturation is in plane averaged over slices corresponding to the regions shown in Fig.2. The catalyst layer is at relative thickness 0 whereas the rib is at relative thickness 100. Note that the GDL is compressed to about $\delta_c = 120$ μm in the rib area (the thickness of the uncompressed GDL is $\delta_0 = 190$ μm). Note however that the experimental evaluation is not fully trustful in the region close to the active layer up to a relative thickness of about 40 due to unevenness of the catalyst layer and blurring of the Platinum catalyst.

A first and crucial observation is that the saturation does not vary monotonously. There is a maximum at about 70% of the relative thickness. The CPNM simulations are in agreement with this feature, i.e. the existence of a maximum, as well as its position at 70% of the relative thickness. Also, it can be clearly seen that the overall saturation is greater at 1.5 A/cm^2 than at 0.9 A/cm^2. This feature is also well predicted by the CPNM. All these elements are in strong contrast with the PN simulation based on the classical IP algorithm (dotted lines with empty symbols in Fig.4) describing the capillary driven process of invasion in liquid phase from the catalyst (or MPL) – GDL interface. This is also illustrated in Fig. 6. Although used in many previous works, this algorithm leads to a monotonously decreasing profile markedly different from the experimental profiles. Also the IP profile is the same for both conditions, which is also a significant difference compared to the experiments.

Moreover, the general shape of CPNM profiles is robust to the exact distribution of the current density at the GDL inlet (as shown in Fig.5a, the shape is similar for the inverted distribution and the reference distribution *i(x)+*, see the appendix for the details on these distributions) as well as the impact of liquid saturation on GDL thermal conductivity (curve referred to as $\lambda(S)$ in Fig. 5b, see again the appendix).

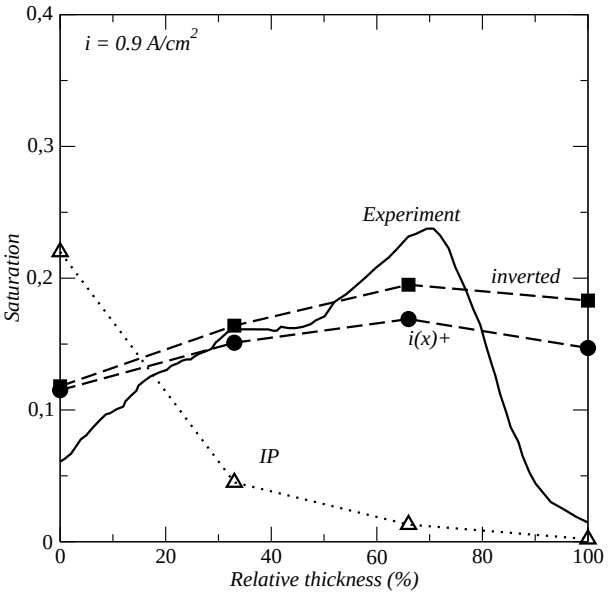

a)

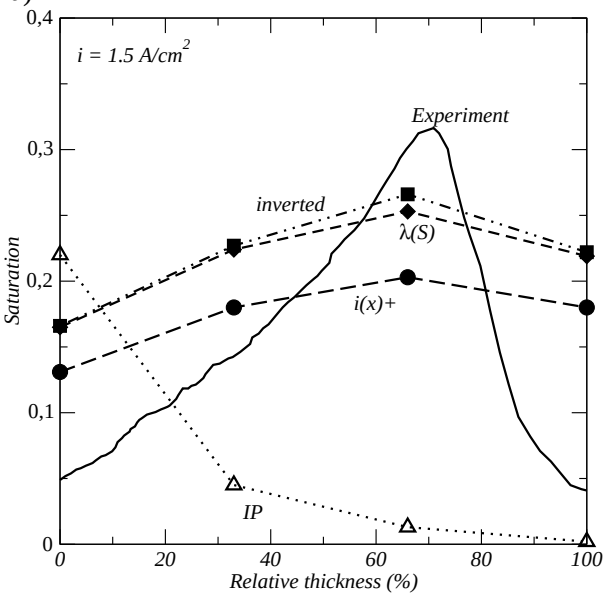

b)

FIG.5. Comparison between the experiments (black solid lines) and the CPNM simulations (curves with filled symbols). In plane slice average liquid saturation in the GDL for the automotive conditions (a) and the limiting current conditions (b). The curve labelled IP corresponds to the saturation profile obtained assuming invasion in liquid phase from the catalyst layer using the IP algorithm as in many previous works.

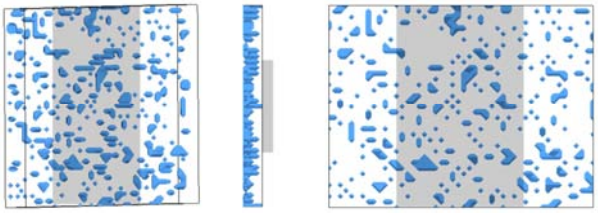

FIG.6. Liquid (in blue) distribution obtained using the standard IP algorithm. The grey area corresponds to the central RIB.

In summary, there is absolutely no doubt that liquid water can be present in the GDL during the operation of PEMFC, at least for sufficiently high current density and relative humidity in the channel. The exact mechanisms explaining the occurrence of liquid water within the GDL were somewhat an object of controversy. For instance, practically all the previous works using PNM were based on the assumption of capillary controlled invasion in liquid phase from the catalyst layer or the MPL. This is in complete contrast with the findings reported in the present article.

We have tested two pore network models aiming at predicting the liquid water distribution in the gas diffusion layers of PEMFC against in-situ distributions obtained using X ray tomographic microscopy. The comparison is unambiguously in favor of the CPNM considering the condensation scenario. According to this scenario, water would migrate from the catalyst layer to the GDL mainly in vapour phase. Then, for sufficiently high relative humidity in the oxygen (air) feeding channel, liquid water forms in the GDL as a result of condensation.

Determining the exact mechanisms leading to the occurrence of liquid water in the GDL is quite difficult from the X ray tomographic microscopy images alone. This is the combination of the images with the numerical simulations which permits to draw conclusions on the mechanisms at play.

The determination of the liquid water invasion mechanisms is crucial for improving the PEMFC technology, both as regards the performance (the polarization curve) and the aging issues.

Naturally, further works is needed to extent the approach to other components of the PEMFC, such as the catalyst layer or the microporous layer (MPL). This is still a difficult challenge, notably in terms of imaging, owing to the much smaller pores in these components compared to the GDL considered in the present study.

Also, mixed scenarios leading to the occurrence of liquid water both as a result of condensation and invasion in liquid phase from the catalyst layer or the MPL are not impossible (for example if condensation occurs in the MPL as well), especially at lower temperatures than considered in the present study.

The authors gratefully acknowledge the funding from the EU project IMPALA ("IMprove Pemfc with Advanced water management and gas diffusion Layers for Automotive application", project number: 303446) within the Fuel Cells and Hydrogen Joint Undertaking (FCHJU).

References

1. M.Eikerling, A.A.Kornyshev, A.R. Kucernak, *Physics Today*, 38-44, October 2006
2. B.Straubhaar, J. Pauchet, M. Prat, *International Journal of Hydrogen Energy*, 40 (35), 11668–11675 (2015)
3. P.K.Sinha, C.Y.Wang, *Electrochimica Acta*, 52:7936-45 (2007)
4. M.Rebai, M.Prat, *J. of Power Sources*, 192, 534-543 (2009)
5. K. J. Lee, J. H. Nam, and C. J. Kim, Pore-network analysis of two-phase water transport in gas diffusion layers of polymer electrolyte membrane fuel cells, *Electrochim. Acta* **54**, 1166-1176 (2009).
6. L.Ceballos, M.Prat, *J. of Power Sources* 195, 825–828 (2010)
7. J.Hinebaugh, Z. Fishman, A.Bazylak, *Journal of the Electrochemical Society*, 157, B1651-B1657 (2010)
8. K.J. Lee, J.H. Kang, J.H. Nam, CJ Kim, *Journal of Power Sources* 195 (11), 3508-3512 (2010).
9. G.Luo, Y. Ji, C.-Y. Wang, , P. K. Sinha, E*lectrochimica Acta* , 55, 5332-5341 (2010).
10. S. P. Kuttanikkad, M. Prat, J. Pauchet, *J. of Power Sources* 196, 1145–1155 (2011)
11. R.Wu, L.Qiang, Z.Xun, W.Hong, *International Journal of Heat and Mass Transfer*, 55, 2581-2589. (2012)
12. R.Wu, X.Zhu, Q. Liao, R. Chen, G.-M.Cui, *International Journal of Hydrogen Energy*, 38 (10), 4067–4078. (2013)
13. E.F.Medici, J.S. Allen, *International Journal of Heat and Mass Transfer*, 65, 779-788 (2013)

14. K.J. Lee, J.H. Kang, J.H. Nam, *International Journal of Hydrogen Energy* 39, 6646-6656 (2014).
15. M Fazeli, J Hinebaugh, A Bazylak, *Journal of The Electrochemical Society*, 162 (7) F661-F668 (2015)
16. C. Qin, *Journal of The Electrochemical Society*, 162 (9) F1036-F1046 (2015)
17. J.H. Nam, M. Kaviany, *Int. J. of Heat and Mass Transfer*, 46 4595-4611, (2003).
18. S.Basu, C.Y.Wang, K.S.Chen., *J Electroche Soc.* 156 (6): B748-B756 (2009)
19. D.A.Caulk, D.R. Baker, *Journal of The Electrochemical Society*, 157 (8) B1237-B1244 (2010)
20. D.A.Caulk, D.R. Baker, *Journal of The Electrochemical Society*, 158 (4) B384-B393 (2011)
21. A. Thomas, G. Maranzana, S. Didierjean, J. Dillet, O. Lottin, *Journal of The Electrochemical Society*, 160 (2) F191-F204 (2013)
22. A. Thomas, G. Maranzana, S. Didierjean, J. Dillet, O. Lottin, *International Journal of Hydrogen Energy*, 39(6):2649–2658, 2014.
23. H. Lin, T.-F. Cao, L. Chen, Y.-L. He, W.-Q. Tao, *Int. J. Hydrogen Energy* 37 (16) (2012) 11871–11886, (2012)
24. T.-F. Cao, Y.-T. Mu, J. Ding, H. Lin, Y.-L. He, W.-Q. Tao, *International Journal of Heat and Mass Transfer* 87, 544–556 (2015)
25. D.Wilkinson, J.F.Willemsen, *J. Phys. A: Math. Gen.*, 16, 3365–3376 (1983)
26. L. Ceballos, M. Prat, P. Duru , *Phys. Rev. E* 84, 056311 (2011)
27. Pending PSI reference in situ experiment
28. F. Marone and M. Stampanoni, *J. synchrotron radiat.*, 19, 1029 (2012)
29. J. Eller, T. Rosén, F. Marone, M. Stampanoni, A. Wokaun, F. N. Büchi, *J. Electrochem. Soc.*,158, B963 (2011).
30. J. Roth, J. Eller, F. Marone, F. N. Büchi, *J. Phys. Chem. C*, 117, 25991 (2013).
31. T.Agaesse, A. Lamibrac, F. N. Büchi, J.Pauchet, M. Prat, submitted to *Journal of Power Sources*

APPENDIX Condensation algorithm, Summary of PNM properties

Similarly as in most of our previous works[1-4], the pore network model (PNM) simulations are performed on a cubic network. This is a mesoscale approach in which the pore space is conceptualized as a network of pores connected by narrower passages of negligible volume corresponding to the constrictions of pore space. The pores are located on a cubic Cartesian mesh. The distance *a* between the centers of two adjacent pores on the mesh is uniform and called the lattice spacing. The analysis of images of SGL 24BA reported in ref.(5) indicates that the lattice spacing is different in the in-plane direction with approximately $a_{//} = 80\mu m$ from the lattice spacing in the through plane direction with approximately $a_{\perp} = 40\mu m$. We considered a cubic network with *a* = 80 μm in both the in-plane and through plane directions but we took into account the fact that the real lattice spacing is actually twice as small in the through plane direction by modifying the transport properties adequately (for example the through plane thermal conductivity was multiplied by a factor 2 so as to have the through plane network thermal conductance $\lambda_{\perp}/\delta$ identical to the GDL one). Based on the size of the domain occupied by the GDL in the experiment, this leads to represent the GDL by a $48\times37\times4$ pore network (the figures indicate the number of pores along the directions of a Cartesian grid).

A distinction is made between GDL compressed regions (GDL under a rib) and GDL uncompressed regions (GDL under a channel). Pore network specifications differ on the type of region (compressed or uncompressed). Experimental data[14] suggest that the GDL fibrous structure is anisotropic with narrower passages (constrictions also referred to as throats) between pores in the in-plane directions compared to the through plane direction with about a factor 2 between the average throat sizes in the in-plane and through plane directions respectively. To reflect this anisotropy, the through plane throat sizes were randomly distributed according to a uniform p.d.f. of mean $\bar{d}_{t\perp}$ = 43 μm, in the range [$d_{t\perp\min}$ - $d_{t\perp\max}$] with $d_{t\perp\min}$ = 32 μm $d_{t\perp\max}$ =54 μm whereas the in plane throat sizes were distributed according to a random distribution of mean $\bar{d}_{t//}$ = 21.5 μm, in the range [$d_{t//\min}$ - $d_{t//\max}$] with $d_{t//\min}$ = 16 μm $d_{t//\max}$ =27 μm.

Note that there is therefore no overlap between the in-plane and through plane throat size distributions.

It was further assumed that these data corresponds to the compressed GDL (regions under the ribs). The GDL was supposed not compressed below the channel assuming that this could be taken into account by considering that the throat size in the through plane direction was not significantly modified whereas the throat sizes in the in-plane directions were larger on average in the uncompressed regions by a factor $\sqrt{\delta_0/\delta_c}$. The volume of a pore is first simply computed from adjacent throat sizes as $V_p = (\max(d_t))^3$ where $\max(d_t)$ is the size of the largest throat to which the pore is connected. Then the pore volume are corrected, i.e. multiplied by a correction factor, so as to obtain the desired porosity in the considered region (ε_0 =74% in the uncompressed regions, ε_c = 59% in the compressed regions, not considering the porosity of the binder).

The CPNM algorithm for simulating the condensation process presents several distinguishing features compared to the PNM traditionally used to simulate scenario #1. It explicitly takes into account the temperature variations within the GDL as well as the water flow rate entering the GDL as the result of the electrochemical reaction. The details of the algorithm are presented in a previous work[1]. It can be summarized as follows. There are three main steps:

- the temperature field computation,
- the initial nucleation step,
- the growth step.

Temperature field computation

The temperature field $T_{i,j,k}$ is computed at each pore of network as an input field for the condensation simulation. This field is determined numerically by solving the steady state heat conduction problem,

$$\nabla.(\lambda.\nabla T) = 0. \qquad \text{(A1)}$$

using a classical finite volume technique taking into account the ribs, the channel and the GDL. The effective thermal conductivity tensor is strongly anisotropic[6], $\lambda^*_{\perp uc}$ = 0.25 $Wm^{-1}K^{-1}$ and $\lambda^*_{//uc}$=40 $Wm^{-1}K^{-1}$in the uncompressed region (subscript "uc").

Table A1. Impact of liquid water on GDL thermal conductivity.

	Thermal conductivity ($Wm^{-1}K^{-1}$)	Dry (S=0)	Fully wet (S=1)	κ
Solid phase[8] $\lambda^*_{\perp s}$ $\lambda^*_{// s}$	≈ 2.5 169.			
Liquid water	0.6			
air	0.027			
$\lambda^*_{\perp c}$		0.675	1.24 (Eq.A3)	2.5
$\lambda^*_{\perp uc}$		0.25	0.65 (Eq.A4)	2.5

The compression rate is $(\delta_0 - \delta_c)/\delta_0 = 37\%$. By analogy with electrical conductivity measurements[7], one obtains, $\lambda^*_{\perp c}$=2.7 ×0.25 = 0.675 $Wm^{-1}K^{-1}$ and $\lambda^*_{// c}$=1.66×40 = 66.4 $Wm^{-1}K^{-1}$ in the compressed regions (subscript "c"). The (isotropic) thermal conductivity in the channel is $\lambda_{chan.}$ = 0.027 W. $m^{-1}.K^{-1}$ (air) and λ_{bp} = 150 W. $m^{-1}.K^{-1}$ in the bipolar plate (RIB, plate where the channels are machined).

In one simulation, we took into account the fact that the GDL through plane thermal conductivity varies with liquid saturation[8]. An estimate of the impact of water content on through-plane thermal conductivity is proposed in ref. [8]:

$$\Lambda^*_{\perp}(S,\varepsilon) = \varepsilon S\kappa\lambda_{water} + (1-\varepsilon)\lambda_{s\perp} + (1-S)\varepsilon\lambda_{air} \quad \text{(A2)}$$

where κ =1.

As reported in ref.(8), Eq.(A2) underestimates the impact of liquid water on through plane thermal conductivity compared to experiments by approximately a factor 1.5. We have therefore introduced a coefficient κ to obtain values in the presence of liquid water consistent with the factor 1.5. Also, Eq.(A2) overestimates the estimate values for the dry material. Correcting this eventually leads to the following formula

$$\lambda^*_{\perp c}(S) = 0.675\frac{\Lambda^*_{\perp}(S,\varepsilon_c)}{\Lambda^*_{\perp}(0,\varepsilon_c)} \quad \text{(A3)}$$

$$\lambda^*_{\perp uc}(S) = 0.25\frac{\Lambda^*_{\perp}(S,\varepsilon_{uc})}{\Lambda^*_{\perp}(0,\varepsilon_{uc})} \quad \text{(A4)}$$

With κ = 2.5 Application of Eq.(A3) and (A4) leads to the values reported in Table A1. As can be seen the increase in the thermal conductivity due to the presence of water is significant.

For the in-plane conductivity, the impact of water is expected to be much less since the dry GDL in –plane conductivity is quite large compared to liquid water thermal conductivity. Therefore, it was assumed that the presence of liquid water can be neglected as regards the in-plane thermal conductivity.

The temperature field is computed at the beginning of simulation and is an input data for the PNM simulation when the impact of liquid water on thermal conductivity is not taken into account. By contrast, the temperature field must be computed after each invasion of a pore by liquid water when the impact of liquid water on thermal conductivity is taken into account

A uniform temperature $T = T_{ext}$ is imposed along the computational domain external boundaries (shown as solid red lines in Fig.1c). We took T_{ext} = 80°C as in the experiments. The electrochemical reaction is exothermic. The corresponding heat production per unit surface area ($W.m^{-2}$) can be expressed as,

$$\Phi = \left(\frac{h_{lv}}{2F} - U\right) i \quad \text{(A5)}$$

where h_{lv} is the enthalpy of reaction (h_{lv} = 242000 $J.mol^{-1}$). It can be reasonably assumed that half of the produced heat goes toward the anode and half toward the cathode GDL. Therefore, the boundary condition imposed at the GDL inlet (shown as a white dashed line in Fig.1c) for the heat transfer problem is

$$0.5\Phi = 0.5\left(\frac{h_{lv}}{2F} - U\right) i = -\lambda_{\perp}^{*} \frac{\partial T}{\partial z} \text{ at } z = 0. \qquad \text{(A6)}$$

where z is a Cartesian coordinate in the through-plane direction (z = 0 at the GDL / finer layer interface).

Spatial distribution of current density at GDL inlet

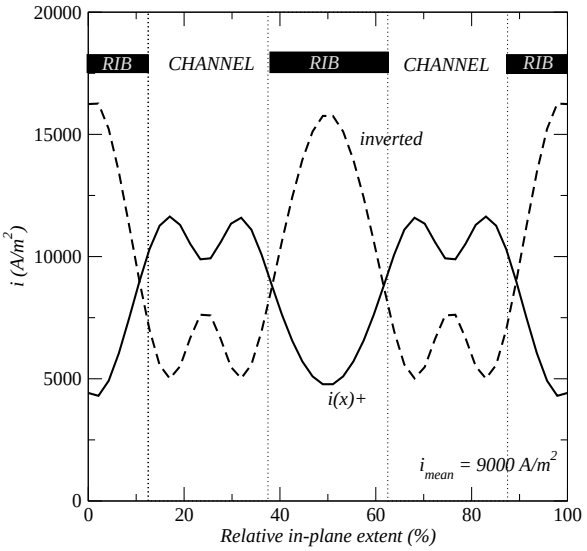

a)

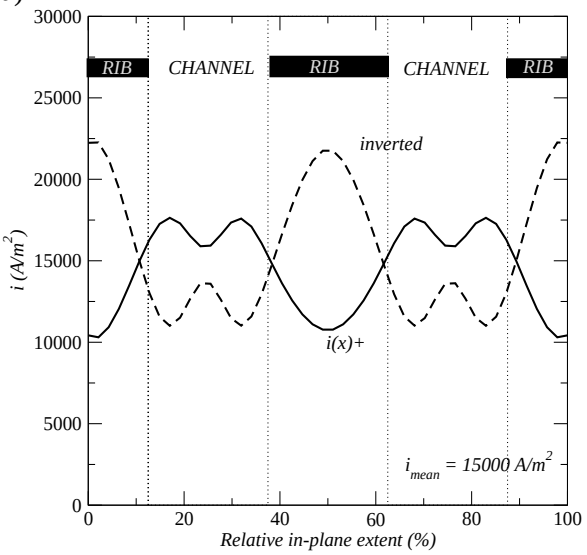

b)

FIG.A1. Current densities distributions at the GDL inlet used in the simulations.

Numerical simulations[9], as well as in situ measurements[10] indicate that the current density is not uniform at the inlet of the GDL. The distributions *i(x)+* shown in Fig.A1 and used in the simulations were deduced from the experimental data reported in ref. (10) for a wet GDL. As can be seen, the current density is minimum under the ribs and maximum in front of the channels. We have also tested distributions, referred to as "inverted", where the positions of the extrema are inverted (minima under the channel and maxima under the ribs), supposedly more representative of a dry GDL.

Nucleation step

The nucleation step begins with the computation of the water vapour molar fraction field within the network assuming that the transport of water vapour in the GDL can be modeled using Fick's law.

The pore network properties should be also specified so that the diffusion transport of the water vapour in the network is consistent with the effective diffusion coefficients $D_{\perp}^{*}$ and $D_{//}^{*}$ of the GDL in the through plane and in plane directions. In spite of narrower passages in the in-plane directions, the effective diffusion coefficient in this direction is greater than the effective diffusion coefficient in the through plane direction by at least a factor 2[11,12] because of a greater tortuosity effect. We took $D_{\perp c}^{*} / D = 0.25$ and $D_{//c}^{*} / D = 0.5$ respectively where D is the diffusion coefficient in a free gas. This was for the compressed region (subscript "c"). In the uncompressed region (subscript "uc" the in –plane coefficient $D_{//uc}^{*}$ was modified using the model proposed in ref.(13), i.e. $\frac{D_{//uc}^{*}}{D_{//}^{*}} = \frac{\varepsilon_0}{\varepsilon_c}\left(\frac{\varepsilon_0 - 0.11}{\varepsilon_c - 0.11}\right)^{0.521} \approx 1.4$. It was assumed that the trough plane coefficient was not significantly affected by the compression.

Expressed in terms of computation on a pore network[14], the vapour diffusion flux between two nodes (pores) *i* and *j* of network is expressed as

$$N_v = g_{ij}(x_{v,j} - x_{v,i}) \qquad \text{(A7)}$$

where x_v is the mole fraction of water vapour and g_{ij} is the diffusive conductivity of the throat connecting the two pores. In the traditional pore network approach[14], the conductivity is expressed as a function of the throat size and therefore varies from

one throat to the other owing to the randomness in the throat size. Here we use a variant, referred to as a mixed pore network model[15], in which the conductivity is directly related to the macroscopic parameters $D_{\perp}^{*}$ and $D_{//}^{*}$. This amounts to specifying the conductivity as indicated in Table 2. This ensures that the CPNM has the correct diffusion properties.

Table A2. Diffusive conductivities in the network. $a_{\perp} = 40\mu m$, $a_{//} = 80\mu m$, $a = a_{//} = 80\mu m$.

Region	direction	
Compressed	Through-plane	$g_{\perp c} = \frac{c a_{//}^2 D_{\perp}^{*}}{a_{\perp}}$
	In-plane	$g_{//c} = c a_{\perp} D_{//}^{*}$
Uncompressed	Through-plane	$g_{\perp uc} = c a_{//}^2 \frac{D_{\perp}^{*}}{a_{\perp}} \frac{\delta_c}{\delta_0}$
	In-plane	$g_{//uc} = 1.4 c a_{\perp} \frac{\delta_0}{\delta_c} D_{//c}^{*}$

In Table A2, c is the mole concentration of the gas phase: $c \approx \frac{P}{RT_{ext}}$ where R is the ideal gas constant and P is gas phase total pressure (P = 1.5 bar); P is supposed uniform and constant over the computational domain. The species conservation equation at each network node is expressed as:

$$\sum_{j=1}^{n} g_{ij}(x_{v,j} - x_{v,i}) = 0. \qquad \text{(A8)}$$

where n is the number of neighbors to considered pore i; $n = 6$ for our cubic network.

Boundary conditions must be specified in order to solve numerically the system given by Eq.(A8). The relative humidity RH_{ch} is imposed in the channel taking as reference saturation vapour pressure p_{vs} the pressure at temperature T_{ext} = 80°C. Thus $x_{vch} = RH_{ch} p_{vs}(T_{ext}) / P$ along the GDL - channel interface. A zero flux condition is imposed at the rib – GDL interface and on the lateral sides of the computational domain. At the GDL inlet (finer layer – GDL interface), the vapour flow rate per unit surface area is imposed using Eq.(A9).

$$q = \alpha \frac{i}{2F} \qquad \text{(A9)}$$

where F is the Faraday's constant (F = *96485.34 C*) Actually not all the water produced at the cathode goes to the GDL. This is taken into account through the partition coefficient α. We took α = 0.8 for all the simulations presented in what follows (we have checked that varying α in the range [0.7 -1] did not change the main features of simulated liquid distributions).

The numerical solution to Eq.(A8) with the associated boundary conditions gives x_v at each node of network, and therefore the vapour partial pressure at each node of network: $p_{vi,j,k} = x_{vi,j,k} P$. We then compute the local relative humidity at each node of network as $RH_{i,j,k} = p_{vi,j,k} / p_{vs}(T(i,j,k))$.

No condensation occurs when $RH_{i,j,k} < 1$ in each node of network, which means that all the water coming from the active layer can be transported in vapour phase across the GDL. Condensation occurs when $RH_{i,j,k} \geq 1$ at least at one node in the network. It often happens that the condensation criterion is met not in a single node but at several nodes in the network. We then proceed step by step considering first only one first condensation node, the one corresponding to $\max(RH_{i,j,k}, RH_{i,j,k} \geq 1)$. At this node, we impose $RH_{i,j,k} = 1$, or more exactly the mole fraction x_v corresponding to $RH_{i,j,k} = 1$. The problem expressed by Eq. (A8) is solved again taking into account the new boundary condition $RH_{i,j,k} = 1$ at the first condensation node. This gives a new field $RH_{i,j,k}$ and we check whether new nodes are such that $RH_{i,j,k} \geq 1$. If yes we repeat this procedure until all the condensation nodes have been identified.

This gives the initial distribution of liquid nodes for the growth step.

Growth step

For simplicity, each liquid node identified at the end of nucleation step is assumed fully saturated by liquid. If two of such liquid nodes are first neighbours, they belong to the same cluster. Thus, a first step consists in identifying all the liquid clusters

formed at the end of nucleation step, where a cluster is defined as a group of connected liquid pores. Starting from this initial distribution of liquid clusters, the growth step is performed using the following algorithm:

1. Determine and label the different water clusters. If two pores – totally or partially saturated in liquid water – are adjacent, they belong to the same cluster.
2. Compute the vapour molar fraction field x_v from the solution of the system represented by Eq.(A8). In each liquid pore (of coordinates x_i,y_i,z_i) in contact with a gas node, the local saturation pressure is imposed. Hence $x_v = p_{vs} / P$, where $p_{vs} = p_{vs}(T(x_i, y_j, z_k))$. The boundary conditions on the sides of computational domain are the same as the ones previously presented.
3. If the vapour partial pressure computed in step 2 is greater than the local vapour saturation pressure in some gaseous pores, then identify the pore among those pores corresponding to $\max(RH_{i,j,k}, RH_{i,j,k} \geq 1)$ and impose $x_v = p_{vs}(T(x_i, y_j, z_k)) / P$ in the corresponding pore.
4. Go back to #2 and repeat steps #2 and #3 until there is no gaseous pore anymore such that $RH_{i,j,k} > 1$.
5. Compute the molar condensation rate F_k at the boundary of each liquid cluster.
6. Apply the invasion percolation rule at each cluster, i.e. determine the throat of larger diameter along the boundary of each liquid cluster.
7. Compute the invasion time t_k of each cluster k, i.e. the time required to fully invade the pore adjacent to the throat determined in #6: $t_k = c_\ell V_{adk} / F_k$, where V_{adk} is the volume remaining to invade in the considered pore, c_ℓ is the mole concentration of liquid water.
8. Compute the time step $dt = min(t_k)$
9. Fully invade the pore corresponding to dt and update the volume of liquid in the invaded pore in the other clusters.
10. Go back to #1 and repeat the different steps 1-9 until a steady-state solution is reached, i.e. the overall phase-change rate becomes nil.

References (Appendix)

1. B.Straubhaar, J. Pauchet, M. Prat, *International Journal of Hydrogen Energy,* 40 (35), 11668–11675 (2015)
2. M.Rebai, M.Prat, *J. of Power Sources,* 192, 534-543 (2009)
3. L.Ceballos, M.Prat, *J. of Power Sources* 195, 825–828 (2010)
4. L. Ceballos, M. Prat, and P. Duru , *Phys. Rev. E* 84, 056311 (2011)
5. A. Lamibrac, J. Roth, M. Toulec, F. Marone, M.Stampanoni, F.N. Büchi, submitted to the *Journal of the Electrochemical Society*
6. N.Zamel, X. Li, *Progress in Energy and Combustion Science* 39, 111-146 (2013)
7. N.Belgacem, Ph.D thesis, University of Toulouse, France (2016)
8. O. S. Burheim, J. G. Pharoah, H. Lampert, P. J. S. Vie, and S. Kjelstrup, *Journal of Fuel Cell Science and Technology*, 8, 021013 (2011).
9. F.Nandjou, Ph.D thesis, Grenoble Alpes University, France (2015).
10. S.Rachidi, Ph.D thesis, University of Poitiers, France (2011)
11. T.-F. Cao, Y.-T. Mu, J. Ding, H. Lin, Y.-L. He, W.-Q. Tao, International Journal of Heat and Mass Transfer 87 (2015) 544–556
12. P.A. Garcia-Salaberri, G.Hwang, M.Vera, A.Z.Weber and J.T. Gostick, *International Journal of Heat and Mass Transfer* 80 319-333 (2015)
13. M.M. Tomadakis, S.V. Sotirchos, AIChE J. 39, 397–412 (1993)
14. J.T. Gostick, M.A. Ioannidis, M.W. Fowler, M.D. Pritzker, *J. Power Sources* 173, 277–290 (2007)
15. L.Mottet, T.Coquard, M.Prat, *Int. J. of Heat and Mass Tr.*, vol. 83, 636-651 (2015)

6.3 Conclusion

We showed that the CPNM qualitatively foresees the saturation profiles i.e a maximum of saturation obtained around 70% of the relative thickness - whereas the IP model is totally unable to predict it. The combination of X-ray micro CT images with numerical simulations allow to understand the mechanisms of condensation process: water would migrate from the Active Layer into the GDL mainly in vapour phase, and would change into water for a sufficiently high relative humidity in the air in the supply channel.

Chapter 7

Conclusion and prospects

Contents

Water in PEMFC is a crucial aspect of the current PEMFC technology. A better understanding of the water formation and transfer in the various components of the fuel cell is required for both improving the fuel cell performances and better control the ageing problem, a related key aspect of the technology.

In this thesis, we focused on the water issue in GDL on the cathode side at the rib – channel scale. To this end, we developed a pore network model enabling us to simulate the formation of water by condensation within the GDL. This pore network model was validated against experiments in micromodel and led to results in quite good agreement (compared with previous pore network models) with X ray tomography data obtained by partner PSI within the framework of European project IMPALA. Perhaps, the most important result from our work is to show and confirm that the water management cannot be decoupled from the heat management since the water formation in the GDL is strongly dependent on the temperature field within the GDL. In terms of mechanisms, this work emphasizes the condensation process as a major mechanism of water formation in the cathode GDL. On the whole, the condensation pore network model leads to much more satisfactory results that the previous attempts based on the assumption of capillary controlled invasion in liquid phase from the MPL or the catalyst layer. This opens up the route toward the numerical optimization of GDL microstructure, an objective only achievable if the mechanisms at play in a fuel cell are sufficiently well understood.

However, the simulations at the rib–channel scales must still be improved before being in a position to really perform studies aiming at improving the design of GDL or more generally better control the ageing problem. One must develop a model coupling the pore network model of the GDL to models describing the transfers and the other phenomena of importance (electrochemical reactions, mechanical deformations, etc) in the other components of the cell. To just mention one issue, oxygen transfer was not considered in our simulations since the current density distribution at the GDL inlet was an input in the simulations and not a result of the computation. Predicting the current density distribution is of course desirable. Such a modeling coupling the components should be extended so as to take into account not only the cathode but the anode and the membrane as well. Such a coupled modeling approach could permit to fully clarify the water transfer mechanisms. This work puts a strong emphasis on the condensation process with the assumption that the water enters the GDL essentially in vapour form. Although there is no doubt in our opinion that condensation is a major mechanism, the situation is probably subtler than considered in the present work. For instance, it is likely that condensation can

also occur in the MPL, leading to a possible mixed scenario combining condensation in the GDL (GDL support) and invasion in liquid phase from the MPL. Clarification on what happens in this respect in the catalyst layer is also needed since this is the place where water is produced.

Appendix A

CPNM: additional information

This appendix gives a few details on the "Pore Network Model" code that has been developed to try to answer the water question in the gas diffusion layers of PEM fuel cells. As mentioned before, a PNM code is based on a representation of the porous medium as a network of pores and bonds. This model can be used in both two and three dimensions. The pore network developed is regular. Each pore has an equal number of neighbours, namely four neighbours in 2D and six neighbours in 3D. The variables that were used, the code structure, and the solved equations are explained below.

A.1 Nomenclature

The variables used in the simulation code are the following.

At the porous medium scale, the fluid saturation S_f in a porous volume is the ratio of the volume occupied by the fluid f in the pore space to the total volume of the pore space:

$$S_f = \frac{V_f}{V - V_s} \tag{A.1}$$

where V is the total volume of the porous medium, V_s is the solid phase volume in V and V_f is the volume of fluid f in V.

Similarly at the pore scale, the fluid saturation S_f in a pore is defined by:

$$S_f = \frac{V_f}{V} \tag{A.2}$$

where V is the total volume of the considered pore and V_f the volume of fluid f contained in V.

A.2 Organization of the code

Before running a simulation it is necessary to specify the input parameters. They are located in several text files:

- A file containing the structure of the pore network: the dimension number (2 or 3), the number of pores in each direction, the presence or not of ribs and their position, le lattice spacing and the presence of periodical boundary conditions.
- A file containing the pore and throat size distribution together with their probability distribution.
- A file containing the parameters of the fluids such as the density, the viscosity, the contact angle, the temperature, the injection flow and the relative humidity in the channel.

- A file containing the initial conditions such as the invaded pores at the initial step.
- A file containing the boundary conditions.
- A file containing the thermal data such as the thermal initial and boundary conditions, the conductivities of the materials, the thermal anisotropy or the type of mean used at the interface between two regions having different thermal properties.
- A file containing the numerical parameters of calculation such as the type of physics (heat transfer, diffusive transfer, etc) or the number of time steps.

A.3 Features

This code is organized with a main routine calling several subroutines doing actions. These actions can be:

A.3.1 Computation of transport equations

A major feature of the code is its ability to compute physical fields like the liquid pressure field or the vapour partial pressure field. The discretization is discussed in what follows.

Convection

To compute the liquid pressure field, the mass conservation is expressed at each pore:

$$\sum_{j=1}^{N} g_{h,ij}(p_j - p_i) = 0 \tag{A.3}$$

Where i is the current pore, j refers to the neighbouring pores, N is the number of neighbours, q_i is the flow between pore i and pore j, $g_{h,ij}$ is the hydraulic conductivity, p_i and p_j are the liquid pressures in pore i and pores j. Assuming a Poiseuille flow in each throat, the hydraulic conductivity is expressed as:

$$g_{h,ij} = \frac{2.28 d_{th,ij}^4}{2 l_{th,ij} \mu} \tag{A.4}$$

with $d_{th,ij}$ the diameter of the throat between pore i and pore j, $l_{th,ij}$ the length of the throat between pore i and pore j and μ the fluid viscosity.

NB: Notice that the hydraulic conductivity is only specified in the throat and not in the pores assuming negligible pressure drops in the pores.

Equation (A.4) is set up for each pore in the network yielding in a system of linear equations that can be solved with the proper boundary pressures on each side of the network.

Diffusion

In the same way, vapour transport by diffusion can be computed. The mass conservation is expressed as:

$$\sum_{j=1}^{N} g_{d,ij}(p_{v,j} - p_{v,i}) = 0 \tag{A.5}$$

with i is the current pore, j refers to the neighbouring pores, N is the number of neighbours, q_i is the vapour flow between pore i and pore j, $g_{h,ij}$ is the throat conductivity, $p_{v,i}$ and $p_{v,j}$ are the vapour pressures in each pore. The conductivity can be expressed as:

$$g_{d,ij} = \frac{c D_{w/a} d_{th,ij}^2}{l_{th,ij}} \tag{A.6}$$

with $d_{th,ij}$ the diameter of the throat between pore i and pore j, $l_{th,ij}$ the length of the throat between pore i and pore j, c the mole concentration: $c = \frac{p}{RT}$ where p is the local gas pressure (in Pa, R is the gas constant (= 8.31 J/K/mol) and T is the local gas temperature (in K) and $D_{w/a}$ is the water vapour diffusion coefficient in air.

Solving (A.5) yields the vapour partial pressure field, i.e. the vapour partial pressure in each pore of the network occupied by gas phase.

PETSc

The linear systems resulting from (A.3) or (A.5) are solved using PETSc. PETSc stands for Portable, Extensible Toolkit for Scientific Computation and is a suite of data structures and routines developed by Argonne National Laboratory for the scalable (parallel) solution of scientific applications modelled by partial differential equations (http://www.mcs.anl.gov/petsc/). Several linear solvers are available from PETSc:

- Preconditioners → Ex: Jacobi, successive over-relaxation (SOR), additive Schwarz method, ILU method, etc.
- Direct solvers → Ex: LU, Cholesky, QR methods, etc.
- Krylov methods → Ex: Richardson, Chebyshev, conjugate gradients, GMRES, bi conjugate-gradients, etc.

As far as we are concerned, we used a ILU preconditioner together with a bi conjugate-gradient method.

A.3.2 Computation of effective permeability

The permeability of the porous medium can be seen as the response of this medium to a flowing fluid. In 3D, the permeability is actually a tensor of permeability. The code can easily compute the permeability: a pressure gradient $P_{in} - P_{out}$ has to be set in the wanted direction and then it computes the resulting flow Q with a network approach, then, doing an analogy with Darcy's law, we have:

$$Q = \frac{K_{ii} A}{\mu L}(P_{in} - P_{out}), \tag{A.7}$$

where A is the area of the network normal to the flow direction, μ is the fluid viscosity and L is the length of the network in the flow direction. Knowing Q from the PNM simulations, the desired permeability coefficient K_{ii} can be easily determined from (A.7).

A.3.3 Invasion Percolation or IP

As discussed in Chapter 2, the two-phase flow regime in a GDL is expected to be a capillary fingering regime. This regime can be simulated on a network using the Invasion Percolation(IP) algorithm [Wilkinson and Willemsen, 1983]. The algorithm can be summarized as follows:

1. Initial state. Suppose for instance the network empty with liquid injection from one side of the network.
2. Determine the throat connected to the liquid phase of largest diameter (it corresponds to the throat of lowest capillary pressure threshold).
3. Invade the throat determined in step #2 and its adjacent "gas" pore.
4. Go back to step #2 until a desired saturation is obtained or until breakthrough.

A.3.4 Condensation

This part corresponds to the main novelty of the thesis. This will be discussed in the "Algorithm part".

A.3.5 Other features

Hoshen-Kopelman algorithm for cluster labelling

Regarding to the water management issue, computations of condensation in pore network models require identifying water cluster in the network. The Hoshen-Kopelman algorithm is a simple algorithm for labelling cluster on a grid. It was originally proposed in 1976 by J. Hoshen and R. Kopelman [Hoshen and Kopelman, 1976]. The grid is made of cells and represents our regular pore network. Each cell can be either "occupied" or "unoccupied". In our case, "occupied" means "full of water" and "unoccupied" means "full of gas or partially filled with gas". NB: if a pore is not completely full of water it will not have the label "occupied". The general idea of this algorithm is based on a raster scan of the grid looking for occupied cells. Each occupied cell is assigned a label corresponding to the cluster to which the cell belongs.

It is necessary to use the well-known union-find functions based on equivalence classes. After the first scan, two neighbouring pores may not have the same label but belong to she same cluster: they belong to the same equivalence class. For a $M \times N$ grid there is a maximum of $M \times N$ equivalent classes. If a link between two clusters has to be made, a union relation is created between these two labels. A second step consists in spanning the lattice a second time and and finding and updating the cluster labels (to ensure each cluster is represented by only one label).

The implementation in two dimensions is explained in details as follows. The **first step** consists in spanning the lattice once and each time an occupied cell is found, the top and left neighbours of the current cell are checked. There are four possibilities:

- Both cells are empty: a new cluster label is created and given to the current cell
- Only one cell is occupied: the cluster label of the occupied cell is given to the current cell
- Both cells are occupied and have the same cluster label: this label is given to the current cell
- Both cells are occupied but have distinct cluster labels. The smallest label is given to the current cell. The union between the two cluster labels is added as a new entry of a table, where the key is defined as the largest label of the two labels and the corresponding value is the smallest one. If the key already exists, the find function has to be used: when a value is equal to its key's label, it means the cluster being represented by this key is not linked to any other cluster. For instance, a label of type L(n) = n is called a good label whereas L(n) = m is a bad label. The goal of the find function is to determine which label is the smallest good label for each cluster.

For this, we use the find function: given a bad cluster, we go recursively through each union in the table (of the type L(n) = m) until the key is equal to the value meaning this is the smallest good label the current label is linked to.

The **second step** consists in scanning the lattice a second time and applying the find function to the cluster label for each occupied cell. Thus each cluster is now represented by only one cluster label, which is the smallest good label. This is illustrated in Fig A.1.

A.3.6 Thermal study

Temperature field

The code can compute the temperature field from the heat conduction equation. It is coded for steady state. The heat conduction equation is:

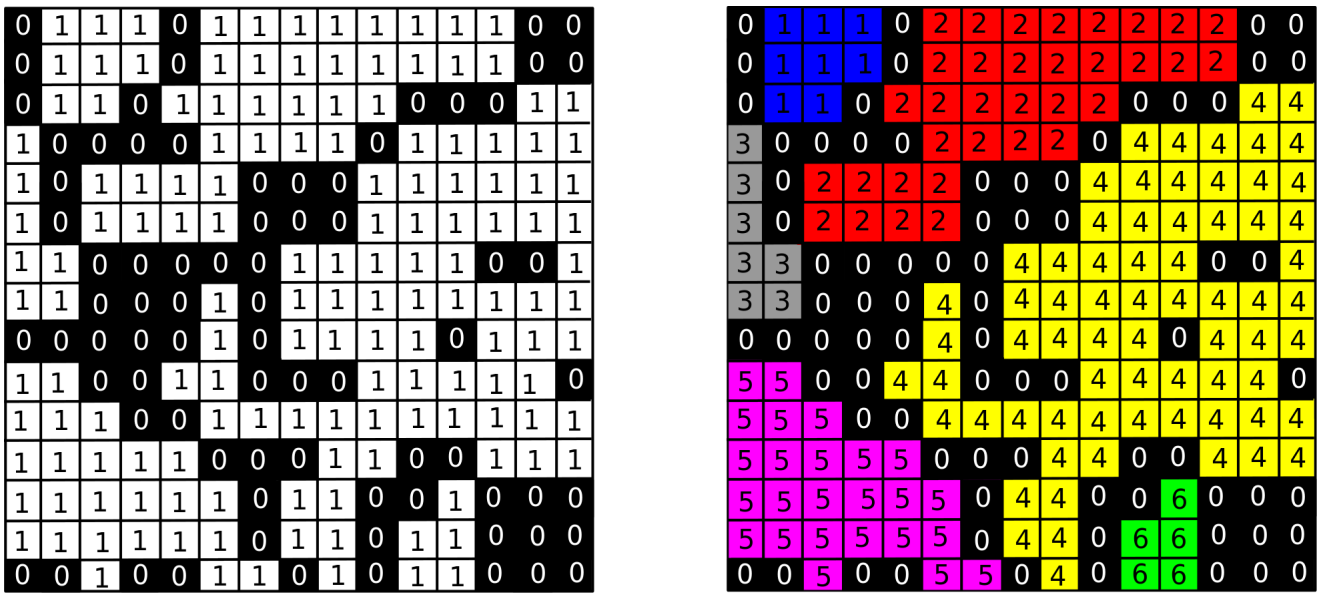

Figure A.1: a) Label 1 represents occupied cells whereas Label 0 is for unoccupied cells; b) All the clusters are labelled after applying the Hoshen-Kopelman algorithm

$$\rho c_p \frac{\partial T}{\partial t} = \nabla.(\lambda \nabla T) \tag{A.8}$$

where ρ, c_p and λ are respectively the mass density, the specific heat capacity and the thermal conductivity of the material.

At the steady state, (A.8) becomes simply:

$$\nabla.(\lambda \nabla T) = 0 \tag{A.9}$$

(A.9) is solved using a finite volume method.

At the interface between two materials it is possible to choose two kinds of mean for the thermal conductivity. If λ_1 and λ_2 are the conductivity respectively of material 1 and material 2:

- Arithmetic mean: $\lambda_{eq} = \frac{\lambda_1+\lambda_2}{2}$
- Harmonic mean: $\lambda_{eq} = \frac{2\lambda_1\lambda_2}{\lambda_1+\lambda_2}$

Bibliography

Rapport final de synthèse du projet pan'h 2006 chameau. Technical report, 2010.

Collaboration ADEME, AFHYPAC, Air Liquide et GDF Suez pour La Recherche. Number 481. November 2013.

R. Alink and D. Gerteisen. Modeling the Liquid Water Transport in the Gas Diffusion Layer for Polymer Electrolyte Membrane Fuel Cells Using a Water Path Network. *Energies*, 6(9): 4508–4530, Sept. 2013.

F. Barbir. *PEM fuel cells: theory and practice*. Academic Press, 2012.

A. Bazylak. Liquid water visualization in PEM fuel cells: A review. *International Journal of Hydrogen Energy*, 34(9):3845–3857, May 2009.

A. Bazylak, V. Berejnov, B. Markicevic, D. Sinton, and N. Djilali. Numerical and microfluidic pore networks: Towards designs for directed water transport in GDLs. *Electrochimica Acta*, 53:7630–7637, 2008. ISSN 00134686.

R. B. Bird, W. E. Stewart, and E. N. Lightfoot. Transport phenomena. 2nd. *New York*, 2002.

M. J. Blunt. Flow in porous media—pore-network models and multiphase flow. *Current opinion in colloid & interface science*, 6(3):197–207, 2001.

M. J. Blunt, M. D. Jackson, M. Piri, and P. H. Valvatne. Detailed physics, predictive capabilities and macroscopic consequences for pore-network models of multiphase flow. *Advances in Water Resources*, 25(8):1069–1089, 2002.

R. Borup, J. Meyers, B. Pivovar, Y. S. Kim, R. Mukundan, N. Garland, D. Myers, M. Wilson, F. Garzon, D. Wood, P. Zelenay, K. More, K. Stroh, T. Zawodzinski, J. Boncella, J. E. McGrath, M. Inaba, K. Miyatake, M. Hori, K. Ota, Z. Ogumi, S. Miyata, A. Nishikata, Z. Siroma, Y. Uchimoto, K. Yasuda, K.-i. Kimijima, and N. Iwashita. Scientific Aspects of Polymer Electrolyte Fuel Cell Durability and Degradation. *Chemical Reviews*, 107(10):3904–3951, 2007.

S. L. Bryant, P. R. King, and D. W. Mellor. Network model evaluation of permeability and spatial correlation in a real random sphere packing. *Transport in Porous Media*, 11(1):53–70, 1993.

M. Carmo, V. Paganin, J. Rosolen, and E. Gonzalez. Alternative supports for the preparation of catalysts for low-temperature fuel cells: the use of carbon nanotubes. *Journal of Power Sources*, 142(1-2):169–176, 2005.

L. Ceballos. *Caractérisation des propriétés fluidiques des couches de diffusion des piles à combustible PEMFC par une approche numérique de type réseaux de pores et par une analyse d'images issues de la tomographie X*. PhD thesis, 2011.

L. Ceballos and M. Prat. Invasion percolation with inlet multiple injections and the water management problem in proton exchange membrane fuel cells. *Journal of Power Sources*, 195(3): 825–828, 2010.

L. Ceballos and M. Prat. Slow invasion of a fluid from multiple inlet sources in a thin porous layer: Influence of trapping and wettability. *Physical Review E*, 87(4), 2013. ISSN 1539-3755, 1550-2376.

L. Ceballos, M. Prat, and P. Duru. Slow invasion of a nonwetting fluid from multiple inlet sources in a thin porous layer. *Physical Review E*, 84(5), 2011.

O. Chapuis, M. Prat, M. Quintard, E. Chane-Kane, O. Guillot, and N. Mayer. Two-phase flow and evaporation in model fibrous media. *Journal of Power Sources*, 178(1):258–268, 2008.

J. Chen, T. Matsuura, and M. Hori. Novel gas diffusion layer with water management function for PEMFC. *Journal of Power Sources*, 131(1-2):155–161, 2004.

P. Cheung, J. D. Fairweather, and D. T. Schwartz. Characterization of internal wetting in polymer electrolyte membrane gas diffusion layers. *Journal of Power Sources*, 187(2):487–492, 2009.

E. Cho, U.-S. Jeon, H. Ha, S.-A. Hong, and I.-H. Oh. Characteristics of composite bipolar plates for polymer electrolyte membrane fuel cells. *Journal of Power Sources*, 125(2):178–182, 2004.

H. Chraïbi, M. Prat, and O. Chapuis. Influence of contact angle on slow evaporation in two-dimensional porous media. *Physical Review E*, 79(2), 2009.

J. H. Chun, K. T. Park, D. H. Jo, J. Y. Lee, S. G. Kim, E. S. Lee, J.-Y. Jyoung, and S. H. Kim. Determination of the pore size distribution of micro porous layer in PEMFC using pore forming agents under various drying conditions. *International Journal of Hydrogen Energy*, 35(20): 11148–11153, 2010.

A. Collier, H. Wang, X. Ziyuan, J. Zhang, and D. Wilkinson. Degradation of polymer electrolyte membranes. *International Journal of Hydrogen Energy*, 31(13):1838–1854, 2006.

C. Darras, M. Muselli, P. Poggi, C. Voyant, J.-C. Hoguet, and F. Montignac. PV output power fluctuations smoothing: The MYRTE platform experience. *International Journal of Hydrogen Energy*, 37(19):14015–14025, 2012.

J. Eller, T. Rosén, F. Marone, M. Stampanoni, A. Wokaun, and F. N. Büchi. Progress in in situ X-ray tomographic microscopy of liquid water in gas diffusion layers of PEFC. *Journal of The Electrochemical Society*, 158(8):B963–B970, 2011.

R. P. Ewing and B. Berkowitz. Stochastic pore-scale growth models of dnapl migration in porous media. *Advances in water resources*, 24(3):309–323, 2001.

J. D. Fairweather, P. Cheung, and D. T. Schwartz. The effects of wetproofing on the capillary properties of proton exchange membrane fuel cell gas diffusion layers. *Journal of Power Sources*, 195(3):787–793, 2010.

I. Fatt et al. The network model of porous media. 1956.

M. Fazeli, J. Hinebaugh, and A. Bazylak. Investigating Inlet Condition Effects on PEMFC GDL Liquid Water Transport through Pore Network Modeling. *Journal of The Electrochemical Society*, 162(7):F661–F668, 2015.

R. Flückiger, F. Marone, M. Stampanoni, A. Wokaun, and F. N. Büchi. Investigation of liquid water in gas diffusion layers of polymer electrolyte fuel cells using X-ray tomographic microscopy. *Electrochimica Acta*, 56(5):2254–2262, 2011.

O. Gharbi and M. J. Blunt. The impact of wettability and connectivity on relative permeability in carbonates: A pore network modeling analysis: WATERFLOOD RELATIVE PERMEABILITY CARBONATES. *Water Resources Research*, 48(12):n/a–n/a, 2012.

J. T. Gostick. *Multiphase Mass Transfer and Capillary Properties of Gas Diffusion Layers for Polymer Electrolyte Membrane Fuel Cells*. PhD thesis, 2008.

J. T. Gostick. Random Pore Network Modeling of Fibrous PEMFC Gas Diffusion Media Using Voronoi and Delaunay Tessellations. *Journal of The Electrochemical Society*, 160(8):F731–F743, 2013.

J. T. Gostick, M. W. Fowler, M. A. Ioannidis, M. D. Pritzker, Y. Volfkovich, and A. Sakars. Capillary pressure and hydrophilic porosity in gas diffusion layers for polymer electrolyte fuel cells. *Journal of Power Sources*, 156(2):375–387, 2006.

J. T. Gostick, M. A. Ioannidis, M. W. Fowler, and M. D. Pritzker. Pore network modeling of fibrous gas diffusion layers for polymer electrolyte membrane fuel cells. *Journal of Power Sources*, 173 (1):277–290, 2007.

C. Hartnig, I. Manke, N. Kardjilov, A. Hilger, M. Grünerbel, J. Kaczerowski, J. Banhart, and W. Lehnert. Combined neutron radiography and locally resolved current density measurements of operating pem fuel cells. *Journal of Power Sources*, 176(2):452–459, 2008.

C. Hartnig, I. Manke, R. Kuhn, S. Kleinau, J. Goebbels, and J. Banhart. High-resolution in-plane investigation of the water evolution and transport in pem fuel cells. *Journal of Power Sources*, 188(2):468–474, 2009.

J. Hinebaugh and A. Bazylak. Condensation in PEM Fuel Cell Gas Diffusion Layers: A Pore Network Modeling Approach. *Journal of The Electrochemical Society*, 157(10):B1382, 2010.

C. W. Hirt and B. D. Nichols. Volume of fluid (vof) method for the dynamics of free boundaries. *Journal of computational physics*, 39(1):201–225, 1981.

J. Hoshen and R. Kopelman. Percolation and cluster distribution. i. cluster multiple labeling technique and critical concentration algorithm. *Physical Review B*, 14(8):3438, 1976.

T. Koido, T. Furusawa, and K. Moriyama. An approach to modeling two-phase transport in the gas diffusion layer of a proton exchange membrane fuel cell. *Journal of Power Sources*, 175: 127–136, 2008. ISSN 03787753.

P. Krüger, H. Markötter, J. Haußmann, M. Klages, T. Arlt, J. Banhart, C. Hartnig, I. Manke, and J. Scholta. Synchrotron x-ray tomography for investigations of water distribution in polymer electrolyte membrane fuel cells. *Journal of Power Sources*, 196(12):5250–5255, 2011.

S. P. Kuttanikkad, M. Prat, and J. Pauchet. Pore-network simulations of two-phase flow in a thin porous layer of mixed wettability: Application to water transport in gas diffusion layers of proton exchange membrane fuel cells. *Journal of Power Sources*, 196(3):1145–1155, 2011.

J. M. LaManna, S. Chakraborty, J. J. Gagliardo, and M. M. Mench. Isolation of transport mechanisms in pefcs using high resolution neutron imaging. *International Journal of Hydrogen Energy*, 39(7):3387–3396, 2014.

J. Larminie. *Fuel cell systems explained*. J. Wiley, Chichester, West Sussex, 2nd ed edition, 2003.

K.-J. Lee, J. H. Nam, and C.-J. Kim. Pore-network analysis of two-phase water transport in gas diffusion layers of polymer electrolyte membrane fuel cells. *Electrochimica Acta*, 54(4): 1166–1176, 2009.

K.-J. Lee, J. H. Kang, J. H. Nam, and C.-J. Kim. Steady liquid water saturation distribution in hydrophobic gas-diffusion layers with engineered pore paths: An invasion-percolation pore-network analysis. *Journal of Power Sources*, 195(11):3508–3512, June 2010a. ISSN 03787753.

K.-J. Lee, J. H. Nam, and C.-J. Kim. Steady saturation distribution in hydrophobic gas-diffusion layers of polymer electrolyte membrane fuel cells: A pore-network study. *Journal of Power Sources*, 195(1):130–141, 2010b. ISSN 03787753.

K.-J. Lee, J. H. Kang, and J. H. Nam. Liquid water distribution in hydrophobic gas-diffusion layers with interconnect rib geometry: An invasion-percolation pore network analysis. *International Journal of Hydrogen Energy*, 39(12):6646–6656, 2014.

R. Lenormand, E. Touboul, and C. Zarcone. Numerical models and experiments on immiscible displacements in porous media. *Journal of Fluid Mechanics*, 189:165–187, 1988.

X. Li and I. Sabir. Review of bipolar plates in pem fuel cells: Flow-field designs. *International Journal of Hydrogen Energy*, 30(4):359–371, 2005.

Z. Lu, M. M. Daino, C. Rath, and S. G. Kandlikar. Water management studies in PEM fuel cells, part III: Dynamic breakthrough and intermittent drainage characteristics from GDLs with and without MPLs. *International Journal of Hydrogen Energy*, 35(9):4222–4233, 2010.

G. Luo, Y. Ji, C.-Y. Wang, and P. K. Sinha. Modeling liquid water transport in gas diffusion layers by topologically equivalent pore network. *Electrochimica Acta*, 55:5332–5341, 2010. ISSN 00134686.

G. Álvarez, F. Alcaide, P. L. Cabot, M. J. Lázaro, E. Pastor, and J. Solla-Gullón. Electrochemical performance of low temperature PEMFC with surface tailored carbon nanofibers as catalyst support. *International Journal of Hydrogen Energy*, 37(1):393–404, Jan. 2012.

I. Manke, C. Hartnig, M. Grünerbel, W. Lehnert, N. Kardjilov, A. Haibel, A. Hilger, J. Banhart, and H. Riesemeier. Investigation of water evolution and transport in fuel cells with high resolution synchrotron x-ray radiography. *Applied Physics Letters*, 90(17):174105, 2007.

B. Markicevic, A. Bazylak, and N. Djilali. Determination of transport parameters for multiphase flow in porous gas diffusion electrodes using a capillary network model. *Journal of Power Sources*, 171(2):706–717, 2007.

H. Markötter, K. Dittmann, J. Haußmann, R. Alink, D. Gerteisen, H. Riesemeier, J. Scholta, J. Banhart, and I. Manke. Influence of local carbon fibre orientation on the water transport in the gas diffusion layer of polymer electrolyte membrane fuel cells. *Electrochemistry Communications*, 51:133–136, 2015.

H. Markötter, R. Alink, J. Haußmann, K. Dittmann, T. Arlt, F. Wieder, C. Tötzke, M. Klages, C. Reiter, H. Riesemeier, J. Scholta, D. Gerteisen, J. Banhart, and I. Manke. Visualization of the water distribution in perforated gas diffusion layers by means of synchrotron X-ray radiography. *International Journal of Hydrogen Energy*, 37(9):7757–7761, 2012.

J. C. Maxwell. On the dynamical theory of gases. *Philosophical transactions of the Royal Society of London*, pages 49–88, 1867.

G. R. McNamara and G. Zanetti. Use of the boltzmann equation to simulate lattice-gas automata. *Physical Review Letters*, 61(20):2332, 1988.

E. F. Médici and J. S. Allen. Evaporation, two phase flow, and thermal transport in porous media with application to low-temperature fuel cells. *International Journal of Heat and Mass Transfer*, 65:779–788, Oct. 2013. ISSN 00179310.

P. P. Mukherjee, Q. Kang, and C.-Y. Wang. Pore-scale modeling of two-phase transport in polymer electrolyte fuel cells—progress and perspective. *Energy & Environmental Science*, 4(2):346, 2011.

J. H. Nam and M. Kaviany. Effective diffusivity and water-saturation distribution in single-and two-layer PEMFC diffusion medium. *International Journal of Heat and Mass Transfer*, 46 (24):4595–4611, 2003.

J. H. Nam, K.-J. Lee, G.-S. Hwang, C.-J. Kim, and M. Kaviany. Microporous layer for water morphology control in PEMFC. *International Journal of Heat and Mass Transfer*, 52(11-12): 2779–2791, 2009.

E. Nishiyama and T. Murahashi. Water transport characteristics in the gas diffusion media of proton exchange membrane fuel cell – Role of the microporous layer. *Journal of Power Sources*, 196(4):1847–1854, 2011.

S. Park and B. N. Popov. Effect of hydrophobicity and pore geometry in cathode GDL on PEM fuel cell performance. *Electrochimica Acta*, 54(12):3473–3479, 2009.

U. Pasaogullari and C. Y. Wang. Liquid Water Transport in Gas Diffusion Layer of Polymer Electrolyte Fuel Cells. *Journal of The Electrochemical Society*, 151(3):A399, 2004.

J. Pauchet, M. Prat, P. Schott, and S. P. Kuttanikkad. Performance loss of proton exchange membrane fuel cell due to hydrophobicity loss in gas diffusion layer: Analysis by multiscale approach combining pore network and performance modelling. *International Journal of Hydrogen Energy*, 37(2):1628–1641, 2012.

M. Prat and T. Agaësse. *Chapter 4: Thin Porous Media, Handbook of Porous Media, Third Edition*. 2015.

Z. Qi and A. Kaufman. Improvement of water management by a microporous sublayer for pem fuel cells. *Journal of Power Sources*, 109(1):38–46, 2002.

C. Qin. Water transport in the gas diffusion layer of a polymer electrolyte fuel cell: Dynamic pore-network modeling. *Journal of The Electrochemical Society*, 162(9):F1036–F1046, 2015.

R. Ramasamy, E. Kumbur, M. Mench, W. Liu, D. Moore, and M. Murthy. Investigation of macro- and micro-porous layer interaction in polymer electrolyte fuel cells. *International Journal of Hydrogen Energy*, 33(13):3351–3367, 2008.

M. Rebai and M. Prat. Scale effect and two-phase flow in a thin hydrophobic porous layer. Application to water transport in gas diffusion layers of proton exchange membrane fuel cells. *Journal of Power Sources*, 192(2):534–543, 2009.

D. H. Rothman. Cellular-automaton fluids: A model for flow in porous media. *Geophysics*, 53(4): 509–518, 1988.

A. D. Santamaria, M. K. Becton, N. J. Cooper, A. Z. Weber, and J. W. Park. Effect of cross-flow on pefc liquid-water distribution: An in-situ high-resolution neutron radiography study. *Journal of Power Sources*, 293:162–169, 2015.

C. F. Schönbein. On the odour accompanying electricity and on the probability of its dependence on the presence of a new substance. *Philosophical Magazine*, 17:293–294., 1840.

M. Shahraeeni and M. Hoorfar. Experimental and numerical comparison of water transport in untreated and treated diffusion layers of proton exchange membrane (PEM) fuel cells. *Journal of Power Sources*, 238:29–47, 2013.

M. Shahraeeni and M. Hoorfar. Pore-network modeling of liquid water flow in gas diffusion layers of proton exchange membrane fuel cells. *International Journal of Hydrogen Energy*, 39 (20):10697–10709, 2014.

T. Shan and T. Kailath. Adaptive algorithms with an automatic gain control feature. *Circuits and Systems, IEEE Transactions on*, 35(1):122–127, 1988.

P. K. Sinha and C.-Y. Wang. Pore-network modeling of liquid water transport in gas diffusion layer of a polymer electrolyte fuel cell. *Electrochimica Acta*, 52(28):7936–7945, 2007.

P. K. Sinha and C.-Y. Wang. Liquid water transport in a mixed-wet gas diffusion layer of a polymer electrolyte fuel cell. *Chemical Engineering Science*, 63(4):1081–1091, 2008.

J. Stefan. Ueber das gleichgewicht und die bewegung insbesondere die diffusion von gasgemengen. *Akad. Wiss. Wien*, 63:63–124, 1871.

B. Straubhaar, J. Pauchet, and M. Prat. Water transport in gas diffusion layer of a polymer electrolyte fuel cell in the presence of a temperature gradient. phase change effect. *International Journal of Hydrogen Energy*, 40(35):11668 – 11675, 2015.

H. Tawfik, Y. Hung, and D. Mahajan. Metal bipolar plates for PEM fuel cell—A review. *Journal of Power Sources*, 163(2):755–767, 2007.

K. E. Thompson. Pore-scale modeling of fluid transport in disordered fibrous materials. *AIChE journal*, 48(7):1369–1389, 2002.

Y. M. Volfkovich, V. S. Bagotzky, V. E. Sosenkin, and I. A. Blinov. The standard contact porosimetry. *Colloids and Surfaces A: Physicochemical and Engineering Aspects*, 187:349–365, 2001.

B. Wang. Recent development of non-platinum catalysts for oxygen reduction reaction. *Journal of Power Sources*, 152:1–15, Dec. 2005.

C. Wang and P. Cheng. A multiphase mixture model for multiphase, multicomponent transport in capillary porous media—i. model development. *International journal of heat and mass transfer*, 39(17):3607–3618, 1996.

X. Wang and T. Van Nguyen. Modeling the Effects of the Microporous Layer on the Net Water Transport Rate Across the Membrane in a PEM Fuel Cell. *Journal of The Electrochemical Society*, 157(4):B496, 2010.

Y. Wang, L. Wang, S. G. Advani, and A. K. Prasad. Double-layer gas diffusion media for improved water management in polymer electrolyte membrane fuel cells. *Journal of Power Sources*, 292: 39–48, 2015.

A. Z. Weber and J. Newman. Effects of Microporous Layers in Polymer Electrolyte Fuel Cells. *Journal of The Electrochemical Society*, 152(4):A677, 2005.

A. Z. Weber, R. M. Darling, and J. Newman. Modeling Two-Phase Behavior in PEFCs. *Journal of The Electrochemical Society*, 151(10):A1715, 2004.

A. Z. Weber, R. L. Borup, R. M. Darling, P. K. Das, T. J. Dursch, W. Gu, D. Harvey, A. Kusoglu, S. Litster, M. M. Mench, and others. A Critical Review of Modeling Transport Phenomena in Polymer-Electrolyte Fuel Cells. *Journal of The Electrochemical Society*, 161(12):F1254–F1299, 2014.

D. Wilkinson and J. F. Willemsen. Invasion percolation: a new form of percolation theory. *Journal of Physics A: Mathematical and General*, 16(14):3365, 1983.

R. Wu, Q. Liao, X. Zhu, and H. Wang. Impacts of the mixed wettability on liquid water and reactant gas transport through the gas diffusion layer of proton exchange membrane fuel cells. *International Journal of Heat and Mass Transfer*, 55(9-10):2581–2589, 2012a.

R. Wu, Q. Liao, X. Zhu, and H. Wang. Liquid and oxygen transport through bilayer gas diffusion materials of proton exchange membrane fuel cells. *International Journal of Heat and Mass Transfer*, 2012b.

R. Wu, X. Zhu, Q. Liao, R. Chen, and G.-M. Cui. Liquid and oxygen transport in defective bilayer gas diffusion material of proton exchange membrane fuel cell. *International Journal of Hydrogen Energy*, 38(10):4067–4078, 2013.

R. Wu, G.-M. Cui, and R. Chen. Pore network study of slow evaporation in hydrophobic porous media. *International Journal of Heat and Mass Transfer*, 68:310–323, 2014.

I. V. Zenyuk, D. Y. Parkinson, G. Hwang, and A. Z. Weber. Probing water distribution in compressed fuel-cell gas-diffusion layers using x-ray computed tomography. *Electrochemistry Communications*, 53:24–28, 2015.

J. Zhang, Z. Xie, J. Zhang, Y. Tang, C. Song, T. Navessin, Z. Shi, D. Song, H. Wang, D. P. Wilkinson, et al. High temperature pem fuel cells. *Journal of power Sources*, 160(2):872–891, 2006.